Magnetic Trapping of Atomic Chromium and Molecular Calcium Monohydride

A thesis presented

by

Jonathan David Weinstein

to

The Department of Physics

in partial fulfillment of the requirements

for the degree of

Doctor of Philosophy

in the subject of

Physics

Harvard University

Cambridge, Massachusetts

December 2001

To my parents,

of course.

Thesis advisor
John Morrissey Doyle

Author
Jonathan David Weinstein

Magnetic Trapping of Atomic Chromium and Molecular Calcium Monohydride

Abstract

In this thesis, I describe two trapping experiments: the magnetic trapping of atomic chromium and the magnetic trapping of molecular calcium monohydride. Experimental work with molecular vanadium monoxide will also be discussed.

Building on previous work trapping atomic europium, the calcium monohydride experiment was a successful demonstration of the feasibility of magnetically trapping a neutral molecule. We studied the dynamics of our molecular cooling and trapping techniques. In addition, cold molecule-atom interactions were explored in the CaH–He system at sub-Kelvin temperatures.

VO was employed in our first attempt, which failed, to magnetically trap a molecule. The reasons for the experiment's failure were investigated, and various properties of VO measured at low temperatures.

The chromium experiment was designed to cool trapped chromium atoms with the goal of creating a coexisting Bose-Einstein condensate and degenerate Fermi gas. The experimental plan was to use buffer-gas loading to magnetically trap large numbers of fermion and boson isotopes of chromium, and then use evaporative cooling to increase the phase space density until degeneracy was reached. Although we have not yet reached quantum degeneracy, we were able to trap and evaporatively cool both desired isotopes simultaneously and measure relevant chromium–chromium collisional properties. These results illuminate some of the broader issues involved with our cryogenics-based experimental techniques.

Contents

Title Page i
Dedication iii
Abstract iv
Table of Contents v
Citations to Previously Published Work xi
Acknowledgements xii

1 Introduction **1**
1.1 Atom trapping and cooling 1
1.2 Bose-Einstein condensates 3
1.3 Degenerate Fermi gases 5
1.4 Molecule trapping 6
1.5 Comparison of atom and molecule cooling methods 7

2 Overview of the Experimental Techniques **13**
2.1 Magnetic trapping 13
2.2 Buffer-gas loading 17
2.3 Laser ablation 25
2.4 Evaporative cooling 27
2.5 Collisions 28

3 Calcium Monohydride **39**
3.1 CaH spectroscopic structure 39
3.2 Cryogenics 41
3.3 Optics 45
3.4 Preliminary experiments 49
3.5 Zeeman structure of CaH 55
3.6 Magnetic trapping 58
3.7 CaH–He collisions 64
3.8 Conclusions and future prospects 71

4 Vanadium Monoxide **72**
4.1 VO spectroscopic structure 72

4.2 Experimental apparatus . . . 73
4.3 Low temperature spectroscopy . . . 74
4.4 VO loss . . . 79

5 Chromium Cryogenic Apparatus 83
5.1 The magnet . . . 83
5.2 Optical access . . . 92
5.3 The copper cell . . . 94
5.4 The composite metal cell . . . 94
5.5 The plastic cell . . . 96
5.6 Failed cell designs . . . 104
5.7 Cryogenic thermometry . . . 108

6 Chromium Experiments 111
6.1 Chromium atomic structure . . . 111
6.2 Spectroscopic detection of chromium. . . . 113
6.3 Buffer-gas loading of chromium . . . 119
6.4 Cr–He collisions . . . 131
6.5 Evaporative cooling of chromium . . . 134
6.6 Cr–Cr Collisions . . . 137
6.7 Possible physical mechanisms behind Cr–Cr collisions . . . 144
6.8 Future prospects . . . 146

A Spectrum Fitting 149
A.1 The two-level atom and inhomogeneous broadening . . . 149
A.2 The atomic distribution and the probe laser . . . 150
A.3 Multi-level atoms and polarization effects . . . 151
A.4 Actual implementation . . . 154
A.5 Additional computational simplifications . . . 157
A.6 Molecules, hyperfine structure, multiple electronic levels, and other reductions of σ . . . 158
A.7 The problem with $\Delta m = 0$ transitions . . . 160

B Adiabatic Expansion 162

C Gravity 164

D Majorana 166

E Elastic Cross-section Measurement 169

F Wind 171

G Noise **173**
G.1 Shot noise 173
G.2 Electrical noise 174
G.3 Absorption vs. fluorescence spectroscopy 175
G.4 Technical noise 176

H Cr Information **178**

I ^{53}Cr Hyperfine Structure **182**

J Symbol Definitions **188**

Bibliography **191**

List of Figures

2.1 Zeeman structure of the ground state of atomic hydrogen 14
2.2 Anti-Helmholtz trap 15
2.3 Helium equilibrium vapor density 19
2.4 Lower limit of the trap lifetime during buffer-gas loading 21
2.5 Simple model of the trap lifetime during buffer-gas-loading in the short-mean-free-path regime 24

3.1 CaH cryostat 42
3.2 Copper cell 43
3.3 CaH detection optics schematic 46
3.4 CaH zero-field spectrum 51
3.5 CaH zero-field spectrum 52
3.6 CaH ablation yield as a function of ablation power 53
3.7 CaH ablation yield as a function of buffer-gas density 54
3.8 CaH ablation glow 55
3.9 CaH Zeeman structure 56
3.10 CaH Zeeman splitting 57
3.11 CaH early time spectrum 58
3.12 CaH spectrum vs. time 60
3.13 CaH spectrum fit 61
3.14 CaH trap population vs. time 62
3.15 CaH trap lifetime as a function of trap depth 63
3.16 CaH diffusion 66
3.17 CaH excited vibrational state lifetime 67
3.18 CaH spectrum vs. time in a high density of ^{3}He 69
3.19 CaH trap population vs. time in a high density of ^{3}He 70

4.1 VO spectrum vs. time 75
4.2 VO translational temperature 77
4.3 VO rotational temperature 78
4.4 VO population vs. time, without the magnetic trap 79
4.5 VO and Eu population vs. time, without the magnetic trap 80
4.6 VO population vs. time, with and without the magnetic trap 81

4.7 VO "glow" 82

5.1 Magnetic field "jumps" 85
5.2 Atom loss due to magnetic field jumps 86
5.3 Field profile of the 3" magnet 87
5.4 3" magnet schematic 89
5.5 Residual magnetic fields 92
5.6 Cryostat windows 93
5.7 Plastic cell 97
5.8 "Lasso" standoff 101
5.9 Thermal conductance of the superfluid heatlink 104
5.10 Thermal conductance of the heat exchanger 105
5.11 Trap loss due to a failed cell design 106
5.12 Changes in the cell design 107
5.13 RuO_2 resistance as the field is ramped 110

6.1 Chromium Zeeman structure 112
6.2 Chromium detection optics schematic 114
6.3 Chromium trap spectrum and fit 119
6.4 Chromium trap lifetime (with buffer gas) as a function of η 122
6.5 Chromium trap loss 123
6.6 Chromium trap loss vs. cell temperature 124
6.7 Cell temperature during a typical loading cycle 125
6.8 Chromium isotopes in the trap 126
6.9 Trap loading with multiple ablation pulses 128
6.10 Cell temperature during warm and cold loading 129
6.11 Atoms loss due to buffer-gas "wind" 131
6.12 Chromium diffusion lifetime 132
6.13 Evidence of inelastic Cr–^{3}He collisions 134
6.14 Evaporative cooling progress 136
6.15 Fit to chromium trap loss 137
6.16 Chromium optical pumping 139
6.17 Chromium optical pumping fit 140
6.18 Chromium collisional rate coefficients 141
6.19 Chromium equilibrium η 143

A.1 Δm selection rules in the trap 153
A.2 Chromium spectrum on a $\Delta m = 0$ transition 161

C.1 The trap potential, including gravity 165

H.1 Chromium Clebsch-Gordan coefficients 181

I.1 ^{53}Cr ground state Zeeman structure 185

I.2 Zeeman shift of the ^{53}Cr $^7S_3 \rightarrow ^7P_3$ transitions 187

Citations to Previously Published Work

Portions of this thesis have appeared previously in the following papers:

"Evaporative cooling of atomic chromium", Jonathan D. Weinstein, Robert deCarvalho, Cindy I. Hancox, and John M. Doyle, accepted for publication in *Physical Review A* (2001).

"Magnetic trapping of calcium monohydride molecules at millikelvin temperatures", Jonathan D. Weinstein, Robert deCarvalho, Thierry Guillet, Bretislav Friedrich, and John M. Doyle, *Nature* **395**, 148–150 (1998).

"Spectroscopy of buffer-gas cooled vanadium monoxide in a magnetic trapping field', Jonathan D. Weinstein, Robert deCarvalho, Karine Amar, Andreea Boca, Brian C. Odom,Bretislav Friedrich, and John M. Doyle, *Journal of Chemical Physics* **109**, 2656–2661 (1998).

"Magnetic trapping of atomic chromium", Jonathan D. Weinstein, Robert deCarvalho, Jinha Kim, David Patterson, Bretislav Friedrich, and John M. Doyle, *Physical Review A* **57**, R3173–3175 (1998).

Acknowledgements

The experimental work described in this thesis is the product of a collaboration of many people to whom I am deeply grateful. It is a pleasure to acknowledge them.

I thank my advisor, John Doyle, for not only providing an exciting research program to work on and the support and guidance to pursue it successfully, but for providing a good environment to work in. I feel I have learned a great deal as a graduate student in his laboratory, and am grateful for being his student.

I thank the many people who have worked with me on these experiments. I especially want to thank Jinha Kim and David Patterson, for their work on the experiment before me and with me; Bretislav Friedrich, for his experimental work and his patient explanations of molecular physics; Cindy Hancox, for her work on the chromium trapping experiment; Dima Egorov, for his work on our superconducting magnet; Robert Michniak, for his laser ablation work; and Robert deCarvalho, for his work on every experiment described in this thesis. It has been a pleasure to work so closely with Robert deCarvalho. This thesis is as much a product of his labratory work as it is mine.

I am deeply grateful for the wonderful friends I have met at Harvard, both in and out of lab. You have truly made graduate school tolerable.

Of course, I thank my family for their continued love and support throughout my life. I am deeply thankful for all they have done for me, and will always feel great gratitude and affection for them.

Finally, I would like to thank all the members of the "physics community", both teachers and fellow students, who have taught and encouraged me. I have found the field of physics to be a surprisingly welcoming place, and I thank you for it.

Chapter 1

Introduction

The central goals of this thesis are the cooling and magnetic trapping of atoms and molecules, the study of atomic and molecular collisions, and the formation of an atomic Bose-Einstein condensate and degenerate Fermi gas.

1.1 Atom trapping and cooling

Atom trapping (the confinement of atoms in vacuum via electromagnetic fields) and atom cooling are symbiotic. Trapping atoms aids in their subsequent cooling, but atoms must be cooled in order to be efficiently trapped.

The primary motivation behind trapping and cooling is to approach the "experimental ideal" of an unperturbed species at rest in space. This will improve spectroscopic sensitivity by reducing motional (Doppler) effects and increasing interaction times. Through appropriate trapping and cooling, one can reduce the usual sources of spectal line broadening and shifts that arise from atomic motions. But in addition to these spectroscopic improvements, remarkable new phenomena have been observed in trapped and cooled atoms.

Ion trapping

The field of neutral atom trapping is predated by the closely related field of ion trapping. Ion traps provide both isolation from the environment and long interaction times: ideal conditions for spectroscopic measurements. By confining an electron in a Penning trap, its magnetic moment (specifically, the electron g-factor, a num-

ber of great consequence) was measured to unprecedented precision [1]. Similarly, trapped and cryogenically cooled atomic ions have allowed mass spectroscopy at an accuracy greater than one part per billion [2]. Optical and microwave spectroscopy of both atomic and molecular ions also benefit from trapping [3]. For example, optical spectroscopy of a single laser-cooled ion in an rf ion trap has afforded sub-dekahertz spectroscopic precision and a fractional accuracy approaching 10^{-14} [4]. This technical achievement will likely play a significant role in future generations of atomic clocks.

But the experimental control offered by ion traps has done much more than improve spectroscopic measurements, and has allowed the creation and observation of exciting quantum-mechanical phenomena. For example, a combination of cooling and trapping techniques has made it possible to deterministically control not only the internal and external state of trapped ions, but also the interaction between them. This has been used to create a quantum-mechanical entangled state. With these techniques, a four-ion "Schrödinger cat" maximally entangled state has been created in an ion trap [5]. This is an explicit demonstration of the nonlocal character of quantum mechanics, and has possible applications in multi-particle intereferometry. When combined with the long decoherence times of ion traps, this engineered entanglement is an important step towards the development of quantum computing [6].

The Achilles' heel of ion traps is their particle number. In a typical $\sim$cm sized trap, it is impractical to store more than 10^6 ions [3]. Additionally, because of the strong coulomb repulsion between ions, trapped ions perturb each other tremendously. This coulombic repulsion also limits the ion density obtainable. Neutral atoms do not suffer from these limitations.

Neutral atom trapping

The field of cooling and trapping of neutral atoms quickly proved to be extremely fruitful. Cooled neutral atoms are used in atom interferometry [7] and atom lithography [8]. The current generation of atomic clocks use trapped and cooled atoms as an atomic source [9]. Studies of ultracold atoms have improved atomic spectroscopy and aided not only in the measurement of single-atom properties, but also of long-range interatomic molecular potentials [10, 11].

Atom trapping and cooling have given rise to a new field of study: ultracold atomic

collisions. At sufficiently low temperatures, atomic collisions are highly quantum mechanical in nature, and differ from "usual" atomic collisions in a variety of ways [12]. As described by Thad Walker and Paul Feng in "Measurements of collisions between laser-cooled atoms",

> Cold and ultracold collisions occupy a strategic position at the intersection of several powerful themes of current research in chemical physics, in atomic, molecular, and optical physics, and even in condensed matter. The nature of these collisions bears critically on optical manipulation of inelastic and reactive processes, precision measurement of molecular and atomic properties, matter-wave coherences and quantum-statistical condensates of dilute, weakly interacting atoms. [13]

Additionally, these ultracold atomic collisions often can be strongly "tuned" through the use of external fields and other means [14].

Finally, perhaps the most exciting product of the trapping and cooling of neutral atoms is the creation of quantum degenerate atomic gases: Bose-Einstein condensates and degenerate Fermi gases.

1.2 Bose-Einstein condensates

Bose-Einstein condensation is a consequence of quantum-mechanical identical particle symmetry and statistical mechanics. If the phase-space density[1] of a weakly interacting boson gas exceeds the threshold value of 2.612, the system undergoes a phase transition and a Bose-Einstein condensate (BEC) forms: a macroscopic number of particles occupy the ground quantum-mechanical state [15].

Atomic BEC's were first seen in alkali atom systems [16, 17, 18], followed by atomic hydrogen [19] and metastable helium [20, 21]. These achievements have met with considerable acclaim. Although manifestations of BEC had previously been observed in superfluid helium and superconductivity, atomic BEC's provide powerful experimental capabilities to manipulate and study them in great detail and are amenable to theoretical analysis because the interatomic interactions are relatively weak [22]. Additionally, as described by Ketterle, Durfee, and Stamper-Kurn in "Making, probing

[1]The peak phase space density of a thermal distribution is equal to the atom density times the cube of the thermal deBroglie wavelength: $D = n\lambda_{dB}^3$, where $\lambda_{dB} = \sqrt{2\pi\hbar/mk_{\mathrm{B}}T}$.

and understanding Bose-Einstein condensates",

> The realization of Bose-Einstein condensation in dilute atomic gases achieved several long-standing goals. First, neutral atoms were cooled into the lowest energy state, thus exerting ultimate control over the motion and position of atoms, limited only by Heisenberg's uncertainty relation. Second, a coherent macroscopic sample of atoms all occupying the same quantum state was generated, leading to the realization of atom lasers, devices which generate coherent matter waves. Third, degenerate quantum gases were produced with properties quite different from the quantum liquids ^{3}He and ^{4}He. This provides a testing ground for many-body theories of the dilute Bose gas which were developed many decades ago but never tested experimentally. BEC of dilute atomic gases is a macroscopic quantum phenomenon with similarities to superfluidity, superconductivity and the laser. [23]

Despite the short period of time (less than a decade) since they were first observed, atomic BEC's have exhibited a wealth of interesting phenomena and found application in a wide variety of experiments. For example, the formation, coherence, and collapse of the condensate have been studied [24, 25, 26, 27]. Superfluidity and the structure of a highly-ordered vortex lattice inside the superfluid condensate have been observed [28, 29]. The condensate is a coherent matter wave and has been used to produce an atom laser [30]. Both coherent matter wave amplification and nonlinear 4-wave mixing effects have been seen [31, 32]. Additionally, BEC's have been vital to a variety of seemingly unrelated atomic physics experiments, such as high resolution molecular spectroscopy and the generation of highly number-squeezed atomic states [33, 34]. The field of atomic Bose condensates is an exciting and active field which shows no signs of abating.

Production of Bose-Einstein condensates

The most common experimental method currently used to produce an atomic BEC is the following: atoms are initially laser cooled, magnetically trapped, and brought to quantum degeneracy through evaporative cooling.[2] A central goal of this thesis is to

[2]These three techniques are discussed in Sections 1.5, 2.1, and Section 2.4, respectively. Other successful experimental paths to BEC replace the magnetic trap by an optical trap [35] or replace the intial laser-cooling step with cryogenic surface thermalization (as discussed in Section 1.5) [19].

explore the feasibility and potential advantages of using buffer-gas loading (Section 2.2) as the intial step in the creation of a quantum degenerate gas.

1.3 Degenerate Fermi gases

As the phase-space density of a weakly interacting Fermi gas approaches unity, its behavior deviates from that of a classical gas. For fermions, the consequence of identical particle symmetry in the degenerate regime is the formation of a "filled Fermi sphere": states with energy less than the Fermi energy (E_F) have an occupation number approaching unity, states with energy greater than E_F have occupation number approaching zero [15]. Perhaps the most famous example of this phenomenon is the behavior of conduction electrons in a metal.

By using experimental techniques similar to those used to create atomic Bose-Einstein condensates, degenerate Fermi gases have recently been created in a variety of atomic systems [36, 37, 38]. The current state of the art for these degenerate Fermi gases is a atom number of $N \lesssim 10^6$, temperatures approaching 20% of the Fermi temperature, and Fermi energies as high as 1 μK.

The field of degenerate atomic Fermi gases is quite young, and many interesting phenomena are expected. Many of these effects are closely related to the modification of the the "available phase space" within the filled Fermi sphere. Because two identical Fermions cannot occupy the same quantum-mechanical state, the presence of the filled Fermi sphere strongly affects any atomic process in which the atom's motional state might be changed.

One consequence of the Fermi sphere is the suppression of collisions: because there are no available states for atoms to scatter into, atom-atom collisions are suppressed.[3] This effect has been experimentally observed by DeMarco, Papp, and Jin in Reference [39].

There should be similar consequences for light-scattering. Much as cavity quantum electrodynamics modifies the interaction of light with atoms by manipulating the structure of the photon phase-space [40], a Fermi degenerate gas will change the light scattering properties of an atom by modifying the available atomic phase-space

[3]This collisional transparency occurs only for collision energies $E \lesssim E_F$, of course. Collsions of energy $E \gg E_F$ are unaffected.

[41, 42, 43, 44]. Such linewidth-narrowing effects have not yet been observed, and require a large Fermi energy ($E_F \gtrsim E_R$, the photon recoil energy) to play a significant role in light scattering.

The more exotic phenomenon of Cooper-pairing is expected to arise in atomic Fermi degenerate gases at very low temperatures. Below a certain critical temperature (which depends strongly on the atom-atom interactions in the Fermi degenerate gas), a BCS-like phase transition to a superfluid state is expected to occur [45, 46]. This is analogous to the condensed-matter phenomenon of superconductivity, which arises from the interaction of a degenerate Fermi gas of electrons in a metal. While there are a variety of proposed methods for creating a Cooper-pairing mechanism in an atomic Fermi gas, they uniformly require a combination of low temperatures, a high Fermi energy, and large atom-atom interactions [47, 48, 49, 50]. These conditions have not yet been realized in the laboratory.

The experimental goal of our chromium experiment is to achieve Fermi degeneracy with a large number of tightly confined magnetically trapped ^{53}Cr atoms. The combination of large number and tight confinement will result in a large Fermi energy, which is favorable for observing the effects of Fermi degeneracy. Additionally, we aim to create an ultra-high vaccum environment, which may help in achieving lower Fermi gas temperatures [51].

1.4 Molecule trapping

Just as the cooling and trapping of ions and neutral atoms has lead to a wealth of important new physics, the trapping and cooling of molecules will likely open up new areas of ultracold molecular physics and, perhaps, chemistry.

As with atoms, a key motivation behind cooling molecules is simply to slow them down. As a gas of molecules is cooled, their average velocity is decreased and the spread of their molecular velocities narrowed. Thus, cooling allows longer measurements (because the molecules move out of the measuring apparatus more slowly) and reduces the Doppler broadening due to the velocity spread. Both of these effects lead to more sensitive measurements and improved molecular spectroscopy.

This is important not only for studying molecular physics, but also for studying fundamental physics. The internal structure of certain molecules provides an ideal "laboratory" for sensitive measurements of fundamental physical quantities. For ex-

ample, highly polar paramagnetic molecules are ideal for searches for the electron's electric dipole moment, a currently undetected physical quantity of significant consequence for fundamental physics [52]. Such experiments are currently underway, using the heavy, polar, and paramagnetic molecules YbF and PbO [53, 54]. The ability to produce large numbers of ultracold molecules could potentially greatly improve such measurements.

Additionally, we expect the collisional properties of ultracold molecules to be of significant interest. Like ultracold atoms, the large de Broglie wavelengths of colliding ultracold molecules will result in non-classical collisional properties. But the internal structure of molecules is more complex than that of atoms, and two colliding molecules can undergo chemical reactions [55]. For these reasons, one would expect the field of ultracold molecular collisions to be richer than that of atoms [56, 57, 58].

The molecular trapping work in this thesis is a preliminary step towards these goals.

1.5 Comparison of atom and molecule cooling methods

In the experimental work of this thesis, atoms and molecules are cooled for trapping via a technique called buffer-gas loading. In the present section, we discuss many methods of producing cold atoms and molecules which were *not* employed in this thesis. It is important to consider these other techniques to understand how the work of this thesis fits into the fields of ultracold molecules and neutral atom trapping.

Laser cooling

The first demonstrated and most widely used method of cooling neutral atoms for magnetic trapping is laser cooling [59, 60]. Laser cooling is a remarkably powerful technique which has been implemented in many different ways [61, 62, 63]. It is commonly used not only to prepare atoms for magnetic trapping, but to provide a high-intensity, low energy source of neutral atoms for a wide variety of atomic physics experiments.

Laser cooling cools atoms by resonantly scattering appropriately tuned laser light. Each scattered photon gives the atom an $\sim \hbar k$ momentum kick and slows the atom's

motion. However, because the momentum of a single photon is so small, thousands of photons must be scattered in order to slow an atom from the high temperatures at which they are typically produced (on the order of 1000 K) to the cold temperatures (on the order of 1 K) required for trapping. For laser cooling to work efficiently, each time the atom scatters a photon, it must return (or be returned) to its original internal state so that it can repeat the light scattering process. This limits the applicability of laser cooling to those atoms with a reliable "cycling transition" at a laser-accessible wavelength. And while there are multiple atoms for which laser cooling works beautifully, the complicated rotational and vibrational internal structure of molecules precludes using laser cooling.

In addition to this limitation on which species laser cooling can be applied to, there are limits to the densities and numbers of atoms that can be obtained through laser cooling. The optical density of the atomic cloud, inelastic collisions between ground-state and excited-state atoms, and laser power requirements all place limitations on the number or density of atoms obtainable through laser cooling.

The current state of the art for the number of atoms that can be laser cooled for magnetic trapping is the magneto-optical trap (MOT). The "dark SPOT" variant of the MOT has been demonstrated to (when fed by a high-intensity atomic beam cooled by a Zeeman slower) trap up to $N \sim 5 \times 10^{10}$ atoms at a density of 7×10^{11} cm^{-3} and a temperature of ~ 1 mK [64]. It should be possible to transfer these atoms into a magnetic trap with efficiency of order unity.

The state of the art phase-space density D which can be achieved by laser cooling is shy of quantum degeneracy, but still quite high. "Laser Raman sideband cooling" has achieved $D \sim 0.01$ with $N \sim 10^8$ at a density of $\sim 10^{12}$ cm^{-3} and a temperature below 1 μK [65, 66]. Doppler cooling of optically trapped strontium on a forbidden optical transition has produced $D \geq 0.1$, but with the comparatively smaller number $N \sim 10^5$ [67].

Cryogenic surface thermalization

Atomic hydrogen can be cooled for magnetic trapping through thermalization with a superfluid helium film on a cryogenically cooled surface [68, 69]. The current state of the art for this cooling method is 10^{14} magnetically trapped hydrogen atoms at a temperature of 40 mK [70]. While this technique can be used to trap many more

atoms than laser cooling methods, it is readily applicable only to atomic hydrogen, as hydrogen's binding properties to superfluid helium are unique.

Producing cold molecules

Neither laser cooling nor cryogenic surface thermalization have yet to be successful in the cooling or trapping of molecules. However, a variety of techniques have recently achieved this goal in different molecular systems.

Molecular beam deceleration

A molecular expansion cools molecules by allowing a gas of molecules to expand out of a nozzle into vacuum, and is a standard tool of molecular spectroscopy [71]. This process can produce a beam of molecules which are vibrationally and rotationally cold and translationally cold with respect to each other, but which all have a very high forward velocity. Because of this peculiar "monochromatic" velocity distribution, specialized methods can be used to decelerate these high velocity molecules in order to potentially capture them with a trap. For example, a molecular beam was slowed mechanically: the nozzle emitting the molecules was simply moved in the direction opposite the molecular flow, producing slower-moving molecules [72]. With this technique,

In other work, pulsed electric fields (on the order of 100 kV cm^{-1}) have been used to slow down a pulsed beam of polar molecules via the molecular Stark shift. With this technique, a pulse of metastable carbon monoxide molecules was decelerated by a series of 63 pulsed electric fields, slowing the beam from 225 m/s to 98 m/s [73, 74]. In subsequent work, ammonia molecules in a pulsed beam were decelerated and loaded into an electrostatic trap. Approximately 10^5 molecules were trapped at a density $n \geq 10^6$ cm^{-3} and temperature $T \leq 0.35$ K. The molecules were then lost from the trap on a timescale of 0.2 s, presumably from collisions with background gas in the vacuum chamber [75].

Photoassociation

An entirely different approach to producing cold molecules is through molecular photoassociation. This elegant technique circumvents the entire problem of directly cooling molecules. In ultracold photoassociation, the atomic constituents of the target

molecule are cooled and ultracold molecules are built directly out of the ultracold atoms. Simple atom-atom collisions alone cannot form a molecule, even if the reaction is energetically favorable. A third body is needed to remove the excess energy and make the reaction possible. Typically, this "catalyst" is a third atom or a photon. In photoassociation, the latter is used to actively form molecules out of individual atoms [76, 77].

The reaction is driven by using a laser to excite two adjacent atoms into an excited state of a bound molecule. The excited molecule will eventually release its extra energy by emitting another photon, a process which will (randomly) produce either a bound molecule or revert the molecule into two unbound atoms. Photoassociation experiments have been conducted with a wide variety of atoms, and ultracold ground state K_2 and Cs_2 molecules have recently been observed to be produced by photoassociation [78, 79]. State of the art production rates are on the order of 10^6 molecules per second (in a variety of rovibrational states), at translational temperatures of hundreds of μK.

Greater efficiency and control can be had over the reaction by using a second laser to actively drive the excited molecule into its ground state. By using stimulated emission rather than spontaneous emission, one can not only increase the likelihood that a molecule is produced, but also use the second laser frequency to select its specific rotational and vibrational state [80, 81, 33].

If photoassociation is conducted inside a trapping potential, the ultracold molecules produced will be trapped. In preliminary experiments, tens of ultracold molecules were trapped [82]. It is expected that with improved production rates, this initial trapping number will soon be greatly increased.

As a side note, we note that photoassociation of ultracold atoms is important not only as a source of ultracold molecules but also as a valuable spectroscopic tool. Photoassociation spectra can provide extremely precise measurements of the interatomic interaction of the molecule's constituent atoms. This has been a vital tool in understanding ultracold atomic collisions [13].

Buffer-gas loading

In this thesis, we use buffer-gas loading to magnetically trap neutral atoms and molecules. Described at length in Section 2.2, buffer-gas loading is a cryogenic tech-

nique which offers significant advantages for neutral particle trapping. The principle virtues of buffer-gas loading are its applicability to a wide variety of both atoms and molecules, and its ability to cool and trap large numbers of them. As described in this thesis, the current state of the art for atomic buffer-gas loading is $N \sim 10^{12}$ magnetically trapped atoms at a temperature of ~ 1 K. With molecules, we have achieved $N \sim 10^8$ magnetically trapped molecules at a temperature of ~ 0.4 K.

Buffer-gas loading as a means of trapping molecules

Of the three techniques demonstrated to produce trapped molecules (photoassociation, pulsed-electric-field beam deceleration, and buffer-gas loading), each is applicable to a different set of molecules. Photoassociation can create only those molecues whose constituent atoms can be precooled; so far, its use has been limited to alkali dimers. Pulsed-electric-field beam deceleration is only applicable to polar molecules with significant Stark shifts. Buffer-gas loading is applicable to magnetic molecules, the majority of which cannot be practically addressed by these other techniques.

The number and density of molecules trapped through buffer-gas loading are much greater than what has been achieved through other methods. The current translational temperatures obtained through buffer-gas loading are comparable to those of pulsed-electric-field beam deceleration, but significantly hotter than those achieved in photoassociation. Potentially, evaporative cooling could be used to further cool buffer-gas loaded, magnetically-trapped molecules.

Buffer-gas loading as a means of trapping atoms

The number and density of atoms trapped by buffer-gas loading are higher than can currently be achieved through laser cooling. Only cryogenic surface thermalization of hydrogen has been shown to trap more atoms. Additionally, buffer-gas loading can be readily applied to atoms (such as europium [83]) which cannot be easily addressed by any other technique. Again, while laser cooling reaches significantly lower temperatures than the *initial* temperature of a buffer-gas-loaded magnetic trap, magnetically trapped atoms can be efficiently evaporatively cooled (as discussed in Section 2.4) to much lower temperatures.

Buffer-gas loading as an initial step towards reaching quantum degeneracy

The largest Bose-Einstein condensates formed from a magnetic trap loaded by laser cooling have $\sim 10^7$ atoms in the condensate [24]. The largest hydrogen BEC's formed are $\sim 10^9$ atoms large, reflecting the larger number of atoms initially trapped through cryogenic surface thermalization [19]. The largest atomic Fermi degenerate gas originated in a magnetic trap loaded by laser cooling, and reached Fermi degeneracy with $\sim 7 \times 10^5$ trapped atoms [36].

We have yet to reach quantum degeneracy with buffer-gas-loaded atoms. However, as described in Chapter 6, buffer-gas loading provides an ideal experimental environment in which to evaporatively cool towards quantum degeneracy. If the atomic collisional parameters were favorable for evaporative cooling, then an extrapolation of the trap numbers obtained in this thesis for atomic chromium would suggest we could form a BEC of $N \sim 5 \times 10^7$ atoms and a Fermi-degenerate gas of $N \sim 5 \times 10^6$ atoms [84].[4] Not only are these buffer-gas loading numbers higher than current state-of-the-art results for all techniques except atomic hydrogen, but (as discussed in Sections 6.3 and 6.8) these numbers have the potential for significant future improvement.

[4] A similar extrapolation for atoms initially cooled by Raman sideband cooling would suggest $N \sim 3 \times 10^7$ at quantum degeneracy [65].

Chapter 2

Overview of the Experimental Techniques

In the experimental work described in this thesis, atoms and molecules are produced by laser ablation, cooled by a helium buffer gas, and magnetically trapped. Additionally, we attempt to increase the phase space density of trapped atomic chromium through evaporative cooling.

2.1 Magnetic trapping

Magnetic trapping uses the atomic (or molecular) Zeeman shift to provide spatial confinement. The Zeeman Hamiltonian [85] is of the form

$$H_{\text{Zeeman}} = (g_e \mu_B/\hbar)\mathbf{B}\cdot\mathbf{S} + (g_l \mu_B/\hbar)\mathbf{B}\cdot\mathbf{L} + \ldots$$

The eigenenergies of this Hamiltonian will depend on the particulars of the species under consideration, but typically it splits degenerate angular momentum states into multiple energy levels. Those states whose energies increase with the applied magnetic field are called "weak-field seekers", while those with decreasing energy in the field are "strong-field-seeking" states. The ground electronic state of hydrogen is shown in Figure 2.1 as an example. In our work, we trap the weak-field seekers by creating a local field minimum in free space. As long as the particle remains in the weak-field-seeking Zeeman level, this field minimum acts as a potential minimum. This

potential well traps atoms of energy less than the trap depth.[1]

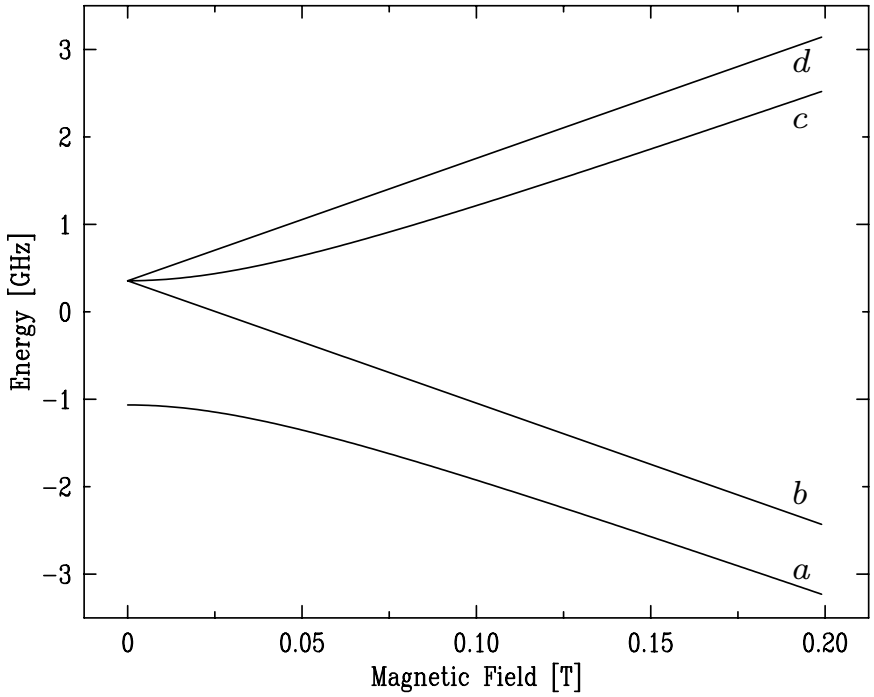

Figure 2.1: The eigenenergies of the ground electronic state of neutral atomic hydrogen as a function of magnetic field. The states labeled c and d are weak-field seeking states, the a and b states are strong-field seeking states.

Various popular methods of constructing magnetic traps are discussed in References [86, 87, 88, 89]. The magnetic trap used in this thesis (and probably the simplest kind of magnetic trap) is the spherical quadrupole field produced by anti-Helmholtz coils. To construct such a trap, two coaxial current loops are run with equal and opposing currents, as shown in Figure 2.2. The fields produced by the two coils cancel at the midpoint between them, creating a local field minimum in free space. The field expansion around that point to lowest order is always (as governed by Maxwell's equations)

$$\mathbf{B} = C \cdot z \cdot \hat{\mathbf{z}} + (C/2) \cdot \rho \cdot \hat{\boldsymbol{\rho}}$$

providing a linear potential to trap weak-field seeking particles.

[1]We define the trap depth as the difference between the minimum energy required for a particle to escape from the trap and the minimum energy inside the trap.

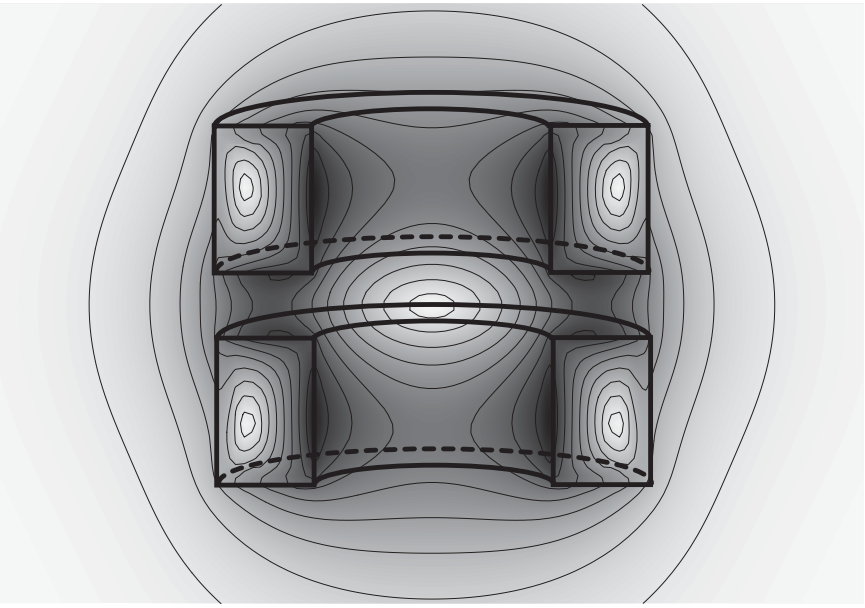

Figure 2.2: A cutaway view of two coils in the anti-Helmholtz configuration and a 2-D contour plot of their magnetic field in the axial plane. Dark grayscale denotes large field and light grayscale indicates small field.

Magnetic Trap Losses

Magnetically trapped atoms are a metastable state[2], and trap loss comes from many sources, both technical and fundamental. These loss sources place limitations on the lifetime of atoms in the trap, cause trap heating, reduce the efficiency of evaporative cooling, and are generally detrimental to our experimental goals.

Majorana loss

As a particle orbits through the trap, it experiences a changing magnetic field. The adiabatic theorem states that if the particle's Hamiltonian changes sufficiently gradually, the particle will remain in the same eigenstate [90]. Here, the condition for adiabaticity is that the rate of change of the magnetic field is "gradual" compared to the Larmor precession frequency. Inside a spherical quadrupole trap, this condition

[2]The low-field-seeking state is a higher energy state than the strong-field seeking state. Additionally, the formation of bound molecules (or a solid) is also energetically favorable.

breaks down near the field zero at the trap center [91]. The non-adiabatic spin flips of weak-field-seeking states to strong-field seekers that occur near the trap center [87, 92] are referred to as Majorana transitions, and cause trap loss.[3]

As discussed in Appendix D, the timescale for Majorana loss is expected to be on the order of thousands of seconds for the experimental conditions in this thesis. Our experimental observations are consistent with this expectation, and Majorana losses are of little consequence in the data presented in this thesis.

Background loss

Other mechanisms for loss are collisions with external particles: both background gas and resonant light cause heating and loss by either transferring momentum to the trapped particles or changing their internal state. Background gases and light are purely technical problems, and both can be made negligible by maintaining good vacuum in the trapping region and probing the atoms with sufficiently weak light.

Although background losses were eventually reduced to negligible levels in the chromium evaporative cooling experiment, the effects of background helium gas dominated the behavior of trapped calcium monohydride. The influence of background losses is discussed separately for each experiment in this thesis.

Radiative loss

In theory, the weak-field-seeking Zeeman state can decay to (lower-energy) strong-field-seeking states by emitting a photon. In practice, because these transitions are both "forbidden" and of such low energy, radiative loss is extremely small on the timescales over which we monitor the atoms (assuming the trapped state is the electronic ground state of the atom). The expected timescale for radiative loss of the trapped particles in this thesis is $\gg 1000$ s.

Collisional loss

Collisions in which the internal states of the colliding particles remain unchanged are called elastic collisions. In an elastic collision, the particles simply exchange

[3]Majorana transitions can be avoided by using a magnetic trap without a field zero [87, 93].

momentum. Elastic collisions can cause loss through evaporation: when two trapped particles elastically collide, one of them can be imparted sufficient momentum that it escapes from the trap. This evaporation can be used advantageously to increase the phase space density of the remaining atoms, as discussed in Section 2.4.

Inelastic collisions, collisions in which the internal state of the trapped particle is changed, also cause trap loss. Although there is a litany of inelastic collisions [84], the most relevant to our work are collisions which change the Zeeman state of the atom from its original weak-field seeking state to one less so. For example, if an inelastic collision causes a transition directly to a strong-field-seeking state (in the case of Figure 2.1, a transition from the d state to either b or a), that particle will be lost. However, even a transition to a less-trapped weak-field seeker (such as a transition from d to c in Figure 2.1) will accelerate trap loss, as these more weakly-bound states will preferentially evaporate from the trap.

Collisional physics as it relates to magnetic trap losses, buffer-gas loading, and evaporative cooling is discussed at greater length below in Section 2.5

2.2 Buffer-gas loading

The trapping potential generated by magnetic traps is somewhat weak. Ion traps, which interact with the large electric monopole moment of a singly or multiply ionized atom or molecule, easily generate trap depths beyond 10^4 Kelvin [3]. But the magnetic moments of atoms and simple molecules are, at best, a few Bohr magneton (μ_B). The interaction energy of the atom with the field is $\boldsymbol{\mu} \cdot \mathbf{B}$. For trapping fields of a few Tesla, this results in trap depths on the order of a few K (using Kelvin as a unit of energy). To efficiently magnetically trap atoms and molecules, they must be cooled from the high ($\sim$ 1000 K) temperatures at which they are typically created.

In this thesis, atoms and molecules are loaded into a magnetic trap with buffer-gas cooling. Buffer-gas cooling was proposed as a general method for cooling neutral atoms and molecules in order to magnetically trap them [94]. Buffer-gas loading cools atoms (or molecules) with a cryogenic refrigerator by using a helium buffer-gas as the thermal link between the atoms and the refrigerator.[4]

[4]This technique is related to hydrogen trapping experiments [68] which thermalize hydrogen atoms with a film of superfluid helium on a cryogenically cooled surface.

One of the primary virtues of buffer-gas cooling is that its success relies only on elastic collisions between the cryogenically cooled helium atoms and the species to be trapped. Because of this, it is largely independent of the internal structure of the atom or molecule to be trapped, so it should be applicable to many atoms and molecules. Additionally, because the cooling power of the cryogenic apparatus and the helium buffer-gas is so large, it should also be possible to use it to cool and trap large numbers of atoms.

In buffer-gas loading, the trapping region is filled with helium buffer gas, and the species to be trapped is introduced. This species diffuses through the helium and comes into thermal equilibrium with it through elastic collisions. The weak-field seeking states are drawn into the magnetic trap; as they descend, they are continually rethermalized by the gas. Once the species is spatially confined by the potential and thermalized, the helium gas can be removed, leaving a trapped, thermally isolated gas of the species of interest.

Buffer-gas loading in detail

Helium buffer-gas

The buffer gas is contained by a cell within the magnet bore. The cell is maintained at cryogenic temperatures by a thermal link to a ^{3}He–^{4}He dilution refrigerator [99, 100]. Because the helium buffer gas is nonmagnetic, it moves freely throughout the magnetic fields.

The density of helium atoms in the cell is controlled through the cell temperature (with an upper limit simply set by the total amount of helium placed inside the cell). Because the equilibrium vapor pressure of helium varies rapidly with temperature, small changes in the cell temperature cause great variation in the helium buffer gas density, as shown in Figure 2.3. Prior to the introduction of the species to be trapped, the cryogenic cell is heated (with resistors mounted on the cell body) in order to

However, that technique is limited to atomic hydrogen, as hydrogen's sticking properties on superfluid helium (with a binding energy of only 1 K [95]) are unique.

It should also be noted that the use of cryogenic helium gases to cool molecules had been independently developed and demonstrated a decade prior to this work as a technique for performing "very low temperature" molecular microwave spectroscopy [96, 97, 98].

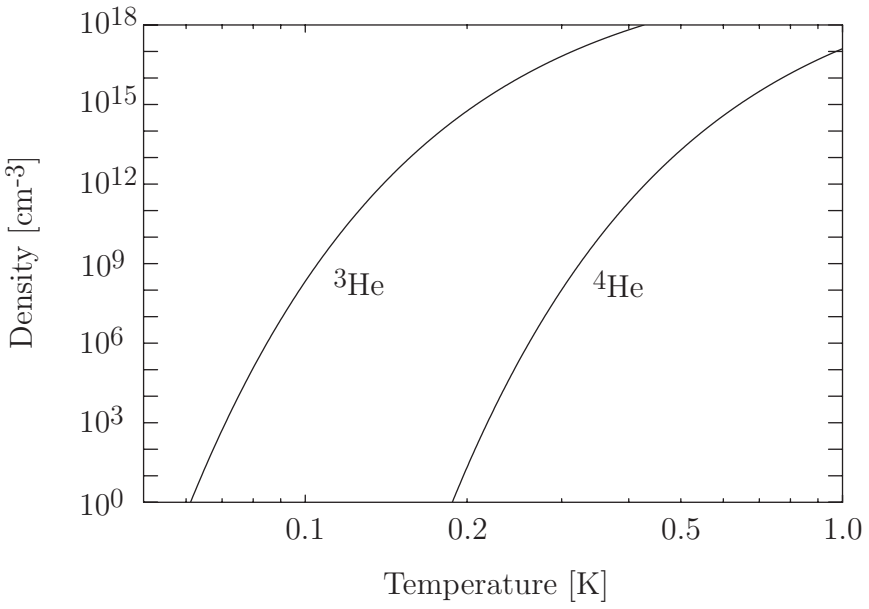

Figure 2.3: The equilibrium vapor density of ^{3}He and ^{4}He as a function of temperature. Based on a simple extrapolation (assuming a constant latent heat of evaporation) from the data presented in references [101, 102], this graph should not be trusted for exact values, but used only as a illustration of approximate behavior.

elevate its temperature and produce the desired density of buffer gas. Once the species is loaded into the trap, the cell heaters are turned off and the cell cools, liquefying the helium and providing a high-vacuum environment.[5]

During the trap loading process, the helium density is chosen such that the species–helium collisional mean-free path is short compared to the size of the trap. This is a necessary requirement for efficient loading because if the incoming species is not thermalized before it traverses the trapping volume, it will collide with the cell wall and

[5]It should be noted that an alternate way to remove the helium buffer gas is with a cryogenic charcoal adsorbent pump [99, 103] . The adsorption of helium onto the large surface area present in charcoal should attain ultra-high vacuum at Kelvin temperatures. This allows the constraints on the cell temperature to be relaxed, with two obvious experimental advantages. One, simpler cryogenic refrigerators could be used. For example, a pumped ^{4}He cryostat could be used to buffer-gas load highly magnetic atoms (such as chromium) into a deep trap at 1.4 Kelvin; a pumped ^{3}He refrigerator would allow loading at lower temperatures. Two, if the cell is subsequently inadvertently heated (due to, for example, laser radiation, radio-frequency radiation, or rapid changes in the magnetic field), it is less likely to have dire consequences.

(presumably with high probability) freeze to it. Models of the thermalization process indicate that on the order of 100 collisions are necessary to achieve thermalization [94, 104]. Typical helium densities are 10^{16} to 10^{17} cm^{-3}.

In our work, we have used both ^{3}He and ^{4}He as buffer gases. Although there may be differences in their collisional properties, they differ predominantly in their vapor pressures, as seen in Figure 2.3. The advantage of using ^{4}He is that the buffer gas can be liquefied and good vacuum obtained at higher temperatures, putting less stringent temperature constraints on the cryogenic system. The advantage of ^{3}He is that its larger vapor pressure allows trap loading to be conducted at lower temperatures (approaching 250 mK). This is important for trapping atoms and molecules with small magnetic moments.

Our experimental cells typically experience significant heating during the introduction of the particles to be trapped, and the cell temperature temporarily rises considerably. We control (and limit) the helium density at these high temperatures through the quantity of helium in the cell.

Because such a small quantity of helium is placed in the cell, we must consider the modification of the helium vapor-pressure curve by its adsorption potential to the wall. Reference [105] cites the binding energy of He to various copper substrates, and References [106, 107] discuss how this adsorption potential changes as a function of film thickness. Although the binding energy of helium atoms directly to copper is quite large (approximately 50 to 100 K, significantly higher than the latent heat of evaporation of bulk ^{3}He and ^{4}He), the adsorption energy of successive monolayers decreases rapidly. By comparing the adsorption energy to the latent heat of evaporation, we conclude that for helium quantities such that approximately three monolayers are present upon the cell surfaces, the helium vapor pressure will be changed negligibly from its bulk values.

Loss during loading

The magnetic trap collects the buffer-gas-cooled weak-field-seeking atoms. However, because the atoms are thermally distributed, they evaporate from the trap. The rate of this evaporation is determined primarily by η, the ratio of the trap depth to the temperature of the atoms. For efficient trap loading, η must be made sufficiently high that evaporation is slow on the timescale required to remove the helium buffer gas (typically 1–10 seconds, as discussed in Section 6.3).

References [94, 104] calculate a lower limit of the trap lifetime due to evaporation during buffer-gas loading. The loss rate of atoms is determined by the the flux of atoms to the cell wall. These references assume both a "continuously thermalized" population (one whose distribution of atoms within the cell walls is unchanged from the untruncated Boltzmann distribution), and ballistic travel of atoms to the walls. These assumptions provide a lower limit on the trap lifetime of

$$\tau \gtrsim \frac{4V}{vA} \cdot e^{\eta} \tag{2.1}$$

where τ is the exponential decay constant characterizing the evaporation, V the effective trap volume (defined as the ratio of total atom number to peak density), v the average thermal velocity, and A the area of surface defined by the trap edge.

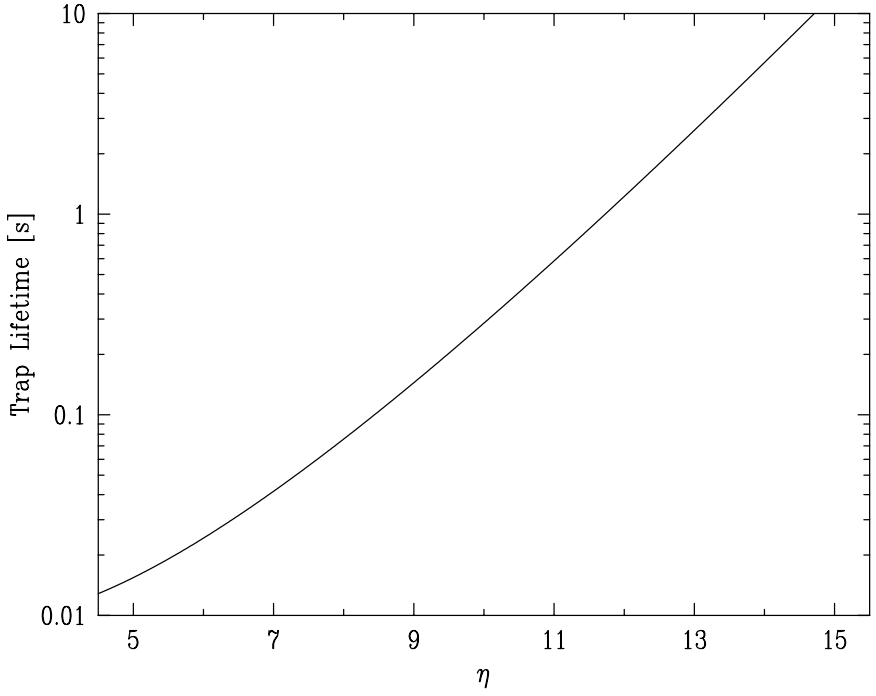

Figure 2.4: The trap lifetime τ as a function of η, as calculated from Equation 2.1. Calculated using the parameters of our chromium experiments, as described in Chapter 6.

This model implies high values of η are needed to obtain long trap lifetimes during loading. The calculated trap lifetime for chromium during buffer-gas loading is shown in Figure 2.4. Fortunately, the experimentally observed loss rate at low η is often

significantly slower than predicted by this model, allowing trap loading at lower values of η.

In the short-mean-free-path regime, the kinetic energy of the magnetically trapped species is rapidly thermalized by the helium buffer gas, but the transit of the trapped particles to the walls is slowed by the presence of the helium gas. The motion of the trapped species through the cell is diffusive, rather than ballistic. The trap lifetime is lengthened considerably by the diffusion constant of the helium, especially at low η. This effect is probably of great importance at short times, where it is likely that the helium gas is heated by the laser ablation used to create the species to be trapped. In the short-mean-free path limit, we expect the trap lifetime to increase with the helium density (assuming η is held constant).

In the long-mean-free-path regime, the trap lifetime is also longer than the lower limit set by Equation 2.1. Although trapped particles are able to travel ballistically to the cell walls, collisions with helium atoms are infrequent (on the timescale of an oscillation period in the trap), and the rate at which trapped particles are imparted sufficient energy to escape is lowered. In this regime, we expect the trap lifetime to increase with decreasing helium density.

Evaporation in the short-mean-free-path regime

In this subsection, we calculate a simple mathematical model of trap loss in the short-mean-free-path limit.[6] While imperfect, this model provides a quantitative understanding the CaH and Cr buffer-gas loading data. For computational simplicity, we study the process of diffusion of trapped particles through a helium gas inside a spherical cell. To model the decay, we assume that when the trap particles collide with the cell walls, they stick with unity probability.

Reference [108] provides a detailed treatment of the diffusion of one gas through another; we provide a recap here. In the absence of a trapping potential, the diffusion equation is

$$\dot{n} = D \cdot \nabla^2 n$$

where D is the diffusion constant of the particles of interest in the helium buffer-gas.

[6]The short-mean-free-path limit is the limit in which the trap species–helium mean-free path is small compared to the trap size.

The spherically symmetric solutions of this equation[7] obey

$$\frac{dn}{dt} = \frac{D}{r^2}\frac{d}{dr}\left(r^2 \cdot \frac{dn}{dr}\right)$$

Inside a sphere of radius R where the diffusing particles are destroyed at the walls, we impose the boundary condition that $n(R,t) = 0$ to find solutions

$$n(r,t) = \sum_{k=1}^{\infty} A_k \cdot \frac{\sin(k\pi r/R)}{r} \cdot \exp(t/\tau_k)$$

where $\tau_k = D^{-1} \cdot (R/k\pi)^2$ and D is the diffusion constant. The long-time behavior is dominated by the $k = 1$ term of this expansion, giving exponential decay of atom number with time. We consider only this term of the expansion.

To model this process in the presence of the magnetic trap, we must add a drift term to the diffusion equation. We model the trap as a linear, isotropic potential, with $U(0) = 0$ and $U(R) = \eta kT$ at the (spherical) cell walls. With v as the drift velocity (a signed quantity, negative for weak-field seekers), the diffusion equation becomes

$$\frac{dn}{dt} = D \cdot \frac{1}{r^2}\frac{d}{dr}\left(r^2 \cdot \frac{dn}{dr}\right) - v \cdot (\frac{dn}{dr} + \frac{2n}{r}) \tag{2.2}$$

From the Einstein relation of drift and diffusion [15], $v = -D\eta/R$.

The relevant solutions [109] to Equation 2.2 are less elegant than in the trap-free case, involving the Kummer confluent hypergeometric function M:

$$n(r,t) = A \cdot e^{-\Gamma t} \cdot \exp\left[-\frac{\eta r}{2R}\right] \exp\left[-\frac{ir\beta}{2R}\right] M\left(1 - \frac{i\eta}{\beta},\ 2,\ \frac{ir\beta}{R}\right)$$

where $\beta = \sqrt{\frac{4\Gamma R^2}{D} - \eta^2}$. By numerically solving for the boundary condition $n(R) = 0$, we find the trap lifetime $\tau = \Gamma^{-1}$ as a function of the trap parameters. We find the somewhat elegant solution that the trap lifetime τ depends only on η and τ_0, the diffusion lifetime in the absence of the trap. The functional dependence of τ on η is are plotted in Figure 2.5 This model is used to fit our experimental chromium and calcium monohydride buffer-gas-loading data.

We note that because of the assumptions of spherical symmetry, this model will tend to overestimate the trap loss rate inside our actual experimental apparatus. In

[7]These are the solutions of interest to us, as they will dominate the long-time behavior.

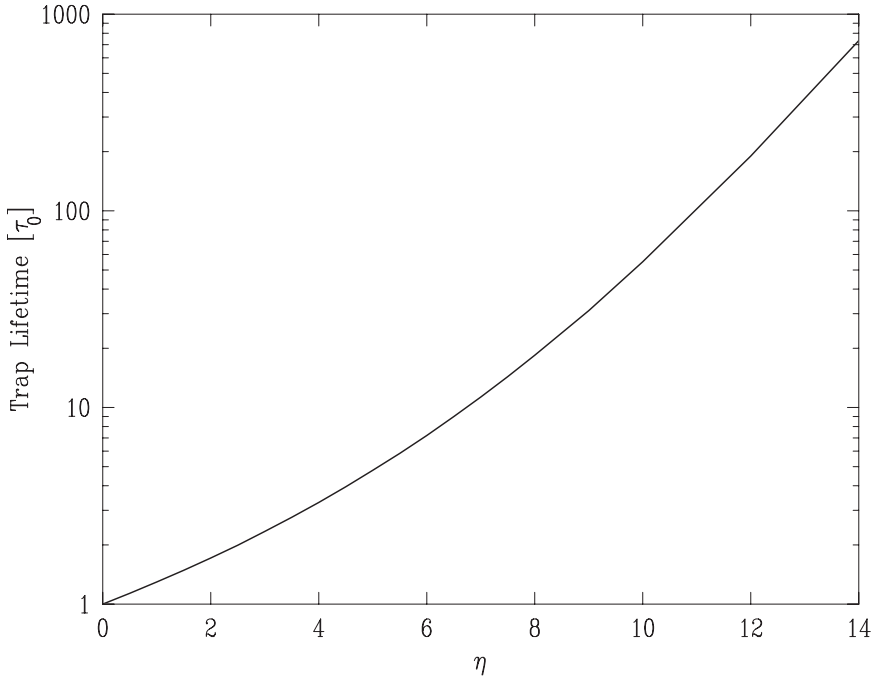

Figure 2.5: The trap lifetime $\tau(\eta)$ in the short-mean-free-path regime as calculated from the solution of Equation 2.2, expressed in units of τ_0, the diffusion lifetime in the absence of a magnetic trap.

the model, the potential at the trap wall is always $\eta k_{\mathrm{B}} T$. In the real trap, as shown in Figure 5.3, particles with energy equal to the trap depth can escape from the trap at certain locations, but the vast majority of locations in the cell require energies $> \eta k_{\mathrm{B}} T$ for particle loss. Comparison of this model to numerical simulations of the trap loss in a realistic field and cell geometry indicates discrepancies of < 20 % in η [110].

Inelastic collisions

The caveat about the general applicability of buffer-gas loading is one concerning inelastic collisions. Buffer-gas cooling relies on the presence elastic collisions, but for buffer-gas loading to work efficiently we must also have an *absence* of inelastic collisions. If the Zeeman level can thermalize through inelastic collisions with the helium buffer gas, it will decay to a strong-field seeking state and be lost from the trap. Our experimental observations of Cr and CaH have shown the rates of such processes are quite low; the underlying physical processes are discussed in Section

2.5.

Other forms of potential inelastic collisions are chemical reactions in the buffer gas: the formation of bound molecules (or clusters) through multi-body collisions with either helium atoms or other substances produced by the ablation pulse. While no evidence of such collisions was observed with CaH or Cr, these or similar processes did occur with VO, as discussed in Chapter 4.

2.3 Laser ablation

The use of laser ablation has a distinguished history in the field of cold atoms. A frequency-doubled pulsed Nd:YAG laser was used to produce atomic sodium for the experiments which first demonstrated optical molasses [61] and the magneto-optical trap [62]. Although ablation has been largely supplanted in the cold atom community by laser-slowed beams, vapor pressure cells, and other variants of thermally produced atoms, we find ablation is particularly well suited for incorporation into our cryogenic environment and robust for creating a variety of atomic and molecular species.

We use laser ablation to produce atoms and molecules inside our cryogenic apparatus. The frequency-doubled output of a Q-switched pulsed Nd:YAG laser [111, 112] at 532 nm is focused onto the surface of a solid sample inside our cryogenic cell. The solid sample is chosen to contain the necessary constituents to produce the species of interest. In the case of atomic chromium, we ablate pure chromium metal; in the case of molecular radicals, we use a target with similar chemical composition to the desired molecule. This solid sample is positioned inside the cryogenic cell closely behind the edge of the magnetic trap.

The laser pulse deposits a large power into the surface of the solid, causing the rapid liberation of atoms, ions, and molecules (including radicals) from the solid. The details of the physics behind laser ablation are quite complicated, and studying ablation is a field unto itself. As described by Richard F. Haglund, Jr. in "Mechanisms of laser-induced desorption and ablation",

> Laser ablation... is a sputtering process in which material removal rates typically exceed one-tenth monolayer per pulse; the surface is structurally or compositionally modified at mesoscopic length scales; and particle yields are superlinear functions of the density of excitation. The formation of an ablation plume–a weakly ionized, low-to-moderate density expand-

> ing gas cloud–adds to laser ablation the complications of plasma-surface interactions, gas dynamics, and laser-induced photochemistry. [113]

In this thesis, we do not concern ourselves with the dynamics of the ablation process. We simply use ablation as a tool to introduce atoms and molecules into our cryogenic cell. We typically ignore short time ($\lesssim 1$ ms) phenomena and begin our studies after the translational thermalization of the species to be trapped with the helium buffer gas. Specific issues concerning ablation are discussed separately for each ablation species; we note various general details here.

We typically ablate with a pulse energy of tens of mJ in a ~ 5 ns pulse. We find the atom (or molecule) yield is not especially sensitive to the focus of the ablation laser.[8] the mode quality of the ablation beam is somewhat poor, and the actual focus obtained is undoubtedly short of the diffraction limit.

The ablation process gives rise to an visible plume at the point of ablation, which extends variable distances into the cell volume. We do not know if this is dominated by ions (or excited neutrals) ejected from the target itself, or in the helium. As a side note, it is possible that some fraction of the ablation laser power is deposited into a discharge in the helium gas rather than into the surface itself.

We are concerned primarily with three criteria during ablation. One, the amount of energy deposited in the cell (which we would like to be small), because it causes heating of the cell and reduction of η. Two, the number of the desired species produced (which we would like to be large). Three, avoiding the production of any unwanted species which will react in an undesirable way with the species of interest (such as removing it from the trap). Controlling the first criteria is straightforward (simply by controlling the laser pulse power), the latter two conditions are less well understood.

In the case of molecules, the yield of an ablation pulse is quite complicated, especially as CaH and VO are both radicals: molecules which are physically but not chemically stable. What determines the ultimate atom number thermalized within our trapping region is not completely understood. In fact, we do not know if the molecules are ejected from the surface directly or formed subsequently in the high density ablation plume. The number of molecules produced is optimized through an experimental process of trial and error, varying the ablation target, laser power,

[8]The laser beam is focused onto the target by a 40 cm focal length lens. The position of this lens can be moved on the order of 1 cm with only modest change in the ablation yield

and helium density. As discussed in Section 3.4, various promising candidates were rejected because we could not reliably produce sufficient numbers with ablation.

Atomic chromium is produced by ablating pure chromium metal, and the ablation power and ambient helium density used are optimized experimentally. The number yield of atomic chromium is much higher than that seen with molecules, and is discussed at greater length in Section 6.3.

The third desirable criterion, which arose from problematic behavior during attempts to magnetically trap VO, is also addressed largely through a process of trial and error, as discussed in Section 3.4 and Chapter 4.

2.4 Evaporative cooling

Once the atoms are magnetically trapped and the buffer gas has been removed, the atoms can be further cooled through evaporative cooling. Evaporative cooling of magnetically trapped neutral atoms is a powerful technique for producing cold and dense atomic gases [114, 115]. Having achieved notoriety from its use in the production of Bose-Einstein condensates [16, 17, 18, 19], it has recently been extended to fermionic atoms and successfully used to create degenerate atomic Fermi gases [36, 37, 38]. Evaporative cooling has been discussed at length in the literature; many of the pertinent details can be found in a review paper by Ketterle et al [84].

The idea is simple. If the highest energy atoms irreversibly escape from the trap, the average energy of the remaining atoms is reduced. If these atoms come into thermal equilibrium with each other, they will thermalize to a lower temperature. To allow the highest energy atoms to escape is straightforward: simply confine them with a finite depth trap. Hot atoms will leave the trap and stick to the walls. Rethermalization of the distribution is then provided by elastic collisions between the trapped atoms. Evaporation (and evaporative cooling) is an unavoidable consequence of elastic collisions inside a finite depth trap.

Although evaporative cooling necessarily reduces the number of remaining atoms, large increases in their phase space density can be achieved. Additionally, evaporative cooling inside a magnetic trap can be used to span many orders of magnitude of temperature because the energy required to escape the trap can be tuned to match the temperature of the trapped atoms. The trap depth is normally set in one of two manners: by reducing the magnitude of the confining potential [115] or through the

frequency of RF or microwave radiation that resonantly couples the trapped weak-field-seeking state to a strong-field-seeking state [116, 84]. Although RF-induced evaporation is generally a superior method [19], reducing the confining fields is considerably simpler to implement in our cryogenic environment and is the only technique used in this thesis.

The key to the success of evaporative cooling is ensuring that all other loss and heating processes are very slow on the timescale of elastic collisions and evaporation from the trap. There are a myriad of mechanisms that cause loss and heating, such as poor vacuum (background gas), stray light, Majorana losses, and heating caused by fluctuations in the trap potential. However, each of these "technical problems" should be controllable through careful design of the experiment.

Inelastic collisions among trapped atoms, however, are inescapable.[9] The collision rates originate in the fundamental atom–atom interaction. Because high atom densities are required to provide the elastic collisions necessary for evaporation, inelastic collisions will be an unavoidable accompaniment. These collisions cause trap loss without the accompanying cooling of evaporation, reducing the phase-space density of the remaining particles. Even more insidiously, because the atom density is higher at lower potentials, collisions occur preferentially among lower energy atoms. Hence, inelastic collisions preferentially remove lower-energy atoms, causing a net heating of the remaining cloud. The ultimate success of evaporative cooling (assuming the "technical" loss and heating processes can be eliminated) depends on the ratio of the atomic elastic collision rates to inelastic collision rates.

2.5 Collisions

Atomic and molecular collisions are of great importance in this thesis. Elastic collisions fuel buffer-gas loading and evaporative cooling, while inelastic collisions have the potential to defeat both.

[9]Inescapable among magnetically trapped weak-field seekers. Optical traps can trap atoms in the lowest-energy strong-field-seeking state, which cannot undergo two-body inelastic collisions.

Elastic collisions

Elastic collisions (collisions in which the internal states of the colliding particles are unchanged) are treated thoroughly in the literature. General quantum-mechanical properties of scattering are discussed in Reference [90]. More specific treatment of atomic scattering is discussed in Reference [117].

Typical elastic scattering cross-sections for atoms and diatomic molecules at 300 K are in the range of 10^{-15} to 10^{-14} cm^2 [118].

At ultracold (see below) temperatures, scattering properties depend extremely sensitively on the phase shift produced by the interatomic potential, and elastic scattering cross-sections are quite varied. The ultracold elastic cross-section $\sigma_{el} = 5 \times 10^{-13}$ cm^2 for the $F = 2, m_F = 2$ state of ^{7}Li [119], 6×10^{-12} cm^2 for the $F = 1, m_F = -1$ state of ^{23}Na [92], and 5×10^{-12} cm^2 for the $F = 1, m_F = -1$ state of ^{87}Rb [120]. Atomic hydrogen exhibits a significantly smaller cross-section with $\sigma_{el} = 1 \times 10^{-15}$ cm^2 for its d state [121].

Inelastic collisions

Because the trapped particles are translationally cold, we are concerned primarily with exothermic inelastic collisions. In this thesis, we magnetically trap particles in the metastable weak-field-seeking state of their electronic ground state. Consequently, the dominant inelastic collision process in this thesis are spin-relaxation collisions which change the Zeeman state of the particle

There are multiple mechanisms by which such spin-relaxation collisions can occur. They are typically divided into two classes: spin exchange and dipolar relaxation. Spin-exchange collisions preserve the total angular momentum projection of the colliding atoms. Dipolar relaxation collisions do not preserve the total internal angular momentum of the colliding particles (but do conserve total angular momentum, of course, by coupling this internal angular momentum to the orbital motion of the two atoms) [84].

Spin-exchange

Inelastic collisions which change the spin of an atom at the expense of the spin of its collisional partner occur very readily in atomic collisions [84, 122].

The mechanism through which spin-exchange collisions predominantly occur is through a coupling of different exit channels through the interatomic (molecular) potential. For simplicity, we initially consider two colliding atoms with no orbital or nuclear angular momentum, electron spins S_a and S_b and spin projections m_a and m_b on the field axis. As the atoms near each other, m_a and m_b are no longer good quantum numbers: only the total molecular spin projection $M = m_a + m_b$ is. The colliding atoms are coupled to the molecular states: $|S = S_a + S_b, M = m_a + m_b\rangle$, $|S = S_a + S_b - 1, M = m_a + m_b\rangle$, ..., $|S = m_a + m_b, M = m_a + m_b\rangle$.[10]

If both colliding atoms are in the same, fully polarized weak-field-seeking state ($m_a = +S_a$ and $m_b = +S_b$), then they will be coupled to a single molecular state and scattered into the same spin states in which they originated.[11] All other combinations of m_a and m_b will be coupled to multiple molecular states. These different states experience different molecular potentials and will acquire different phase shifts.[12] Consequently, the outgoing molecular wavefunctions will interfere in such a way that the final state has nonzero projections on all $|m_a, m_b\rangle$ states with $m_a + m_b = M$. Thus, all atom collisions between atoms not both in their fully polarized weak-field-seeking state (or both in their maximally strong-field-seeking state) will readily undergo spin-exchange collisions which change their individual m states (while conserving M).

In the case of atoms with nonzero nuclear spin, the hyperfine coupling results in eigenstates which are mixtures of the various m_S states. Because the hyperfine eigenstates contain $m_S \neq \pm S$ components, they are expected to rapidly undergo spin-exchange collisions with each other. The singular exceptions are the two fully polarized "stretch states" $|m_S = +S, m_I = +I\rangle$ and $|m_S = -S, m_I = -I\rangle$. These states are eigenstates of the hyperfine Hamiltonian at all fields with $m_S = \pm S$. Thus, in collisions with other atoms in the same state, they will be unable to undergo spin-exchange collisions through the above process.[13]

[10] With the implicit assumption of a non-adiabatic traversal of the interatomic potential.

[11] The same applies, of course, to two scattering atoms in the $m_a = -S_a$ and $m_b = -S_b$ states.

[12] Because the electron spin-symmetry affects the electron wavefunction symmetry requirements, the molecular potential depends very strongly on S.

[13] Of course, these states are prohibited from undergoing spin-exchange processes by definition because of conservation of total angular momentum.

As an explicit example, we consider the states of hydrogen, as shown in Figure 2.1. The states d and b are stretch states ($|m_S = +1/2, m_I = +1/2\rangle$ and $|m_S = -1/2, m_I = -1/2\rangle$, respectively), but c and b are mixtures of $m_s = +1/2$ and $m_s = -1/2$ states. Thus, while every energy eigenstate can undergo a spin-exchange collision with an atom in a different eigenstate, and c and b state atoms can undergo spin-exchange collisions with other c and b state atoms, the d state cannot undergo a spin-exchange collision with another d state atoms, and b cannot spin-exchange with b.

Typical spin-exchange collision rate coefficients of ultracold atoms are on the order of 10^{-12} cm^3 s^{-1} [122, 84]. Because this rate is so large, it tends to rapidly lead to a "self-purification" of a magnetically trapped ensemble, so that only the doubly-spin-polarized, weak-field-seeking stretch-state remains.

Spin-exchange collisions with helium

Because the ground state of helium has zero spin ($S = 0$), the strong coupling mechanism discussed above is missing. But through different mechanisms, a polarized atom can undergo a spin-exchange collision with an unpolarized ^{3}He atom by transferring its angular momentum to the spin of the ($I = 1/2$) ^{3}He nucleus. One mechanism for the transfer of the electron spin to the ^{3}He nucleus is through the coupling of their magnetic moments (as given by Equation 2.3 below). This weak process is usually overshadowed by the spin-exchange caused by the direct $\mathbf{S} \cdot \mathbf{I}$ hyperfine interaction (the "Fermi contact interaction") of the scattering particle's electrons with the ^{3}He nucleus [85, 123, 124]. In the case of Rb–^{3}He collisions, the resulting rate coefficient for spin-exchange is 1×10^{-19} cm^3 s^{-1} [125]. As there is nothing unusual about either the Rb–^{3}He dipolar interaction or $\mathbf{S} \cdot \mathbf{I}$ interaction, we would expect this spin-exchange rate to be typical for atom–helium collisions. Such low rates of spin exchange are good news for buffer-gas loading with ^{3}He.

Because the ground state of ^{4}He has neither electron spin, nuclear spin, or orbital angular momentum ($L = S = I = 0$), it has no internal "structure" to which angular momentum could be transferred in a collision. Thus, a doubly-polarized atom cannot undergo a spin-exchange collision with a ^{4}He atom.[14]

[14]It is conceivable that ^{4}He could cause a spin-exchange collision in which the ^{4}He would facilitate the transfer of the colliding particle's electron spin to its nuclear spin.

Dipolar relaxation

As discussed above, spin-exchange can be avoided by working with a fully-polarized sample of atoms. Dipolar relaxation cannot.

The spin-spin dipolar interaction can cause dipolar relaxation [122].[15] The magnetic dipole moments $\boldsymbol{\mu}$ of two colliding atoms at a distance $\mathbf{R}$ interact with an energy (ignoring the "Fermi contact term") given by [126, 127]

$$H_{\text{dipole}} = \frac{\boldsymbol{\mu}_1 \cdot \boldsymbol{\mu}_2 - 3(\hat{\mathbf{R}} \cdot \boldsymbol{\mu}_1)(\hat{\mathbf{R}} \cdot \boldsymbol{\mu}_2)}{R^3} \tag{2.3}$$

This dipole-dipole interaction clearly leads to a coupling between the magnetic moments of the colliding particles and their relative motion. Through H_{dipole}, spin-polarized particles can relax to less-polarized states by coupling their angular momentum to their orbital motion. The resulting loss rate will depend on the specifics of the atom's scattering properties. Typical rates for dipolar relaxation for the alkali atoms and atomic hydrogen range from 10^{-16} cm^3 s^{-1} to 10^{-14} cm^3 s^{-1} [122, 128, 129, 130, 131].

But the direct dipole-dipole interaction of magnetic moments isn't the only game in town: dipolar relaxation can also occur through a second-order spin-orbit interaction. While the spin-relaxation rate of the lighter alkali-dimer systems is controlled primarily by the spin-spin dipole interaction, the second-order spin-orbit interaction plays an important role in heavier atomic systems [131]. As explained by Mies et. al. in "Estimating bounds on collisional relaxation rates of spin-polarized ^{87}Rb atoms at ultracold temperatures",

> [The indirect second-order spin-orbit interaction] originates when the atomic charge clouds overlap as a molecule is formed, and the interaction between the ground state spins are modified due to couplings mediated through distant excited electronic states of the molecule. These interactions are well known in molecular spectroscopy and mimic the direct spin-spin coupling. [130]

Through this second-order coupling of the spin to the interatomic axis, dipolar relaxation loss can occur. It is also important to note that (unlike the gentler R^{-3}

To the best of our knowledge, this process has never been observed, and the expected rates or physical mechanisms have not been discussed in the literature. We would expect them to be small.

[15] Which is probably how dipolar relaxation obtained its name.

direct dipole-dipole coupling) the spin-orbit coupling depends very strongly on the internuclear distance (and is typically modeled as $V \propto e^{-C \cdot R}$) [131].

Detailed spin-orbit calculations for ^{87}Rb are presented in Reference [130]. In this work, the authors find that the spin-orbit term is smaller than the spin-spin term, and their relative signs lead to the happy consequence of a reduction in the total spin-relaxation rate (compared to spin-spin alone). Reference [131] treats spin-relaxation of doubly polarized ^{133}Cs atoms, and spin-orbit coupling is found to be the dominant effect. The resulting large inelastic collision rate prevented the attainment of a Cs BEC [132].

For collisions between ground-state ^{4}He (with $J = I = 0$) and spin-polarized atoms, spin-orbit coupling is, of course, the dominant source of dipolar relaxation collisions. Helium has remarkably small spin-orbit interactions, so that the resulting spin-relaxation rates are on the order of 10^{-27} cm^3 s^{-1} [133], with considerable variation depending on the collision partner.

Molecular spin-rotation interaction

Molecules can undergo spin-relaxation collisions through an additional mechanism, unique to molecules. Molecular spin-state-changing collisions are driven by spin-rotation interactions, wherein electronic spins are influenced by their coupling to rotational motion, which is in turn dependent on torques exerted by the anisotropic potential energy surface between the molecule and its collision partner [134].

We expect this effect to play the dominant role in molecule–helium spin-relaxation collisions. John Bohn, in "Cold collisions of O_2 with helium", calculates that the rate coefficient of O_2 spin-relaxation in collisions with ^{3}He is approximately 10^{-15} to 10^{-14} cm^3 s^{-1} in the sub-Kelvin temperature regime in which we conduct buffer-gas loading [135].

In this thesis, we measure such collision rate for CaH.

Chemical reactions

The previously discussed inelastic collisions are expected to occur among cold atoms because the Zeeman state of weak-field-seeking particles is metastable. There is another class of collisions which cause decay because any ultracold atomic gas is metastable: bound molecules are a lower energy state than atoms, and a solid is a

lower state still. Atoms can be lost from the trap through the exothermic formation of bound molecules. For energy and momentum to be conserved, a third body must be involved in the collision. Most commonly, this is another atom.

Because the formation of bound molecules requires three atoms, the loss rate scales as $\dot{n} = -\Gamma_3 \cdot n^3$.[16] Thus, we can distinguish this decay from two-body decay by its behavior as a function of density.

The rate coefficient for 3-body loss for atoms is expected to be quite small. Calculations indicate typical loss rates of $\Gamma_3 < 10^{-27}$ cm^6 s^{-1} [136]. The ^{23}Na 3-body loss rate was measured to be 1×10^{-30} cm^6 s^{-1} [137].

The above discussion has been for atoms, but molecules can also be lost from the trap through the exothermic formation of larger molecules or other chemical reactions. An important difference is that molecules can undergo chemical reactions without the presence of a third body. For example, the chemical reaction $F + H_2 \rightarrow FH + H$ does not require a third body. Interestingly, this reaction has been calculated to continue at a finite rate in the zero-energy collision limit [55].

Cold and ultracold collisions

Definitions of "cold" and "ultracold" collisions differ. One popular atomic physics convention cites "cold" collisions being those at temperatures between the Doppler cooling and optical molasses temperature range (roughly 1 mK to 1 μK); "ultracold" collisions are any collisions at lower temperatures [13]. However, these definitions (derived from the performance of optical cooling techniques and commonly applied to collisions of excited-state atoms) are of little relevance to us. What is important is the underlying physics of the collisions themselves.

The important distinction for us is between the temperature regime where multiple partial waves contribute to the partial-wave expansion of the scattering process, and what is commonly referred to as the zero-energy scattering limit.[17] In the zero-energy limit, the energy of the incoming particle is small compared to the other relevant energy scales (including the relative position of the final bound state of the attractive interatomic potential), and the scattering process assumes its asymptotic

[16] All the previously discussed collisional loss processes have required two colliding bodies, so that the loss rate is expected to scale as $\dot{n} = -\Gamma_2 \cdot n^2$

[17] Also known as the $E \rightarrow 0$, $T \rightarrow 0$, or quantum threshold scattering limit.

behavior. We break with laser-cooling convention and refer to the former regime as "cold" scattering, and behavior in the $E \to 0$ limit as "ultracold".

In the ultracold limit, the cross-section for neutral atom elastic scattering goes to zero for all higher order partial waves ($l \geq 1$) as the collision energy goes to zero.[18] As these other partial waves are suppressed, ultracold elastic scattering is dominated by s-wave scattering, which has a constant cross-section in the $T \to 0$ limit [90].

On the other hand, exothermic inelastic collisions typically have a constant rate in the ultracold limit. While higher order partial waves are expected to vanish at least as fast as $\sigma_{in} \propto k$ as $E \to 0$, the s-wave inelastic scattering cross-section is expected to diverge as $1/k$ [13, 139]. It should be noted that this result relies on the assumption that the amount of energy released in the collision is a constant, finite value. For magnetically trapped atomic hydrogen, this is a good assumption, as transitions from the weak-field-seeking c and d states (see Figure 2.1) will always release at least 1.4 GHz of energy upon decay to the a state. For zero-nuclear-spin ^{52}Cr (see Figure 6.1), the energy released in a spin-changing collision goes to zero in the limit that $B \to 0$. Hence, it may be possible to suppress the inelastic collision rate in the ultracold limit by reducing the magnetic field [140].

The vast majority of evaporative cooling experiments have been conducted in the ultracold collision regime. However, our experiments begin with our atoms well above this limit. In the temperature region in which we begin evaporatively cooling atomic chromium ($\sim$ 100 mK), multiple partial waves contribute to collisions, and the phase shift varies greatly over the scattering energies over which the atoms are

[18] For finite-range potentials of extent R, the threshold for freezing out higher order partial waves is $kR \lesssim 1$. In this limit, the elastic scattering cross-section σ_{el} of the lth partial waves scales k^{4l} [90].

Similarly, for power law potentials with $V = C_n r^{-n}$, if $n > 2$ then $\sigma_{el} \to 0$ in the ultracold limit for all higher order order partial waves. In the specific case of $V = -C_6 r^{-6}$ (a good model for the long-range interatomic potential of two $L = 0$ ground-state atoms) we find the σ_{el} contribution of the $l = 0$ partial wave is constant, while $l \geq 1$ partial waves all vanish as $\sigma_{el} \propto k^4 \propto T^2$ in the ultracold limit [117]. The threshold for the onset of this behavior is estimated to be

$$k_{\mathrm{B}} T \sim \frac{2}{9\sqrt{6C_6}} \cdot \left(\frac{\hbar^2 l(l+1)}{\mu} \right)^2$$

where μ is the reduced mass of the colliding particles [138].

thermally distributed. The thermal averaging over these phase shifts leads to elastic scattering behavior which is much less closely related to the precise structure of the interatomic potential and its final bound state than in the case of ultracold scattering. An unfortunate consequence of this averaging is that the asymptotic behavior in the ultracold limit cannot be accurately extrapolated from observations in the cold regime.

Scattering resonances

Resonances can play an extremely important role in atomic scattering. At a resonance, the elastic and inelastic collision cross-sections can be greatly modified. There are two kinds of resonances that play a significant role in cold atom collision physics: shape resonances and Feshbach resonances.

Feshbach resonances

Moerdijk, Berhaar, and Axelsson, in "Resonances in ultracold collisions of ^{6}Li, ^{7}Li, and ^{23}Na", explain Feshbach resonances by the following:

> A Feshbach resonance... results when true bound states belonging to a closed channel subspace match the energy of open channels and a coupling exists between them so that temporary transitions are possible during the collision process. [141]

These resonances, which (depending on the structure of the atom) can often be tuned with external magnetic fields, allow manipulation of the sign and magnitude of the scattering length and affect the rate of inelastic collisions [142, 14, 143]. But these resonances typically have very narrow energy widths ($\ll 1$ mK [141]). As such, we expect them to have little impact on the data in this thesis (which is at temperatures ≥ 10 mK), and on non-ultracold collisions in general.

Shape resonances

Shape resonances are resonances which arise because of the shape of a single potential energy curve. Specifically, higher order partial waves ($l > 0$) scattering off attractive potentials experience a centrifugal barriers which creates and confines "quasibound states". These quasibound states decay by tunneling through the barrier. Scattering states with energies on resonance with these quasibound states will have their scattering properties markedly changed by them. Also known as "potential resonances",

"resonance scattering" or "pseudo-bound-state resonances", shape resonances can cause dramatic changes in the behavior of higher-order partial waves at energies below the height of the angular momentum barrier [90]. Shape resonances and their effects have been observed in rubidium [144] and potassium [145, 146, 147].

Shape resonances can be of consequence in the ultracold limit if they occur near $E = 0$, but we would generally expect them to be of more universal consequence for cold atom scattering. In the cold-collision temperature regime, the thermal distribution of atoms will include atoms at energies on resonance with shape resonances. As the distribution of atoms cools, the fraction of atoms on resonance with the shape resonances will change, and we would expect their scattering behavior to be correspondingly affected.

Shape resonances will have only modest consequences for elastic scattering in the cold regime. Because the thermal averaging over collision energies already incorporates a complete range of phase shifts, the change in the scattering wavefunction at the shape resonance will have little effect. This arguement does not apply to inelastic collisions: at a shape resonance, the wavefunction inside the angular momentum barrier will be significantly increased [90]. If the inelastic loss processes increase at small distances (true for spin-spin dipole interactions and especially for spin-orbit-coupling induced loss), the loss rate will be enhanced at the resonance. Thus, we would expect that, in the non-ultracold regime, shape resonances will act to decrease the ratio of elastic to inelastic collisions [148].

Identical Fermion scattering

Special considerations are required to evaporatively cool fermionic atoms. In the ultracold limit, the elastic scattering cross-section of all higher order partial waves goes to zero.[19] Identical fermions cannot undergo s-wave scattering because s-wave scattering is symmetric under particle exchange. Thus, for a trapped ensemble of fermions prepared in the same internal state, the elastic collision rate will rapidly decrease as the temperature is lowered [147]. This will likely prevent the use of

[19]It is difficult to accurately predict the threshold temperature for chromium, as the interatomic potential (and C_6 coefficient) are not known well. However, we would estimate that the threshold temperature (based on what is observed for other, similar mass atoms) is on the order of $\sim$100 μK [138, 147].

evaporative cooling.

This problem can be circumvented and evaporative cooling implemented by trapping multiple species. Although two identical state fermions cannot undergo s-wave collisions with each other, they certainly can s-wave scatter with a second species.

A successful potassium evaporative cooling experiment achieved Fermi degeneracy by trapping a single fermion isotope (^{40}K) in multiple hyperfine states ($|F = 9/2, m_F = +9/2\rangle$ and $|F = 9/2, m_F = +7/2\rangle$) to permit evaporation [36]. Two successful lithium evaporative cooling experiments both increase their fermion phase space density by trapping a small number of fermionic ^{6}Li atoms with a larger number of boson ^{7}Li and selectively evaporating the ^{7}Li to cool both species [37, 38]. In our chromium experiment, we trap multiple isotopes of chromium. This combination of species will provide elastic collisions for both isotopes in the ultracold regime.

Chapter 3

Calcium Monohydride

We chose to trap calcium monohydride (CaH) because it is a simple paramagnetic molecule that had been previously studied and was well understood at zero field [149, 150]. Its ground state, $X\ ^2\Sigma$, is magnetically trappable, with a 1 Bohr magneton magnetic moment. Additionally, the ground state is a relatively simple Hund's case (b), with small coupling between its spin and rotation.[1] CaH has a strong electronic transition ($B \leftrightarrow X$) at 634 nm, allowing for convenient and efficient spectroscopic detection. Finally, it is straightforward to produce CaH via laser ablation, a process particularly well suited to our cryogenic environment.

3.1 CaH spectroscopic structure

Molecular Structure

The relevant rotational and vibrational constants of CaH are shown in Table 3.1. Because of the large rotational and vibrational spacings, we expect only the ground rovibrational state to be populated after buffer-gas cooling.

The nuclear properties of CaH are quite simple. The dominant hydrogen isotope is, of course, ^{1}H. ^{1}H has a natural abundance of 99.985%, and a nuclear spin $I = 1/2$. The most common isotope of calcium is ^{40}Ca, with 96.94% natural abundance and $I = 0$ [155]. Because of the dependence of a molecule's vibrational energy on its atomic

[1] Molecular notation, the various Hund's cases, and molecular structure are explained in References [151, 152, 153].

	$X^2\Sigma(\nu''=0)$	$X^2\Sigma(\nu''=1)$	$B^2\Sigma(\nu'=0)$
T_ν	0	1260.15	15752.61
B_ν	4.23	4.13	4.35
γ	0.04	0.04	-0.88

Table 3.1: Rotational constants of CaH, expressed in wavenumbers (cm^{-1}) [149, 150, 154]. The energy of the rotational levels of CaH are given by
$E = T_\nu + B_\nu \cdot N(N+1) + \frac{\gamma}{2} \cdot N$ when $J = N + 1/2$
$E = T_\nu + B_\nu \cdot N(N+1) - \frac{\gamma}{2} \cdot (N+1)$ when $J = N - 1/2$
where ν is the vibrational quantum number and $N = J \pm 1/2$ is the rotational number. Terms of higher order in N and ν have been omitted, so this expression should be used only as a guide to the properties of CaH, and not for finding exact line positions. Additionally, the complex spin-splitting behavior of $B^2\Sigma(\nu' = 0)$ is not adequately described by γ alone.

masses, molecular isotopic shifts are large. Although we conducted our experiments with CaH that had not been isotopically enriched, we observed only $^{40}Ca^{1}H$, and did not attempt to detect other isotopes.

Spectroscopic detection

We detect CaH by absorption spectroscopy and laser-induced-fluorescence spectroscopy on the $B \leftrightarrow X$ transition. $B \leftrightarrow X$ is a strong transition: the lifetime of the $(\nu'=0)$ excited state is 58 ± 2 ns [156]. We excite the ground rotational and vibrational X state on the

$$|B^2\Sigma, \nu'=0, N'=1, J'=3/2\rangle \leftarrow |X^2\Sigma, \nu''=0, N''=0, J''=1/2\rangle$$

R-branch transition at 15761.96 cm^{-1} [157].

Initial measurements of the CaH molecules were performed with absorption spectroscopy. However (as discussed in Appendix G) we find we obtain superior signal-to-noise using laser-induced fluorescence. In this technique, we monitor the light scattered from the atoms. However, there is also a large amount of light scattered by the apparatus itself. To obtain good signal-to-noise, it is necessary to be able to distinguish the light scattered by the molecules from this background. This differentiation is done through the photon's color: the cell mirror, windows, and other inadvertently illuminated surfaces predominantly scatter photons elastically, but molecules

can scatter photons inelastically if they decay to a different vibrational level than that which they originated in. Here, calcium monohydride's large vibrational splitting is advantageous.

We detect the CaH fluorescence emitted on the $|B^2\Sigma, \nu' = 0\rangle \rightarrow |X^2\Sigma, \nu'' = 1\rangle$ transition at 690 nm and use color filters to block elastically scattered probe light at 634 nm. The fraction of the excited $|B, \nu' = 0\rangle$ molecules which decay to a given vibrational level of the X state is given by the the Franck-Condon factor [151]. The Franck-Condon factor for the $|\nu' = 0\rangle \leftrightarrow |\nu'' = 0\rangle$ transition has been calculated to be 0.971; the Franck-Condon factor for the $|\nu' = 0\rangle \rightarrow |\nu'' = 1\rangle$ decay was calculated to be 0.027 [158]. This reduces the efficiency of our frequency-resolved laser-induced fluorescence; about 3% of the emitted photons will be of the correct frequency for detection.

Although the theoretically determined Franck Condon coefficients are convenient for qualitative considerations, it is difficult to assess their quantitative accuracy. This uncertainty is just one of many potential sources of inaccuracy in determining the true optical density from the fluorescence: the captured solid angle, the detector quantum efficiency, and the transmission of the various optics and filters are all difficult to measure precisely. To avoid any such problems, we calibrate our fluorescence spectroscopy directly with absorption spectroscopy measurements.

3.2 Cryogenics

A diagram of the cryostat is shown in Figure 3.1. A copper cell contains the buffer gas and the CaH_2 ablation target. It is thermally connected to a dilution refrigerator through a copper "heatlink". The cell and refrigerator are sealed inside a stainless steel "inner vacuum chamber" (IVC), which in turn runs through the 2" diameter bore of the superconducting trap magnet. Both the IVC and magnet are immersed in liquid helium. So that the optical path to the cell does not run through the helium, the IVC is sealed to the bottom of the helium dewar with a flexible welded metal bellows to facilitate the mechanical connection. A window seals the bottom of the IVC and separates its vacuum from the dewar vacuum. All vacuum seals in Figure 3.1 are made with indium O-ring face seals [159], using 0.030" or 0.040" diameter indium wire [160]. The joints are typically machined to a 0.003"$\pm$0.002" radial clearance.

The cryostat window system is explained in greater detail in section 5.2. The

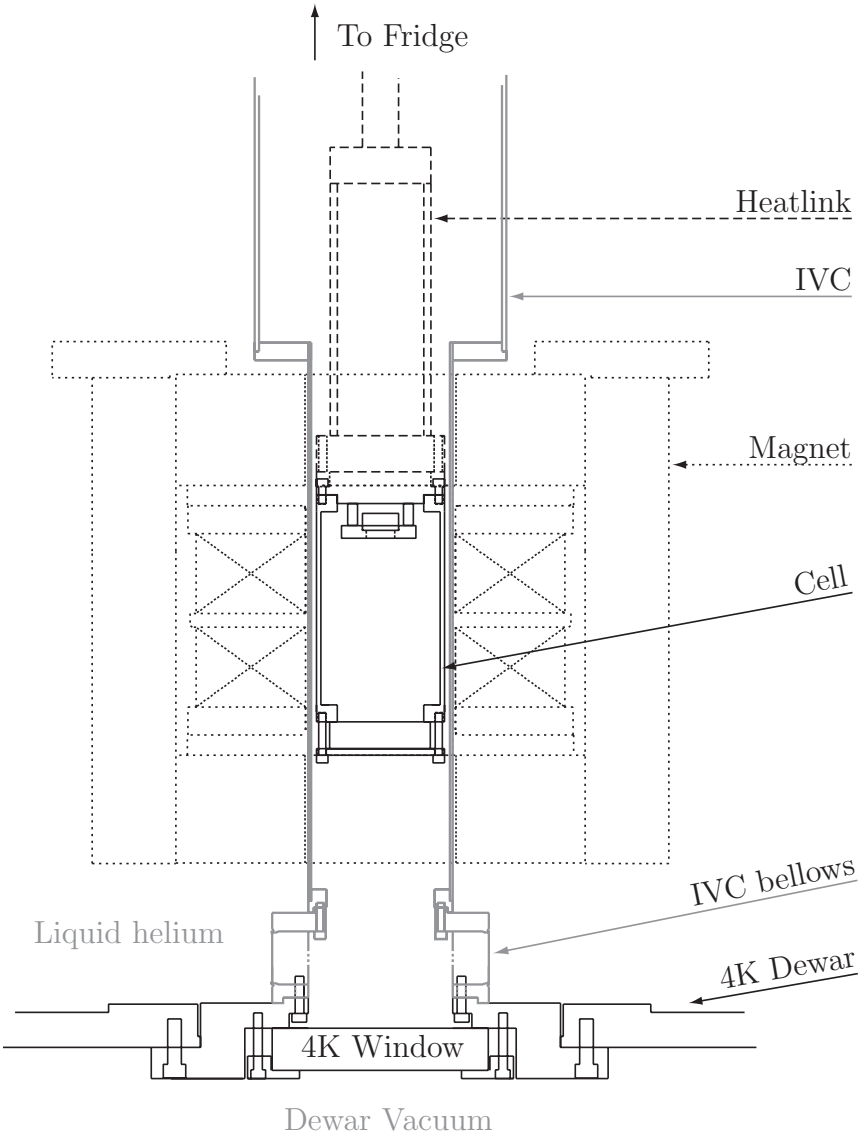

Figure 3.1: The cryostat, as used with the CaH experiment.

relevant details of the trap magnet are described in Section 5.1, where it is referred to as "The Old Magnet".[2] The copper cell is described below.

[2]The "jump behavior" described in Section 5.1 is irrelevant for our CaH work.

Copper Cell

A diagram of the copper cell is shown in Figure 3.2. It is a slight variant of the copper cell used to trap atomic europium, described at length in the thesis of Jinha Kim [104].

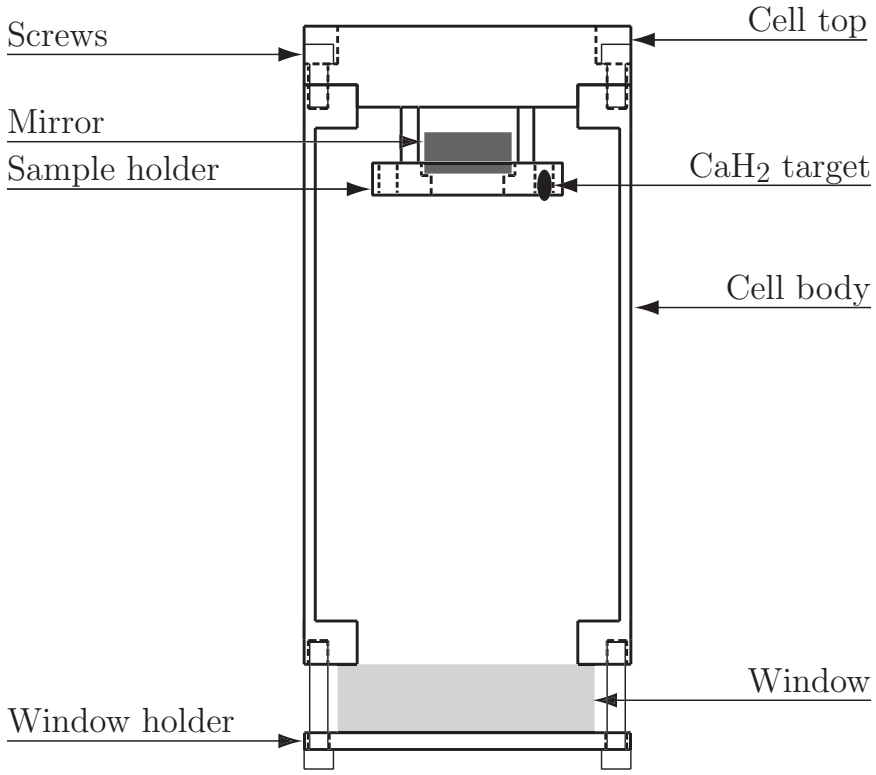

Figure 3.2: The copper cell, as used for the CaH experiment. Cylindrically symmetric, with the exception of the ablation targets and other details.

The cell body, top, and heatlink are are machined out of OFE 101 copper (oxygen-free high conductivity copper, alloy 101) to provide good thermal conductivity [161]. The heatlink serves to thermally anchor the cell to the dilution refrigerator (as shown in Figure 3.1) and it is attached and thermally connected to the cell top with nine 4-40 brass screws. The heatlink is designed to allow the cell to be heated (to produce the desired density of buffer gas for trap loading) without appreciably heating the dilution refrigerator. This is crucial because the dilution refrigerator is extremely slow to cool. Once the atoms have been loaded into the magnetic trap, the thermal link must then provide good thermal conductivity to cool the cell and reliquefy the buffer gas.

As a compromise between these requirements, we use a 0.5" diameter, 8" long OFE copper rod as the heatlink between the cell and the dilution refrigerator. The heatlink was measured to have a thermal conductance (in the temperature range of 100 mK to 600 mK) of approximately $\kappa \sim 20 \cdot (\frac{T}{\mathrm{K}})\ \mu\mathrm{W/mK}$.[3]

Attached to the cell top via screws and copper standoffs is the "sample holder". The sample holder is positioned closely behind the saddle point of the magnetic trap. CaH_2 ablation targets [162] are held into sockets in the sample holder with screws (not shown). To prevent the decomposition of CaH_2 that occurs in air, the cell is assembled in an inert atmosphere of N_2 gas. Once assembled, it is pumped out and filled with helium buffer gas. The cell mirror is held to the back of the sample holder with a thin aluminum strap (also not shown).

The cell top and window are sealed to the cell body with indium face seals.[4] Although it complicates indium removal after breaking the seal, we do not apply vacuum (or any other) grease to our indium seals. Brass screws are used to tighten the cell seals. Brass was chosen because it is nonmagnetic and its relative thermal contraction is such that it continues to provide compression on the copper joint during cooldown. With this technique, we have obtained an extremely low failure rate of indium vacuum seals at cryogenic temperatures.

Omitted from Figure 3.2 are the cell fill line, "^{3}He can", and Vespel standoffs. The fill line is a thin stainless steel tube (1/8" outer diameter, 1/16" inner diameter) connecting the cell to a room temperature pumping station. The fill line allows the cell to be pumped out and helium introduced. The fill line is brazed to the cell, and cryogenic vacuum connections between segments of the steel tube are made with Swagelok VCR fittings with stainless steel gaskets [163]. These fittings were found to be reliable under cryogenic cycling.

The ^{3}He can is a copper reservoir connected to the cell by a stainless tube. Its intended function was to liquefy the buffer-gas when cooled by the dilution refrigerator to provide good vacuum even if the cell was at elevated temperatures. Unfortunately,

[3]This conductance is slightly less than one would estimate for a copper heatlink of this size, but given the large variation of the thermal conductivity of copper depending on its purity and structure, it is not too surprising a result [99].

[4]Sealing the window with an indium seal has much simpler machining requirements and more reliable performance than the thin-walled socket epoxy seal previously employed [104].

it did not work. To provide rapid pumping speed, the tube connecting the ^{3}He can to the cell must have a large diameter and short length. This combination prevented obtaining thermal separation between the cell and ^{3}He can, and the ^{3}He can could not be cooled independently of the cell. The ^{3}He can served no role in this experiment (that we are aware of) and was eliminated from subsequent versions of the cell.

The Vespel standoffs are three sharpened, $\sim$ 0.3 mm diameter Vespel-22 rods attached to a brass ring [164]. The standoffs (described in greater detail in the thesis of Jinha Kim [104]) fit between the cell and IVC to prevent the cell from touching the IVC directly. Although the standoffs themselves touch the IVC, the combination of a sharpened tip, small diameter, and low thermal conductivity [99] results in only a minor ($\lesssim 10$ μW) heat load on the cell.

Finally, the temperature of the refrigerator, ^{3}He can, and cell are monitored with ruthenium oxide thermistors, as described in Section 5.7.

3.3 Optics

To generate narrow-band light to probe CaH, we use a continuous-wave dye laser. To produce molecular CaH, we use a pulsed YAG laser [112]. The optics chain for both systems is shown in Figure 3.3.

Probe laser

The probe beam begins with a Coherent Model I-200 argon ion laser [165, 166] which produces 10 Watts of multiline green power. This laser is used to pump the Kiton Red Dye lasing medium of a Coherent model 899-21 continuous-wave ring laser [165, 166]. This laser is frequency stabilized to a built-in reference cavity, yielding a linewidth on the order of 1 MHz (less than the natural linewidth of the B state of CaH), and can be continuously scanned up to $\sim$ 30 GHz.

To aid in finding the correct laser frequency, the output of the ring laser is monitored with a Burleigh Wavemeter [167]. Used for all the work in this thesis, the Wavemeter is invaluable for initially finding the transition frequency, in day-to-day operations, and for diagnosing problems. Further calibration of the laser frequency is provided through absorption spectroscopy of a vapor-pressure iodine cell (not pictured) [168].

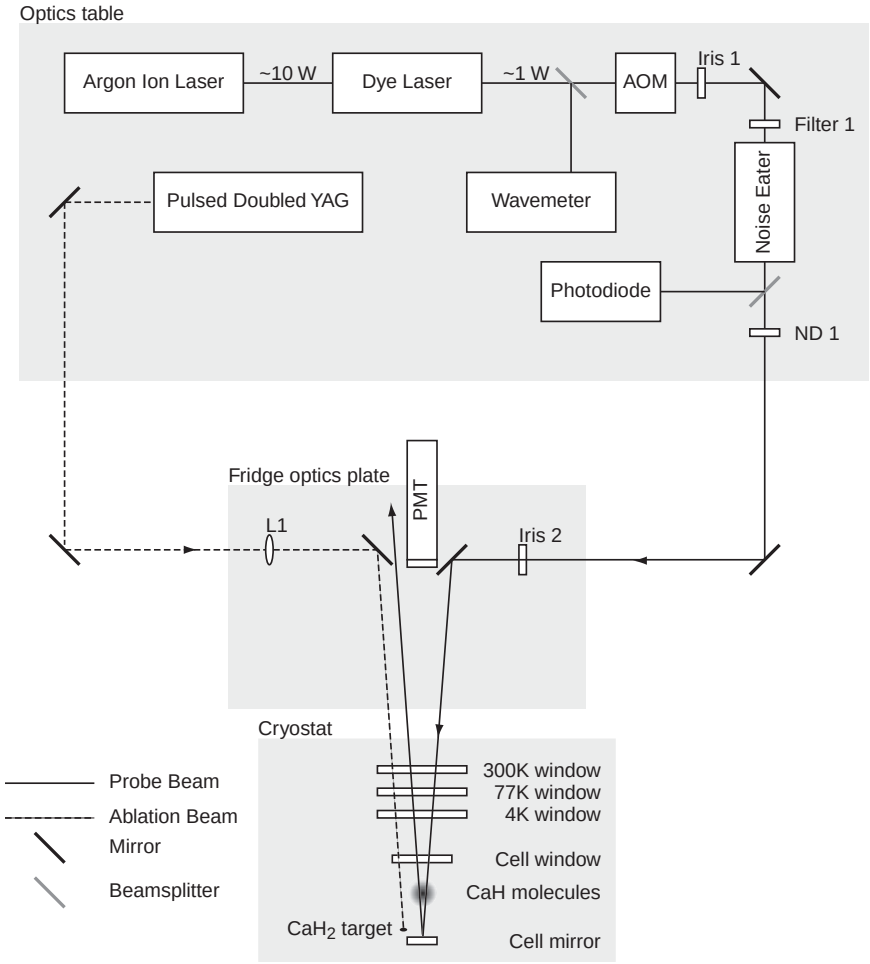

Figure 3.3: Optics setup for the CaH experiment. Various mirrors and other "passive" optical components have been omitted to simplify the drawing. The mirrors which are not part of the optics table, fridge optics plate, or cryostat are mounted to the floor.

Symbol	Optic	Function
L1	400mm lens on translation stage	Focus YAG beam onto CaH_2 target
Iris 1	Adjustable iris	Block zeroth order AOM beam
Iris 2	Adjustable iris	Control probe beam diameter
ND1	Adjustable neutral density filter	Adjust probe beam power
Filter 1	632 nm (×10 nm) bandpass filter	Block scattered light from laser

The output of the dye laser is chopped at 10 kHz with an acousto-optic modulator [169], its average amplitude stablilized using a commercial polarizer system [170], and reduced in power with reflective neutral-density filters [171]. The beam is sent off the

optics table and steered by mirrors mounted to the floor to optics mounted on the bottom of the cryostat. An iris on the bottom of the dewar controls the beam size entering the cell, typically to ~ 5 mm diameter. Typical probe powers are ~ 1 mW. The probe beam is then directed in and out of the cell, and a photomultiplier tube monitors the fluorescence from the cell.

Light detection

The basic arrangement of our light detection optics is shown in Figure 3.3. Omitted from this figure is a "tent" of black fabric placed over the cryostat frame to shield the detection optics from ambient light in the room. As discussed in Section 3.1, we detect CaH primarily through laser-induced fluorescence spectroscopy. To detect the light, we use a Hammamatsu R669 photomultiplier tube (PMT) [172].

Color filters are placed over the face of the PMT to block the scattered probe radiation at 634 nm and pass the frequency shifted molecular fluorescence at 690 nm. We use the combination of a narrow band interference filter ($\sim$ 10 nm transmission FWHM) [173] followed by two Schott Glass absorptive color filters [174] placed over the opening of the PMT housing ($\sim$ 1 inch from the PMT face). The Schott color filter glass is specified to provide a large extinction ratio: $\sim 0.2\%$ transmission at 634 nm with nearly full ($\sim 80\%$) external transmission at 690 nm. Unfortunately, when the filter absorbs light at 634 nm, it fluoresces red-shifted light. This strongly reduces the gains that can be made by stacking successive filters. We find the best performance is obtained with a single narrow band interference filter followed by two colored glass filters.

Additional steps further reduce the PMT signal from non-CaH sources. Previous cryogenic cells exhibited "false fluorescence": downconversion of the incident probe light by materials in the cell. Little downconversion was exhibited by metal surfaces, but substances such as Kapton, epoxy, and mylar tape all exhibited "false fluorescence" at our detection wavelength. To improve our experimental sensitivity, we strove to minimize the presence of such materials in the cryostat.[5] Additionally, we place an Ealing 35-3912 632 nm ($\times$10 nm) bandpass filter on the table to block the

[5]One of the normal luxuries of cryogenic vacuum is the freedom to use materials which are antithetical to room temperature ultra-high vacuum because of their outgassing properties [118]; nothing outgasses at 100 mK.

errant fluorescence at ~ 690 nm emitted from the dye medium in the laser.

The electrical current output of the photomultiplier tube is converted to a voltage by passing it through a resistor, and this signal is fed into a lock-in amplifier [175] which demodulates the fluorescence signal with the AOM chopping of the probe beam. This lock-in detection allows the laser induced fluorescence to be distinguished from room lights, the ablation plume, PMT dark current, and other forms of errant signal.

To calibrate the observed fluorescence signal with the true optical density in the cell, absorption measurements were made simultaneously with a photodiode. Although we were able to observe an absorption signal on the photodiode only at conditions of high absorption levels, the linear response of the PMT allows us to extrapolate to lower signal levels.

The noise in our laser-induced-fluorescence measurements was dominated by the shot noise of the PMT photocurrent. This photocurrent had roughly equal contributions from three errant sources (in addition to the CaH laser-induced fluorescence): the dark current of the uncooled PMT, light sources in the laboratory which were incompletely shielded by the fabric "tent" over the cryostat, and laser-induced "false fluorescence". Their resulting shot noise limited the low-signal sensitivity of our detection. Simple calculations concerning shot noise are discussed at greater length in Appendix G.

The combination of this noise floor and our fluorescence-detection efficiency resulted in a sensitivity to, with a probe power of 100 μW and a 1 ms measurement, an absorption of $\sim 10^{-4}$. With the same probe power, we are equivalently sensitive to an absorption level of 1 part in $\sim 10^5$ in a 100 ms measurement. This corresponds to a "minimum detectable number" of $\sim 10^6$ CaH molecules in the trap.

On a separate note, it is important to shield the PMT from the fields of the magnetic trap. To detect the maximum number of photons, it is desirable to place the PMT as close as possible to the bottom of the cryostat. Unfortunately, magnetic fields reduce the PMT gain. Unshielded, the PMT output drops an order of magnitude with the magnet fully energized. We shield the PMT by placing it inside a tube of high-permeability metal [176]. With the magnet energized, the PMT gain is then reduced by less than 25%.

Ablation Optics

The optics necessary to produce CaH by laser ablation are straightforward, as shown in Figure 3.3

The ablation laser used is a Q-switched pulsed Nd:YAG laser [111, 112]. Our laser is equipped with a doubling crystal for second harmonic generation, and its doubled output at 532 nm is used for ablation. The doubled green output was chosen largely for operator convenience when positioning the beams. The ablation pulses are steered to the cryostat with a series of broadband dielectric mirrors [177]. The pulse is focused onto the solid CaH_2 [162] ablation target by a 400 mm lens mounted on a translation stage. The focal length of the lens is chosen so that the beam is not too tightly focused while passing through windows, but also of a length such that the partial back-reflections of the cryostat windows are not focused at inconvenient locations. This is important to avoid the inadvertent ablation of our optics.

3.4 Preliminary experiments

"High temperature" experiments

For the experiments described in this thesis, it was standard practice to perform room temperature ablation experiments prior to experiments with the dilution refrigerator. These "300 K" experiments provide a rough gauge of how effective laser ablation is for producing the species of interest and a means of testing the method of detection to be used.

Because our prior vanadium monoxide experiment had failed to trap molecules (as described in Chapter 4), we were apprehensive that calcium monohydride might undergo a similar process of rapid, trap-independent loss. To test for such a problem, we conducted additional ablation tests inside a 4 K cryostat to verify that the molecular loss was dominated by the expected process of diffusion to the walls.

The room temperature ablation experiments were conducted inside a Conflat cross, and the CaH atoms were detected with absorption spectroscopy. The 4 K experiments are conducted in a copper cell similar to the cell described in Section 3.2. The cell is attached to the bottom of a liquid helium tank and surrounded by a liquid nitrogen cooled radiation shield inside a small ($\sim$ 2') vacuum container. Optical access to the cell is provided through BK7 windows at 300 K and attached to

the 77 K shield. The molecules produced were detected through both absorption and laser-induced-fluorescence spectroscopy.

Experiments were performed to attempt to produce and detect TiN, CaH, and CaF molecules through ablation of a 99.5% purity TiN sputtering target, 99.95% purity "vacuum deposition grade" CaF_2, and 95% purity CaH_2 "lumps", respectively [178]. We chose to trap CaH because of its larger rovibrational spacings and because we found that CaH was ablated not only in the greatest abundance, but also the most reliably.

Inside the 4 K cell, CaH diffusion times on the order of 50 ms were observed at a helium density of 5×10^{16} cm^{-3}. This is comparable to the diffusion timescales previously seen with atomic species under similar conditions, and is consistent with loss dominated by diffusion to the walls. (A mathematical description of diffusion to the walls is discussed in greater detail below in Section 3.7.) Additionally, this loss was appreciably slower than the rapid initial loss previously observed with VO (described in Section 4.4), whose non-diffusive loss prevented trapping. These tests provided the confidence to proceed to attempt to trap CaH.

Zero-field dilution refrigerator experiments

A spectrum of ablation-produced CaH in the experimental cell in the absence of the magnetic trap is shown in Figure 3.4.

Hyperfine structure

The two resolved peaks of Figure 3.4 are fit well by the known CaH hyperfine structure, as discussed in References [179, 180]. The splitting of the transition is dominated by the hyperfine structure of the ground state. The left-hand peak originates from the $F'' = 1$ ground state, the right-hand peak from the $F'' = 0$ ground state. As expected from their respective degeneracies, the $F'' = 1$ peak is larger than the $F'' = 0$.

The CaH hyperfine splitting is small compared to the Zeeman shift of the energy levels of CaH in the trapping fields, and we ignore hyperfine effects in our subsequent discussion of CaH.

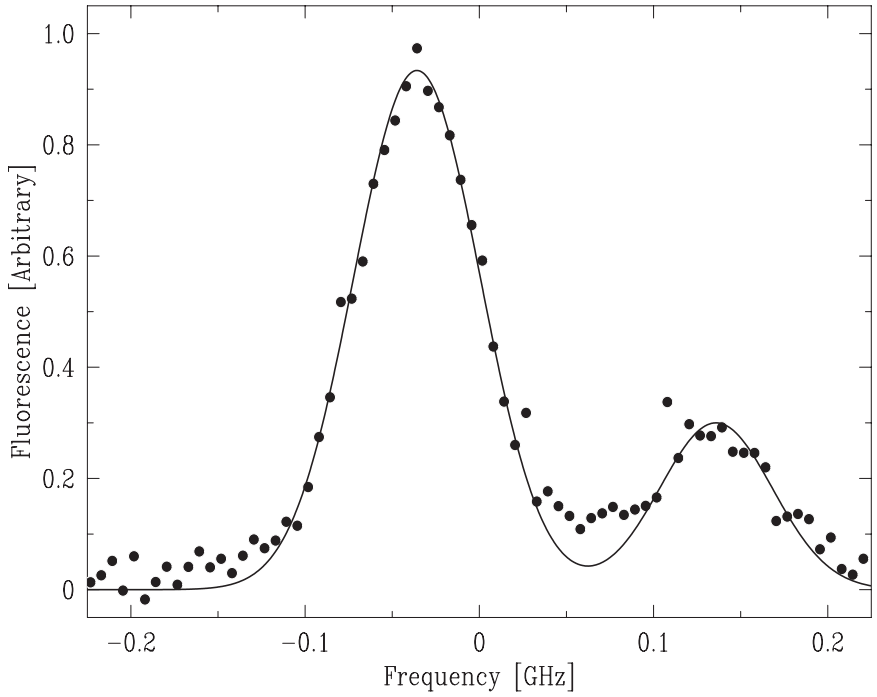

Figure 3.4: Spectrum of ground-state CaH at zero field, taken from 25 to 50 ms after the ablation pulse. The spectrum is fit to the multiple hyperfine transitions of the CaH ground state, each with a Gaussian lineshape. The only free parameters in this fit are two peak heights, a single Gaussian width, and the overall frequency zero.

Lineshape

As seen in Figure 3.4, the zero-field spectral peaks of CaH are fit reasonably well by the Gaussian lineshape expected for Doppler broadening. However, if we assume that Doppler broadening is the only broadening mechanism, the fit indicates a translational temperature of 2.2 ± 0.5 K temperature. This temperature is surprisingly high, and inconsistent with calcium monohydride's subsequent behavior in the magnetic trap.

The zero-field spectral peaks fit equally well to Lorentzian lineshapes, as shown in Figure 3.5. However, it is similarly difficult to physically account for the Lorentzian linewidth. Expected sources of Lorentzian broadening are the natural lifetime of the excited state, intensity broadening, and pressure broadening. But the natural lifetime gives a Lorentzian with a FWHM of 2.7 MHz, and we experimentally verified that the linewidth is independent of the probe laser intensity. Extrapolating pressure-broadening measurements of atoms in helium [181], we would naively expect the pressure-broadening effects of the buffer gas to be over an order of magnitude smaller

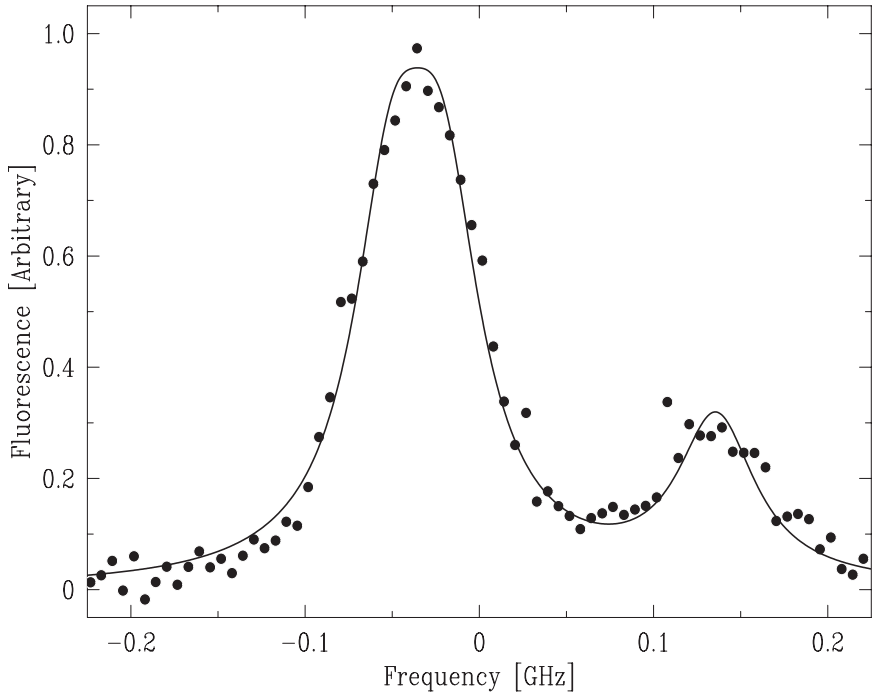

Figure 3.5: Spectrum of ground-state CaH at zero field, identical to Figure 3.4 but fit to Lorentzian lineshapes. The peculiar shape of the left hand peak results from two unresolved hyperfine transitions. The fit determines a Lorentzian full-width-at-half-maximum (FWHM) of 54 ± 10 MHz

than the observed linewidth.

Because we cannot cleanly distinguish the different possible broadening mechanisms, we are unable to draw any firm conclusions about the origins of the field-free CaH linewidth.[6] For example, the spectrum would be better fit by a Voigt profile [182]. But because both pure Lorentzian and Gaussian lineshapes fit the spectrum reasonably well, it is impractical to extract their relative contributions to the composite Voigt lineshape. Additional broadening mechanisms may also play a role: inhomogeneous magnetic fields on the order of tens of gauss would provide a significant contribution to the observed linewidth.

Ablation Yield

The CaH ablation yield inside the experimental cell is shown in Figure 3.6 as a function of pulse energy. The number produced plateaus at high power. As a compromise

[6]My current personal guess is pressure broadening.

between good atom production and minimizing the heating of the cell during the ablation process, we typically ablate with a single ~ 3 mJ pulse.

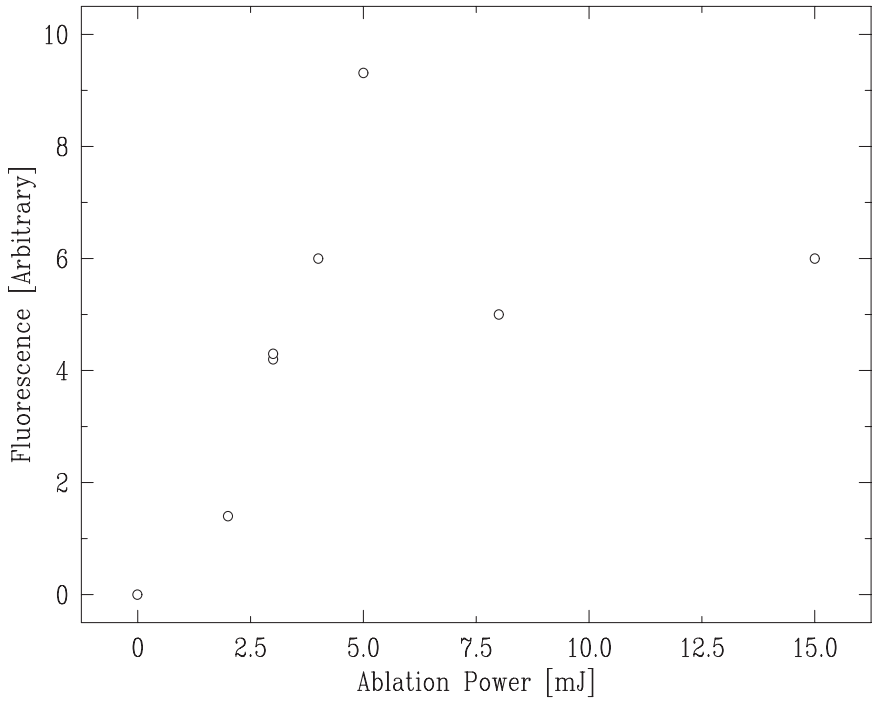

Figure 3.6: CaH ablation yield as a function of ablation pulse power; atom number is proportional to fluorescence. Measured with the magnetic trap off, at a cell temperature of 300 mK (prior to ablation), and a helium density of 1×10^{17} cm^{-3}. Due to a lack of a contemporary calibration of the ablation laser power, the x-axis scale is suspect, so this graph should be interpreted qualitatively.

The amount of calcium monohydride thermalized within the cell is strongly dependent on the helium buffer-gas density, as shown in Figure 3.7. The CaH yield increases with the helium density, but this process is not well understood. It is possible that the small molecule numbers seen at low helium pressures is due to a failure of the low-density buffer gas to thermalize the CaH before it travels to the walls. The fact that when the thermalized CaH is first observed it is seen to be nearly evenly distributed across the cell volume would support this reasoning. Alternatively, it may be the case that a high density of helium encourages the production of CaH molecules in the ablation plume; because we did not observe the CaH at short times, we cannot conclusively distinguish between these two possible mechanisms.

Unfortunately, we are unable to take full advantage of the increased CaH production seen at high helium densities. As discussed in Section 3.7, inelastic CaH–^{3}He

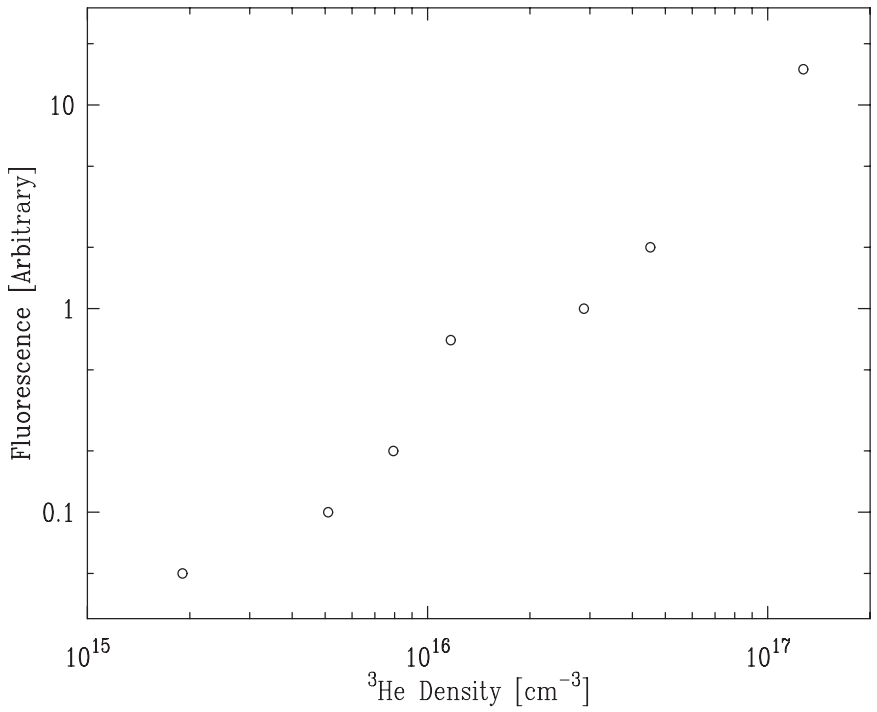

Figure 3.7: CaH ablation yield as a function of helium gas density, with constant ablation power. The fluorescence level is proportional to molecule number.

spin-changing collisions limit the ^{3}He density which can be used.

Ablation "Glow"

There is a great deal of scattered light during the 5 ns laser pulse used to ablate CaH. Long after the ablation pulse, light continues to be emitted from the cell, at least partially by the ablation plume. The time profile of this fluorescence is shown in Figure 3.8; its source of origin is unidentified. We note however, that its time behavior is appreciably different from that on which the CaH molecules disappear from the cell. After its initial abrupt decay, the fluorescence level is seen to drop exponentially with a $\sim$ 10 ms timescale. Under the same experimental conditions, LIF measurements indicate that CaH molecules are lost (through diffusion to the walls) on a 200 ms timescale.

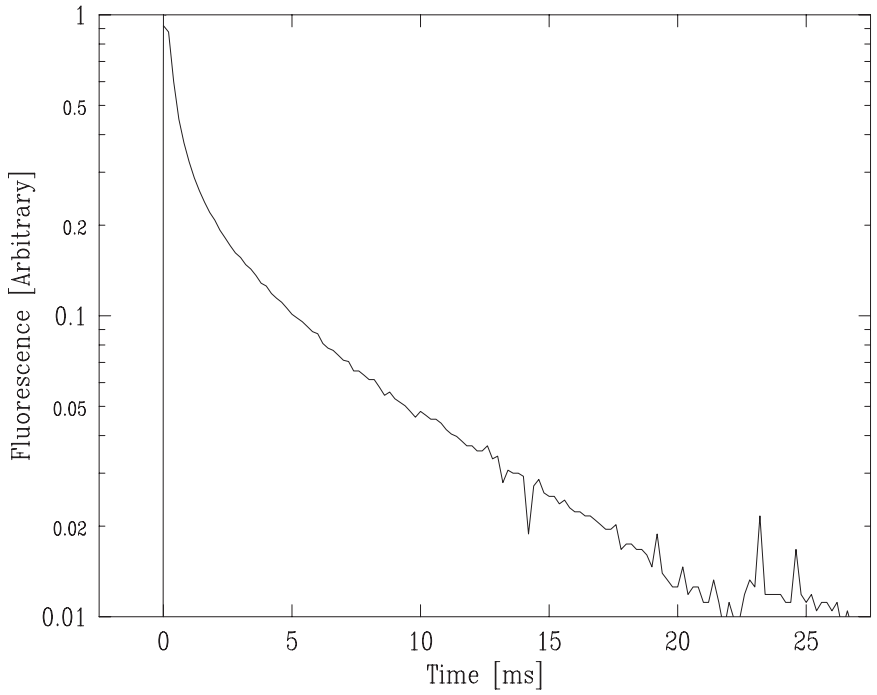

Figure 3.8: Light emitted by the ablation plume (as monitored by the PMT of Figure 3.3). In this data, the probe laser and trap are turned off.

3.5 Zeeman structure of CaH

Understanding calcium monohydride's Zeeman spectroscopy is vital for understanding its behavior in our trap. Inside the trap, the CaH spectrum will be broadened according to its Zeeman shift and the inhomogeneous magnetic trapping fields. We rely on this broadening to spectroscopically determine the distribution of molecules throughout the trap. The Zeeman structure of the relevant states of CaH are shown in Figure 3.9.

In nonzero magnetic field, the $J'' = 1/2$ ground state splits into two levels: a trappable $m''_J = +1/2$ weak-field seeker and an untrapped $m''_J = -1/2$ strong-field seeker. For brevity, we will only discuss the transitions from the $m''_J = +1/2$ weak-field seeker. The behavior of transitions from the strong field seeking state are, with the appropriate sign changes, identical.

When excited on its R-branch transition to $|B^2\Sigma, N' = 1, J' = 3/2\rangle$, the weak-field seeking ground state $|m''_J = +1/2\rangle$ can make one of three possible transitions: $\Delta m = -1$, 0, or $+1$, to $m'_J = -1/2$, $+1/2$, and $+3/2$, respectively. Naively, one

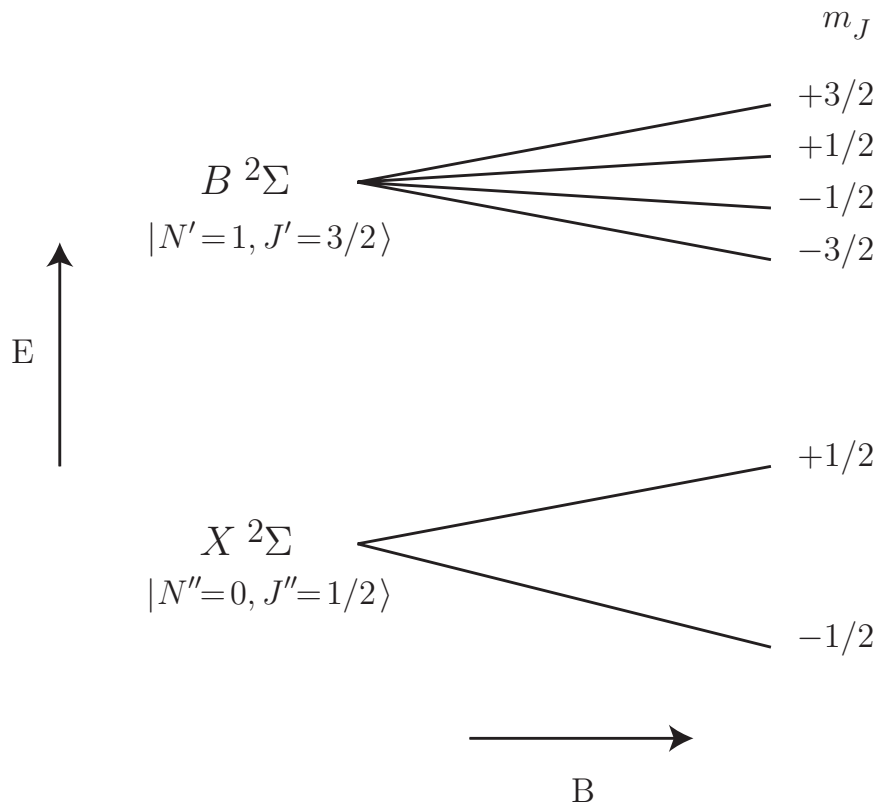

Figure 3.9: The Zeeman level structure of the lowest energy level of CaH and the excited state used for detection (not to scale). Hyperfine structure is omitted, as it is from all of our considerations of CaH in high field.

would expect the magnetic moment of the $|m'_J = +3/2\rangle$ excited state to be well matched to the 1 μ_B moment of $|m''_J = +1/2\rangle$ ground state. This would result in large Zeeman broadening ($\Delta\mu \sim 2/3\mu_B$ and $\sim 4/3\mu_B$) of the transitions to the $|m'_J{=}+1/2\rangle$ and $|m'_J{=}-1/2\rangle$ excited states, and narrow broadening of the transition to the $|m'_J{=}+3/2\rangle$ excited state. Indeed, if both X and B were perfect Hund's case (b) states (with no coupling between the spin and the molecular axis or its rotation), we would expect the only difference in their magnetic moments to be due to the additional molecular rotation of the excited state, which would change μ by less than a part in one thousand.

Although the Zeeman effect in CaH had been previously studied in the year 1930 [183], this work was of insufficient spectral resolution to be of use to us. We experimentally measured the splitting of the CaH spectra in the trapping fields. This data was taken with the same experimental apparatus (described in Sections 3.2 and 3.3)

used for the magnetic trapping of CaH. While an isotropic magnetic field would have been preferable for spectroscopic simplicity, ease in distinguishing transitions, and signal-to-noise, the structure of CaH is sufficiently simple that such measurements were unnecessary. The measurements were performed in the trap under conditions such that the atoms were distributed throughout the trapping fields. The frequency shift at the known magnetic field of the trap "saddle point" was used to determine the Zeeman shift of the transition as a function of field.

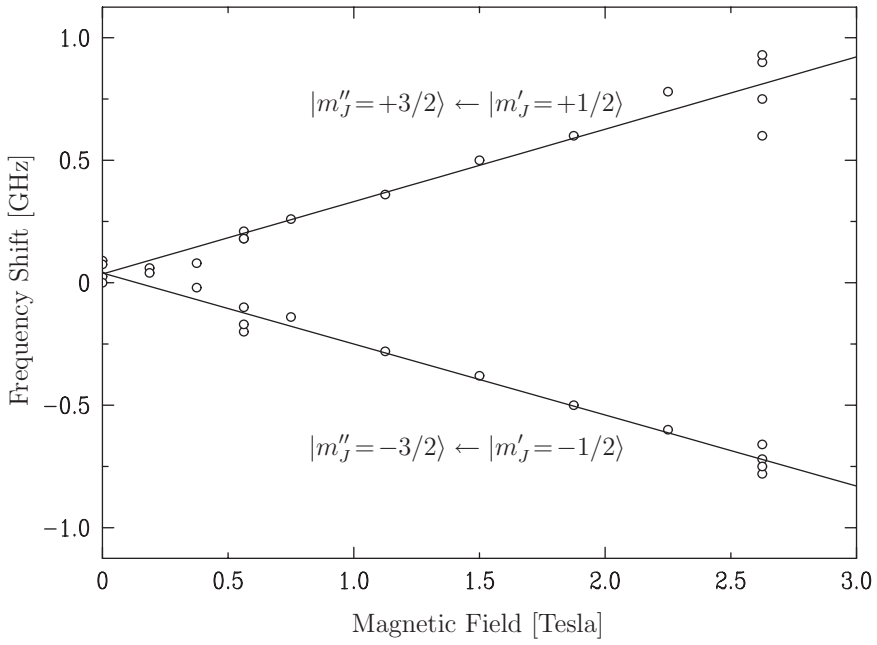

Figure 3.10: The two least-broadened transitions of the $|B^2\Sigma, N' = 1, J' = 3/2, \nu' = 0\rangle \leftarrow |X^2\Sigma, N'' = 0, J'' = 1/2, \nu'' = 0\rangle$ R-branch transitions. The broadening corresponds to a mismatch of 0.02 μ_B in the magnetic moments of the ground and excited states. The upper transition originates from molecules in the weak-field seeking ground state; the lower from strong-field seekers.

As expected, we observe multiple transitions which are strongly broadened (with $\Delta\mu \sim 1\mu_B$) in the magnetic field. As expected, we also observe two narrow transitions, shown in Figure 3.10. These narrow transitions are the $|m'_J = \pm 3/2\rangle \leftarrow |m''_J = \pm 1/2\rangle$ CaH transitions. Their broadening is dominated by the perturbation of the excited state by the nearby $A^2\Pi(\nu = 1)$ state, which is evidenced by the large spin-splitting of the B state) [149, 150, 184]. The identification of the narrow transitions was based on the expected structure and influence of the A state perturbation and the behavior of these states in the trap.

The CaH ground state is expected (but not measured) to have a magnetic moment of $\pm 1.00\ \mu_B$. With this assumption and the measured splitting, we conclude the $|B^2\Sigma, \nu'=0, N'=1, J'=3/2, m'_J=\pm 3/2\rangle$ states have magnetic moments of $\pm 1.02\ \mu_B$, respectively. While we were unable to accurately numerically predict the observed Zeeman splitting from the previously published zero-field CaH data, it was possible to construct a consistent model to explain the observed value. This is explained in greater detail in Reference [185].

3.6 Magnetic trapping

We investigate the behavior of CaH in the trap by observing its spectrum as a function of time. To do so, we fix the frequency of the probe laser, fire the ablation laser to produce CaH, and continuously observe its laser-induced-fluorescence at that excitation frequency as a function of time. Then, the laser frequency is changed and the process repeated until a complete spectrum is obtained. This method of spectra measurement relies on the consistency of the ablation and magnetic trapping from shot-to-shot and requires many loading runs to produce a complete spectrum. We use it because it provides the best temporal resolution of the behavior of CaH in the trap.

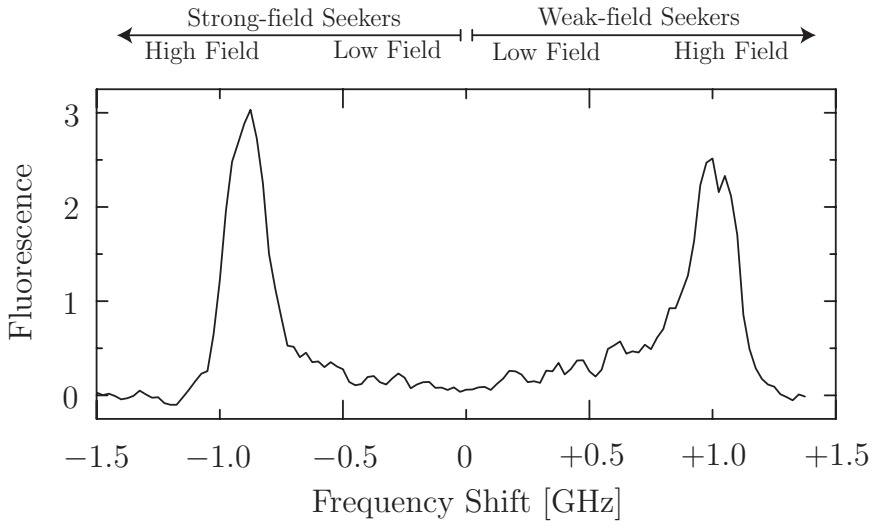

Figure 3.11: Laser-induced fluorescence spectrum of CaH integrated from 10 to 25ms after the laser ablation pulse. The frequency shift is plotted with respect to the field-free line. Shown above the graph is a guide to interpreting the data.

Figure 3.11 shows a spectrum of CaH taken soon after ablation. It is interpreted via the measured Zeeman shift, shown in Figure 3.10. Because the shift is linear in magnetic field (over the range of fields in our trap), the magnitude of the frequency shift is simply proportional to the field the molecule is in. The transition of CaH molecules in the low-field-seeking $|m''_J = +1/2\rangle$ ground state is shifted to lower frequencies (the left hand side of our spectrum). The signal at higher frequencies comes from molecules in the high-field seeking ground state.

The spectrum in Figure 3.11 is nearly symmetric, clearly indicating that at short times after the production of CaH, the distribution of the high field seekers is the same as that of the low field seekers. What is less obvious is that this strange "peaked" spectral shape corresponds to an even distribution of molecules throughout the trap volume. The increase in fluorescence with frequency shift is due to the greater volume of high field regions within the cell, and the peaks correspond to the trap saddle point. At early times, we find equal numbers of strong-field and weak-field seekers, both spread homogeneously throughout the cell.

The subsequent evolution of the molecular distribution is shown in Figure 3.12. After the ablation pulse, the high-field-seeking CaH molecules rapidly leave the trap, as expected. This decay is exponential with roughly the same time constant as that of CaH produced with the magnetic trap off (under otherwise similar conditions). We believe this to be the timescale on which the CaH diffuses to the walls, where it sticks.[7]

In sharp contrast to the high-field-seeking distribution, the low-field-seeking distribution changes shape dramatically, and exists for a longer time. The movement of the right hand side spectral feature towards lower shifts indicates that the low-field-seeking CaH molecules are moving in towards lower field. The CaH molecules move from their initial spatial distribution to a thermal, trapped distribution. In the process, their density increases by over an order of magnitude. This occurs on the same diffusion timescale discussed above. Figure 3.12 provides a clear illustration of the dynamics of the buffer-gas-loading procedure.

[7]For our typical trapping parameters, the drift and diffusion timescales (for CaH to travel to the cell walls) are comparable, so we expect (and observe) little change in the loss rate of the strong-field seekers in the presence of the trap.

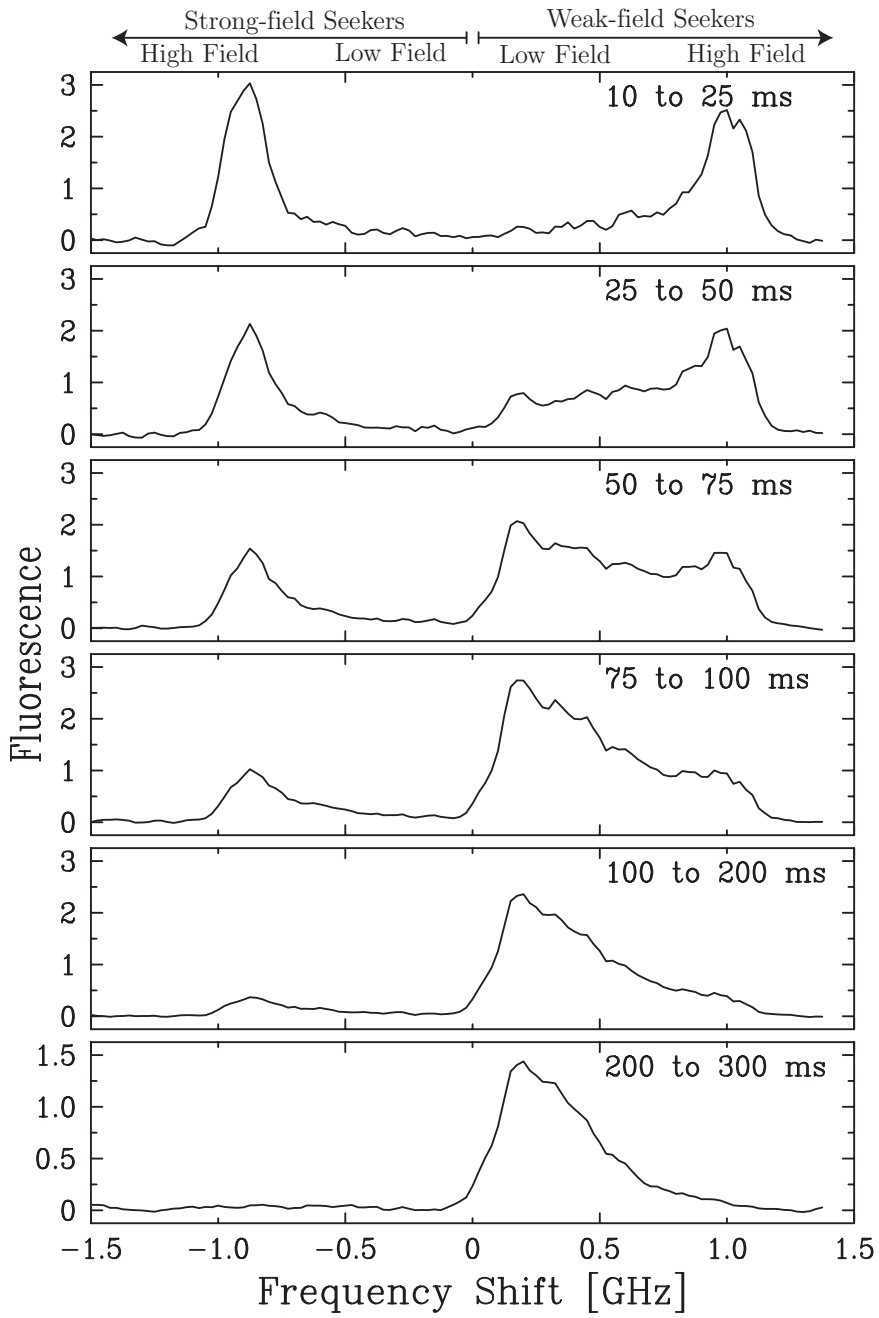

Figure 3.12: Spectra of CaH in the magnetic trap as a function of time after the ablation pulse. There is minimal change in the shape of the spectrum at later times.

Distribution of trapped molecules

After the spectral shape has equilibrated, it fits well to the simulated spectrum of a thermal, Boltzmann distribution of trapped molecules, as shown in Figure 3.13. From

this fit, we determine there are 1×10^8 CaH molecules trapped at a temperature of 400 ± 50 mK and peak density of 8×10^7 cm^{-3}. Details of the spectrum fitting procedure are discussed at length in Appendix A.

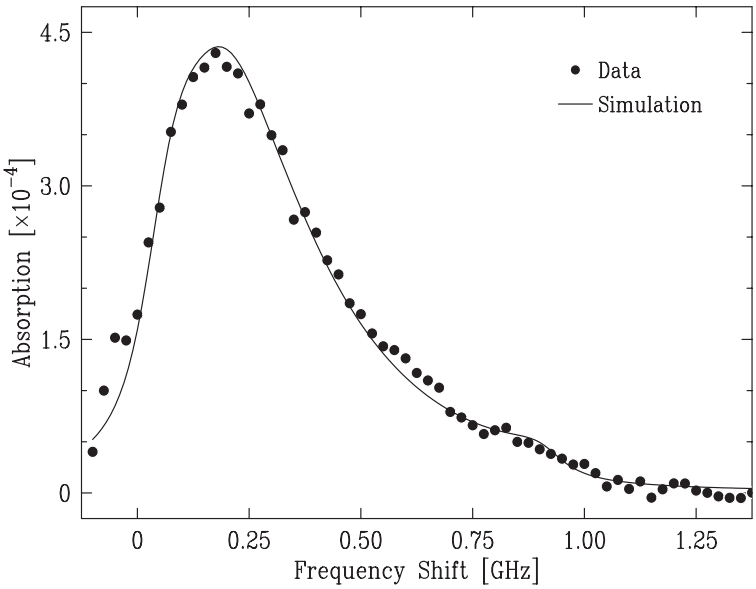

Figure 3.13: Spectrum of magnetically trapped CaH, fit to $N = 10^8$, $T = 400$ mK.

Ablation under comparable conditions without the magnetic trap produce 3×10^8 CaH molecules at densities of only 4×10^6 cm^{-3}. So $\sim 30\%$ of the molecules thermalized (and over half of the weak field seekers produced) are trapped; the buffer-gas-loading procedure is highly efficient. Additionally, the compression provided by the magnetic fields increases the density by a factor of 20. (Quoted numbers and densities are accurate only to within a factor of two.)

The measured temperature is somewhat high; the temperature of the cell before ablation is ~ 300 mK. Subsequent to the ablation pulse, however, the cell heats considerably. Although our cryogenic thermometry cannot accurately measure the cell wall temperature at short times after the ablation pulse, it does indicate a rise in temperature which is consistent with our spectroscopic CaH temperature measurements. It is likely that the CaH is well thermalized with the buffer gas.

A possible systematic in our measurement of the temperature arises from the assumption that the density of CaH is given purely by the Boltzmann factor $n =$

$n_p e^{-E/k_B T}$ (where n_p is the density at the trap center). Even in the absence of a trap, we would expect the density at the edge of the cell to be reduced due to the steady-state diffusive loss of CaH to the walls (as described in Section 2.2). We neglected such effects in the computation of our spectrum; this would cause us to underestimate the true temperature of the CaH. Estimates indicate a systematic error of $\sim 10\%$.

Trap loss

After the CaH molecules reach their equilibrium spatial distribution, they continue to be lost from the trap. As shown in Figure 3.14, this loss is considerably slower than that of the strong-field seekers, and (at long times) appears purely exponential. The trap loss is dominated by evaporation over the trap edge. Evidence for this is seen in Figure 3.15: as the trap depth is increased, the loss rate slows. An additional increase in the trap depth (or a reduction in the temperature) should further extend the trap lifetime.

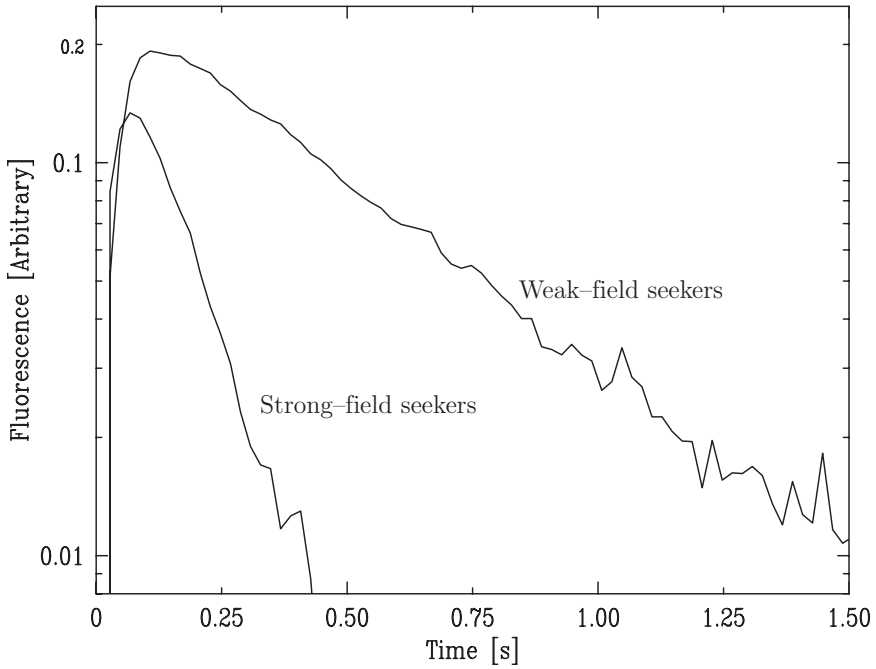

Figure 3.14: Peak fluorescence from strong-field and weak-field seeking states of CaH in the magnetic trap. The population of strong-field seekers decays exponentially with a time constant of 0.12 ± 0.02 s. The weak-field seekers are lost exponentially with a time constant of 0.45 ± 0.05 s. With the trap off, CaH is lost on a timescale of 0.11 ± 0.02 s.

Because our magnetic trap is somewhat shallow for 1 μ_B particles and the translational temperature of our molecules (and buffer-gas) is not as cold as we had hoped, the CaH leaves the trap at a rapid pace. The short time for which we can observe the CaH is insufficient to remove the buffer gas. If the buffer gas could be removed, the CaH loss rate would dramatically slow and we would obtain long trap lifetimes, as demonstrated with atomic chromium (described in Section 6.3).

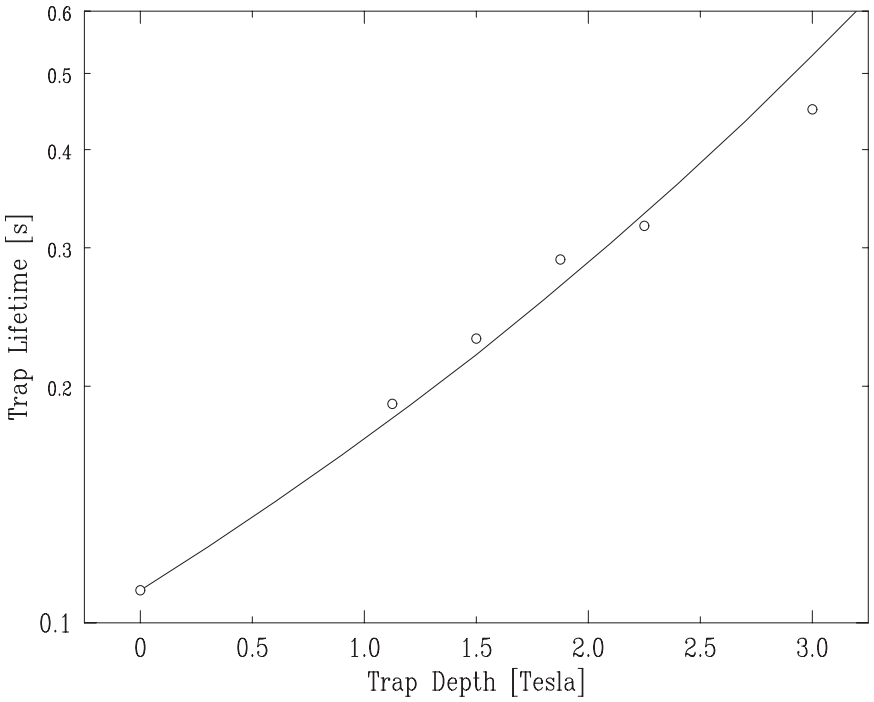

Figure 3.15: The lifetime τ of the trapped weak-field seekers ($N \propto e^{-t/\tau}$) as a function of trap depth, and the expected lifetime as determined from the solution of Equation 2.2. No adjustable parameters are used to fit the data: the "trapless" diffusion time τ_0 is obtained from experimental measurements, and η determined from the trap depth and the temperature measured in Figure 3.13.

The lengthening of the trap lifetime with the trap depth is strong evidence that the molecules are lost primarily through evaporation. Shown in Figure 3.15 are the observed CaH loss rates and the expected lifetime as determined from the analytical diffusion model described by Equation 2.2.[8]

The behavior shown in Figures 3.14 and 3.15 is typical of that observed over a

[8]A comparison of a numerical simulation of the trap loss to the data of Figure 3.15 indicates that the CaH temperature is 480 ± 50 mK [110].

wide range of buffer-gas densities, except at high helium densities, where inelastic CaH–He collisions begin to adversely affect the lifetime of the weak-field seekers. These collisions are discussed below in Section 3.7.

3.7 CaH–He collisions

Collisions between CaH and the ^{3}He buffer gas are of paramount importance for buffer-gas loading of magnetic traps. Elastic collisions are necessary to thermalize the translational motion of CaH. But inelastic spin-changing collisions (which change the Zeeman level of CaH) would be disastrous because they would allow CaH to thermalize to its strong-field seeking state. Elastic and spin-changing collisions are of concern for any species to be magnetically trapped via buffer gas loading. In addition, molecules can also undergo inelastic rotation- and vibration-changing collisions.

Inelastic rotational collisions are important because they allow the helium to cool the rotational energy of the CaH and enhance the ground state population. Not only does this give a number enhancement of the desired molecular state, but eliminates a potential problem. Any rotationally excited molecules within the magnetic trap could undergo inelastic collisions with other molecules in the trap, causing significant heating from the release of their rotational energy.

Similarly, inelastic vibrational collisions enhance the number of molecules in the desired vibration state. Unlike rotational collisions, however, our data suggests that inelastic vibrational collisions of cold molecules (in low-lying vibrational states) occur at a sufficiently slow rate that vibrationally excited molecules could be trapped with minimal losses due to inelastic vibrational collisions.

Elastic collisions

We determine the CaH–He collisional cross-section by measuring the diffusion of chromium through helium in the absence of trapping fields. As usual, we produce CaH via laser ablation in ^{3}He buffer gas. Once the CaH is thermalized, we observe the time decay of its population as it diffuses through the helium to the walls and is lost. To model this decay, we assume that when the molecules collide with the cell walls they stick with unity probability.

Reference [108] provides a detailed treatment of the problem of the diffusion of

one gas through another, and finds a diffusion constant of approximately

$$D = \frac{3\sqrt{2\pi}}{16} \cdot \frac{1}{n\sigma} \left(\frac{kT}{\mu}\right)^{1/2} \tag{3.1}$$

where μ is the reduced mass of the two gases.

Inside a cylindrical volume of height h and radius r_0 where particles are destroyed at the walls, the time evolution of the system is given by

$$n(r,z,t) = \sum_{i=1}^{\infty}\sum_{j=1}^{\infty} C_{ij} \cdot J_0(\alpha_i r) \cdot \cos((2j-1)\pi z/h) \cdot \exp(-t/\tau_{ij})$$

where the τ_{ij}'s are determined by

$$\frac{1}{D\tau_{ij}} = \alpha_i^2 + ((2j-1)\pi/h)^2$$

and α_i is determined by the requirement that $\alpha_i \cdot r_0$ is equal to the ith root of the Bessel function J_0 [108].

The long time behavior of the diffusing cloud of molecules is dominated by the $i = 1$, $j = 1$ term in the above expansion. The decay as a function of time is given by a single exponential with a time constant

$$\tau \simeq 2.1\ n\sigma \cdot (kT/\mu)^{-1/2} \cdot \left((2.4/r_0)^2 + (\pi/h)^2\right)^{-1} \tag{3.2}$$

It is straightforward to apply Equation 3.2 to our experimental observations to find the CaH–He elastic cross-section.[9] From the data shown in Figure 3.16 and similar data taken at various helium gas densities, we find a CaH–^{3}He elastic scattering cross section at ~ 400 mK of

$$\sigma_{\mathrm{el}} = (1.5 \pm 0.6) \times 10^{-14}\ \mathrm{cm}^2$$

Inelastic collisions

Rotational inelastic collisions

Due to the large rotational spacing of CaH (see Table 3.1), we expect to see no rotationally excited molecules. If the rotational temperature is in thermal equilib-

[9]We note that the answer obtained through Equation 3.2 is similar to that obtained from the simple model of the diffusion of CaH as a one-dimensional random walk of a distance r_0, if we assume that the velocity of the CaH is randomized every m_{CaH}/μ collisions.

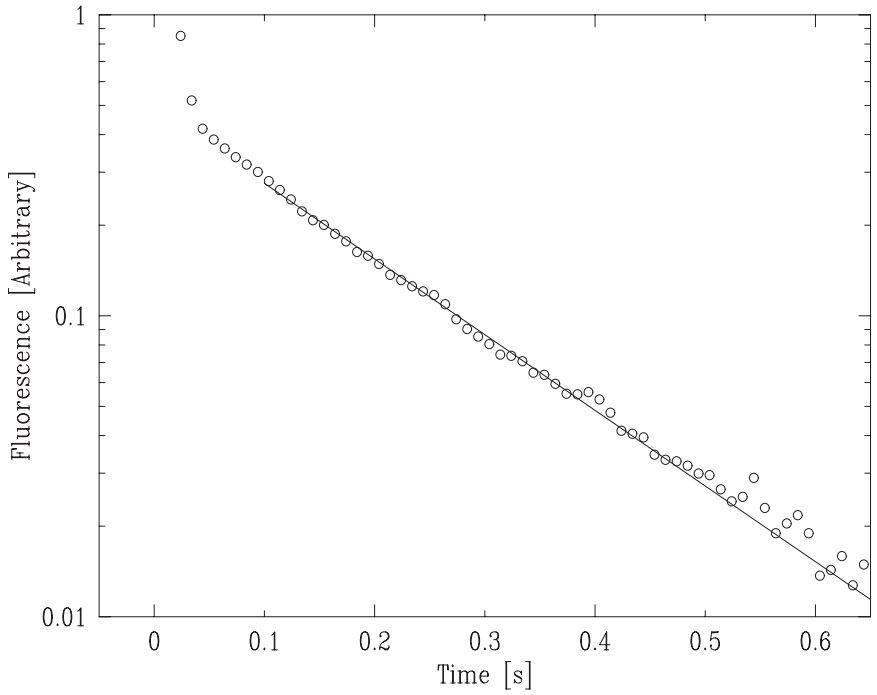

Figure 3.16: The observed CaH fluorescence (proportional to atom number) as a function of time inside the cell in the presence of ^{3}He buffer gas, but without a trap. Shown are data and a fit to $e^{-t/\tau}$.

rium with the measured translational temperature of 400 mK, fewer than 1 in 10^{10} molecules will be in an excited rotational state.

Experimentally, when looking for signal on the

$$|B^2\Sigma, \nu'=0, N'=2, J'=5/2\rangle \leftarrow |X^2\Sigma, \nu''=0, N''=1, J''=3/2\rangle$$

transition, we see no evidence of $|N = 1\rangle$ rotationally excited CaH. From this, we determine that the $|N = 1\rangle$ state population is $\geq 10^3$ times smaller than the $|N=0\rangle$ population within 10 ms after the ablation pulse. This gives an upper limit on the CaH rotational temperature of $T < 2$ K.

This thermalization is due to inelastic rotational collisions. Unfortunately, because it occurs before we can observe it (our early-time measurements are obscured by the ablation), we cannot directly measure the collisional rate coefficient, and can only determine a lower limit of $\Gamma_{\text{rotational}} \geq 10^{-15}$ cm^{3}s^{-1}.

Vibrational inelastic collisions

After ablation, we were able to detect vibrationally excited $|\nu=1\rangle$ molecules. These molecules (with an energy of $\sim 10^3$ K above the ground state) are vibrationally excited far out of thermal equilibrium with their translational degrees of freedom. The time behavior of vibrationally excited CaH in the presence of helium buffer gas is shown in 3.17. From such data, we were able to determine that the vibrational relaxation rate coefficient of the $|\nu=1\rangle$ CaH state is $\Gamma_\nu < 10^{-16}$ cm^3 s^{-1} for collisions with ^{3}He at temperatures of ~ 0.5 K.

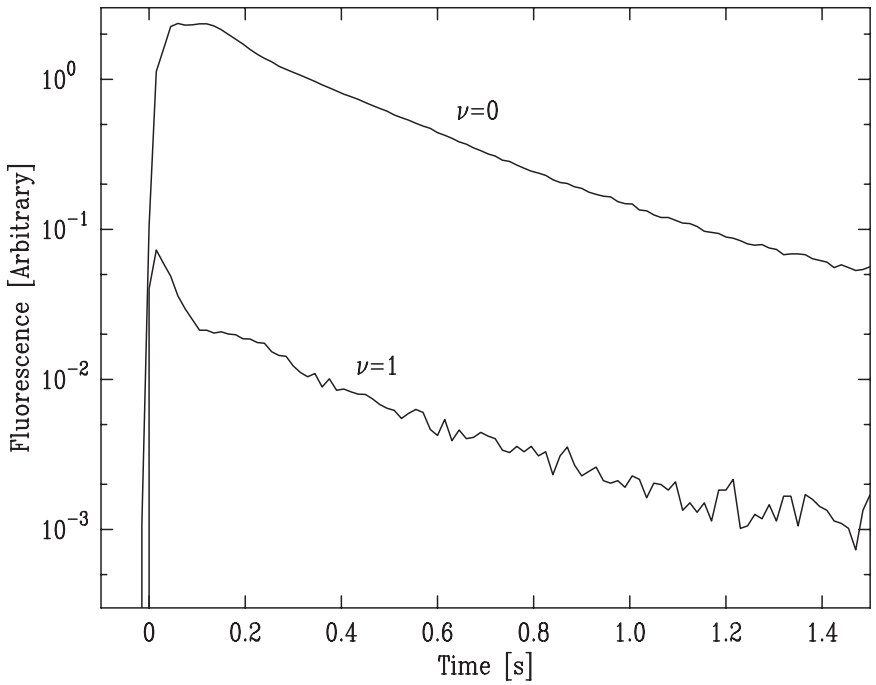

Figure 3.17: Signal from the ground and first excited vibrational states of CaH as a function of time with no trap. A high buffer gas density provides the long time constant.

At first glance, it is surprising that this highly energetic state would be so reluctant to release its energy in a collision. However, this low rate coefficient is consistent with theoretical predictions of vibrational relaxation in other systems. Reference [186] calculates the rate coefficients for the vibrational quenching of H_2 in collisions with helium, and predicts a rate coefficient of $\sim 10^{-18}$ cm^3 s^{-1} for $|\nu=1\rangle$ H_2 with ^{3}He in the 100 mK to 1 K range.

The cross section for vibrational relaxation is sufficiently low that it should be

possible to magnetically trap these molecules via buffer-gas loading. However, few $|\nu=1\rangle$ molecules were observed (typically the $|\nu=1\rangle$ population was a factor of 100 smaller than that of $|\nu=0\rangle$). Due to this lower signal, we did not attempt to observe the vibrationally excited molecules inside the magnetic trap.

Zeeman thermalizing collisions

Vital to the success of buffer gas loading is a small cross section for "spin-flip" collisions between the buffer gas (helium) and the molecules to be trapped. A low-field-seeking molecule is in a higher energy state than a high-field-seeking molecule, and has the possibility of relaxing to the high-field-seeking state during a collision. In order for buffer gas loading to work efficiently, this spin relaxation cross section (σ_{Z}) must be much smaller than the elastic cross section (σ_{el}) to allow kinetic thermalization to take place before spin relaxation.

In the data shown in Figure 3.15, spin-changing collisions play a minor role in the loss of atoms from the trap. However, at higher buffer-gas densities, spin-changing collisions begin to strongly affect the lifetime of molecules in the trap.

Figure 3.18 shows the spectrum of CaH in the trap in the presence of a high density of ^{3}He buffer gas. We compare Figure 3.18 to the buffer-gas loading shown in Figure 3.12. In both, we start with comparable numbers of low- and high-field seeking CaH molecules, with similar distributions throughout the trap. In both, the strong-field seekers are driven to the walls on their diffusion timescales (considerably longer in Figure 3.18 due to the higher buffer-gas density). And in both, we still see a change in the spectral shape of the weak-field-seeking CaH molecules that demonstrates that they are driven to the trap center by the magnetic fields. But with the high buffer-gas densities of Figure 3.18, we observe that the weak-field seekers are lost from the trap more rapidly than the high-field seeking molecules. They are lost due to spin-changing collisions, which allow them to relax into the high-field seeking state.

Figure 3.19 shows the relative timescales of the weak- and strong-fields seeking CaH molecules in the presence of a high density of buffer-gas. The exponential timescale indicates that the loss is not due to collisions with other CaH molecules, and the increased loss of weak-field seekers that we observe at still higher helium densities confirms that this loss is due to collisions with the helium atoms. From Figure 3.19 and similar data, we find a rate coefficient for inelastic CaH–^{3}He Zeeman-state-changing collisions of $\Gamma_{\mathrm{Z}} = 10^{-17}$ cm^3 s^{-1}. This measurement is accurate to within

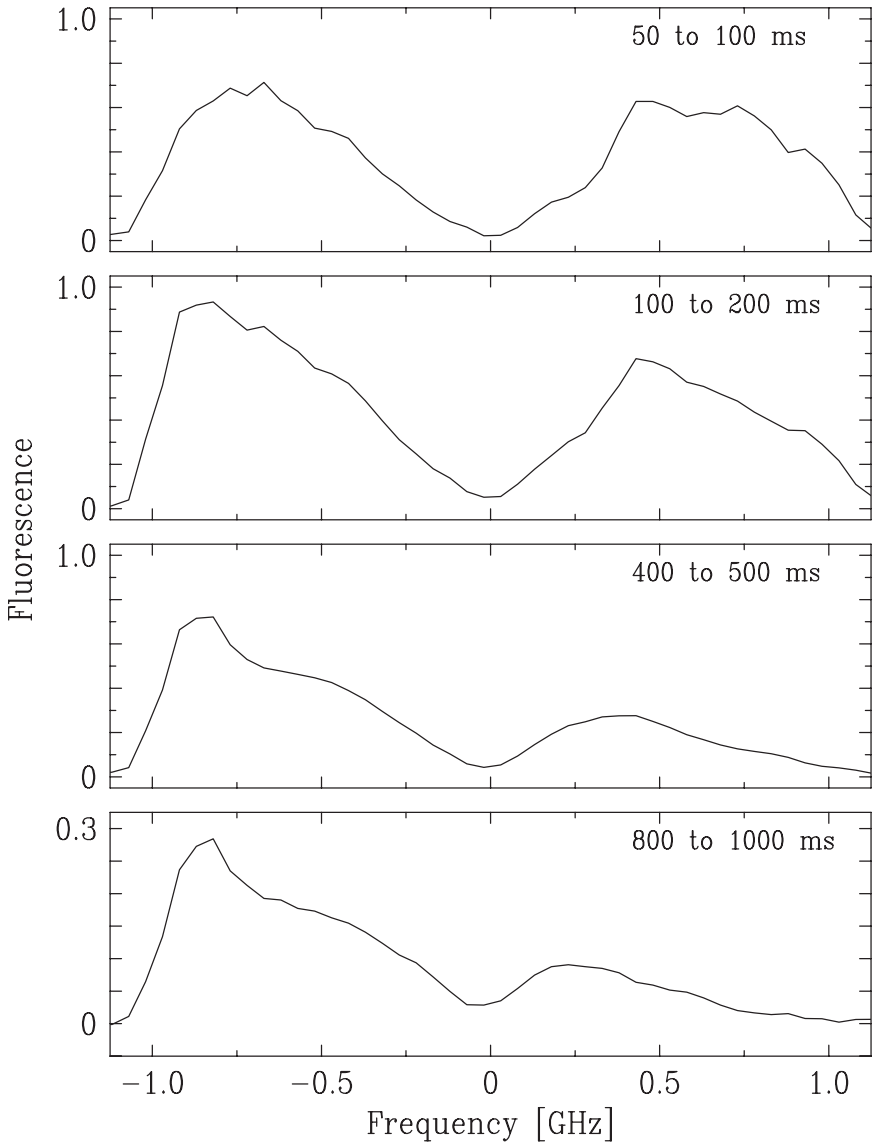

Figure 3.18: Spectra of CaH in the magnetic trap as a function of time after the ablation pulse. Data taken with a trap depth of 3 Tesla and a ^{3}He density of 5×10^{16} cm^{-3}.

an order of magnitude.[10]

[10]The low accuracy of this measurement is due to two experimental difficulties. At low helium densities, the low-field seekers experience loss from both inelastic collisions and loss to the walls. At high helium densities, the suppression of the weak-field seekers is so large that by the time the plume glow has subsided, it is difficult to observe the remaining weak-field seekers.

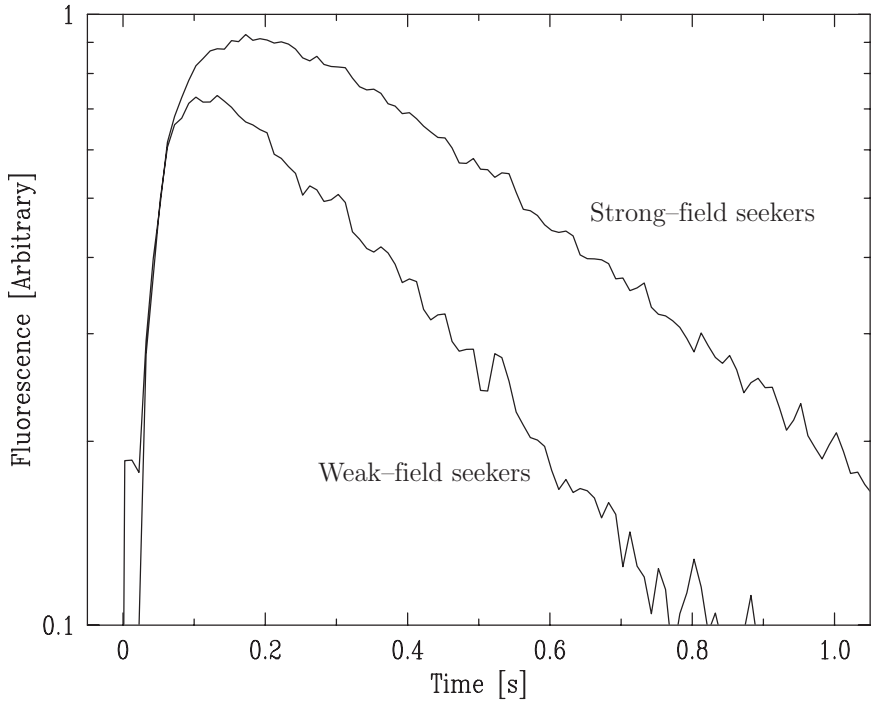

Figure 3.19: Fluorescence signal of the weak- and strong-field seeking states of CaH in the magnetic trap as a function of time after the ablation pulse. Taken with a trap depth of 3 Tesla and a helium density of 5×10^{16} cm^{-3}.

As discussed in Section 2.5, typical rates for spin-exchange collisions with ^{3}He mediated by the $\mathbf{S} \cdot \mathbf{I}$ hyperfine interaction are on the order of 1×10^{-19} cm^3 s^{-1}, and dipolar relaxation is slower still. Consequently, we suspect that the dominant loss process is through the molecular spin-rotation interaction (also discussed in Section 2.5). It is remarkable is how low the observed CaH–^{3}He inelastic rate truly is. We note that because the ground state of CaH has both a very low spin-axis coupling and a sufficiently large rotational spacing that its excited rotational states have a negligible chance of being populated in a collision, it is naively an ideal molecule for minimizing the spin-rotation interaction's contribution to spin-changing collisions.

Comparing this inelastic rate coefficient to the CaH–^{3}He elastic collision rate, we have a ratio between elastic cross section and the spin-flip cross section of greater than 10^5. While there are no guarantees that these collision properties will hold generally for all molecules, they are extremely promising for future work.

3.8 Conclusions and future prospects

We have used buffer gas loading to magnetically trap 10^8 CaH molecules at ~ 400 mK. Because this technique relies only on elastic collisions between the buffer gas and on the magnetic state of the species, it should be applicable to many paramagnetic atoms and molecules. Implementation of evaporative cooling could lead to the production of large numbers of ultracold molecules. Immediate applications of this work include high resolution spectroscopy and studies of cold collisions. Future opportunities may include the production of quantum degenerate molecular gases and improving experimental searches for permanent electric dipole moments of elementary particles using polar molecules.

Removal of the buffer gas after trapping should lead to evaporative cooling. However, the cryopumping procedure used with Cr (described in Section 6.3) requires longer times than we can currently observe trapped CaH. Improvements in the experiment such as a deeper trap, more efficient CaH production, or higher detection sensitivity would lead to longer observation times and time to pump out the helium. Alternatively, more rapid pumping methods could be developed.

Chapter 4

Vanadium Monoxide

Prior to our magnetic trapping of calcium monohydride, we attempted to magnetically trap buffer-gas-cooled vanadium monoxide. Vanadium monoxide (VO) has many properties advantageous for buffer-gas loading and magnetic trapping. VO has a large magnetic moment in its ground state, it has a strong and easily accessible optical transition, its molecular structure was previously well studied and understood at zero field, and we found that VO could be produced in abundance through laser ablation. For these reasons, one would expect VO is a superior species for buffer-gas loading and magnetic trapping with the same techniques later employed for CaH. However, this was not the case, and our efforts to trap VO failed.

4.1 VO spectroscopic structure

The level structure of vanadium monoxide has been well studied, and has many advantageous properties for both buffer-gas loading and detection of the molecules produced. Except where noted, all information about the molecular structure of VO is obtained from Reference [187], and we use its notation.

The ground state of VO is $X^4\Sigma^-$. With three unpaired electron spins, this state is highly magnetic, with a magnetic moment of up to 3 μ_B in its lowest energy rotational state. We detect VO spectroscopically through its $|C^4\Sigma^-, \nu' = 0\rangle \leftarrow |X^4\Sigma^-, \nu'' = 0\rangle$ transition at 574 nm. The frequency is easily accessible with a dye laser (using Rhodamine 6G Dye), and the transition is strong: the radiative lifetime of the excited state is 73 ± 2 ns [188]. Because of the similar structure of the ground and excited states (both are $^4\Sigma$), we would expect to find spectroscopic transitions which have

narrow Zeeman broadening.

We observe VO through both absorption and laser-induced-fluorescence (LIF) spectroscopy. As with CaH, we distinguish VO fluorescence from apparatus-scattered light by detecting the frequency shifted molecular fluorescence from the $|\nu' = 0\rangle \rightarrow |\nu'' = 1\rangle$ decay at 609 nm. This detection is aided by VO's large Frank-Condon factors and large vibrational spacing [189].

The nuclear spin of VO is $I = 7/2$, and its various hyperfine transitions are well separated and easily resolvable. The ground state rotational constant is $B = 0.546$ cm^{-1}. VO's combination of hyperfine structure and small rotational spacing leads to a much larger number of detectable states and transitions than CaH.

4.2 Experimental apparatus

The experimental apparatus used for the production, detection, buffer-gas cooling, and attempted trapping of VO is nearly identical to that used for CaH, as described in Sections 3.2 and 3.3. Specifics of the VO experiment are described below.

Laser ablation

VO molecules are produced by laser ablation of a solid sample of specially prepared solid vanadium oxide. A variety of solid vanadium oxide compounds[1] are chemically stable and easily available for purchase. Unfortunately, most of these compounds proved problematic for the ablation production of VO. Not only was their yield of VO molecules low, but copious amounts of dust were produced during ablation. This dust would (over time) obscure the cell optics, and we were concerned that the dust would interact with the VO molecules in unfortunate ways.

To reduce these ablation problems, we specially prepared (through a process of trial and error) a solid ablation target. To create this solid, fine V_2O_5 powder [190] was compressed into a 3 mm diameter copper tube with a pressure of $\sim 10^5$ psi. This assembly was baked in air at a temperature of ~ 600 °C for approximately 1 minute. The resulting material looks dull and black. Samples prepared in this manner exhibit much less (visible) dust produced during ablation than compressed powder.

[1] V_2O_3, V_2O_4, and V_2O_5

Optical detection

VO is detected through laser absorption or laser-induced fluorescence spectroscopy by exciting the $C^4\Sigma^- \leftarrow X^4\Sigma$ $(0,0)$ transition at 574 nm.

Absorption spectroscopy was most effective at short times ($\lesssim$ 10 ms) after the ablation pulse, as the initial absorption in the cell was high. However, vibrations of the cryogenic apparatus limited the sensitivity of absorption measurements at low optical density, and fluorescence spectroscopy was used at later times. As with CaH, the absorption spectroscopy was used to calibrate the fluorescence spectroscopy.

In the case of fluorescence spectroscopy, to differentiate molecular fluorescence from apparatus-scattered light, color filters are used to block light at the excitation frequency and pass light from the decay of VO to its $\nu'' = 1$ electronic ground state. Similar to the optical detection of CaH, elastically scattered probe light was blocked by a single bandpass interference filter [191] followed by an absorptive colored glass filter [192] placed in front of the photomultiplier. In addition, a shutter was placed in front of the PMT to shield it from the ablation pulse.

Fluorescence spectroscopy was performed with a photomultiplier tube, and, separately, with an intensified CCD camera. The PMT was used in the lock-in detection of fluorescence induced by an acousto-optically modulated beam. The performance of this detection was limited by a background from fluorescing epoxy glue present in our cell [193]. We were able to obtain an optical density sensitivity 10^{-5} (on the relevant timescales) providing us with observations of VO densities spanning 6 orders of magnitude. VO densities as low as 10^5 cm^{-3} were detectable; detection sensitivity is discussed at greater length in Appendix G.

Finally, the laser frequency was calibrated with the Wavemeter [167] and absorption spectroscopy of an I_2 vapor cell [168].

4.3 Low temperature spectroscopy

Early-time absorption spectra, along with an identification of the lines, are shown in Fig. 4.1. To obtain these spectra, the absorption at a given frequency and time was obtained by setting the frequency of the laser, ablating VO, measuring the absorption as a function of time, and averaging the absorption over the appropriate time window. The ablation process is sufficiently consistent shot-to-shot that meaningful spectra

can be taken in this manner. At 10 ms, the spectra can be clearly identified as VO. However, the signal observed at earlier times ($\lesssim 4$ ms) cannot be entirely reconciled with the known VO lines in this spectral region; lines which are not $|X^4\Sigma^-, \nu'' = 0\rangle$ VO are present. This indicates that other molecular species or excited states of VO are formed and destroyed over this short time period.

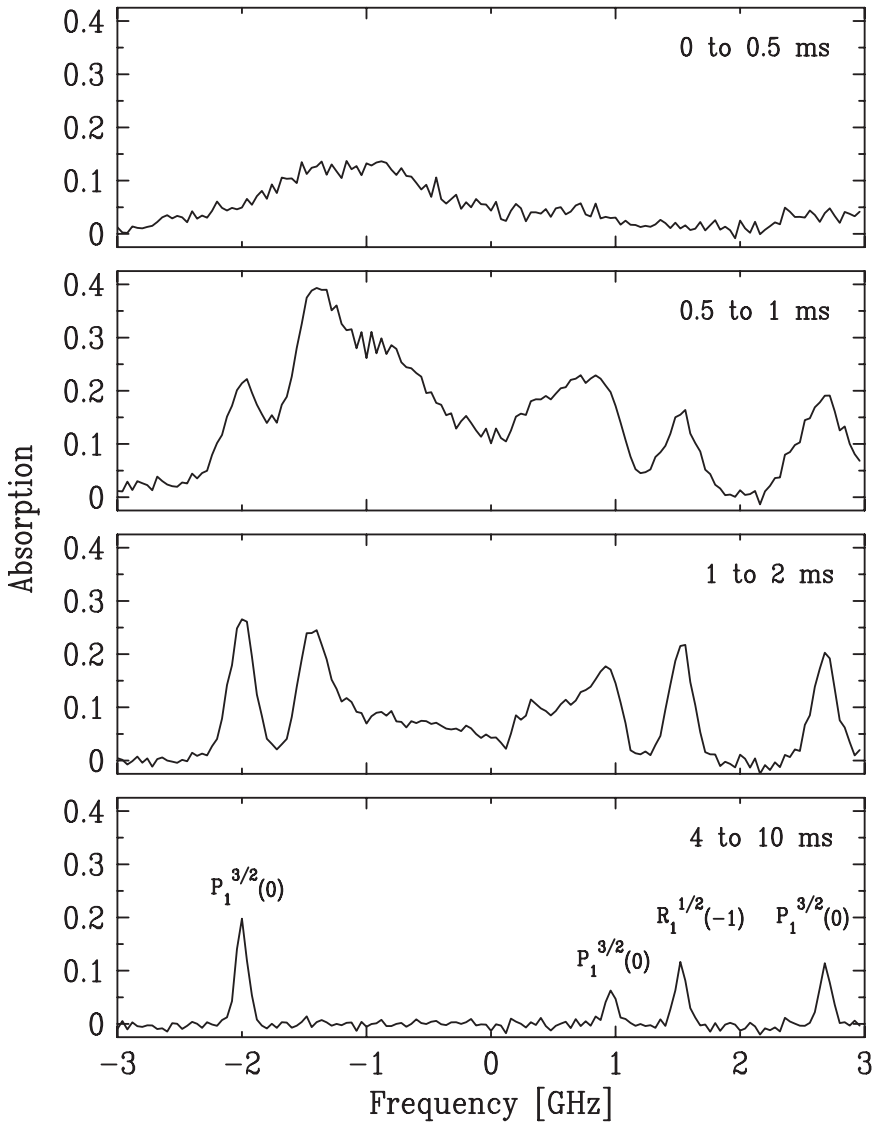

Figure 4.1: VO spectra as a function of time after the ablation pulse. Note the narrowing of the spectrum as the translational motion cools, and the presence of unidentified lines at early times. Negligible change in the spectral shape is seen at subseqent times.

At later times ($t \gtrsim 10$ ms), all the lines in the spectral region of Figure 4.1 are all

identifiable as VO ($X^4\Sigma^-$, $\nu'' = 0$). However, this is not the case in all spectral regions. Unidentified lines of intensity one-tenth that of the strongest VO lines were found at 17423 cm^{-1}. The source of these spectral features was not determined. However, they are not due to any known line of atomic vanadium, atomic or molecular oxygen, or $|X^4\Sigma^-, \nu'' = 0\rangle$ VO.

Combining the absorption spectra and camera images with the published radiative lifetime of the $|C, \nu' = 0\rangle$ state of VO, we determine that we produce and cool 10^{12} VO molecules, which are roughly evenly distributed throughout the cell volume at a density of 10^{10} cm^{-3}. Approximately 80% of these molecules are in the two (closely spaced) lowest energy levels $|X; N'' = 1, J'' = 0.5\rangle$ and $|X; N'' = 0, J'' = 1.5\rangle$.

Translational Temperature

As can be clearly seen in Figure 4.1, the spectral lines of VO rapidly narrow as the VO cools in the buffer gas. The cooling of VO's translational temperature takes approximately 3 ms. Assuming Doppler broadening to be the sole source of spectral broadening, the translational temperature of the VO molecules is obtained from the width of the spectral lines, as shown in Figure 4.2. We find the VO is cooled to a temperature of 1.8 ± 0.2 K within 10 ms following its production.

This temperature is strikingly higher than the 0.3 K temperature of the cell prior to ablation. However, this does not necessarily mean that the VO is out of thermal equilibrium with the buffer gas and cell walls. Using resistance thermometers (as described in Section 5.7, the cell temperature is observed to rise due to heating by the ablation pulse. Although our thermometry is not responsive on millisecond timescales, a temperature rise to about 1 K is seen on a 1 s timescale. Thus, the measured VO translational temperature is not inconsistent with the cell temperature measurements, and it is likely that the translational temperature of the VO has come into thermal equilibrium with the buffer gas.

As an important caveat, we note that it is also possible that there are other line-broadening mechanisms and that the translational temperature may be somewhat colder than given by this Doppler fit.

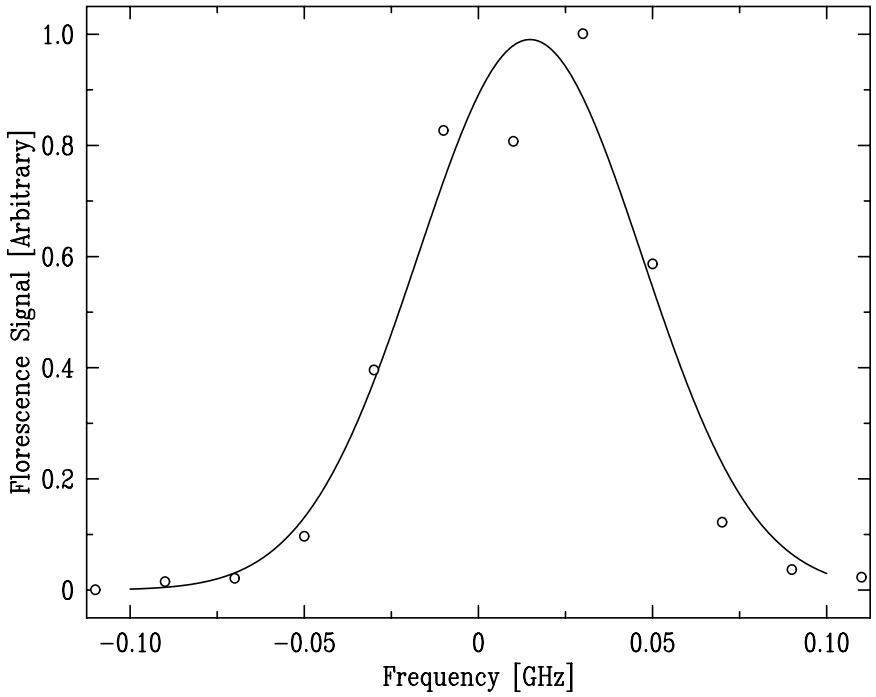

Figure 4.2: Single-line spectrum of buffer-gas cooled VO in the absence of the magnetic trapping fields. Taken from 50 to 200 ms after the ablation pulse. Fit to a gaussian, giving a full-width at half-maximum of 63 ± 6 MHz and a translational temperature of 1.8 ± 0.2 K.

Rotational Temperature

The rotational temperature of the VO is determined through analysis of the relative strength of the VO rotational spectral lines. The spectroscopic lines of VO and the energies of the ground electronic rotational and hyperfine states from which they originate have been identified [187]. The LIF signal (normalized for the degeneracy of the various states) as a function of the energy of the state from which it originates is shown in Figure 4.3. We assume that the observed transitions have identical oscillator strengths, and fit the state populations to a Boltzman distribution. From this, we find a rotational temperature of $T_{\rm rot} = 1.5 \pm 0.8$ K.

The rotational temperature thermalizes with the translational temperature on an unmeasured timescale ≤ 10 ms. This sets a lower limit on the rate coefficient for VO–^{3}He rotation-changing inelastic collisions of $\Gamma_{\rm rot} > 10^{-15}$ cm^{-3} s^{-1} at a temperature of ~ 1 K.

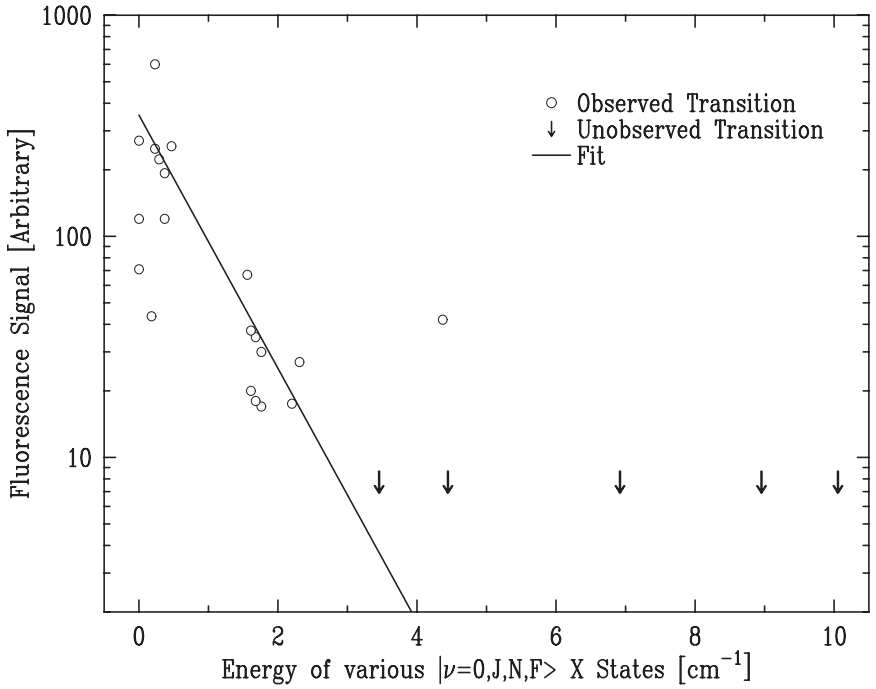

Figure 4.3: Fluorescence signal of various rotational transitions, plotted as a function of the energy of the state excited and normalized for its degeneracy. Fit to a Boltzman distribution, which indicates a temperature of 1.5 ± 0.8 K. The data was taken with the magnet off, and the fluorescence signal integrated over a time window from 3 to 23 ms after ablation (with the exception of three data points which have integration windows from 1-11 ms and were normalized to compensate for the time difference).

Zeeman spectroscopy

Each observed VO transition splits into multiple narrowly ($\Delta\mu \sim 0.1\ \mu_B$) broadened and widely broadened ($\Delta\mu \sim 1\ \mu_B$) features in the magnetic field. Although attempts were made to theoretically calculate the magnetic shifts of VO based on molecular parameters measured in zero field [187] and the Hamiltonian presented in Reference [194], we were unable to reproduce the observed structure and hence unable to conclusively identify the features.

Although disappointing, this is not surprising; the structure of the VO molecule is very complex with significant (multiple wavenumber) spin splitting. Although the spectrum is modeled and fit well at zero field, it is done so without a knowledge of the true form of the molecular Hamiltonian or a detailed understanding of the physical interactions underlying the behavior.

4.4 VO loss

The early time behavior of VO is shown in Figure 4.1. At subsequent times, the molecules are not observed to cool appreciably; they simply go away. We use fluorescence spectroscopy to track VO behavior after $t = +20$ ms; the behavior at $t < 20$ ms is obscured by the closed PMT shutter.

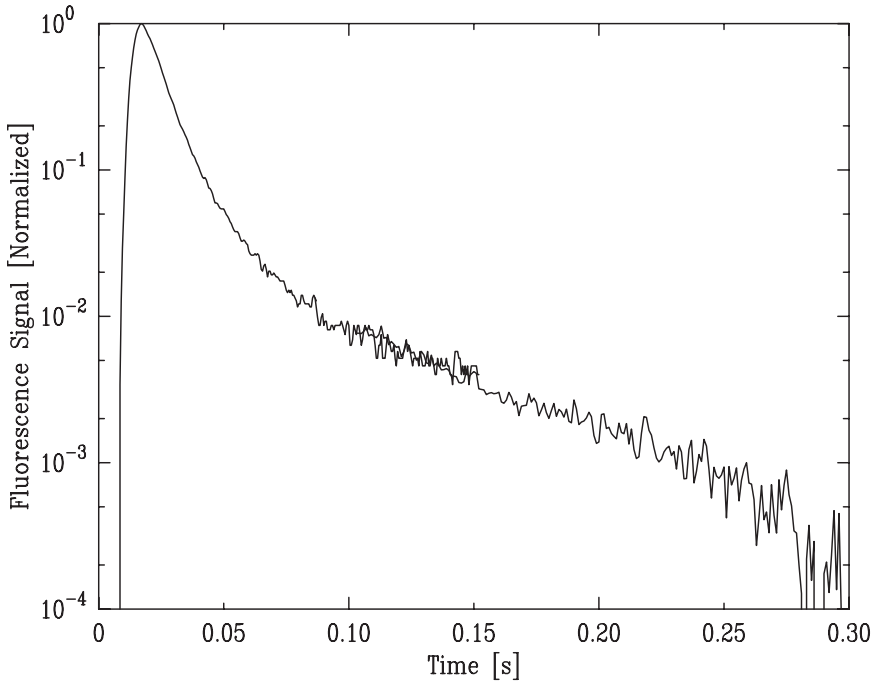

Figure 4.4: VO fluorescence signal from the cell in the presence of buffer-gas but without trapping fields. The VO is detected on the $P_1^{3/2}(0)$ transition.

We observe the ground rotational and vibrational state of VO via the $P_1^{3/2}(0)$ transition. The fluorescence signal as a function of time in the absence of the trapping fields is shown in Figure 4.4. The time behavior is somewhat peculiar. Rather than the simple exponential loss expected for diffusion to the walls, the VO loss has a "knee" in it. After the knee, the molecules disappear with an exponential time constant of ~ 60 ms.

The time constant on which the ground state VO molecules disappear from the cell is inconsistent with simple diffusion to the walls. Atomic europium produced under identical buffer-gas conditions (and detected via absorption spectroscopy) exhibits a significantly slower loss rate to the walls. And as can be seen in Figure 4.5, the VO lifetime is largely independent of the density of helium buffer gas. This is conclusive

evidence that the dominant loss process of VO molecules from the cell is *not* diffusion to the walls.

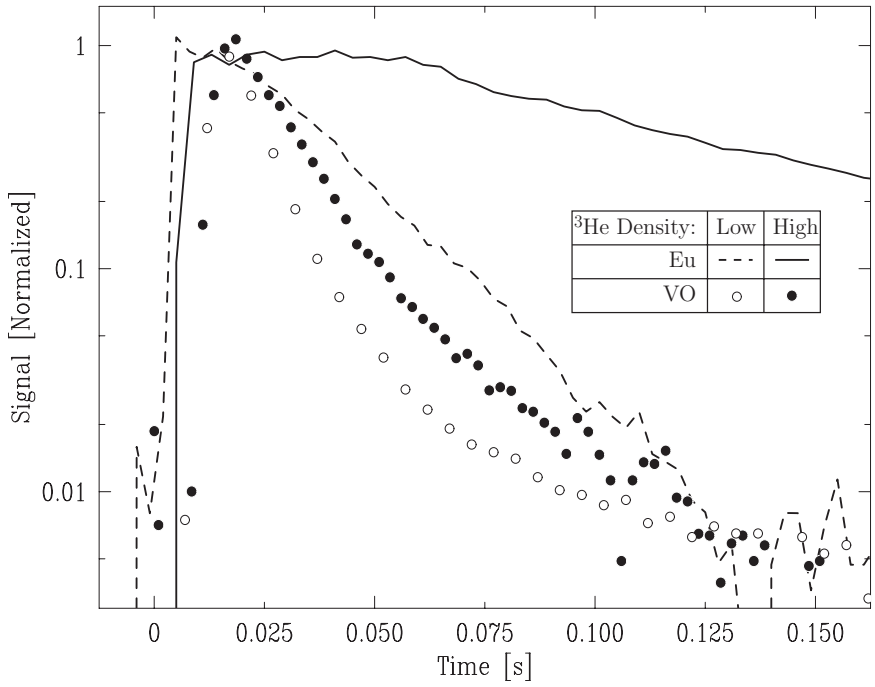

Figure 4.5: Time behavior of VO and Eu signal (in the cell in the absence of trapping fields) at two different buffer-gas densities. The Eu lifetime shows a dramatic increase as the buffer-gas density in increased, indicating that the loss is dominated by diffusion to the walls. The VO lifetime, by comparison, is largely unaffected by the ^{3}He density.

The process that is causing loss of VO from the trap has not been conclusively identified. Because the loss rate does not increase with the helium density, we conclude that the loss is not due to interactions of VO with the ^{3}He buffer gas (although multiple-body collisions involving helium are a conceivable loss candidate if the helium is not a limiting reagent). We surmise that the loss is due to a reaction of VO with either another chemical species or dust produced during the laser ablation.

VO behavior in the trap

Because the VO is lost through some mechanism other than traveling to the cell walls, we would expect the spatial confinement offered by the magnetic trap to have a negligible effect on VO loss from the cell. This is what we observe. Although the Zeeman broadening causes this transition to split into multiple features in the trap,

they all exhibit roughly the same time dependence, shown in Figure 4.6 alongside the time behavior in the absence of the magnetic trap.

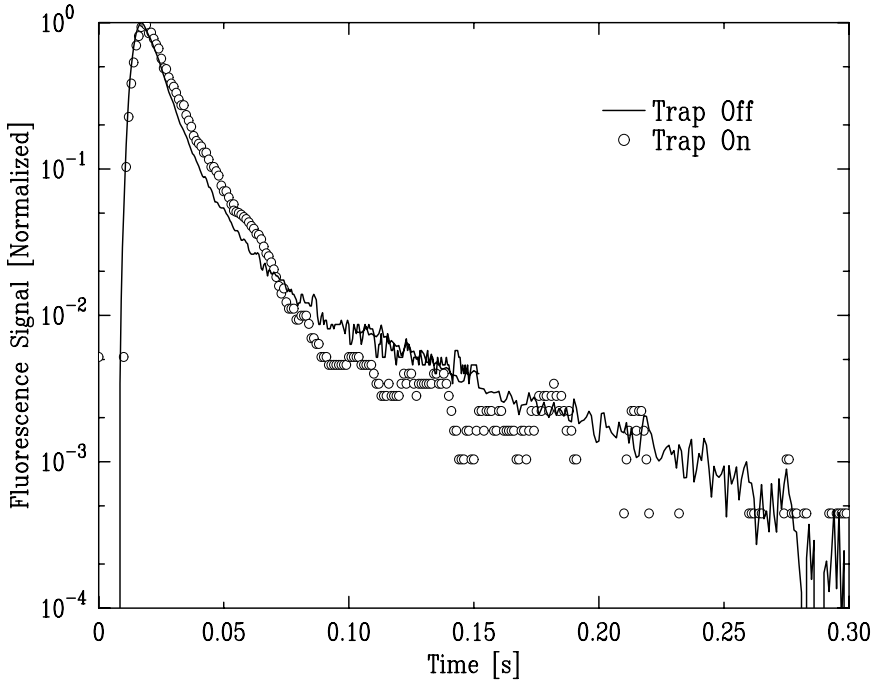

Figure 4.6: VO fluorescence signal with the trapping fields off and with a trap depth of 2.3 Tesla. The VO is detected on the $P_1^{3/2}(0)$ transition.

Glow

In the absence of an exciting laser, we still observe fluorescence emitted from the trap. Although ablation normally creates a light-emitting plume, the plume fluorescence is typically short-lived, as shown in Figure 3.8. In the case of VO, not only is the fluorescence long-lived, but it follows the same time behavior as the molecule population. This glow is shown in Figure 4.7. Although the source of the glow has not been identified, its timescale suggests that it is related to the loss process responsible for the disappearance of VO from our trap.

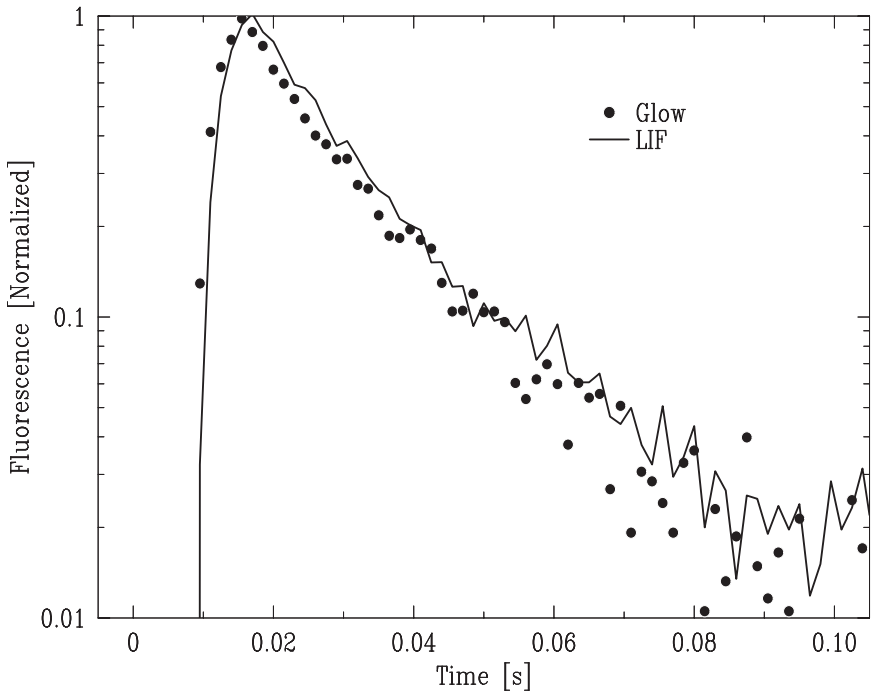

Figure 4.7: The nefarious glow of VO. The laser-induced-fluorescence signal (LIF) of VO is shown alongside the fluorescence signal in the absence of any exciting laser, normalized to the same initial level. As with all our VO fluorescence work, the signal at times < 20 ms is meaningless because of the closed shutter protecting the PMT from the ablation flash.

Chapter 5

Chromium Cryogenic Apparatus

Our initial experiments to evaporatively cool atomic chromium were conducted in a cryogenic apparatus similar to that used for the calcium monohydride work. Unfortunately, technical problems with the magnet (discussed below) required that it be replaced. While the new magnet was under construction, we also rebuilt the cell. The new magnet avoids the problems that plagued its predecessor. The new cell is electrically insulating to allow faster magnet ramping and achieves ultrahigh vacuum to provide long trap lifetimes.

5.1 The magnet

The old magnet

The first magnet (used for europium, vanadium monoxide, calcium monohydride, and initial chromium buffer-gas loading experiments) is described in detail in Jinha Kim's thesis [104]. Briefly, it consists of two superconducting solenoids run in an anti-Helmholtz configuration to generate a spherical quadrupole trapping field. The solenoids consist of approximately 5000 turns of multifilamentary niobium-titanium superconductor embedded in a copper matrix. This magnet generates a trap depth of 380 Gauss per Ampere (at a cell wall radius of 2.1 cm) and a field gradient of $\frac{dB}{dz} = 250$ G cm^{-1} A^{-1} at the trap center. The magnet was operated up to a maximum current of 86 A.

The solenoids are wound on and contained by a titanium alloy cask. Titanium alloy was chosen because it is strong, nonmagnetic, and well characterized at low

temperature [195]. The cryogenic structural properties are important because the titanium cask must support the large repulsive force generated by the coils when they are energized. The specific titanium alloy chosen was Ti-6Al-4V ELI annealed (titanium alloyed with 6% aluminum and 4% vanadium, extra-low-interstitial level and annealed). Unbeknownst to us at the time, this alloy of titanium is superconducting at liquid helium temperatures [196].

Jump behavior

When the magnet is brought to high field, we observe no aberrant behavior and the field profile is unperturbed. We believe the cask is driven normal by the magnetic fields. As the magnet is ramped to lower fields, the cask becomes superconducting. This superconductivity causes problematic behavior, which we dub "jumps". During a "jump", the magnet current and the magnetic field both abruptly change value.

Hall probe [197] measurements indicate that during a jump, the change in the field is simply a change in an overall bias field in the trapping region. Typical jumps are on the order of 200 gauss, and little evidence of any additional distortion of the shape of the magnetic field was seen. Typical jump behavior is shown in Figure 5.1.

We believe the field jumps arise out of a simple process. Once the magnetic field falls below its critical value, the titanium alloy cask becomes superconducting. Consequently, it attempts to shield out any changes in the magnetic flux through it, and as the magnet is ramped down the current circulating in the titanium cask rises until it exceeds its critical current. At this point, the titanium cask is driven normal, resulting in a rapid change in its current and the magnetic field. Then, the entire process begins again.

Experimentally, we observe that the field jumps are roughly repeatable when the magnet is ramped under similar conditions, but the number, magnitude, and location of the jumps all vary with the ramp speed and the maximum current to which the magnet is ramped. The process is hysteretic, and jumps are not observed if the magnet current is not brought above 10 A. In addition, jumps are typically not seen when the magnet current is changed at speeds less than 0.1 A/s.

While (accidentally) running the magnet while it was positioned above, but not immersed in, liquid helium, no jumps occurred. Consistent with the attribution of the jumps to a superconducting cask, we believe that under these conditions the magnet was at an elevated temperature such that the solenoids were superconducting but the

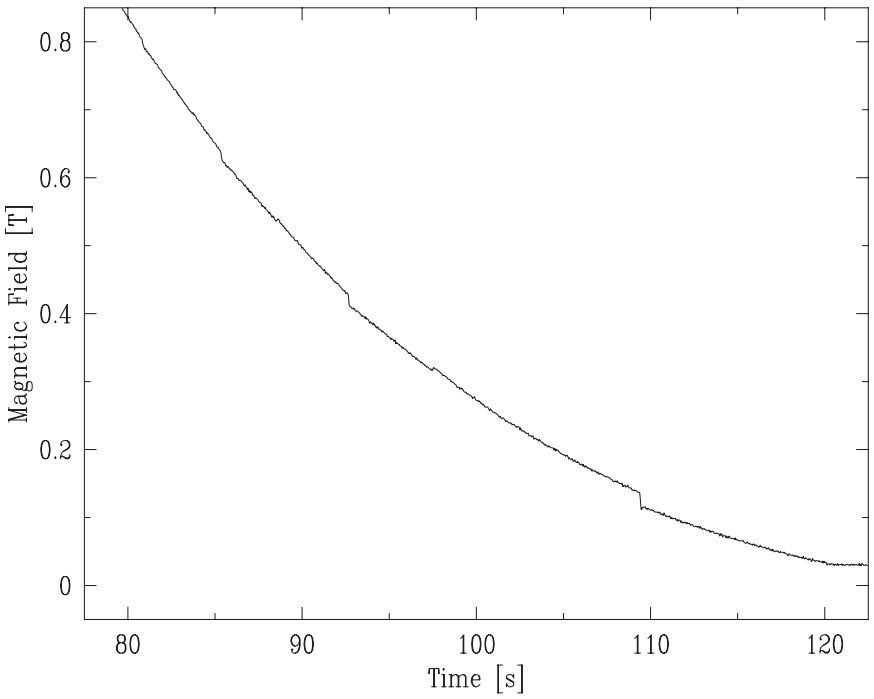

Figure 5.1: The measured magnet field at the trap saddle point as the magnet current is ramped down from 40 A to 0 A. The discontinuous "jumps" on top of the smooth rampdown and the residual nonzero field at t > 120 s are attributed to the superconducting titanium form.

cask was not.

The field jumps are accompanied by a rapid change in the current running through our magnet (as monitored by the voltage across a small resistor in series with our magnet). This is due to magnetic induction and was our first experimental indication of the jump behavior. The jumps are also accompanied by a small, rapid increase in the temperature of the cell, attributed to eddy current heating of the metal cell by the rapidly changing magnetic field.

The most important feature of the field jumps is the associated loss of atoms: the jumps cause a dramatic reduction in the number of atoms remaining. An example of this loss is shown in Figure 5.2. Certain jumps cause large atom loss (as indicated by the reduced optical density), while others leave the atoms largely unchanged. Because the cell heating is proportional to the magnitude of the current jump, this inconsistent behavior indicates that the atom loss is not due to bad vacuum caused by the heating of the cell.

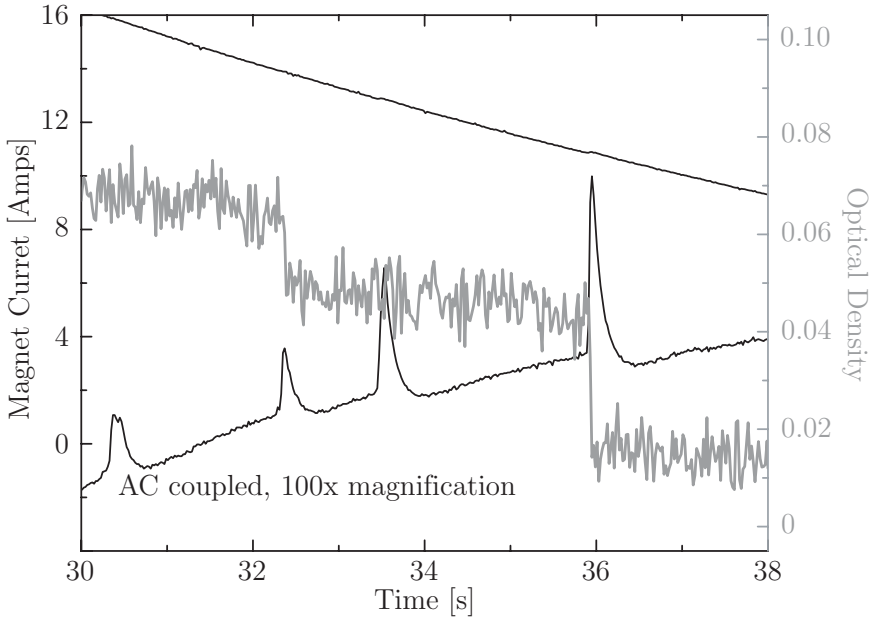

Figure 5.2: Chomium atom loss, due to field jumps, as the magnet current is ramped down. The atomic signal is shown in gray, the magnet current in black. The field jumps are identified through the corresponding jumps in the magnet current. A 100 times magnification of an AC coupled (1 Hz high pass filter) magnet current is shown to identify the location of jumps.

Irrespective of its origin, the atom loss was unacceptably large. We rebuilt the magnet using a nonsuperconducting cask.

The New Magnet

Magnet coils

The new magnet was wound with Supercon 54S multifilament superconducting wire [198], which consists of T48 superconducting filaments (niobium alloyed with 48% titanium) embedded in copper wire. The wire used had a 1.3:1 copper to superconductor ratio, a 0.016" outer diameter, and was insulated with Formvar. The magnet coils were wound by American Magnetics, Inc. [199].

The finished magnet consisted of two coils, each with 8266 turns, a 3.26" inner diameter, a 5.73" or 5.78" outer diameter, and a length of 1.995". The coils are vertically separated by 0.793" (equivalently, their centers of mass are positioned at

z = ±1.394"). The magnet's room temperature resistance is ∼ 1.3 kΩ, and its calculated field is shown in Figure 5.3. The field gradient at the trap center for a 1 A current is $\frac{dB}{dz}$ = 235.4 G/cm. The trap depth at the plastic cell wall ($\rho = 3.14$ cm) is 450 G A^{-1}.

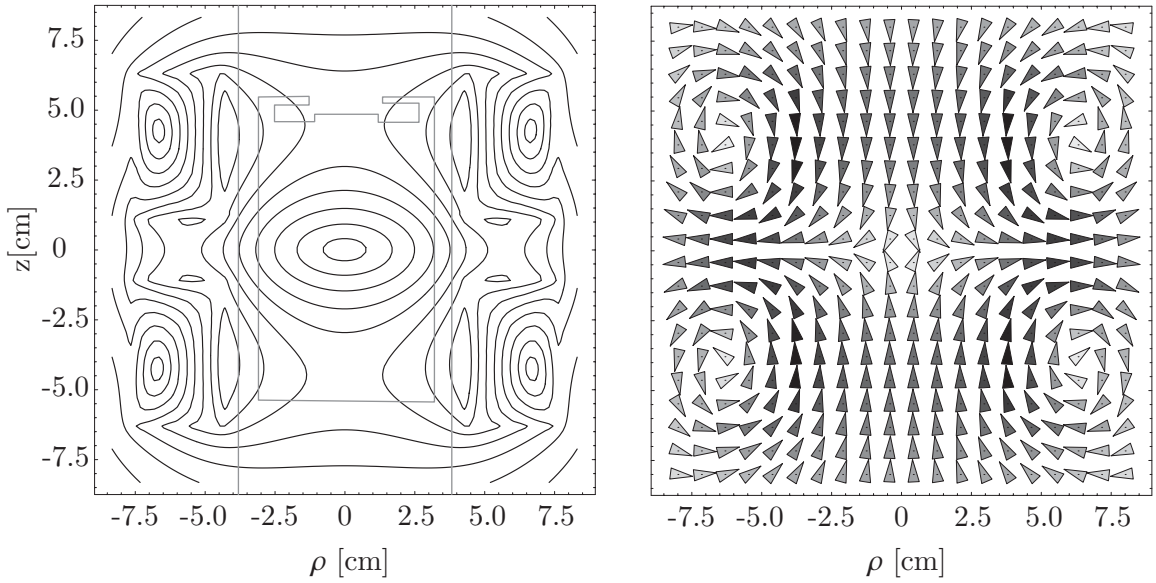

Figure 5.3: The field contours of the 3 inch bore magnet at a 1 A current, as calculated from the winding specifications [200]. Contours are plotted every 0.01 T. Shown alongside is an "arrow-plot" indicating the direction and magnitude of the field. The walls of the magnet are at $\rho = 3.81$ cm and the walls of the plastic cell at $\rho = 3.14$ cm. Both are indicated in the contour plot by gray lines.

The magnet training behavior [201] is shown in Table 5.1. Essentially no training was observed: the magnet reached its maximum current by the second, if not first, quench. The maximum current obtained is consistent with the expected limitations due to the short sample critical current of the superconducting wire itself [198, 200].

#	I [A]
1	$78 + 1 - 0$
2	78.4 ± 0.1
3	78.4 ± 0.1

Table 5.1: Quench behavior of the 3 inch magnet. The current at which the magnet quenched is listed as a function of the number of the attempt.

Magnet cask

When the magnet is energized with a current I, the coils are calculated [200] to repel each other with a force of 38 N $\cdot$ $(I/\mathrm{A})^2$, giving a maximum force of 2.3×10^5 N at the critical current. Structural support of the coils is provided by a cask made of Ti-5Al-2.5Sn normal interstitial level titanium alloy [202]. This alloy has comparable cryogenic structural properties to 6-4-ELI [195, 203], and does not superconduct at 4.2 K [196].[1] Using electrical conductivity measurements, we experimentally confirmed that the 5-2.5 titanium stock used to construct the magnet was normal at liquid helium temperatures.

A schematic of the magnet cask is shown in Figure 5.4. As shown in Figure 5.4.A, the two magnet coils are wound on the inner wall of the titanium cask; not shown are G-10 "winding flanges" (supplied by American Magnetics during the magnet winding) which fill the space between the coils and the form.

When the magnet is energized, the repulsive force between the coils is opposed by the 1/8"-thick inner wall of the titanium cask and the eight 1/2"-thick outer support plates, as shown in Figure 5.4.B. 1/2"-diameter pegs mechanically connect the outer support plates to the top and bottom of the cask, as indicated in Figures 5.4.C and 5.4.D. To hold these plates to the sides of the cask and to keep the pegs in place, thin titanium cover plates are bolted (through clearance holes in the support plates) to the cask with titanium screws and lock-washers.[2] To prevent any pressure buildup inside the cask peg-holes (which are partially sealed by the pegs when assembled), the peg-holes are vented through thin holes drilled into the top and bottom of the cask, as indicated in Figures 5.4.C and 5.4.D.

Our 5-2.5 titanium was specified to have a tensile yield strength of 800 MPa at room temperature; this was confirmed by materials testing [202]. Thus, the yield strength of the cask inner wall is calculated to be 6×10^5 N at 300 K. Our 5-2.5 titanium was specified (but not tested) to have an ultimate shear strength of 500 MPa at 300 K. The strength of the outer support structure is calculated to be limited

[1]Unfortunately, it has the disadvantage that it is less commonly available, especially in the sizes required for this work.

[2]The non-load-bearing titanium cover plates, screws, and lock-washers are commercial purity titanium; the cask, pegs, and outer support plates are all Ti-5Al-2.5Sn normal interstitial level titanium alloy.

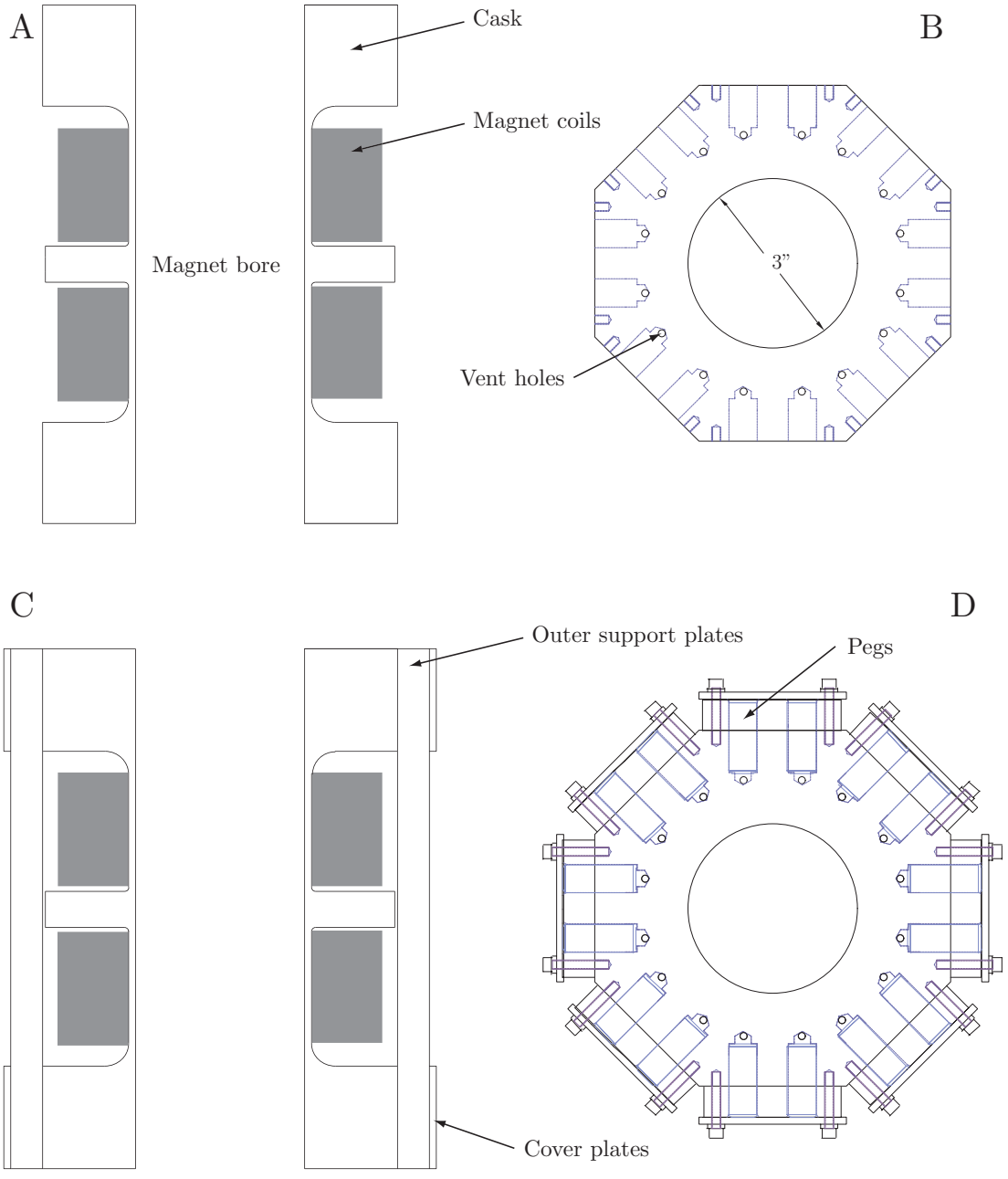

Figure 5.4: Schematic diagram of the 3” magnet, as discussed in the text. Figure A shows a cross-section of the magnet taken through an axial plane. Figure B shows a cross-section of the magnet through a plane 1” below the top surface of the magnet. Figures C and D show the magnet cask fully assembled, with the outer structural plates and support pegs attached. Minor details have been omitted for simplicity.

by the pegs, which should have a combined ultimate shear strength of 1×10^6 N at 300 K. Thus, the inner and outer support structure for the magnet coil should, at room temperature, each be able to accommodate over twice the force generated by the magnet coils at their critical current.[3] Additionally, the strength of the titanium structure will increase as it is cooled to 4 K [203, 206].

Because of the fatigue properties of repeatedly stressed materials, careful consideration is required to determine when the magnet should be retired from use. Data on the 4 K fracture toughness and fatigue crack growth rate for Ti-5Al-2.5Sn is given in References [195] and [203]. Although it becomes more brittle as it is cooled, Ti-5Al-2.5Sn still exhibits good toughness at low temperatures. Depending strongly on the size of existing cracks in the machined titanium form and regions of stress concentration, the magnet will eventually become unsafe to use. While this is not anticipated to occur in the near future, determining when this will occur is an important issue left unanswered in this thesis.

Bucking coil

While using this magnet with our plastic cell (see Section 5.5), we observed heating as the magnet current was changed. The dominant heating process was eddy current heating of the cell's metal cell heat exchanger and the refrigerator mixing chamber. To reduce this heating, we built a bucking coil to reduce the magnetic field at these locations. The bucking coil consists of a varied-density winding of superconducting wire (0.035" diameter Teledyne wire) on an aluminum cylinder. It is positioned around the heat exchanger and mixing chamber, well above the magnet. Although the field cancellation is not perfect, it greatly reduces the heating during magnet ramping.

Without the bucking coil, if the magnet current is changed 30 A at a linear rate of 6 A/s, the cell and heat exchanger both increase in temperature by over 100 mK from an initial temperature of 200 mK. This is an unacceptably large heat load, as

[3]These quoted strengths were calculated naively, ignoring stress concentration effects. Numerical simulations of the geometrical stress concentration factor K_t (using the terminology of Reference [204]) indicate that $K_t < 2.5$ everywhere in the magnet form [205]. Because 5-2.5 titanium has relatively poor ductility at liquid helium temperatures [195], we estimate this will lead to a reduction of the strength of $\lesssim 30\%$ [204].

it will ruin the cell vacuum (as shown in Figure 6.6). Under comparable conditions with the bucking coil, the cell is heated less than 30 mK. Unfortunately, it is difficult to precisely quantify this minor heating, as our thermometry exhibits strange effects in rapidly ramped fields (see Section 5.7).

Residual fields

The magnetic field is expected to be predominantly linear in the magnet current with the exception of a residual field "trapped" in the superconducting wire which persists even when the net magnet current is zero. This residual field is important because it affects how shallow a trap can be generated while maintaining the desired trap shape.

Measurements of the magnetic fields inside the trap with a Hall probe [207] confirm these expectations. The measured magnetic field at the saddle point of the trap is linear in the magnet current, with maximum deviations on the order of 10 gauss. These deviations are hysteretic and depend on the recent history of the magnet current.

Figure 5.5 shows the residual fields along the center of the magnet. After ramping the magnet down from 50 A to 0 A, we observe residual fields of up to ~ 10 G. These residual fields have a similar shape to the trapping fields and are roughly comparable to the fields that would be produced by a magnet current of 0.02 A. Efforts to further reduce these residual fields by running an opposing current through the magnet are only partially successful, and reduce the fields along the trap axis to $\lesssim 5$ G. These remaining fields bear little resemblance to the original trap. The field at the magnet wall (not shown) behaves in a qualitatively identical manner. The zero amp residual fields at the walls are approximately 40 G, and they can be canceled only to a level of roughly 30 G.

Comparing the effects of the residual fields to other mechanisms which distort the shape of the trap, we note the residual fields in the cell are much larger than the earth's magnetic field ($\lesssim 1$ G). Coincidentally, the residual fields will significantly distort the trap shape only at currents comparable to those at which gravity begins to play an important role (see Appendix C).

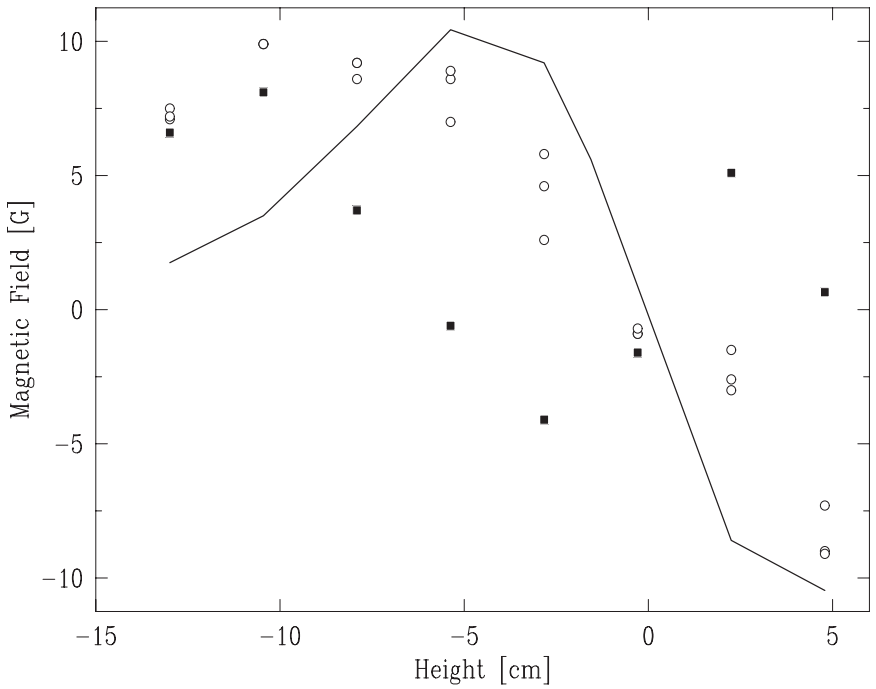

Figure 5.5: Plot of the residual field in the magnet along the $\hat{\mathbf{z}}$ axis of the trap. The line shows the magnetic field at a current of 50 A, divided by a factor of 3000. The open circles show the magnetic field after the magnet has been ramped down from 50 A to zero current, and include data from three different rampdowns. The black squares show the magnetic field while a small negative current is run through the magnet in an attempt to cancel the residual fields.

5.2 Optical access

With the cryogenic apparatus fully assembled, the trap magnet is immersed in liquid helium. The "inner vacuum chamber" (IVC) runs through the magnet bore, and contains the dilution refrigerator and the experimental cell in an arrangement similar to that shown in Figure 3.1. A series of windows through the bottom of the dewar provides optical access into the cell.

The three dewar windows are each 3" diameter, 0.5" thickness BK7 windows [208]. The windows are wedged, antireflection coated, and mounted at skew angles to prevent errant reflections from interfering with the probe beam. The windows are mounted to surfaces at 300 K, 77 K, and 4 K, as shown in Figure 5.6. The role of the 300K window is to form a vacuum seal to provide optical access while maintaining the cryostat vacuum. The 77K window forms no seal; its only role is to

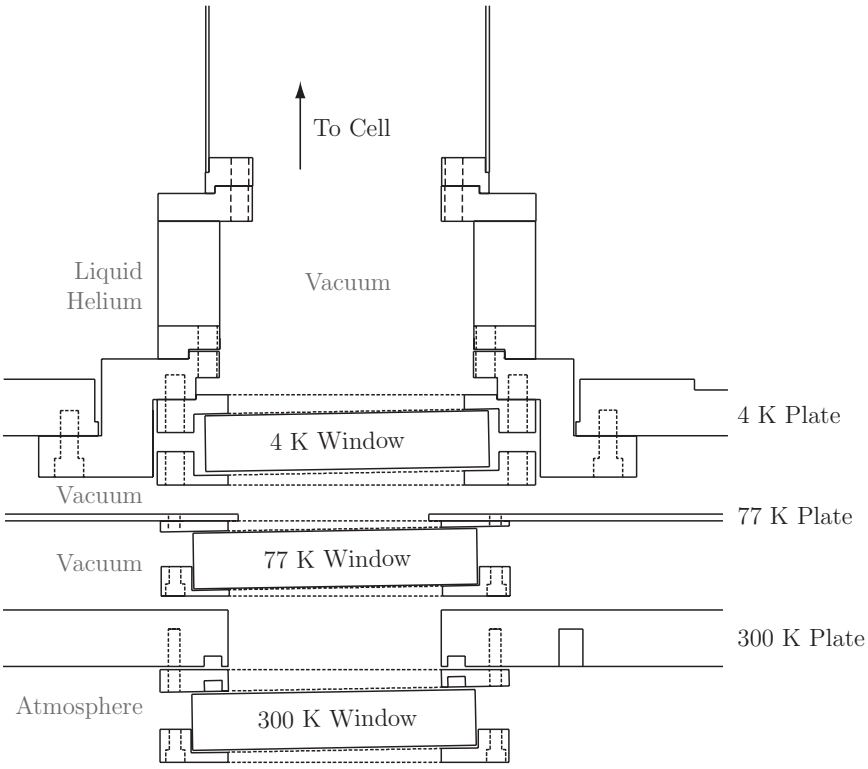

Figure 5.6: The cryostat windows (as constructed for the 3" magnet IVC). The 300K window is sealed (via an intermediate plate) to the outside of the dewar with a rubber O-ring. The 77K window is held against the liquid nitrogen dewar plate for thermal contact. The 4K window is sealed (via an intermediate plate) to the liquid helium dewar with an indium seal. The intermediate plates serve to position the windows at skew angles. The 4K window's intermediate plate also aids in removal of the window during disassembly, as the window's glass-to-metal indium seal is difficult to break.

block infrared radiation from the room to reduce the heat load on the liquid helium dewar and the cell. The purpose of the 4K window is to both shield the cell from infrared radiation and to form a vacuum seal to isolate the inner vacuum chamber and the cryostat vacuum. From the base temperature reached by the cell (and the measured conductance of its thermal link), we find an upper limit on the black body heat load on the cell is ≤ 30 μW.

The 2" bore magnet setup

The above description applies to the optics as they were used with the 3" bore "new" magnet. A very similar arrangement was used with the 2" bore "old" magnet. In that setup, the cryostat windows used were also 3" diameter antireflection-coated BK7 windows, although of different origin [209]. During one cooldown with these optics, the thermal link was not securely fastened to the refrigerator. This resulted in an extremely weak thermal connection to the cell, and certain doom for that experimental run. However, it supplied a very sensitive measurement of the heat load on the cell. From this data, we can place an upper limit on the cell heat load from blackbody radiation of 5 μW.

5.3 The copper cell

Initial chromium trapping experiments were conducted in the same copper cell used for the CaH trapping work (described in Section 3.2). This cell is unsuitable for evaporative cooling (which we implement in this thesis by changing the magnetic field, and plan to eventually implement through RF radiation) because it is incompatible with both rapidly ramped magnetic fields and RF. Both of these techniques would induce eddy currents in the copper cell walls, which would cause heating of the cell and ruin the cell vacuum.

It is also important to note that despite the low cell temperatures that were obtained with the copper cell (T $<$ 100 mK), we observed exponential loss from the cell on a timescales of $\sim$ 60 seconds (while using ^{4}He as a buffer gas). This exponential loss suggests loss due to background processes. This loss is conceivably due to poor vacuum in the cell, despite the low temperature of the cell wall. Similar phenomena seen in early versions of the plastic cell are discussed in Section 5.6.

5.4 The composite metal cell

The composite metal cell was built and used chronologically between the original copper cell and the subsequent plastic cell design. It was designed to allow the magnet to be rapidly ramped without heating. To accomplish this without the complexity of the subsequent plastic cell design, we built a cell whose thermal conductivity was

supplied by thin, insulated copper wires [99].

The cell was constructed from a 0.035" wall, 1.5" diameter stainless steel tube. The combination of the thin wall and stainless's comparatively poor electrical conductivity should exhibit greatly reduced eddy current heating in comparison to a copper cell. To provide thermal conductivity along the length of the cell, 99 insulated copper wires (0.033" diameter with SPN insulation) are run down the length of the cell, held in place by kevlar thread wrapped around the cell, and anchored to the cell wall with 1266 epoxy [193]. The top ends of the wires are flattened, stripped, and soldered to a copper plate positioned above the regions of high field. This plate is, in turn, connected via a copper heat link to the dilution refrigerator mixing chamber. The cell window is sealed to the bottom via a standard indium face seal [159].

The thermal conductance down the length of the cell was high. It was measured to be ~ 10 μW/mK at 200 mK (and scales linearly with the cell temperature). This conductance is overkill for our requirements and a functional cell could be built with fewer and thinner copper wires.

Eddy current heating is quite considerable with this cell. The heat load on the cell during a magnet ramp is roughly 2 mW at a ramp rate of 2.5 A/s (using the "Old Magnet"). The heating is expected to scale as the square of the ramp rate. To change the magnet current 50 A while maintaining the cell temperature below 200 mK requires that the magnet be changed at a rate below 1 A/s. This performance is marginal for our evaporative cooling experiments.

Calculations indicate the dominant source of heating during magnet ramps was the large diameter copper plate which served to thermally connect the cell wires and the copper heatlink to the mixing chamber. As such, it should be possible to considerably improve the performance of the cell by adding a bucking coil to reduce the magnetic field at this plate. Alternatively, the top could be redesigned to reduce its heating.

The combination of the magnet jumps and the poor ramping capabilities of the composite metal cell prevented us from making meaningful measurements of the evaporative cooling properties of atomic chromium. To overcome this, we rebuilt both the cell and the magnet. Rather than attempt to fix the problems of the composite metal cell design, we decided to replace it entirely with the plastic cell. We had sufficient time to do so while waiting for our new magnet to be constructed, and believed the performance of the plastic cell would be superior.

5.5 The plastic cell

To create a cell which would allow fast field ramping (and high power RF radiation) without heating, we redesigned the cell to use thermally conducting but electrically insulating materials. Following the design of the MIT Hydrogen experiment [19, 210], we constructed a double-walled cell which uses superfluid helium to provide thermal conductivity. A schematic of the cell is shown in Figure 5.7; we call it the "plastic cell".

The cell body is constructed out of G-10, a fiberglass-epoxy composite with well-characterized low temperature properties [203]. The cell walls are custom diameter Spaulding G-10-Cr natural spauldite tubing [211], with a 1/32" wall thickness. All of the other G-10 cell components were constructed from stock G-10 tubing and 1/4" plate [212]. To ensure that the tubing was superfluid leak tight, the surfaces were coated with 1266 epoxy [193].[4] To facilitate coating the surfaces with epoxy, the surfaces were first sanded, cleaned with ethanol, and then cleaned briefly with acetone. The 1266 epoxy was applied and wiped with a Kimwipe [213] in order to remove excess epoxy and encourage surface wetting .

1266 epoxy was also used to seal the G-10 joints, which were machined to 0.001–0.002 inch clearances. This clearance was chosen because it was the minimum clearance which exhibited good wicking of epoxy into the joint. The joints were designed with "elbows" such that one of the mating pieces would extend past the joint by 0.050" or greater. This would facilitate application of the epoxy to the joint, which was usually done in such a manner that gravity would assist in drawing the epoxy into the joint. The G-10 surfaces were prepared for epoxy application by sanding, followed by cleaning with acetone. Sufficient epoxy was applied that a small fillet ($\sim$ 0.020") of epoxy remained at the joint "elbow" after the epoxy wicked into the joint.

Cell heaters and thermometers (as described in Section 5.7) are mounted inside the cell walls. The immersion in liquid helium supplies sufficient thermal contact for accurate thermometry at reasonable ($\sim$ 300 μV) excitation voltages. The electrical

[4]It is interesting to note that a complete version of the cell was assembled without coating the tube surfaces with epoxy and found to be superfluid leak tight. However, during the construction of subsequent cells, some G-10 tube sections used were found to leak at room temperature and were coated with epoxy to eliminate the leaks.

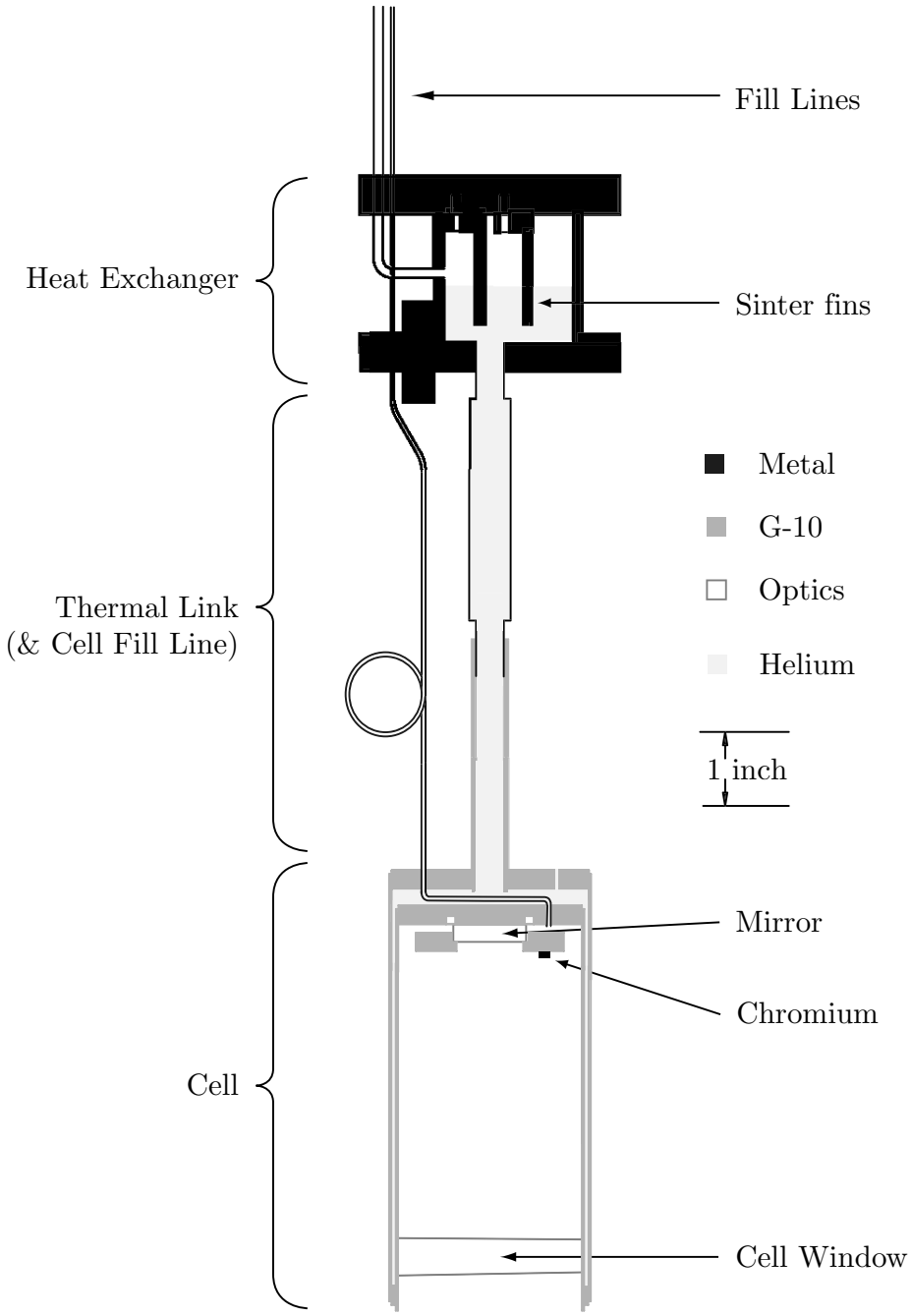

Figure 5.7: Diagram of the plastic cell. The inner wall inner diameter of the cell is 2.484 inches. Not shown are the standoffs on the top and bottom of the cell: see Figure 5.8.

connection to the wires is supplied with twisted-pair manganin wires [214] which exit the cell through a 1/16" diameter hole which is sealed with 2850 epoxy [215].

The Heatlink

The thermal link (also shown in Figure 5.7) must allow the cell to be heated (to produce the desired density of buffer gas for trap loading) without appreciably heating the dilution refrigerator. This requirement is crucial because the dilution refrigerator is extremely slow to cool. Once the atoms have been loaded into the magnetic trap, the thermal link must then provide the thermal conductivity to cool the cell and reliquefy the buffer gas. The thermal conductance of the heatlink is chosen as a compromise between these two requirements.

The heatlink consists of two sections: the superfluid helium thermal link, which provides a thermal connection between the the cell and the "heat exchanger", and the heat exchanger, which provides a thermal connection between the superfluid and the metal surface of the dilution refrigerator.

Superfluid helium thermal link

The design of the superfluid heat link is complicated by the rapid variation of superfluid helium's conductivity with temperature. In the temperature range of interest, the thermal conductivity of copper scales as T, but the conductivity of superfluid helium scales as T^3 [99, 216]. For ^{4}He inside a (rough-surfaced) tube of diameter d and length L (with pressure less than 2 atmospheres, $T \lesssim 0.5$ K, and a small temperature gradient across the tube), the thermal conductance along the length of the tube is approximately

$$\kappa \sim 16 \, \frac{\mathrm{W}}{K} \cdot \left(\frac{d}{\mathrm{cm}}\right)^3 \cdot \left(\frac{L}{\mathrm{cm}}\right)^{-1} \cdot \left(\frac{T}{\mathrm{K}}\right)^3$$

The superfluid-helium section of the heatlink is a 3/8" diameter, $\sim$ 7" long column of superfluid helium contained by a G-10 tube and a flexible thin-walled formed stainless bellows [217], as shown in Figure 5.7. As shown in Figure 5.9, its thermal conductance was experimentally measured to be $670 \pm 20 \, \frac{\mu\mathrm{W}}{\mathrm{mK}} \cdot \left(\frac{T}{\mathrm{K}}\right)^3$, within 20% of the predicted value.

Heat exchanger

The copper heat exchanger provides thermal contact between the superfluid heatlink and the mixing chamber via silver-sinter-covered copper fins descending into the liquid helium. The heat exchanger itself is then thermally anchored to the mixing chamber through direct contact. The fins are covered with silver sinter in order to create a large surface area between the metal and helium. This is necessary because of the large Kapitza resistance at the metal-helium interface [99]. By changing the height of the helium in the heat exchanger, we can tune the heat exchanger's thermal conductance, as seen in Figure 5.10, and limit the total cell-to-refrigerator thermal conductivity.

The two sinter plates are constructed in a manner similar to that outlined in Reference [218]. Each consists of a $\sim$ 2" by 1.5" copper plate which is electroplated with a $\sim$ 100 μm layer of silver [219]. Approximately 20 grams of 1 micron silver powder [220] are applied to each side of the plate, compressed (between teflon-covered plates) to 2000 psi, and baked in air at 100 degrees Celsius for twenty minutes. After cooling in air, the sinter fins are extracted from the compression assembly and screwed into the top of the heat exchanger can.

Care must be taken to ensure that the surface to which the sinter is bonded is clean of chemical residue which might interfere with the adhesion of the silver sinter to the plate. Early attempts at forming the sinter plates encountered problems with the sinter flaking off in bulk, attributed to poor cleaning of the plate. Similar flaking problems were encountered with a silver sinter [221] that did not meet its purity specifications due to an organic compound on the surface of the sinter. When replaced with "clean" silver sinter and a well-cleaned silver-coated plate[5], we found good adhesion to the plate.

[5]Before silver plating, the copper plates are sanded with 100 grit sandpaper to roughen the surface, annealed at 460 Celsius in a H_2 atmosphere, gold plated, washed in acetone, rinsed in distilled water, silver plated, rinsed in distilled water, rinsed in 10:1 water-to-sulfuric acid solution (as part of the silver-plating process), then rinsed in distilled water again. I cannot recall why the plates were gold plated; it seems an unnecessary step.

The Helium Dump

To accurately meter helium into the cell jacket and heatlink, we use a large stainless steel cylinder of known volume as a helium reservoir. This helium dump has a capacitance manometer gauge to measure its pressure. The volume of this resevoir is 7×10^4 cm^3, yielding 0.11 cm^3 of condensed liquid per Torr of room-temperature helium gas in the dumps.

Standoffs

The trap depth in our cell is set by the magnetic field at the cell wall. To obtain as large a trap depth as possible, a large inner diameter cell is desired. The diameter is limited ultimately by the magnet bore and in practice is additionally reduced by the thickness of the IVC, the cell walls, and the clearance between them. Thus, it is desirable to minimize the clearance between the cell and the IVC. If the cell wall directly touches the IVC, however, it typically results in a disastrous heat load on the cell from the 4 K IVC.

The original copper cell was build with a 2 mm radial clearance inside the IVC and a rigid connection to the refrigerator. Initially, it was assembled by iteratively positioning it via an adjustable joint at the mixing chamber until it did not contact the IVC. During one experiment, a magnet quench caused the cell to collide with the IVC, where it remained, intolerably warm, for the remainder of the run. To avoid such mishaps and simplify the assembly procedure, we use "standoffs": low thermal conductivity spacers which mechanically anchor the cell to the IVC with extremely low heat flow.

The standoff used with the plastic cell is a Kevlar "lasso", shown schematically in Figure 5.8. The lasso consists of a thin G-10 ring of an inner and outer diameter such that it fits between the cell and the IVC. Pairs of shallow notches ($\sim$ 1 mm wide and deep) are filed into the top of the G-10 ring. Kevlar thread [222] is strung tautly between the notches and held in place with 2850 epoxy. Two such lassos are made, and the Kevlar thread is glued to the top and bottom of the cell (with G-10 spacers and directly, respectively) with 2850 epoxy. These lassos are quite stiff against horizontal displacement; they are considerably stiffer than the flexible heatlink. Because the thermal connection between the cell and IVC walls is along a long, thin Kevlar thread, the heat load on the cell is very small. Measurements of

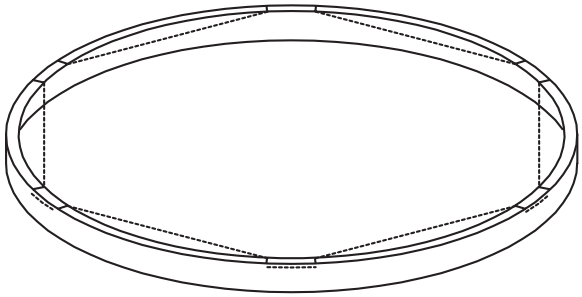

Figure 5.8: The cell bottom standoff. The ring is made of G-10, the kevlar thread is shown as a dotted line. The thread is epoxied to the bottom of the cell inner wall at the midpoint of each of the six sections of thread.

this heat load provide an upper limit of 30 μW as the total heat load through both standoffs. Calculations predict a total heat load of less than 20 μW [223, 224].

An additional benefit of the standoffs (and flexible heatlink) is that the IVC is typically more vibrationally stable than the refrigerator. By mechanically anchoring the cell and its mirror to the IVC, we obtain superior beam pointing stability.

The cell interior

A "UV-enhanced" aluminum mirror [225] is placed at the top of the cell to reflect the probe beam. A G-10 plate attached to the cell top by nylon screws holds the mirror loosely against the cell top. Despite its name, the reflectance of the mirror is poor at 425 nm, and it absorbs more than 10% of the probe beam power. While this absorption is benign with our $\sim$ nW probe beam powers, it proved to be problematic with high power beams used for optical pumping.

Our chromium ablation targets are positioned on the same G-10 plate holding the cell mirror. Four ablation targets are in the cell, each a high purity chromium lump roughly 2 mm in size [226]. We place multiple targets at various locations in the cell primarily for convenience in aligning the ablation laser; we typically use only one lump. To provide thermal conductivity to the walls, the lumps of chromium are epoxied to 20 gauge copper wires with 2850 epoxy. The other ends of the wires are epoxied to the junction of the walls and the cell top with 1266 epoxy along a length of a few centimeters.

The bottom of the cell is sealed with a wedged, antireflection-coated BK7 window

[227]. It is manufactured to fit into the cell inner wall with a 0.001" radial clearance. It is epoxied directly to the cell inner wall with 1266 epoxy.

Fill lines

"Fill lines", thin vacuum tubes connecting the cell vacuum spaces to room temperature pumping ports, are necessary for condensing helium into the cell jacket and placing buffer gas in the cell.

The cell buffer gas fill line is a 1/8" diameter seamless 316 stainless steel tube which runs down from the top of the cryostat (at 300 K) and is thermally anchored to the IVC top (at 4 K) and the refrigerator's 1K pot. At the height of the refrigerator mixing chamber, a 0.020" diameter pinhole is placed in the fill line, and the fill line diameter is reduced to 1/16" outer diameter (0.04" inner diameter) which continues until it reaches the cell. The vacuum connection between the two tubes is made with Swagelok VCR connectors [163], and the pinhole is simply a modified VCR gasket. As shown in Figure 5.7, the 1/16" fill line enters the cell top, bends through the superfluid helium inside the cell top, and enters the cell interior. Both G-10 penetrations are sealed with 1266 epoxy.

A large diameter fill line is desirable to supply a high cell pumping speed [118] and allow the quantity of buffer gas inside the cell to be varied while still maintaining the apparatus at cryogenic temperatures. Unfortunately, a large diameter fill line is disastrous for the thermal load on the cell. Various mechanisms, including superfluid film flow, cause significant power transport down the tube [210]. The small pinhole in the fill line is intended to reduce superfluid film flow (which is a surface effect) between the cell and warmer sections of the fill line without significantly reducing the pumping speed of the line. The bend of the tube through the cell helium jacket is intended to condense any errant helium gas flow down the fill line. The 1/16" line was chosen for the final section of the fill line not only for its its reduced conductance but also to simplify construction of the "bend" through the cell top. This design keeps the heat load on the cell at an acceptable level: when the buffer gas is added to the cell, the additional heatload on the cell is ~ 10 μW.

The fill line for the heatlink (and cell jacket) is similar in both intent and construction. It consists of a 1/8" outer diameter stainless fill line from 300K to the cell heat exchanger. This fill line is thermally anchored to the IVC top and the re-

frigerator's 1K pot, still, and cold plate. A 0.020" diameter pinhole is placed in this line at the height of the mixing chamber. This fill line provides a nice compromise between pumping speed and thermal isolation. The additional heatload on the cell heat exchanger when the cell jacket is full is $\lesssim 100$ μW. To pump out the cell jacket (while the cell is kept below 4 K and hence at sub-atmosphere pressure) requires less than 2 hours.

The motivation behind the design of the fill lines is discussed further in Section 5.6.

Performance

With this cell and ^{4}He buffer gas, we were able to achieve cold cell temperatures and good vacuum, as described in Section 6.3.

The thermal conductance of the superfluid heatlink and the sinter are shown in Figures 5.9 and 5.10. While the superfluid heatlink shows the expected temperature behavior, the thermal conductivity of the sinter scales as T^2, rather than the T^3 scaling expected for Kaptiza resistance [99]. The T^2 scaling is to our advantage, as it allows us to attain higher thermal conductivity at low temperatures without excessive thermal conductivity at trap loading temperatures.

A plot of the cell temperature during a typical loading cycle is shown in Figure 6.7. Despite the high specific heat of the helium in the cell walls [99, 228], the cell cools and the buffer-gas is liquefied on a timescale of a few seconds. Additionally, the refrigerator mixing chamber undergoes quite modest heating during the loading cycle, as indicated by the cold temperature to which the cell quickly returns.

The thermal conductance along the length of the cell (between the cell top and bottom) is extremely high, making it difficult to accurately measure. We can place a lower limit on the cell thermal conductance of 200 μW/mK at a temperature 400 mK. This is considerably higher than the thermal link conductance at the same temperature, and is overkill. However, little would be gained by reducing the thickness of the superfluid jacket: this thickness is convenient for mounting thermometers and heaters, the gain in trap depth would be minor, and the cell cooling rate would be improved only modestly.

From the final temperatures reached by the cell and heat exchanger, their individual heat loads (with buffer-gas in the cell and the helium thermal link full) are

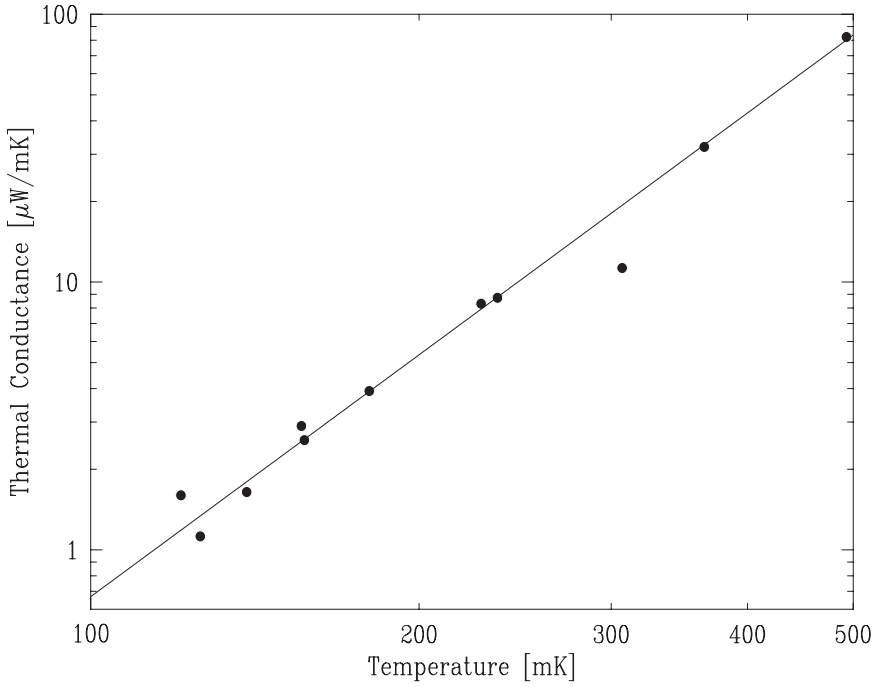

Figure 5.9: Thermal conductance of the cell heatlink (the thermal connection between the cell and heat exchanger), fit to $\kappa = C \cdot T^3$.

less than 30 μW each. However, the base temperature reached by the refrigerator (and its rated cooling performance) indicates that its total heat load is approximately 300 μW. Such inconsistencies have been seen with other versions of the cell; it is not known how to reconcile these numbers.

5.6 Failed cell designs

Prior to the plastic cell design described in Section 5.5, multiple designs were used which failed to attain good vacuum and long trap lifetimes. Some of these cells failed because they were unable to reach sufficiently low temperatures. Insidiously, certain cells showed trap loss despite cold cell wall temperatures. The observed loss would also often occur in counterintuitive manners.

Examples of this "counterintuitive" cell loss are shown in Figure 5.11. The loss rate due to bad vacuum is naively expected to be exponential; the loss rate from Cr–Cr interactions should slow even more rapidly as the density of trapped atoms

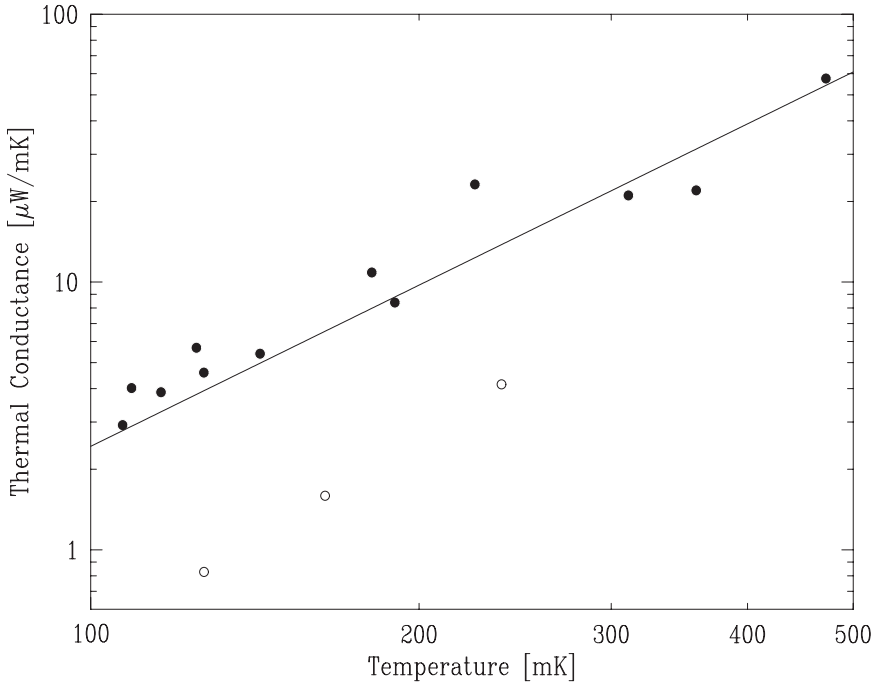

Figure 5.10: Thermal conductance of the heat exchanger, fit to $\kappa = C \cdot T^2$. The black dots show the thermal conductance of the heat exchanger at a calculated helium depth such that 0.3 inches (out of 1.5") of the sinter fins are immersed in liquid helium. The open dots show the conductance with only 0.1 inches of sinter fin immersion.

decreases. The behavior shown in Figure 5.11 exhibits a loss rate (per atom) which increases with decreasing Cr density.

Although the exact mechanism behind the behavior in Figure 5.11 remains unexplained, the effect was attributed to background helium because it increased with marginally increased cell temperatures. We suspect it is to the presence of local, unmeasured "hot spots" in the cell or fill line. The liquefied ^{4}He in the cell is superfluid, and the resulting superfluid film will coat all surfaces inside the cell. If there is a local spot which remains warm (such as the cell window or mirror), helium will continually flow to this point and evaporate from it. Similarly, superfluid flow up the fill line to warmer regions may produce a continuous flux of helium gas into the cell. This theory is supported by the additional heat load observed when buffer gas was placed in these older versions of the cell.

The (known) changes to the cell design between the working and the various failed cells are shown in Figure 5.12. As shown in 5.12.A, the method of window mounting

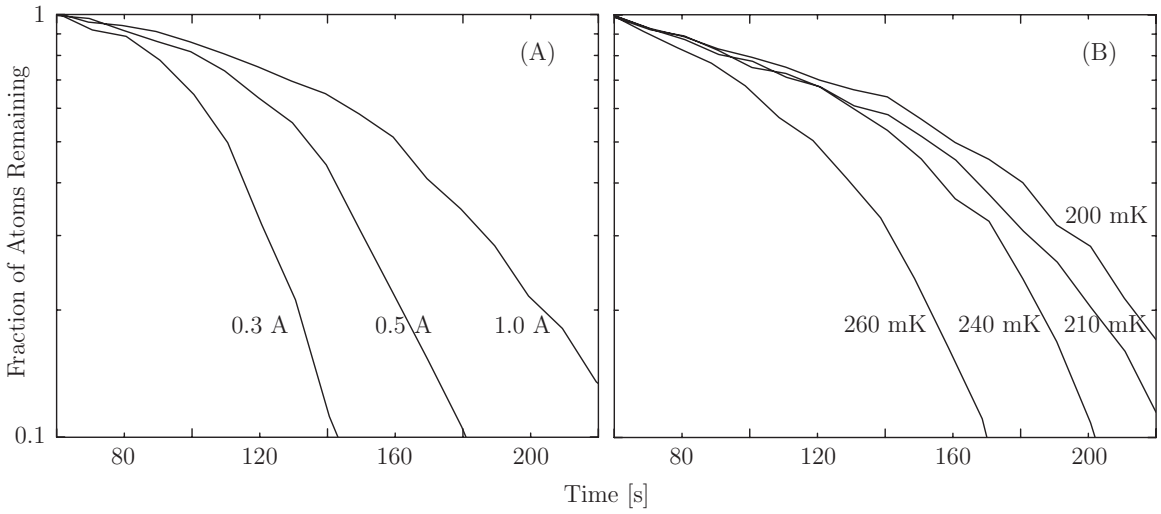

Figure 5.11: Atom loss from the trap with a failed version of the plastic cell. To obtain the data, the trap is loaded at high field. Then the cell is cooled and the magnet ramped down to a lower trap depth. For times after +60 seconds, the magnetic field and cell temperature are held constant. In Figure (A), the temperature of the cell walls is 200 mK. In Figure (B), the magnet is kept at 1 amp. For comparison, our final cell version exhibited long lifetimes at 200 mK, as shown in Figure 6.6

was changed. In the initial arrangement, a 2" diameter window was epoxied to a G-10 ring epoxied to the inner cell wall. The redesigned version is simply a custom diameter window which is glued directly to the inner cell wall at a height such that the superfluid helium extends below the window. Although the new version requires a precisely manufactured custom window, it increases the thermal conductivity to the window. As an added benefit, the new design should produce less mechanical strain on the window when it is cooled; the old design was prone to cracking the window.

As shown in 5.12.B, the cell fill line below its aperture was changed from a 1/8" diameter tube to a 1/16" outer diameter (0.010" wall) tube. Perhaps more importantly, the new tube is run through the cell top to provide a better thermal connection to the superfluid helium and eliminate any line-of-sight path into the trap. Additionally, the new fill line was curlicued a couple of times (as shown in Figure 5.7) between the cell and the "pinhole".

A change omitted from Figure 5.12 is the placement of pinholes in the cell fill lines and thermal anchoring of the fill lines. These details were absent in early versions of the cell, and the heat load from the fill lines is on the order of 500 μW. With

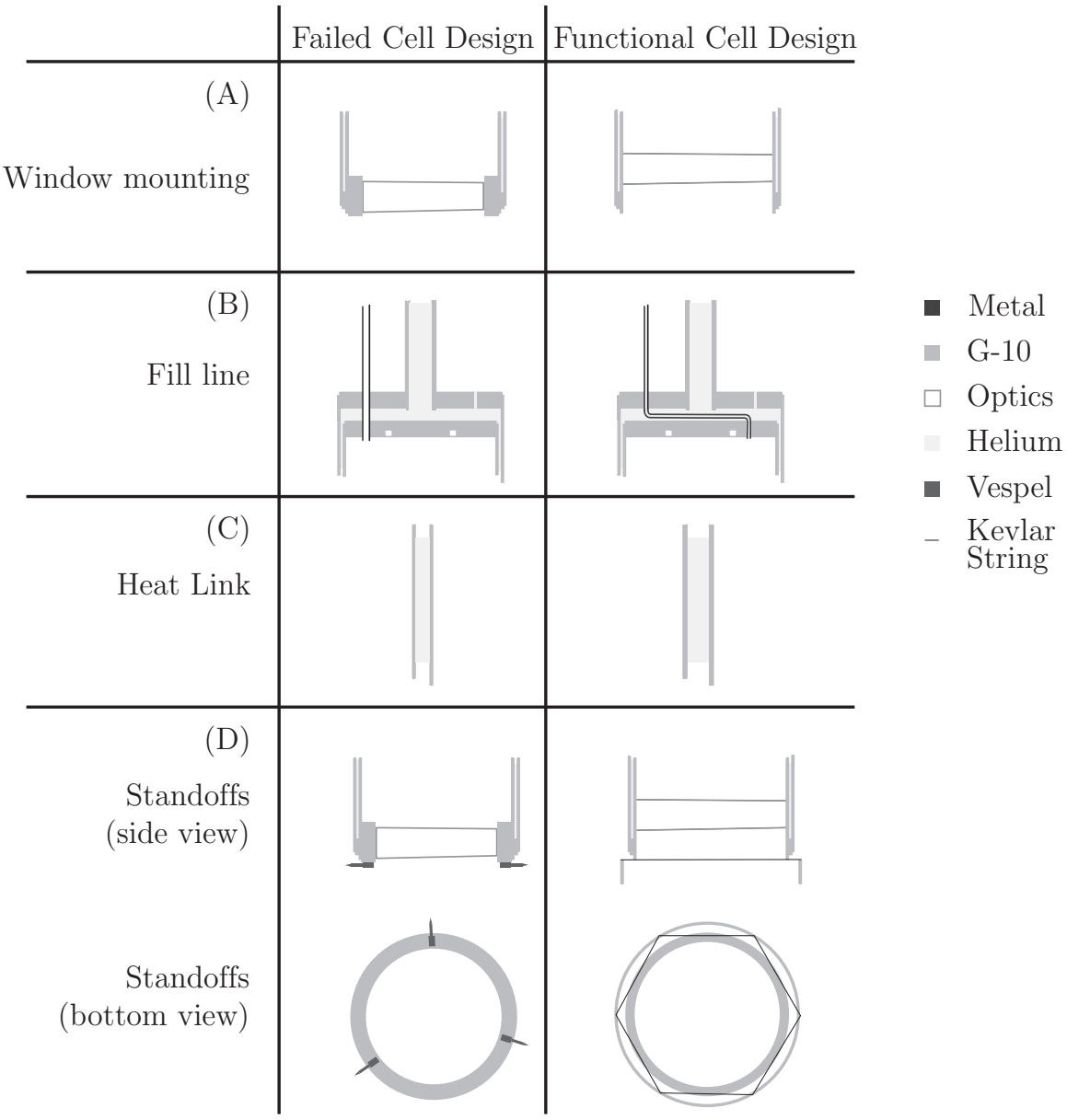

Figure 5.12: Changes in the cell design from our non-functional plastic cell, which was unable to attain good vacuum, to our working cell, which produced long-lived trapped species. The details of the changes are discussed in the text.

the pinholes and thermal anchoring to the refrigerator, this heat load is reduced to $\lesssim 100\ \mu$W.

As indicated in Figure 5.12.C, the inner diameter of the heat link was increased from 1/4" to 3/8". Because the sinter limits the high-temperature thermal conduc-

tivity to the mixing chamber, the conductance of the superfluid heatlink (which is the limiting conductance at low temperatures) could be increased without putting an undue heat load on the mixing chamber during the loading procedure. This allowed lower cell temperatures to be obtained.

As shown in Figure 5.12.D, the cell standoffs (top and bottom) were also changed. Our original design used rigid Vespel pegs [164] to mechanically anchor the cell to the walls. While the heat load of the pegs was not measured, they were replaced with the Kapton lasso to reduce the likelihood of problematic heat conduction through the standoffs, as it was believed the lasso design would have lower thermal conductivity. The Kapton lasso replacement performed well (≤ 30 μW total heat load) and in our experience was less likely to be damaged during assembly, adding convenience and reliability.

It is not known which of the changes in the cell design were responsible for eliminating the problematic behavior; the only cell which achieved good vacuum incorporated all of them.

5.7 Cryogenic thermometry

Our cryogenic thermometry was performed with ruthenium oxide chip resistors. These resistors exhibit increasing resistance as their temperature decreases. Ruthenium oxide resistors are seemingly ideal thermometers for our temperature range of interest (0.1 K to 1 K): they change resistance dramatically over this temperature range, have relatively low magnetoresistance, are small, and are inexpensive (when available). Importantly, the resistors are also relatively consistent both within a batch and over time and thermal cycling [99, 229].

In addition to the resistors supplied with and attached to the dilution refrigerator, we monitored the cell temperature using custom mounted thick-film RuO_2 chip resistors. The resistors were taken from a single batch of Dale 1 kΩ (1% tolerance) resistors [230]. The temperature calibration of their resistance was obtained from measurements of resistors from the same batch; the measurements were performed previously at MIT [210].

The resistances of our thermometers are measured with two-wire measurements via an AC resistance bridge [231] and the offsets of the lead wires are subtracted. While four-terminal measurement would provide superior accuracy, the two-terminal

measurement is typically sufficient for our needs.

To measure the temperature of metal objects, the thermometers were epoxied (with an insulating sheet of cigarette paper) either directly or to copper lugs which were attached via screws. For monitoring the temperature of the plastic cell, the thermometers were simply immersed in the superfluid helium at various locations inside the cell walls and cell heat exchanger. Cell heaters (also chip resistors) were mounted in the same manner.

RuO_2 "Dynamagnetoresistance"

As a perplexing side note, we found our RuO_2 resistors exhibit quite unusual behavior in changing magnetic fields. Our cell resistors exhibit very low magnetoresistance, giving measured temperatures at multi-Tesla fields consistent with field-free measurements to better than 10%. However, they exhibit strong changes in their reading when the magnetic field is ramped rapidly at low fields. We do not understand the physical mechanism behind these effects, and cannot explain them. Instead, we give a comprehensive description of the phenomena observed.

As the magnetic fields are increased, the resistance is observed to temporarily decrease (indicating heating). As the magnetic fields are decreased, the resistance increases (indicating cooling). Typical behavior is shown in Figure 5.13, as the magnet current is ramped from 2 A to 0.1 A and back at a linear rate of 2 A/s.

This "dynamagnetoresistive" behavior is independent of the bridge excitation voltage used to monitor the resistor (observed over the range from 100 μV to 3 mV). Similarly, if the resistors are measured with a DC excitation current and a preamp, the same qualitative behavior is seen. Additionally, the behavior is independent of the sign of the field: ramping from -10 A to 0 A magnet current produces the same effect as +10 A to 0 A. These measurements indicate that the behavior is not due to an induced EMF in the resistor or similar phenomena.

The dynamagnetoresitance effects are suppressed by high fields, reduced ramp rates, and high temperatures. The effect was also observed with a RuO_2 resistor of separate origin [232], which exhibited qualitatively identical behavior. The effect was observed both with the plastic cell and with the composite metal cell. We do not know whether this effect is due to an actual change in the temperature of the resistor due to, perhaps, a process such as adiabatic demagnetization [99], or a purely

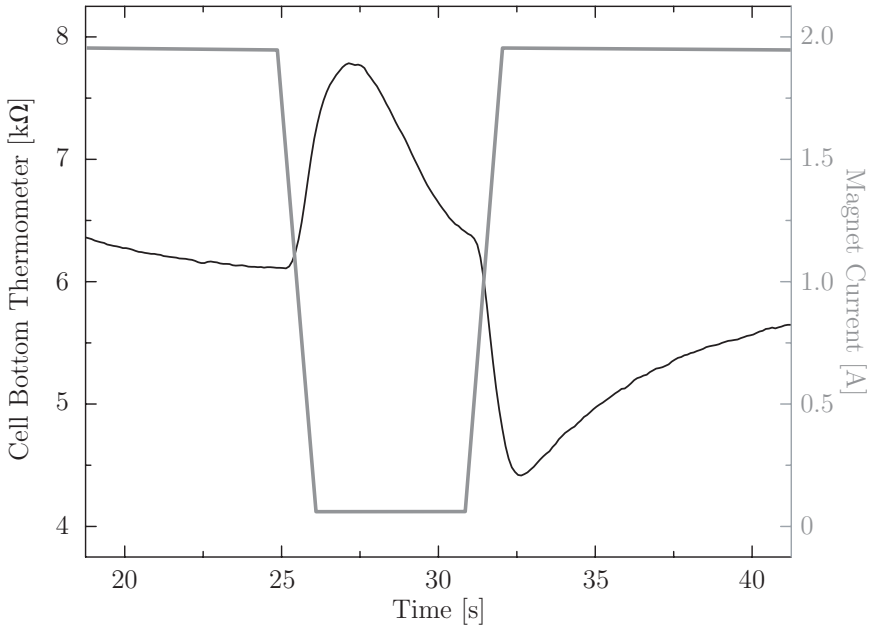

Figure 5.13: A plot of the resistance of one of the plastic cell's ruthenium oxide thermometers as the trapping fields are ramped at low currents. The thermometer is immersed in superfluid helium inside the cell wall. When the magnetic fields are changed from higher to lower magnitude values, the resistance temporarily increases; as the field increases in magnitude the resistance decreases.

electrical effect.

Chapter 6

Chromium Experiments

Chromium (Cr) is a nice atom for buffer-gas loading. It has a highly magnetic weak-field seeking ground state with a 6 μ_B magnetic moment, permitting efficient trapping at elevated temperatures. It is straightforward to detect chromium optically, with a strong transition from the $^7S_3$ ground state to the ^7P excited state at 425nm. And it can be produced in large abundance via laser ablation ($\sim 10^{13}$ atoms per ablation pulse). As such, it is a good choice for developing the technology to combine buffer-gas loading with evaporative cooling.

We are interested in neutral chromium atoms because of its fermion isotope. Chromium has four stable isotopes, and we concern ourselves primarily with ^{52}Cr, the dominant boson isotope, and ^{53}Cr, a fermion isotope with almost 10% natural abundance. By trapping and evaporatively cooling a combination of these isotopes, we hope to create coexisting chromium Bose condensates and degenerate Fermi gases.

6.1 Chromium atomic structure

A summary of chromium's spectroscopic (and other) properties can be found in Appendices H and I. We repeat some of the salient details here.

For magnetic trapping, the only important consideration is the structure of the ground state. ^{52}Cr, ^{50}Cr, and ^{54}Cr have no nuclear spin, and the Zeeman structure of their ground states, shown pictorially in Figure 6.1, is extremely simple. We aim to trap the $m_J = +3$ state, which has a 6 μ_B magnetic moment. Although ^{53}Cr's nuclear spin complicates its low-field Zeeman structure, as plotted in Figure I.1, it has high field Zeeman levels similar to that of ^{52}Cr.

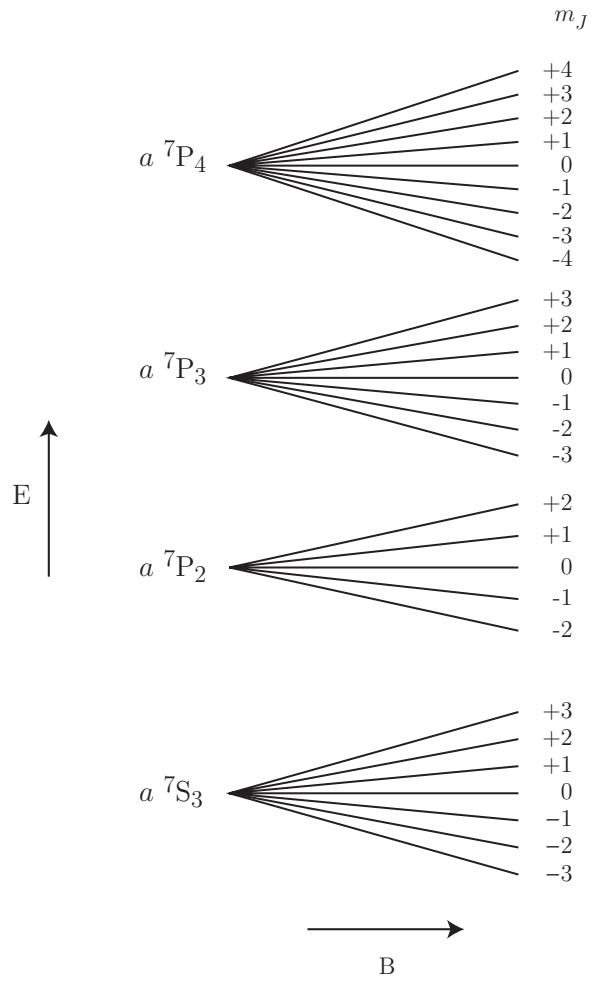

Figure 6.1: Zeeman structure of chromium's ground and excited states, not to scale. Hyperfine structure (relevant only for ^{53}Cr) is omitted.

The transitions to the $^7P_2$, $^7P_3$, and $^7P_4$ states (at 429.1, 427.6, and 425.5 nm, respectively) all offer different advantages for spectroscopic detection.

The $|^7S_3, m_J = +3\rangle \rightarrow |^7P_3\rangle$ transition has very narrow broadening on $\Delta m = 0$ transitions. This small splitting is advantageous for resolving the different isotopes of chromium at elevated trap temperatures. However, these $\Delta m = 0$ transitions are poor choices for determining the temperature and density of trapped atoms, as discussed in Appendix A.

The $|^7S_3, m_J = +3\rangle \rightarrow |^7P_4\rangle$ transition offers a strong, moderately broadened $\Delta m = +1$ transition (along with a similar $\Delta m = 0$ and a weaker $\Delta m = -1$ transition). This is a good transition for taking spectra, and the multiple transitions are

convenient for determining the position of the beam in the trap from the observed spectra.

The $|^7S_3, m_J = +3\rangle \rightarrow |^7P_2\rangle$ transition offers a strong $\Delta m = -1$ transition which is ideal for optically pumping atoms out of the trap. Additionally, because all the weak-field-seeking states *except* $|^7S_3, m_J = +3\rangle$ can undergo $\Delta m = 0$ transitions (which exhibit a frequency shift opposite from the $\Delta m = -1$ transitions), this transition can cleanly resolve the presence of other m_J states in the trap.

6.2 Spectroscopic detection of chromium.

Chromium detection

We monitor the trapped chromium atoms with absorption spectroscopy. We tune the probe laser to one of the ${}^7S_3 \rightarrow {}^7P_{2,3,4}$ transitions and monitor its transmitted power. By using a a low probe beam power (on the order of 1 nW), we can continuously observe the trapped chromium atoms without significantly perturbing them.

We typically take data by continuously sweeping the frequency of the probe laser over one of chromium's Zeeman-broadened transitions. This method is advantageous because it allows a complete spectrum to be obtained in a single ablation shot. This speeds the rate of data acquisition and the spectrum obtained does not rely on shot-to-shot ablation consistency. Additionally, if the laser frequency drifts during a single observation (which is sometimes a problem for longer data sets), it can be compensated for. However, for this to give meaningful data, the rate of change of the chromium cloud must be small compared to the timescale on which the spectra are obtained. Consequently, this method lacks the time resolution of the "1-ablation-1-frequency" method used for the CaH and VO experiments.

Optics setup

To generate narrow-band blue light to probe (and occasionally optically pump) the chromium atoms, we use a external-cavity-doubled titanium-sapphire laser. To produce chromium atoms, we use a pulsed Nd:YAG laser [112]. The optics chain for both systems is shown in Figure 6.2.

The optics chain begins with a Coherent Model I-200 argon-ion laser [165] which produces 10 Watts of multiline green power. This is used to pump the titanium-

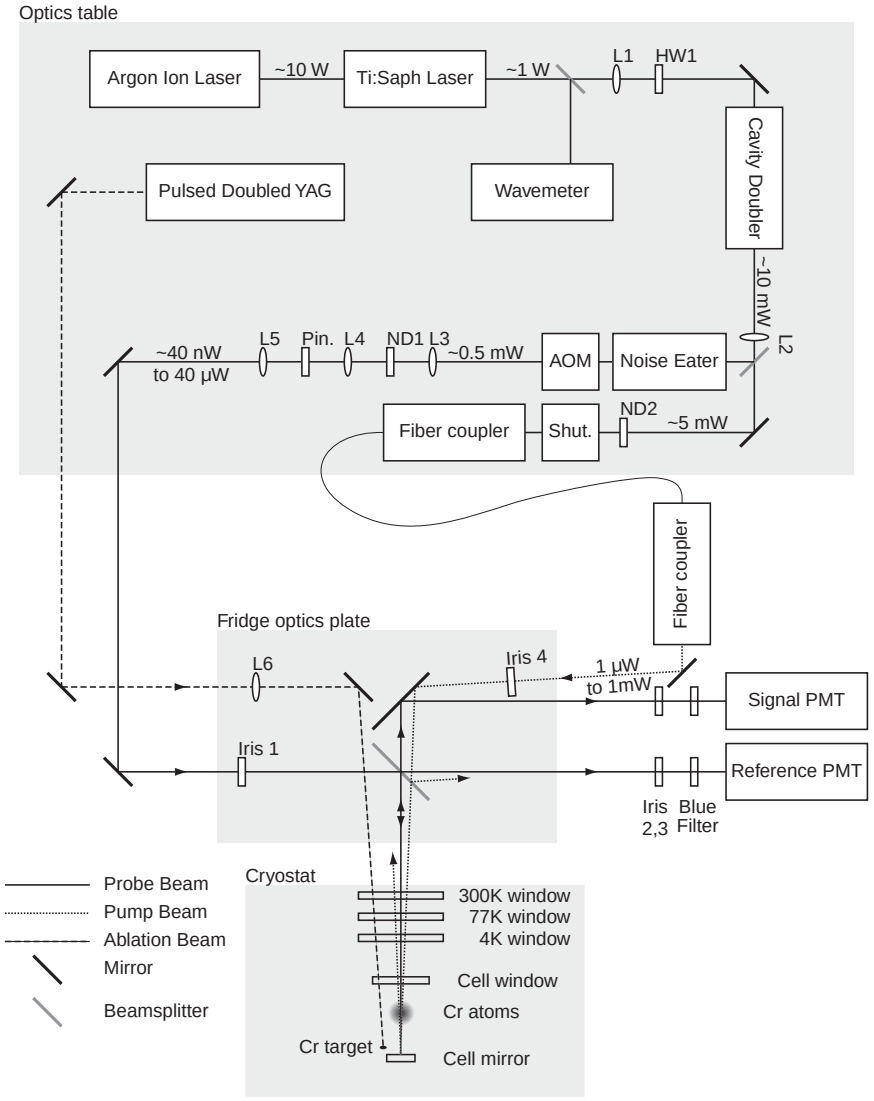

Figure 6.2: Optics setup for the chromium experiment. See Table 6.1 for an explanation of labels; see the text for a description of the setup. Various mirrors and other "passive" optical components have been omitted to simplify the drawing. Optics shown which are not part of the optics table, dewar bottom optics plate, or the cryostat itself are mounted to the floor.

sapphire lasing medium of a Coherent Model 899-21 continuous-wave ring laser [165, 166]. This laser is frequency stabilized to a built-in reference cavity, yielding a linewidth on the order of 1 MHz (measured on a 1 second timescale), and can be continuously scanned up to 30 GHz. This scan width was calibrated with the Wavemeter (see below) for large scans and the ^{53}Cr hyperfine structure for narrower scans. Un-

Symbol	Optic	Function
L1	lens	Mode match to doubler
L2	200mm lens	Reduce blue beam divergence
L3	150mm lens	
L4	50mm lens	Focus through pinhole
L5	200mm lens	Reduce beam divergence
L6	400mm lens on translation stage	Focus YAG beam onto Cr target
HW1	Half-wave plate	Match polarization to doubler
Pin.	50 μm pinhole	Clean probe beam spatial profile
Iris 1	Adjustable iris	Control probe beam diameter
Iris 2	Adjustable iris	Block PMT from scattered light
Iris 3	Adjustable iris	Block PMT from scattered light
Iris 4	Adjustable iris	Reduce pump beam diameter in cell
ND1	Adjustable neutral density filter	Adjust probe beam power
ND2	Adjustable neutral density filter	Adjust pump beam power

Table 6.1: Guide to the optics diagram.

fortunately, the laser exhibits a slow frequency drift on the order of 50 MHz per hour.

To aid in finding the correct laser frequency, the output of the ring laser is monitored with a Burleigh Wavemeter [233]. Used for all experiments in this thesis, the Wavemeter is invaluable for intially finding the transition frequency, in day-to-day operations, and for diagnosing problems.

The ring laser is tuned to half the frequency of the chromium transition, and its ($\sim$ 1 Watt) output is frequency-doubled with a LBO crystal inside a commercial resonant cavity doubler system locked to its input [234].

The output of the cavity doubler is first amplitude stabilized using a commercial polarizer system [170], reduced in power with reflective neutral-density filters [171], then spatially cleaned by focusing it through a pinhole. After this "conditioning", the beam is sent off the optics table and steered by mirrors mounted to the floor to optics mounted on the bottom of the cryostat. The probe beam is typically $\gtrsim$ 1 cm in diameter at the dewar. An iris on the bottom of the dewar controls the beam size entering the cell, typically 1–2 mm diameter, and further reduces the power in the process. The "dewar optics" then send a partial reflection of this beam to a detector as a reference, and direct the probe laser beam in (and out) of the cryogenic cell and to a separate detector. Because of fluctuations of the probe beam intensity,

it is vital that we measure a "reference" beam in addition to the probe beam. We split the reference beam from the probe at the last convenient location so that they share as much optical path history as possible. The signals from the "reference" and "signal" beams are digitized separately, and the power fluctuations seen on the reference divided out of the probe beam signal on the data acquisition computer.

The probe beam itself is typically arranged to pass through the trap center and reflect back onto itself after reflecting off the cell top mirror. Determining accurate numbers from spectra fits requires accurate knowledge of the beam position inside the cell. The case of two overlapping beams passing through the trap center is convenient for spectrum fitting, and provides good sensitivity to the density at the center of the trap. Additionally, it is the simplest probe beam arrangement to accurately set up by monitoring the spectrum inside the trap.

The probe beam passes through a large number of optics on its way to and from interrogating the atoms. To suppress etalon effects which cause intensity fluctuations when the probe frequency is scanned, we use wedged windows (2 degree wedge) with both faces mounted at askew angles ($\sim$ 1 degree from horizontal) to prevent inter- and intra- window reflection etalons. Additionally, the windows are anti-reflection coated at 425 nm [208].

In addition to the probe beam, the output of the cavity doubler is used for an "optical pumping beam", also shown in Figure 6.2. This pumping beam is not normally used during the trapping and cooling of chromium, but is sporadically used as a diagnostic tool, as described in Section 6.6. The optical pumping beam's power is controlled with an adjustable reflective neutral density filter, and it is turned on and off with a physical shutter [235]. The beam is transported from the table to the cryostat via a multimode fiber [236]. Fiber transmission is advantageous because it simplifies the optics arrangement and allows the "optics table" optics to be realigned without affecting the alignment of the beam through the trap. The pumping beam is large inside the cell, typically $\sim$ 2 cm in diameter.

Unfortunately, we are strongly limited in the amount of power we can use for the optical pumping beam. If too much power is used, or it is applied for too long a time, we see atom loss independent of the laser frequency (that is, we see loss even if the laser is far detuned from the atomic transition). We attribute this loss to local heating in the cell evaporating helium background gas. The most likely candidate for this heating is absorption by the cell top mirror; the thermal anchoring of the cell mirror

is poor. Table 6.2 tabulates how long the pump beam may be shone through the cell with only minimal ($< 10\%$) "thermal" atom loss at various pump powers. Typically, minimal loss is seen only for pump exposure energies less than 20 μJ. Focusing the beam through the cell causes even greater losses (for comparable powers and times).

Power (μW)	Exposure Time (s)
100	0.2
30	1
10	2
3	5
1	15

Table 6.2: List of maximum exposure times (as a function of beam power) that can be used for optical pumping with minimal ($< 10\%$) non-resonant atom loss.

Finally, the ablation optics are arranged in the same straightforward manner used for the production of CaH, as described in Section 3.3.

Light detection

We monitor the probe and reference beam intensities with two photomultiplier tubes (PMT's). To reduce errant signal from the room lights, bandpass interference filters [237] are placed over the photomultiplier tube faces and a black fabric "tent" covers the area around the optics near the dewar. The filters also protect the photomultiplier tubes from scattered light from the ablation pulse.

The high gain and low noise of the PMT's are important for use with our low-power probe beam. Additionally, their large active area makes alignment convenient and reduces beam pointing stability problems (from, most commonly, vibrations in the cryostat).

Photomultiplier tubes act as current sources, with an average current proportional to the intensity of the incident light. We convert this current to a voltage simply with a 10 kΩ resistor; this voltage is amplified (and bandwidth limited) with a voltage preamplifier [238] before measurement by our data acquisition system. For the conditions used in this thesis, the additional noise introduced by the electronics is negligible, as discussed in Appendix G.

To suppress any reduction of the PMT gain from ambient magnetic fields (predominantly from our trap magnet), we surround the photomultiplier tube with a

sheath of high-permeability metal [176]. Although this reduces the effect of the magnetic fields, it does not entirely eliminate them, and a change in the signal is seen as the magnet current is changed. Typical changes are a few percent, with the PMT's positioned ~ 2 m from the trap.

Additionally, data was taken by monitoring the probe beam with an intensified CCD camera. This data is not included in this thesis. Because of the inherent convolution of the spatial information with the frequency information (see Appendix A), along with the slow read-out rate of a CCD, it has been generally advantageous to simply take spectra with a narrow-profile beam monitored by a photomultiplier tube. However, at low temperatures, where the Zeeman broadening and Doppler broadening of the line become small compared to the natural linewidth, a camera will likely be the best tool to probe the atom distribution inside the trap.

Baseline

To quantitatively measure the absorption spectrum of the atoms, one must know the transmitted power with no atoms. Ideally, this transmitted power would be independent of frequency, and off-resonance measurements would suffice. Unfortunately, this is not the case, and a "baseline" measurement of the transmitted power as a function of frequency (in the absence of atoms) is taken with every trap loading cycle. Taking a baseline with every data set is not only convenient for subsequent data analysis, but prevents errors due to laser drift (in either frequency or power) between scans. Additionally, because the gain of the photomultiplier tubes is affected by the magnetic field, the baseline must be obtained at the same (or similar) magnet current as the data.

For data in which the magnet current is unchanged, the baseline is taken before the ablation laser is fired. To ensure that no chromium atoms (from an earlier trap loading cycle) remain in the trap during the baseline, the magnet is ramped to zero current between data sets.

If the magnet current is ramped down during a data set, the baseline is typically taken subsequently to the atomic data by increasing the cell temperature until the atoms are driven out of the trap.

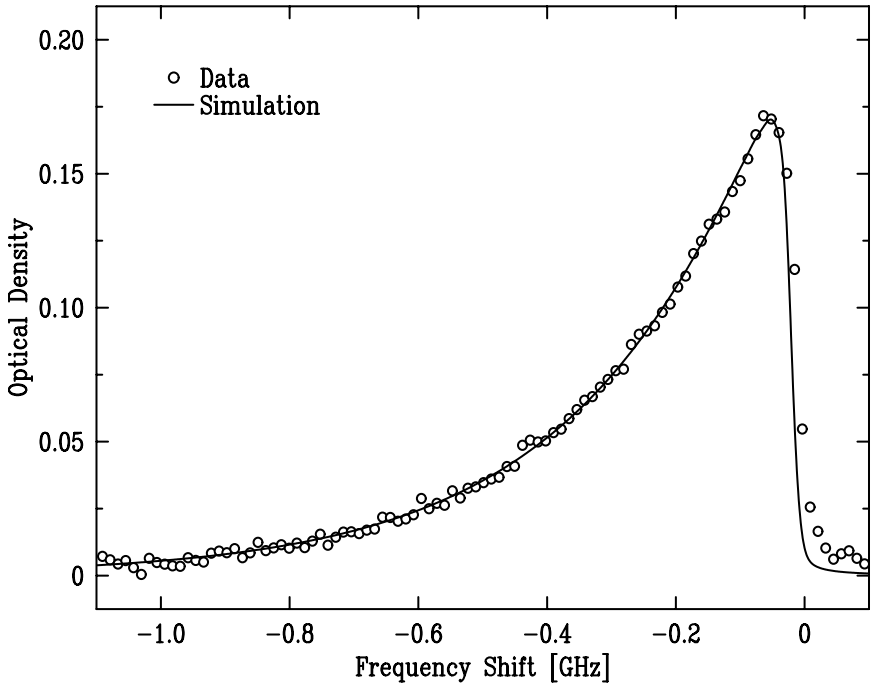

Figure 6.3: The spectrum of trapped chromium atoms, taken on the $^7P_2$ transition, in a 0.36 K deep trap. Fit to $n = 4.6 \times 10^{10}$ cm^{-3}, $T = 55$ mK ($N = 9.1 \times 10^{10}$).

Spectrum Fitting

The details of the spectrum-fitting process are described at length in Appendix A. Figure 6.3 shows a typical fit to a spectrum of trapped atoms. The only free parameters in the fit are the chromium temperature (T) and peak density (n), and the overall frequency shift of the spectrum relative to the field-free line. The other parameters that are required to simulate the spectrum (such as the beam size and position, the magnetic field distribution, and the atomic Zeeman structure) are obtained independently through measurement or calculation. The accuracy of the fit to the data gives faith in the accuracy of the model, and demonstrates that our atomic distribution inside the trap is close to a Boltzmann distribution.

6.3 Buffer-gas loading of chromium

Chromium is magnetically trapped via buffer-gas loading. The cryogenic apparatus employed is described in in Chapter 5, and the buffer-gas-loading procedure described in 2.2. The majority of the chromium data presented in this thesis was obtained using

the plastic cell under the following conditions:

^{4}He was used as the buffer gas, and a quantity of is placed into the cell such that the helium density is limited to 2×10^{16} cm^{-3}. We typically load with a magnetic trap depth of 2.3 Tesla. To bring the helium into the gas phase, the cell is heated for 1 second prior to ablation with approximately 50 mW, bringing the cell to a temperature of $\sim$ 700 mK. We then ablate a solid sample of natural isotopic abundance chromium metal [226] with a single $\sim$ 20 mJ laser pulse and turn off the cell heater.

Chromium Ablation Yield

Under these standard conditions, we buffer-gas cool $\sim 10^{13}$ chromium atoms, and trap $\sim 10^{12}$ of them. The trapped atoms are predominantly in the $m_J = +3$ state: all other m_J states (which are less strongly bound in the trap) are lost on a timescale of a few seconds. The disappearance of the less magnetic weak-field seekers is consistent with evaporation from the trap.[1] The buffer-gas loading procedure is highly efficient; of order unity of the $m_J = +3$ state atoms thermalized are trapped. It is interesting to consider the efficiency of the ablation process.

If the entire energy of the ablation pulse went solely into the creation of atoms, we would expect (from estimates of the heat of vaporization of atomic chromium) a 20 mJ laser ablation pulse to produce 10^{16}–10^{17} chromium atoms. This "100% efficient" assumption is unattainable, as not all the pulse energy will be absorbed by the chromium, and some residual energy will be left as heat in the ablation target.

What does limit the number of chromium atoms thermalized is not clear. Because we do not monitor the early time (unthermalized) behavior of the chromium, it is possible that we "miss" some of the atoms produced because they transit through the cell and stick to the walls before we observe them.

Additionally, it is possible that some chromium atoms are lost to clusters formed in the ablation plume. Indeed, laser ablation of chromium into high density helium gas (up to 6 bars He) is used as a means of deliberately producing multi-atom chromium clusters [239].[2] Similarly, experiments examining the ablation of copper atoms into

[1] After loading, the trap is "self-purifying" because the lower m_J states evaporate preferentially.

[2] As an interesting and potentially important side note, chromium clusters were created in Reference [239] in order to investigate their magnetic properties. The

high densities of room temperature helium gas observe a dramatic decrease in the density of atomic copper due to condensation of metal vapor to form fine particulate within a few milliseconds following ablation [240].

The quantity of buffer-gas used is chosen experimentally by trial and error to maximize the number of chromium atoms thermalized within the cell. It is plausible that the optimal density of buffer-gas is a compromise between the two effects of not thermalizing all the atoms (at low density) and losing atoms to the formation of clusters (at high density). However, there are additional complications to this model. With it, we would expect multiple ablation pulses to load more atoms into the trap (as long as they do not cause excessive heating). But multiple pulses typically do not provide any appreciable advantage; this is discussed in greater detail for chromium in Section 6.3.

We do not understand the physics behind our ablation yield, and it may be due to phenomena such as shock waves propagating through the cell, hydrodynamic helium flow, the plasma produced during ablation (which, to the eye, appears to extend through a significant fraction of the cell volume), other non-atomic ablation products produced, or a variety of other phenomena associated with the violent, distuptive ablation process.

Finally, it should be noted that although the number of chromium atoms produced and cooled per Joule of energy deposited in the cell is three to four orders of magnitude short of the theoretical limit, that really ain't so bad.[3]

Trap Depth

The trap depth is chosen as a compromise between loss over the trap edge and loss due to inelastic chromium–chromium collisions.

The number of atoms in the trap soon after the ablation pulse is largely independent of the trap depth. However, the rate at which they are subsequently lost depends

conclusion of that paper is that the chromium clusters formed (of sizes of 9–31 atoms per cluster) were nonmagnetic, with a mean magnetic moment per atom of $0.000 \pm 0.014\ \mu_B$.

[3]Additionally, in the case of chromium inside our current trap, the losses due to two-body inelastic collisions during buffer-gas loading (discussed in Sections 6.5 and 6.6) would significantly diminish any gains resulting from increased production

strongly on the trap depth, as shown in Figure 6.4. To suppress this exponential loss from the trap, it is advantageous to work at high trap depth.

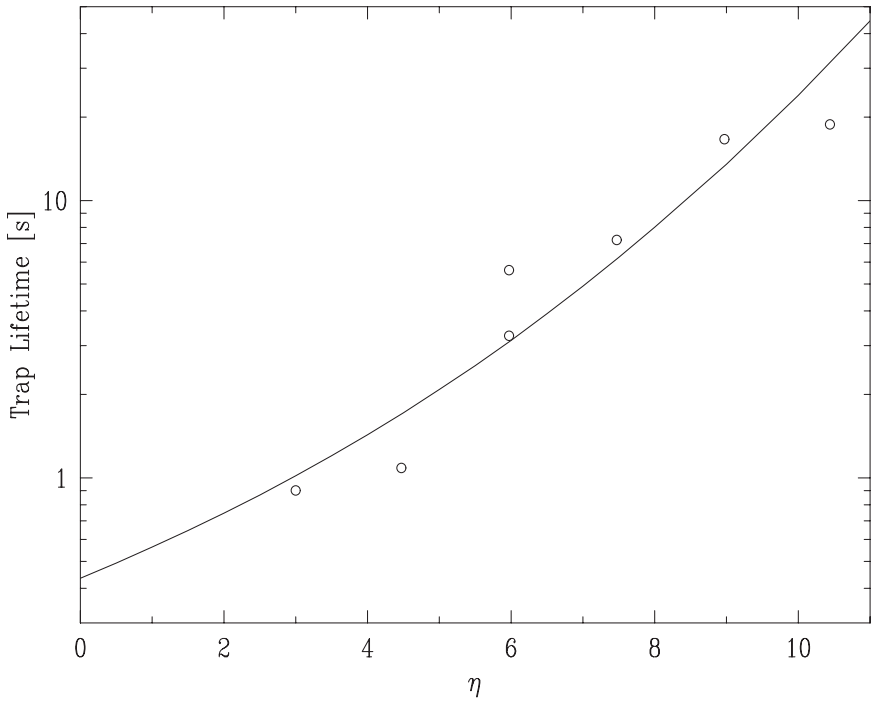

Figure 6.4: Chromium lifetime in the presence of buffer gas as a function of η. The data was taken with the cell temperature fixed at 700 mK, and a ^{3}He buffer-gas of density 2×10^{16} cm^{-3}. The lifetime τ was obtained by fitting the number of trapped atoms to $N(t) \propto e^{-t/\tau}$, which fit the data accurately. η was calculated from the cell temperature and the trap depth. The dependence of the lifetime on η was fit to the expected trap lifetime in the short-mean-free-path limit, as shown in Figure 2.5. The only free parameter in the fit was τ_0, the diffusion time at zero trap depth.

However, the two-body loss due to inelastic chromium–chromium collisions increases with the trap depth because the chromium atoms (whose temperature is fixed by the buffer gas) are confined more tightly and hence at higher density. The trap depth is chosen as a tradeoff between loss over the trap edge and inelastic decay.

As mentioned above, under standard loading conditions the cell begins cooling immediately following the ablation pulse. Additionally, we often begin ramping down the magnet immediately following the ablation pulse. The rate of ramping is also a compromise between loss due to evaporation and inelastic collisions: if done too fast, atoms will be lost due to collisions with the not-yet-removed helium gas; if done too slowly, additional atoms will be lost to inelastic collisions during the time spent

ramping the fields.

Vacuum

With the cell walls cold, we achieve good vacuum inside our cell. The vacuum quality is evidenced by long trap lifetimes, as seen in Figure 6.5. Not only do atoms remain in the trap for long times, but the functional form of the atom loss ($\dot{n} \propto n^2$; see also Figure 6.15 and Table 6.3) indicates that the dominant source of atom loss is Cr–Cr interactions, rather than a "background" process. If there is any "background" loss, we can put a limit on such loss to a timescale > 200 seconds.

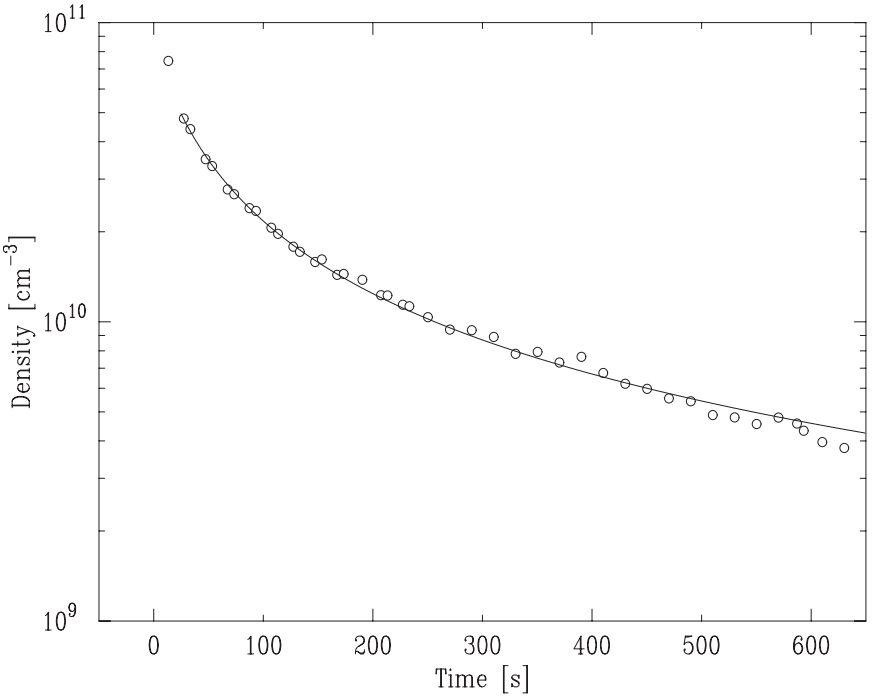

Figure 6.5: Peak trap density as a function of time in a 0.2 K deep trap, fit to the expected functional form for loss due to Cr–Cr collisions.

At elevated temperatures the cell vacuum quickly becomes poor. The trap loss as a function of temperature with ^{4}He buffer gas is shown in Figure 6.6. For this shallow trapping potential, a single collision with a helium atoms is likely to cause loss from the trap. Below 200 mK, we have good vacuum and little loss from the trap. Above 250 mK, the vacuum quickly becomes poor, and atoms are rapidly lost

from the trap.[4]

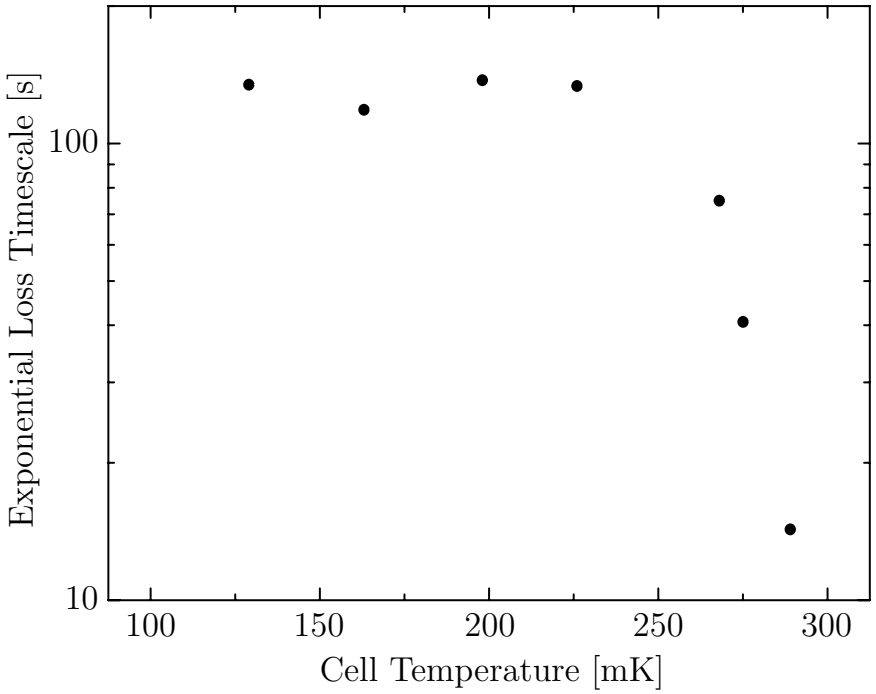

Figure 6.6: The loss rate τ of chromium in a shallow (0.2 K deep) trap as a function of the cell wall temperature, with ^{4}He buffer gas. τ is calculated by fitting the trapped chromium population to $N \propto e^{-t/\tau}$ (despite the known presence of two-body decay mechanisms).

It should be noted that the data below 200 mK in Figure 6.6 represents a lower bound on the trap lifetime: to obtain the exponential loss timescale shown, it was assumed that all observed loss was one-body. Although one-body decay fits the $T > 250$ mK data well, in the lower temperature data, two-body Cr–Cr decay was "aliased" into the measurement, and the actual loss due to the background vacuum is on a longer timescale than is shown.

We should also note that the ^{4}He buffer gas used for these measurements was isotopically pure ^{4}He. Obtained from the Harvard neutron-trapping experiment, this helium was specified to a ^{3}He:^{4}He ratio of $< 5 \times 10^{-13}$ [241, 242]. While we would not expect the ^{3}He levels occurring inside natural isotopic abundance helium to compromise our vacuum, we did not attempt to use natural helium.

[4]Of course, this loss is suppressed if the trap depth is much greater than these temperatures, as it is during trap loading.

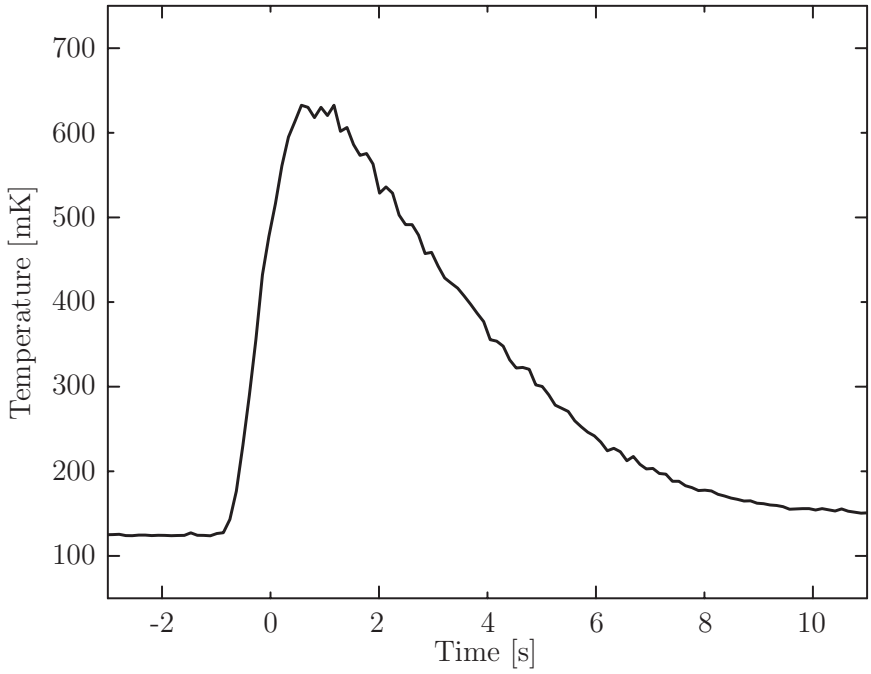

Figure 6.7: The cell temperature during our typical buffer-gas loading. It should be noted that the time response of the cell thermometry is limited to ~ 1 second, and it is possible that the buffer-gas density may lag the equilibrium value predicted by the bulk cell wall temperature.

Comparing the lifetime data of Figure 6.6 with the cell cooling rate, as shown in Figure 6.7, we would predict that we have good vacuum within 10 seconds of the ablation pulse. However, because the trap must be ramped to a shallow depth to verify that good vacuum has been achieved, we have only been able to directly measure attaining good vacuum within 20 seconds of the ablation pulse.

^{3}He Buffer Gas

Unfortunately, we were unable to attain good vacuum while using ^{3}He as a buffer gas. At cell wall temperatures as low as 130 mK (the lowest temperatures obtained with the plastic cell used), we see "shallow trap loss" on a < 10 s timescale. We attribute this loss to bad vacuum; 130 mK is not cold enough to sufficiently reduce the ^{3}He vapor pressure. The loss is consistent with expectations based on our extrapolation of the ^{3}He equilibrium vapor pressure (shown in Figure 2.3) and our measured value of the ^{3}He–Cr elastic collision cross section (discussed in Section 6.4).

A cell redesign to increase the conductivity of the thermal link may allow ^{3}He

operation. If the cell could be brought cold enough to achieve good vacuum, we would expect ^{3}He to be advantageous because it (unlike ^{4}He) is not superfluid in our temperature regime. Without superfluid film flow, we would expect the experiments to be considerably more tolerant of localized hot spots in the cell (due to, for example, the probe laser on the cell top mirror, or RF fields heating the chromium ablation targets) and its fill lines.

Isotopic loading efficiencies

One of the primary virtues of buffer-gas cooling is that, unlike laser cooling, it does not rely on level-structure specifics to cool atoms and molecules. It is straightforward (and requires no additional work on the part of the experimenter) to simultaneously cool all the isotopes of chromium. The effectiveness of this can be readily seen in Figure 6.8, a spectra of trapped chromium atoms in which multiple chromium isotopes can be resolved.

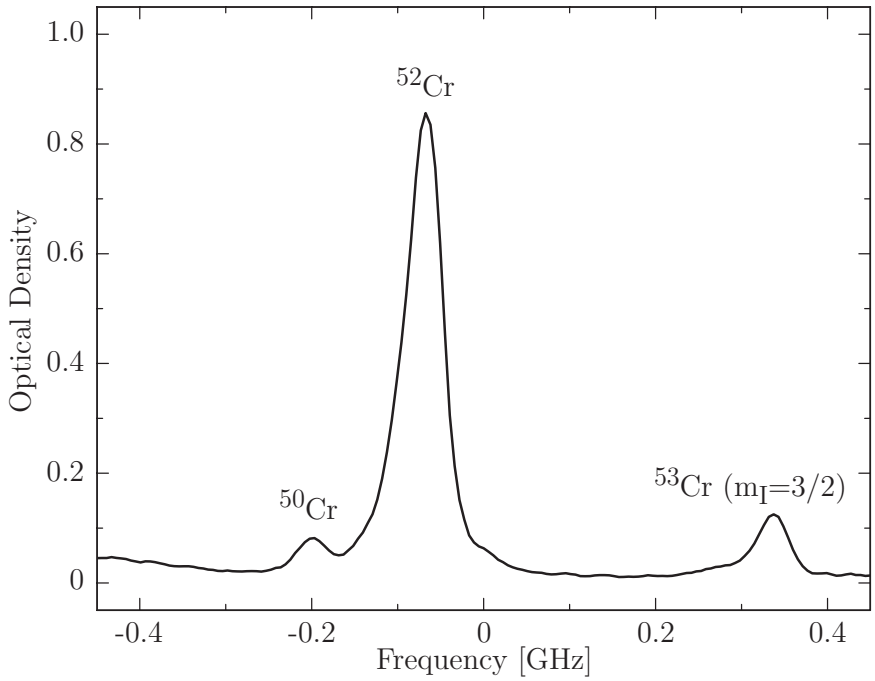

Figure 6.8: Absorption spectrum of trapped Cr on the $a^7S_3 \rightarrow z^7P_3$ transition. The $A = 50$, 52, and 53 isotopes can be clearly resolved and appear in their approximate natural abundances. The spectrum was taken with a trap depth of 0.7 K and 2×10^{11} atoms at a temperature of 100 mK. The broad spectral feature at the left edge of the spectrum is from a $\Delta m = -1$ transition.

The data in Figure 6.8 was obtained by loading the trap under standard conditions and lowering the trap depth (and consequently the atom temperature) to aid in resolving the spectroscopic lines of the various isotopes. All the isotopes can be resolved, with the exception of $A = 54$, which is not sufficiently shifted to be differentiated from the $A = 52$ atoms.

Only one ^{53}Cr hyperfine state is observed in the trap: the $|m_J = +3, m_I = +3/2\rangle$ fully polarized "stretch state". For the data shown in Figure 6.8, the trap depth should be nearly equal for all the $|m_J = +3, m_I = +3/2, +1/2, -1/2, -3/2\rangle$ states.[5] We believe that the loss of the $|m_J = +3, m_I \neq +3/2\rangle$ states is due to spin-exchange collisions. The spin-exchange coefficients are discussed Section 6.6.

Additionally, the population of the $|m_J = +3, m_I = +3/2\rangle$ hyperfine state of ^{53}Cr is larger than one would naively expect from the relative natural abundances. We would expect that ablation-produced atoms would have all their Zeeman/hyperfine states populated equally. Thus, while the population of ^{52}Cr atoms would initially be divided equally among ^{52}Cr's 7 different $|m_J\rangle$ states, the ^{53}Cr atoms would be divided equally among ^{53}Cr's 28 $|m_J, m_I\rangle$ states. Because only ^{52}Cr in its $|m_J = +3\rangle$ state and ^{53}Cr in $|m_J = +3, m_I = +3/2\rangle$ survive in the trap, we would therefore expect the ratio of ^{52}Cr to ^{53}Cr in the trap to be 4 times that given by the natural abundances. But what is seen in Figure 6.8 corresponds (approximately) to the ratio given by the natural abundances.

The probable explanation is that spin-exchange collisions not only help to depopulate the $|m_J = +3, m_I \neq +3/2\rangle$ states of ^{53}Cr, but also serve to increase the population of the $|m_J = +3, m_I = +3/2\rangle$ state. When other ^{53}Cr states collide with ^{52}Cr (or each other), they can make transitions to the $|m_J = +3, m_I = +3/2\rangle$ state via spin-exchange collisions (at the expense of the spin of their collisional partner).

Trap loading with multiple ablation pulses

One might expect that by using multiple ablation pulses, a greater number of atoms could be loaded into the trap. Typically, however, this is not the case. Not only are multiple small ablation pulses generally inferior to a single high-energy pulse, but

[5]The ^{53}Cr hyperfine structure is shown in Figure I.1. Here, we have adopted the convention of labeling the ^{53}Cr hyperfine eigenstates by their corresponding high-field quantum numbers.

often two ablation pulses result in no more atoms than would be generated by the first pulse alone. An example of this behavior is shown in Figure 6.9. This data was chosen so that the cell temperatures were comparable for both cells after the ablation.

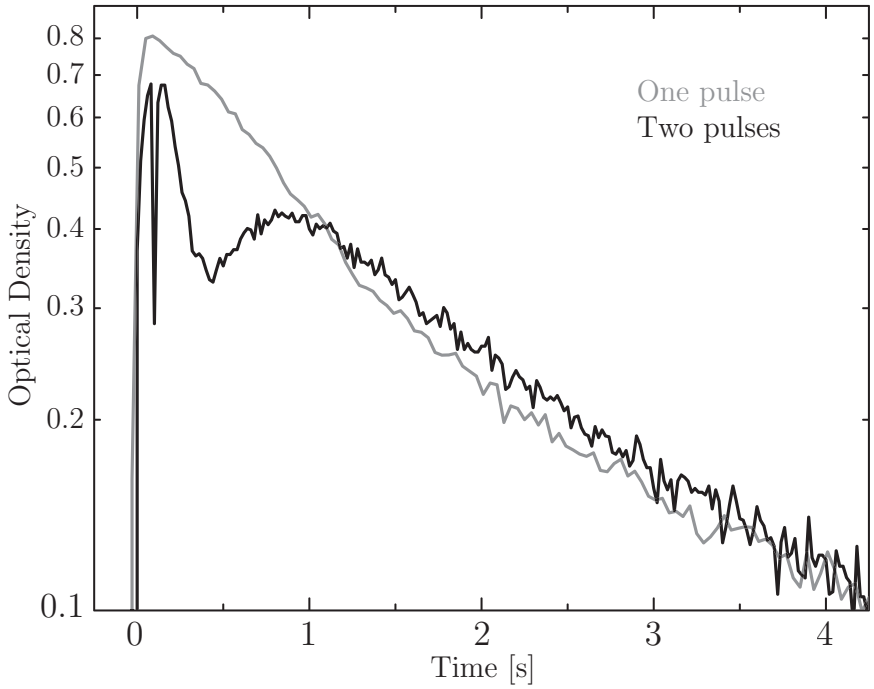

Figure 6.9: Multiple ablation pulse loading. Data is shown for single and double ablation pulses, of equal power. The sharp dip in the double-pulse data at +110 ms is an artifact due to the flash of the second ablation pulse. This data was taken with ^{3}He buffer gas in the composite metal cell.

Why multiple pulses offer no advantage is not completely understood. It may be partially due to the additional heating of the cell, which reduces η and increases trap loss. But this explanation is incomplete: with a large time separation between ablation pulses, so that the cell temperature can be well controlled, we often find no more atoms remain after the second pulse than did after the first.

Cold loading

We find it is possible to trap atoms without heating the cell prior to ablation. We ablate while the cell is cold ($\lesssim$ 200 mK) so that a negligible amount of helium is in the gas phase. However, atoms are still successfully loaded into the trap. We attribute the success of this "cold loading" to evaporation of the helium by the ablation process.

Once the helium evaporates, buffer-gas loading proceeds as usual.

The advantage of this method is that no heating of the cell other than the ablation pulse itself is required. For comparison, the cell temperature during warm and cold loading cycles are shown in Figure 6.10. The reduced quantity of heat deposited during cold loading produces colder buffer gas temperatures and faster subsequent cooling of the cell and removal of the buffer-gas. Both of these effects should be advantageous for loading at reduced trap depths.

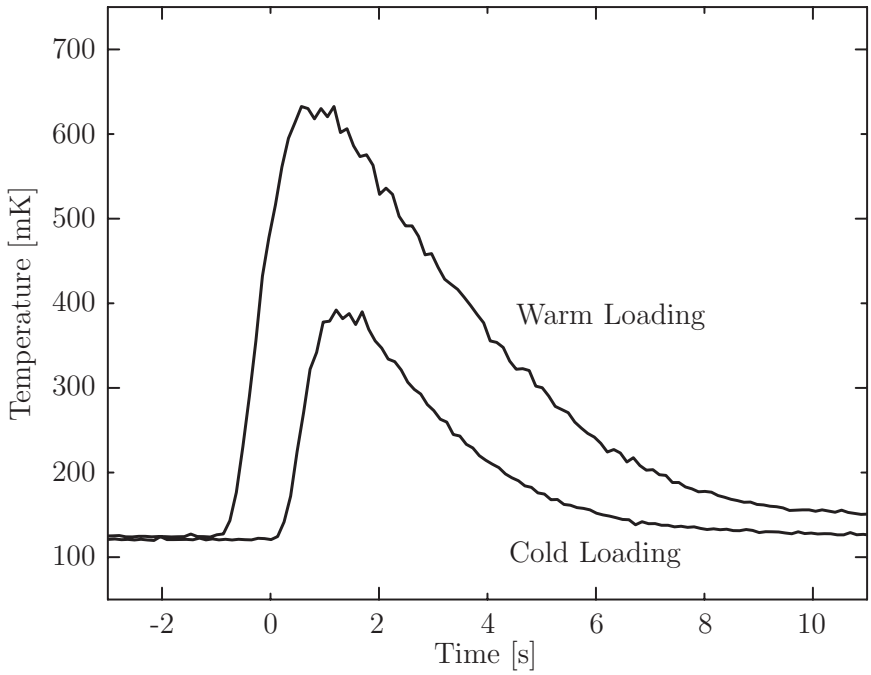

Figure 6.10: The cell temperature during warm and cold loading, with the plastic cell. The cold loading offers modest improvements in cooling rates. It should be noted that the time response of the cell thermometry is limited to ~ 1 second.

However, any advantage to be gained from the more rapid cooling is typically more than offset by an inferior initial trapping efficiency observed with cold loading. Although we did not conclusively determine the cause of the lower number trapped[6],we were unable to attain the same number of trapped atoms through cold loading that

[6]One plausible source is a reduced thermalization efficiency due to a lower buffer-gas density. Another possibility is that a reduced buffer-gas density would produce an accelerated trap loss rate if the buffer-gas was temporarily at an elevated temperature immediately following ablation (as discussed in Section 2.2).

we can achieve with our standard procedure. Because of this, we do not typically use it.

Additionally, the inferior efficiency of cold loading is observed to worsen with reduced trap depth. Loading with our "usual" 2.3 Tesla deep trap, we obtain roughly an order of magnitude fewer atoms in the trap with cold loading than with normal loading. With a 1.8 T trap depth, cold loading is inferior to warm by two orders of magnitude.

Hot loading

We were also able to buffer-gas load Cr atoms into the trap with the cell at a temperature of 1.4 K. Under such conditions, the atoms were lost from the trap with an exponential lifetime on the order of 10 s. Loading at such elevated trap temperature is pointless in our current dilution-refrigerator-based apparatus. However, this data is suggestive that future generations of buffer-gas loading experiments could be conducted at similarly elevated temperatures using a simpler refrigerator, such as a pumped–^{3}He or –^{4}He cryostat. To make such an apparatus viable, the only additional development needed is a method to pump out the buffer gas (such as a charcoal adsorbent pump [99, 103]).

Gone With the Wind

With a large density of helium buffer-gas in the cell, if the buffer gas is removed sufficiently rapidly after loading, we observe severe atom loss. An example of this loss is shown in Figure 6.11. In Figure 6.11.A, the cell is cooled gradually (thus removing the buffer-gas slowly), and a sizeable fraction of the atoms remain subsequent to the removal of the buffer-gas. In 6.11.B, the cell heaters are turned off at the ablation pulse (t=0), and the cell cools rapidly. The chromium atoms are quickly lost from the trap. We believe this loss is due to the force of the "wind" of helium atoms sweeping past the chromium as the helium is cryopumped to cold surfaces.

The attribution of the loss to the wind is supported by the changes in the loss rate as the buffer-gas density is varied. For the data shown in Figure 6.11, the amount of helium buffer gas introduced into the cell limits the density to $\leq 5 \times 10^{16}$ cm^{-3}. If we add more helium to the cell (to give a density of 1×10^{17} cm^{-3}), we find the cell must be cooled even more slowly to avoid atom loss. Correspondingly, with the

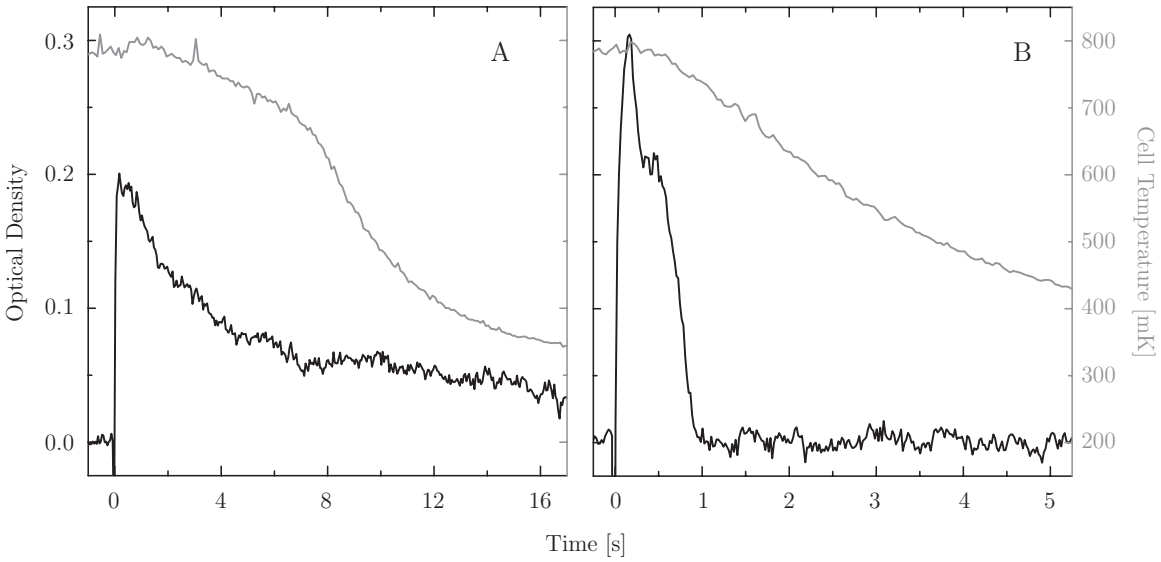

Figure 6.11: Loss of atoms due to wind. Shown is the optical density of magnetically trapped chromium atoms (shown in black) as a function of time for two different cell cooling rates (shown in gray). Please note the different horizontal scales for the two figures. Also note that the initial cooling rate is the most important: by 700 mK, the majority of the buffer-gas should be liquefied. This data was taken with ^{4}He buffer gas and the composite metal cell (described in Section 5.4). The temperature was monitored via a RuO_2 thermometer attached to the side of the cell, ~ 3" from the cell top.

"reduced" helium density of 2×10^{16} cm^3, we can cool the cell as rapidly as in Figure 6.11.B without the accompanying loss.

Crude calculations of the effects of the wind and comparison to the observed behavior are discussed in Appendix F.

6.4 Cr–He collisions

Collisions between chromium and helium are vital for buffer-gas loading. Elastic collisions are needed to cool the translational motion of the chromium atoms. However, inelastic collisions which thermalize the spin of chromium would cause the chromium atoms to decay into strong-field-seeking states and be lost from the trap. By studying the behavior of chromium in the presence of a high density of buffer-gas, we were able to make measurements of the elastic and inelastic collision rates at T $\sim$ 1 K.

Elastic collisions

We determine the Cr–He collisional cross-section by measuring the diffusion of chromium through helium in the absence of trapping fields. We produce chromium via laser ablation in buffer gas. Once the chromium is thermalized, we observe the time decay of its population as it diffuses through the helium to the walls and is lost. We fit this decay to exponential loss (as shown in Figure 6.12) and calculate the Cr–He cross-section in an identical manner to that described in Section 3.7.

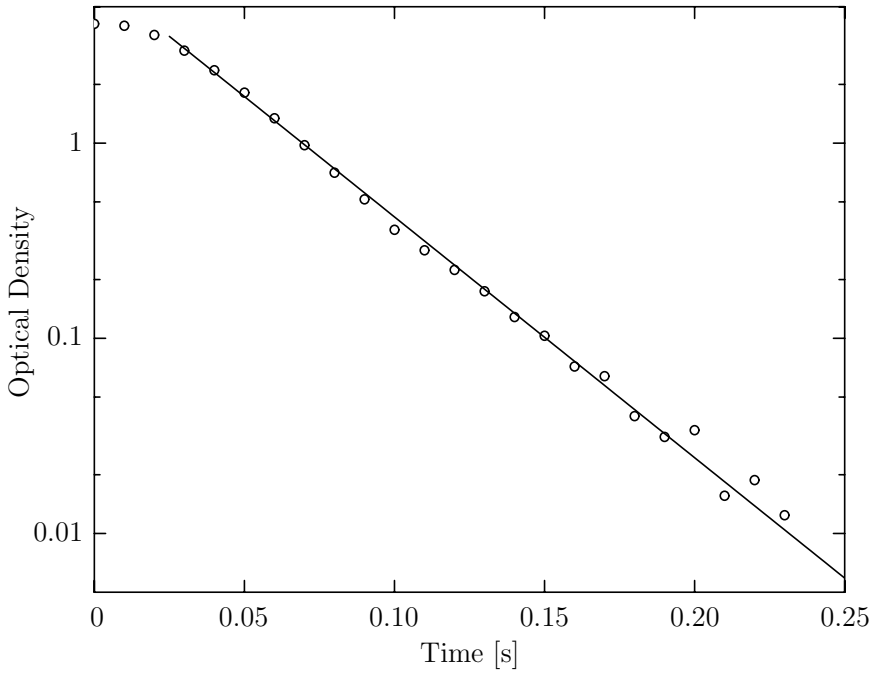

Figure 6.12: The observed peak optical density as a function of time from chromium in the cell in the presence of ^{4}He buffer gas but without trapping fields. Shown are data along with a fit to $OD \propto e^{-t/\tau}$.

With ^{4}He buffer gas, we find an Cr–^{4}He elastic collision cross-section of $\sigma_{el} = (1.2 \pm 0.5) \times 10^{-14}$ cm^2 at 4 K. Unfortunately, at lower temperatures we are only able to measure the elastic scattering cross-section to within an order of magnitude because of uncertainties in the density of helium buffer-gas in the cell. At ~ 700 mK, we find 2×10^{-15} cm^2 $\leq \sigma_{el} \leq 4 \times 10^{-14}$ cm^2.

With ^{3}He buffer gas, we find that the ^{3}Cr–He collisional cross-section at 300 mK is $\sigma_{el} = (1.1 \pm 0.4) \times 10^{-14}$ cm^2.

Inelastic collisions

To measure Cr–He inelastic collisions, we monitor the decay of chromium inside a deep trap while we maintain the cell walls at elevated temperatures. The helium gas produced will cause loss from the trap from both elastic collisions (which cause evaporative losses) and inelastic collisions (which cause transitions to untrapped states). By monitoring the loss as a function of trap depth, we can distinguish inelastic collision loss from evaporative losses. By fitting the chromium density to $\dot{n}_{\mathrm{Cr}} = -\Gamma_{in} n_{\mathrm{He}} n_{\mathrm{Cr}}$, we can obtain the inelastic collision rate coefficient.

^{4}He

With ^{4}He buffer gas, we were unable to conclusively observe any inelastic collisions, and could only place an upper limit on the inelastic collision rate coefficient of $\Gamma_{in} < 10^{-16}$ cm^3 s^{-1}. (Equivalently, the upper limit on the inelastic collision cross-section is $\sigma_{in} < 10^{-20}$ cm^2.) Our ability to measure loss due to inelastic collisions was limited by the rate of evaporation from elastic collisions.

^{3}He

Because the equilibrium density of ^{3}He is much greater than that of ^{4}He in this temperature range, we are able to perform more sensitive measurements of ^{3}He–Cr inelastic collisions. With ^{3}He buffer gas, we measure an inelastic collision rate coefficient of $\Gamma_{in} = (2 \pm 1)10^{-18}$ cm^3 s^{-1} at 700 mK.

We can identify the inelastic collision loss from the data shown in Figure 6.13. At low trap depths, the loss of chromium atoms is dominated by evaporation over the trap edge. However, this trap loss is suppressed at high trap depths where the loss is dominated by inelastic Cr–^{3}He collisions, which we expect to be independent of the trap depth.[7]

As discussed in Section 2.5, the dominant spin-relaxation process for collisions between a spin-polarized atom and unpolarized ^{3}He is expected to be spin-exchange between the atom's electronic spin and the ^{3}He nuclear spin. Our observed Cr–^{3}He inelastic rate is consistent with previously measured rates for spin exchange with

[7]The fields encountered by the atoms are (for high η) largely independent of the magnet current, and simply given by the atom temperature.

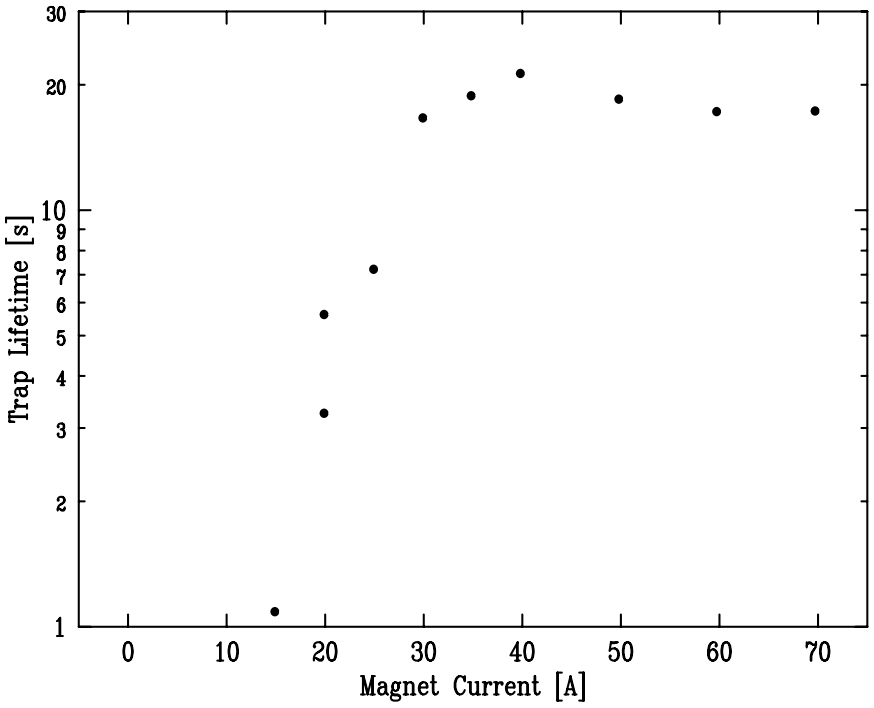

Figure 6.13: Evidence of inelastic Cr–^{3}He collisions, as discussed in the text. The data was taken with the cell temperature fixed at 700 mK and a ^{3}He density of 2×10^{16} cm^{-3}. The trap lifetime τ is measured by fitting the number of trapped atoms to $N \propto e^{-t/\tau}$. All the data shown in this plot fits well to this functional form.

^{3}He. Although the Cr–^{3}He spin-exchange rate is roughly an order of magnitude larger than the measured Rb–^{3}He rate discussed in Section 2.5, one would naively expect the chromium rate to be larger due to its larger spin.

6.5 Evaporative cooling of chromium

The results of buffer-gas loading put us in an ideal situation to begin evaporative cooling. We trap a large number of ^{52}Cr and ^{53}Cr at high density, the chromium atoms are in a region of good vacuum, and background losses are low (the dominant source of loss in the trap is due to Cr–Cr collisions).

Evaporation Method

We control the evaporation of the chromium atoms through the trap potential. By lowering the magnet current, we reduce the magnetic fields and hence the energy

threshold for a particle to escape (to the walls, where it is presumed to stick). Because the field gradient is simultaneously reduced, we also lose spatial confinement of our atoms as we lower the trap depth. Although this loss of confinement leads to a reduction in density, it also cools the atoms. For our linear trap potential, both the trap depth and the field gradient scale linearly as I, the magnet current. Adiabatic expansion (in the absence of evaporative cooling) in this potential will cause the temperature to scale as $T \propto I^{2/3}$ and the density to scale as $n \propto I^{-1}$. The mechanics behind adiabatic expansion are discussed in greater detail in Appendix B.

Evaporative Cooling Results

The evolution of the trapped chromium as we lower the trap depth and evaporatively cool is shown in Figure 6.14.

As can be seen from the plot of total atom number, significant atom loss is seen during the ~ 10 seconds required to remove the buffer-gas from the cell. This loss is due predominantly to inelastic Cr–Cr collisions. As the trap depth is lowered, the number of atoms continues to decrease through both evaporation and inelastic collisions.

As the trap depth is lowered, the temperature is reduced through both evaporation and adiabatic expansion. Although most implementations of evaporative cooling increase the density of the atoms as they cool, ours does not. This is primarily due to the reduction in the trap gradient as the magnetic fields are lowered.

The most illustrative information can be found in the phase-space density data. First, we should note that the phase space density starts at conditions far from quantum degeneracy (and considerably lower than the $\sim 10^{-6}$ phase-space densities commonly obtained from a MOT). However, we would hope that through evaporative cooling, we could use our large initial number to compensate for this.

The increase in phase space density as we begin to lower the trap depth is a clear signal that we are evaporatively cooling the atoms: the reduction in temperature is not due to adiabatic expansion alone. Additionally, because we see an increase in phase-space density at temperatures below that of the trap walls, we are certain that the effect is not due to cooling from the background helium gas.

Unfortunately, we see only modest gains in the phase-space density as we begin to evaporatively cool, and at the lowest temperatures measured, we actually see a *loss*

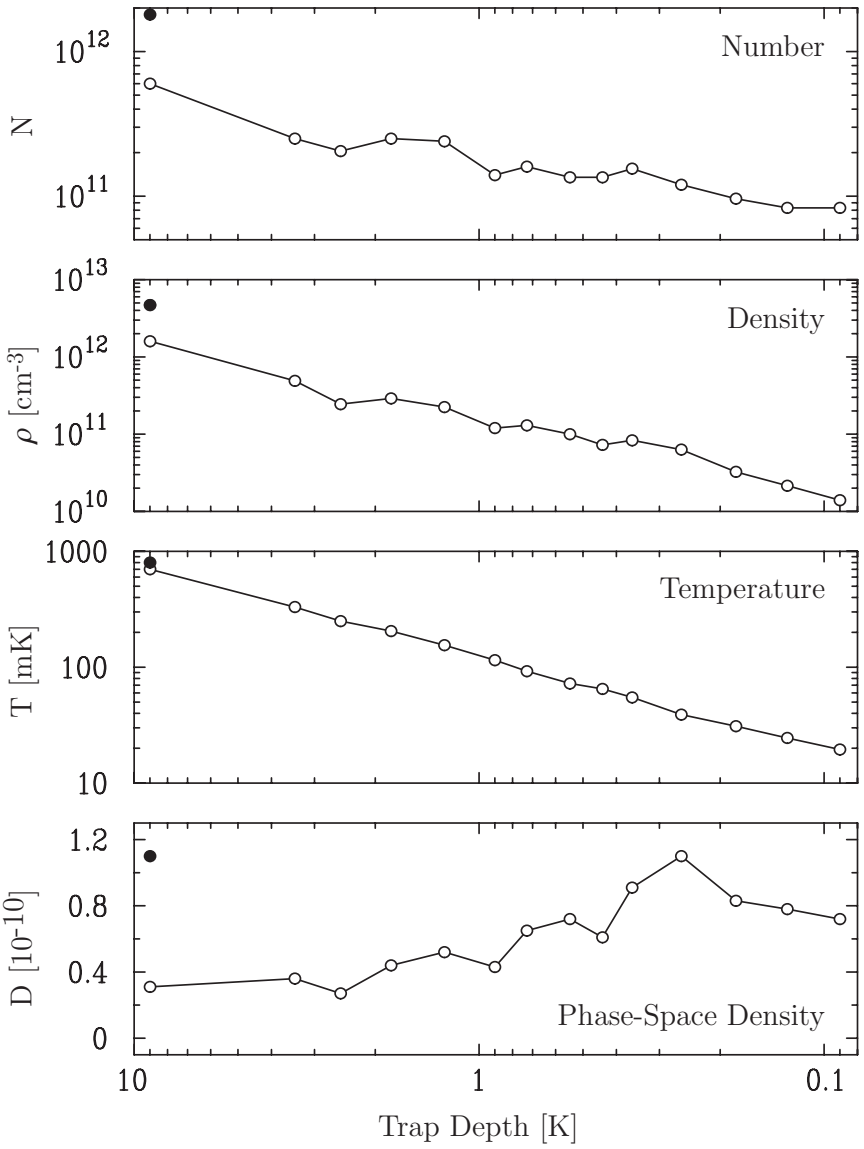

Figure 6.14: Progress of various chromium parameters as the trap depth is lowered from the initial loading depth of $\sim$ 10 K. The black dots indicate trap parameters immediately following thermalization of the chromium atoms in the trap; the open circles represent conditions after the buffer-gas has been removed.

of phase-space density as we continue to reduce the trap depth. This breakdown of evaporative cooling is not due to "technical" problems. There is no indication of any significant loss or heating due to external background processes. The poor performance is not because of the rate at which the fields are reduced: at low temperatures, the parameters obtained are largely independent of the field ramping rate, until the

ramping rate becomes so slow that there is significant loss due to inelastic collisions. The reason why evaporative cooling isn't working well lies in the Cr–Cr collisional cross-sections.

6.6 Cr–Cr Collisions

Inelastic Collisions

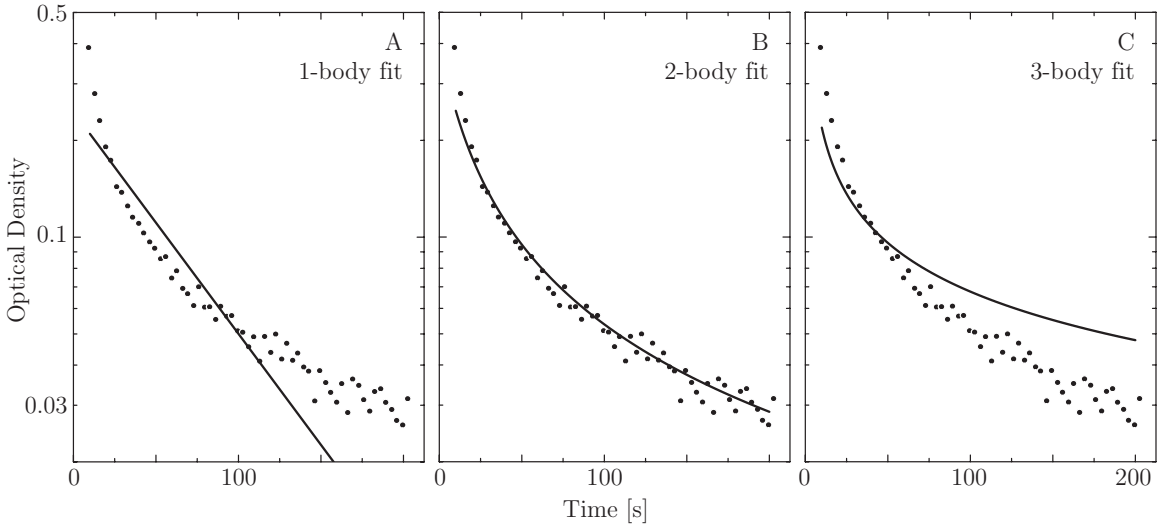

Figure 6.15: Chromium trap loss fit to the expected functional forms for purely A: 1-body loss, B: 2-body loss, and C: 3-body loss. Data taken with a 50 A trap, and fit at times after the cell has cooled following ablation. The χ^2 for the fits are A: 44.8, B: 3.4, and C: 60.8.

Measuring the inelastic collision rate is straightforward, as Cr–Cr collisions are the dominant source of loss in our trap. This can be seen in Figure 6.15. Plotted are fits of the chromium signal to the expected functional forms for one, two, and three-body loss, as listed in Table 6.3. As seen in Figure 6.15 , our data exhibits much better agreement with 2-body loss than with other forms. Because in this data the chromium density is directly proportional to the optical density, we conclude that the source of the loss must be Cr–Cr collisions.

Determining Γ_2 from the data is slightly complicated by the inhomogeneous density distribution in the trap. The total atom loss rate is given by $\dot{N} = -\int d^3r\ \Gamma_2 \cdot n^2$, where the total number $N = \int d^3r\ n$. If the distribution of trapped atoms remains

Loss	Loss Equation	Expected Functional Form of the Density
1-body	$\dot{n} = -\Gamma_1 \cdot n$	$n(t) = n_0 \cdot e^{-\Gamma_1 t}$
2-body	$\dot{n} = -\Gamma_2 \cdot n^2$	$n(t) = n_0 \cdot (1 + t \cdot \Gamma_2 \cdot n_0)^{-1}$
3-body	$\dot{n} = -\Gamma_3 \cdot n^3$	$n(t) = n_0 \cdot (1 + t \cdot (n_0^2/2\Gamma_3)^2)^{-1/2}$

Table 6.3: The expected functional forms of one, two, and three-body loss in a magnetic trap.

the same during loss, we have $\dot{n} = n \cdot \frac{\dot{N}}{N}$.

If we model our atoms as an untruncated Boltzmann distribution with a peak density n_p trapped inside an infinite linear potential, we find $\dot{n}_p = \frac{1}{8}\Gamma_2 n_p^2$. If we fit the peak density to two body loss, the "correction factor" to determine the true Γ_2 is 8. This model should provide accurate results at high η (where we expect the distribution to be modeled well by an untruncated Boltzmann). To better fit our data at small η, we model the distribution as a Boltzmann distribution truncated in potential energy at $U = \eta T$.[8] With this assumption and the above equations for N and $\dot{N}$, we find a correction factor of

$$\frac{8 - e^{-\eta}(4\eta^2 + 8\eta + 8)}{1 - e^{-2\eta}(2\eta^2 - 2\eta - 1)}$$

To obtain Γ_2 in the trap, we fit the spectrum to obtain η and to convert the observed OD into the peak trap density n_p. We then fit $n_p(t)$ to the expected form for 2-body loss and apply the correction factor.

To extract the inelastic collision rate coefficient from the two-body loss, we simply assume all atom loss is due to inelastic collisions, and take Γ_{in} equal to the Γ_2 obtained from the data. The justification for this assumption is not obvious: two-body inelastic collisions cause not only direct trap loss, but also trap heating, as discussed in Chapter 2. It is conceivable that the heating from a single inelastic collision could result in the subsequent evaporation of multiple atoms. To check this possibility, we calculated an upper limit on the rate of particle evaporation using measurements of the elastic cross-section and the temperature in the trap.[9] From this, we concluded that the

[8]This model of the distribution overestimates the available phase space near the trap edge, as it includes atoms with velocities which would allow them to escape the trap.

[9]From the partition function, we can place an upper limit on the fraction f of

dominant loss mechanism in the trap was direct loss due to inelastic collisions, rather than atoms lost to evaporation.[10] Thus, taking $\Gamma_{in} = \Gamma_2$ is justified.

The majority of our data was taken with all the isotopes present in the trap, but while monitoring the density of ^{52}Cr alone. As a check to verify that our observed inelastic collision rates are not due to the influence of the other isotopes, we occasionally optically pumped the ^{53}Cr out of the trap and observed the subsequent decay of the ^{52}Cr. Such "checks" produced equivalent results.

Elastic Collisions

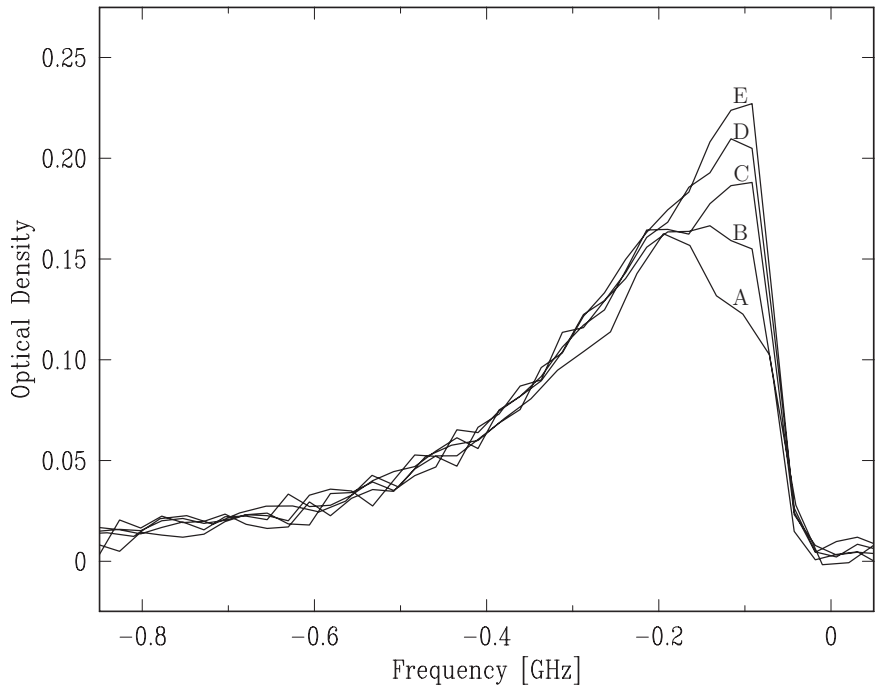

Figure 6.16: Spectra taken after optically pumping atoms out of the trap, showing a return of the distribution to thermal equilibrium. The successive spectra A–E were taken at 1 s intervals following the optical pumping (the pumping beam was tuned to -0.12 GHz).

elastic collisions events which result in evaporation of $f < \frac{\int_R^\infty 4\pi r^2 e^{-\eta r/R} dr}{\int_0^\infty 4\pi r^2 e^{-\eta r/R} dr}$. Due to the truncated energy distribution of particles in the trap, the actual evaporation rate will be slower [243, 244].

[10] A more detailed model of the trap dynamics confirms this result even under those conditions where we were unable to directly measure the temperature [245].

We measure the elastic collisional cross section by optically pumping atoms selectively out of one part of the thermal distribution and observing the re-equilibration of the atoms, as shown in Figure 6.16. Experimentally, the optical pumping is accomplished by briefly opening the shutter to allow the fiber-coupled pumping beam into the cryogenic cell (as shown in figure 6.2) while holding the laser frequency fixed. The laser frequency is selected to drive $\Delta m = -1$ transitions on the ${}^7S_3 \rightarrow {}^7P_2$ transition for efficient pumping of chromium into less-trapped and untrapped states. Typical optical pumping beam parameters are powers of ~ 30 μW and exposure times from 10 ms to 1 s. These exposure times are sufficiently small that background-induced losses are minor.

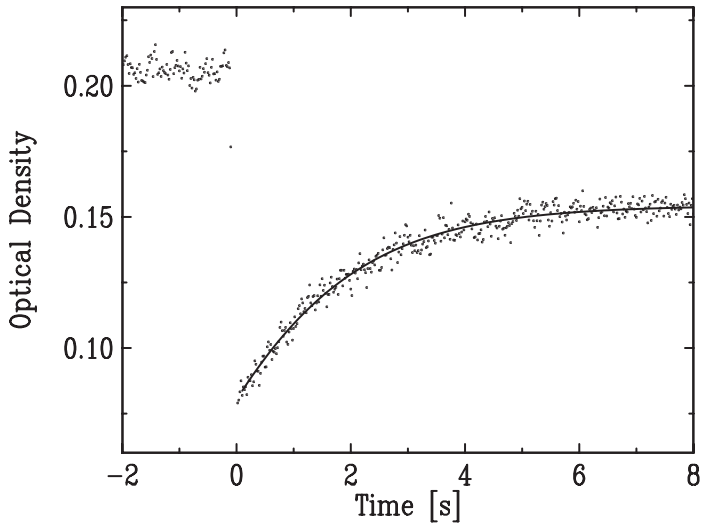

Figure 6.17: Optical pumping data, as used to determine the elastic collision cross-section. Shown is the optical density at the pumping frequency as a function of time, fit to the expected functional form.

The elastic collisional cross sections are calculated from the atom equilibration rate and a simple model of the equilibration process, described in Appendix E. A fit of optical pumping data to the functional form predicted by this model is shown in Figure 6.17. Γ_{el} is extracted from this fit.

Results

The ^{52}Cr–^{52}Cr elastic and inelastic collision rate coefficients are shown in Figure 6.18. The ratio of these collision rates is poor for evaporative cooling.

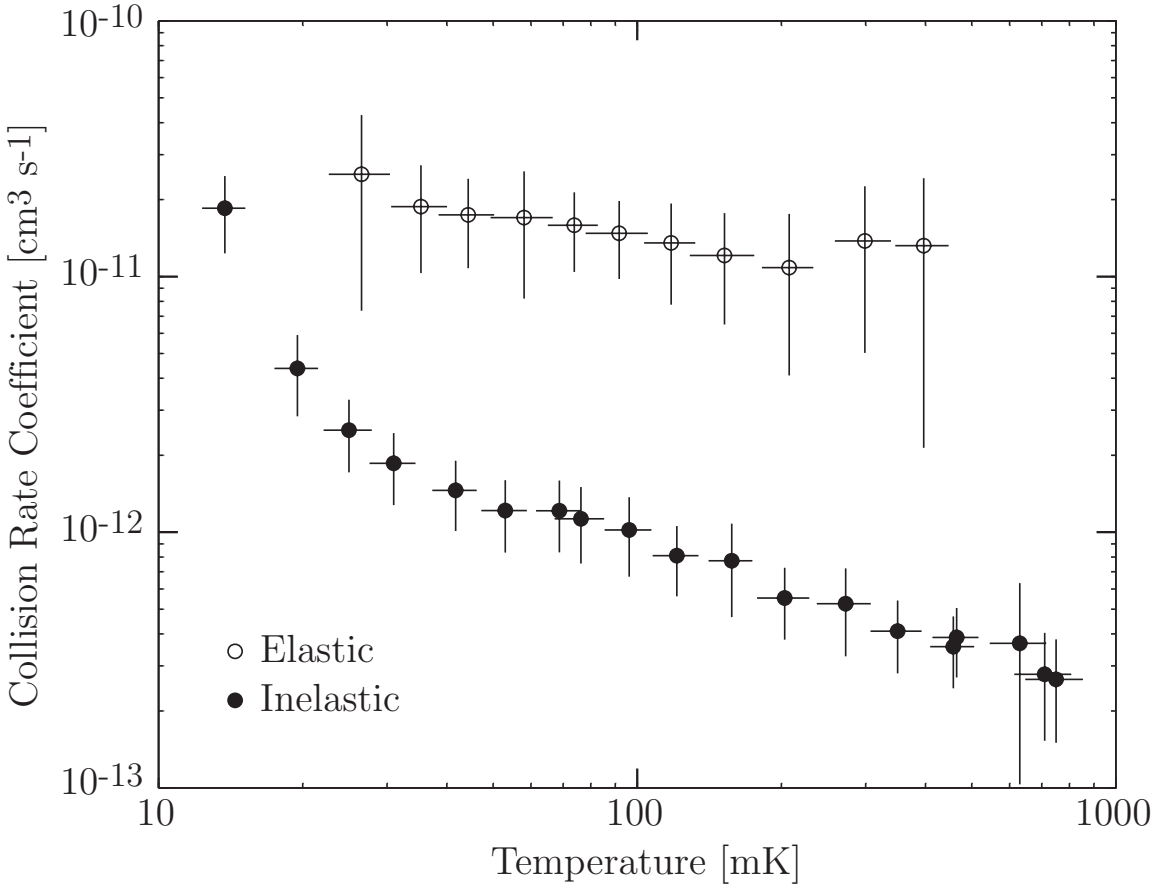

Figure 6.18: The collisional rate coefficients for elastic and inelastic Cr–Cr collisions as a function of temperature.

The elastic collision cross-section varies from approximately 10^{-14} to 10^{-13} cm^2 over this temperature range. While this is smaller than the typical alkali atom ultracold collisional cross-sections ($\sim 10^{-12}$ cm^2, see Section 2.5) , it is considerably larger than that of atomic hydrogen (1×10^{-15} cm^2 [121]). When comparing this cross-section to other atoms, is important to remember that our chromium collision measurements are not in the ultracold scattering limit. Our scattering measurements thermally average over a wide range of collision energies and phase shifts.

The inelastic collision rate is remarkably large: typical dipolar inelastic collision rates for ultracold, double-polarized low-field-seeking alkali atoms are $\leq 10^{-14}$ cm^3 s^{-1} (see Section 2.5). Additionally, chromium's large inelastic collision rate is observed to appreciably increase as the temperature is reduced.

When considering the data of Figure 6.18, it is important to note that as the

temperature of the atoms decreases, both the average collision energy and the average ambient magnetic field are reduced. Because we could not independently vary either of these parameters, we cannot conclusively determine whether the observed change in the collisional properties as a function of temperature is due to the change in the collision energies, the change in the magnetic field, or a combination of the two.

Equilibrium η

As an independent method of determining the ratio of elastic collisions to inelastic collisions, we measure the equilibrium temperature of the atom cloud inside the trap as a function of trap depth. Because elastic and inelastic collisions provide competing cooling and heating mechanisms, their ratio determines the equilibrium temperature of the atom cloud. The equilibrium η is measured over a wide range of temperatures from the same data used for the inelastic collision rate measurements; this data is shown in Figure 6.19. By combining the experimental measurements with a model of the trap dynamics (assuming that the only heating from inelastic collisions is the preferential removal of atoms at higher densities) we can extract the collision ratio [244, 245]. We find that the observed equilibrium temperatures are consistent with the measured ratios of the collision rates (to within the stated error bars).

Consequences of the collisional properties

As discussed in Section 2.4, the efficiency of evaporative cooling depends only on the ratio of Γ_{el} to Γ_{in} (assuming no other sources of loss). Below a certain minimum ratio of elastic to inelastic collision rates, it is impossible to increase the phase-space density of the trapped atoms with evaporative cooling. Simple calculations using the evaporative cooling model of Reference [84], suggest that this critical ratio is somewhere in the range of 10 to 100. While these calculations are of limited accuracy because of the model's assumption of large η, this general guideline is consistent with our observations. At our highest measured temperatures, the ratio of elastic to inelastic collisions is approximately 10^2. At lower temperatures, this ratio decreases, and we are unable to increase the phase-space density through evaporative cooling.

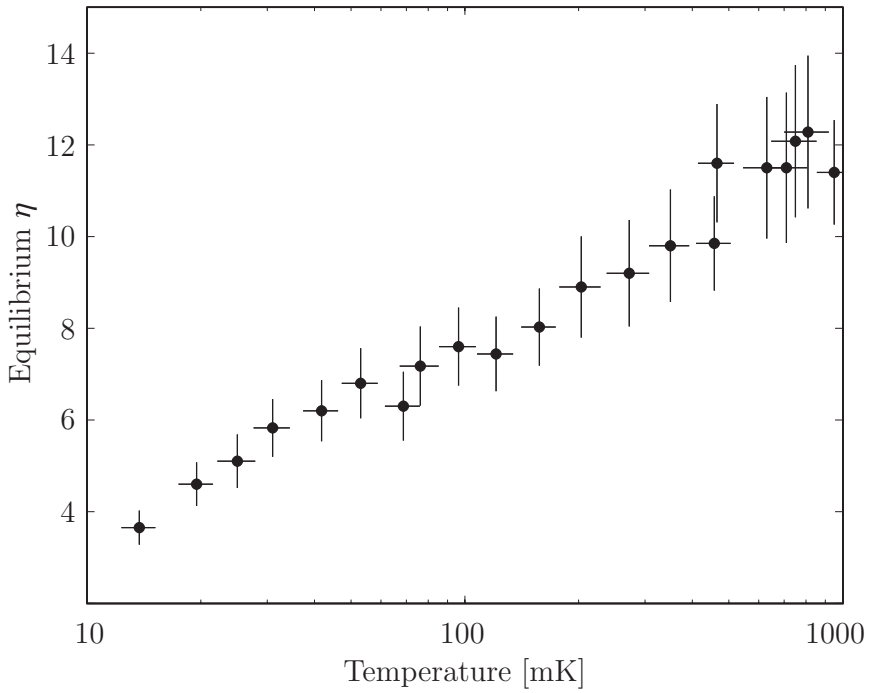

Figure 6.19: Chromium equilibrium η as a function of temperature. The dramatic decrease in equilibrium η as the temperature is lowered reflects the decrease in the ratio of elastic to inelastic Cr–Cr collision rates.

^{53}Cr spin-exchange collisions

^{53}Cr spin-exchange collisions are not crucial for either evaporative cooling or reaching quantum degeneracy: by working with a fully polarized sample of atoms, spin-exchange collisions are eliminated. In our spectra of chromium at low temperatures we observe ^{53}Cr only in its fully polarized $|m_J = +3, m_I = +3/2\rangle$ state, and ^{52}Cr only in its $|m_J = +3\rangle$ state. Neither of these states can undergo spin-exchange collisions, with themselves or each other.

The "purification" of ^{53}Cr into its stretch state is assumed to be due to spin-exchange collisions which cause trap loss for all other weak-field-seeking hyperfine states. Unfortunately, these other states of ^{53}Cr cannot be spectroscopically resolved while the sample is still warm, and they are lost from the trap by the time we cool to a temperature where they can be resolved. This prevents us from measuring the rate coefficient for spin-exchange collisions. However, we are able to put a lower limit on what the rate must be.

We would expect both ^{53}Cr–^{53}Cr and ^{53}Cr–^{52}Cr collisions to cause spin-exchange

loss of the $|m_J = +3, m_I \neq +3/2\rangle$ state of ^{53}Cr.[11] Because of the higher density of ^{52}Cr in the trap, we would expect that ^{53}Cr–^{52}Cr would dominate this spin-exchange loss. If we assume all loss is due to ^{53}Cr–^{52}Cr spin exchange collisions, we find a lower bound of $\Gamma_{ex} > 3 \times 10^{-13}$ cm^3 s^{-1}. This is consistent with our expectations for spin-exchange rates, as discussed in Section 2.5.

6.7 Possible physical mechanisms behind Cr–Cr collisions

While we cannot offer conclusive identification of the origins of chromium's large and increasing inelastic collision rate,[12] we offer speculation concerning its behavior [246].

Shape resonances

The sharp increase in the inelastic collision rate observed as the atoms are cooled from $\sim$ 1 K to $\sim$ 10 mK could be due to the presence of a shape resonance in a higher-order partial wave. This is precisely the temperature regime where we would expect shape resonances to play a large role. The temperature is sufficiently high that multiple partial waves contribute to atom scattering, and we would expect the thermal distribution to be on resonance with various quasibound states. But the temperature is also sufficiently low that an appreciable fraction of the thermal distribution can be on resonance with such a state. As we cool the distribution, the inelastic collision rate is likely enhanced as a large fraction of the thermal distribution of atoms come into resonance with a quasibound state.[13] It is also possible that the changes in magnetic

[11] The helium buffer-gas could conceivably cause ^{53}Cr–He spin-exchange collisions in which angular momentum was transferred from ^{53}Cr's electron spin to its nuclear spin. The expected rate for such processes is unknown. If the disappearance of the ^{53}Cr $|m_J = +3, m_I \neq +3/2\rangle$ states is due to collisions with helium, the inelastic collision rate coefficient for this process must be larger than 10^{-17} cm^3 s^{-1}.

[12] Indeed, with the Cr–Cr molecular potential presently known only very roughly, it is dubious whether rigorous calculations could be performed.

[13] As a caveat, preliminary calculations concerning sodium–sodium atomic scattering (with simplified inelastic collision calculations which neglect hyperfine structure and include loss contributions only from the spin-spin dipole interaction) showed

field over this temperature rage contribute to the changes in the inelastic scattering rate.

Physical process

We believe shape resonances contribute to the *increase* in the inelastic collision rate, but they are not sufficient to explain why the *initial*, high temperature rate is so high. We discuss the underlying physical mechanism.

Because the trapped ^{52}Cr is fully polarized, loss cannot be due to spin-exchange collisions. Because the loss rate is proportional to the second power of the chromium density, the loss cannot be due to three-body collisions, chemical reactions, or collsions with another species. From this, we conclude that the loss must be due to dipolar relaxation.

The spin-spin dipolar interaction

As discussed in Section 2.5, the spin-spin dipolar interaction is the "standard" mechanism for dipolar relaxation, and produces typical inelastic rates in the range of 10^{-14} cm^3 s^{-1} to 10^{-16} cm^3 s^{-1} for 1 μ_B magnetic moment atoms. The 6 μ_B magnetic moment of chromium is significantly larger, and this plays an important role in chromium's inelastic decay.

If we examine the spin-spin interaction Hamiltonian, given by Equation 2.3, we see that the strength of the interaction (for two identical atoms) scales as the second power of the atomic dipole moment. From Fermi's golden rule [85], the inelastic collision rate of this perturbing Hamiltonian therefore scales as the *fourth* power of the magnetic moment.[14] Semiclassical calculations of the scattering rate (as described in Reference [131]) give the same result. Thus, with no other knowledge of the scattering properties of ^{52}Cr, we would expect its dipolar relaxation rate to be roughly $6^4 = 1296$ times

only modest increases in the elastic collision rate (by a factor of ~ 5) due to shape resonances in this energy range. Reductions in the ambient field were predicted to increase the inelastic rate by a comparable amount. These calculations call into question whether shape resonances alone would be sufficient to explain the factor of 100 increase seen in the Cr–Cr inelastic collision rate [247].

[14] Of course, for any real atom, many additional parameters play an important role in determining spin-spin dipolar inelastic collision rate [130].

larger than the rates observed for the weak-field-seeking states of atomic hydrogen and the alkali atoms. This is consistent with the observed Cr–Cr inelastic scattering rate.

Second order spin-orbit coupling

As discussed in Section 2.5, spin-orbit coupling can also make significant contributions to dipolar relaxation. While this coupling is generally expected to be small for light atoms such as ^{52}Cr, it is possible that the strange molecular potential of $^{13}\Sigma$ Cr_2 exhibits significant second-order spin-orbit coupling. Additionally, because of the sensitive dependence of the spin-orbit interaction on the internuclear distance, we would expect a significant increase in the loss rate at a shape resonance, consistent with the observed behavior. Unfortunately, without detailed, quantitative knowledge of Cr–Cr interatomic interactions, it is difficult to judge the likelihood that spin-orbit coupling plays an important role in chromium's large loss rates.

6.8 Future prospects

Chromium

Using buffer-gas loading, we have simultaneously magnetically trapped 10^{12} ^{52}Cr atoms and 10^{11} ^{53}Cr atoms at a temperature of ~ 700 mK and a density of 10^{12} cm^{-3}. We have demonstrated evaporative cooling with these trapped atoms.

Our current efforts to evaporatively cool have been stymied by the poor collisional cross-sections of chromium over the temperature range of 10 mK to 100 mK. However, the inelastic rate may be enhanced by shape resonances at elevated collision energies, and the ratio of the elastic and inelastic cross-sections may improve in the ultracold limit.[15] If that is the case, then chromium would remain a promising candidate for achieving Bose and Fermi degeneracy.

To achieve this, however, we would need to reach the ultracold regime[16] with high

[15]Unfortunately, we have no means of extrapolating the cold scattering cross-sections to determine their behavior in the ultracold limit

[16]Very crudely, we estimate the ultracold threshold is $T \lesssim 100$ μK for atomic chromium. However, if the large inelastic collision rate is due to a higher-order partial

density (to provide the elastic collisions necessary to continue evaporative cooling), and hopefully large number (so that we can create large degenerate Fermi gases). Our current experimental route is unable to achieve these goals. As we cool below 10 mK, the cloud density becomes so low that the elastic collision rate becomes too slow ($\lesssim 0.1$ Hz per atom at the peak trap density) to practically evaporatively cool.

The chromium density obtained at these low temperatures cannot be improved simply by changing the manner in which we implement our evaporative cooling. In this temperature range, the chromium elastic-to-inelastic collision ratio is too small to increase the phase-space density through evaporative cooling. Consequently, any form of evaporative cooling will (at a given temperature) produce equal or inferior densities than adiabatic expansion.

One promising experimental route is to laser cool chromium inside the magnetic trap [248]. By laser cooling the Doppler motion of the atoms along one axis, elastic collisions will provide cooling of our atoms in all three dimensions. It is straightforward to laser cool ground state atomic chromium on its ${}^7S_3 \rightarrow {}^7P_4$ transition [249, 250]. While its cycling properties may not be as favorable as the alkali atoms [251, 252], it should be possible to efficiently laser cool chromium with only modest losses. Through a combination of laser cooling and adiabatic expansion, it should be possible to cool the atoms, increase their phase space density, and measure their collisional properties at lower temperatures. If these properties are favorable, we can then continue to evaporatively cool towards quantum degeneracy. This plan is an appealing combination of the large numbers, multiple isotopes, and excellent vacuum conditions of buffer-gas loading with the efficient cooling properties of laser cooling.

Finally, we note that the ultracold collisional properties of chromium may also be unfavorable for evaporative cooling. If that is the case, we will be unable to achieve quantum degeneracy with evaporative cooling.

Other atoms

The problems encountered while evaporatively cooling buffer-gas-loaded chromium are worrisome not only for the future of atomic chromium, but for other evaporative cooling experiments starting with buffer-gas loading. Little evaporative cooling has been conducted in this cold-collision, many-partial-wave regime. If the large in-

wave resonance, this resonance may "freeze out" at considerably higher temperatures.

elastic rate is a symptom of a shape resonance, will similar collisional problems be encountered with all species in this temperature regime?[17]

Reference [83] observed buffer-gas-loaded europium magnetically trapped in an anti-Helmholtz trap at a temperature of $\sim$ 200 mK. Similar to ^{52}Cr, the observed Eu–Eu inelastic loss rate coefficient was a large $(2.5 \pm 1.5) \times 10^{-13}$ cm^3 s^{-1}, suggesting that this may be a general trend.

Nevertheless, we believe that the collisional problems encountered with chromium will *not* be universal. Whether the dipolar loss originates in chromium's large magnetic moment or in a large spin-orbit coupling, not all atoms will share these properties with chromium; there is no reason to expect all species will exhibit similar behavior. Indeed, preliminary calculations of the evaporative cooling behavior of sodium in this temperature range indicate that this temperature regime is as favorable, if not more so, than the ultracold limit [247]. However, given the high dipolar loss observed for both 7 μ_B atomic europium and 6 μ_B atomic chromium, along with the expected scaling of the spin-spin dipolar interaction (as discussed in Section 6.7) it may be judicious to avoid atoms with large magnetic moments.

We remain optimistic that, with the right atomic system, quantum degeneracy can be achieved through buffer-gas loading, magnetic trapping, and evaporative cooling.

[17] We expect shape resonances to be present for almost all atoms in this temperature range.

Appendix A

Spectrum Fitting

The majority of the atomic and molecular data in this thesis are obtained by fitting the observed spectrum of the atoms (or molecules) in the magnetic trap. To do so, one must know the structure and natural lifetimes of the atomic and molecular states and their Zeeman shifts. Unfortunately, even with this information there is no simple way to analytically convert the observed spectrum directly into the distribution of atoms within the trap. Instead, we simulate the spectrum of a thermal distribution of atoms in the trap, and vary the number and temperature until a good fit is obtained. While this technique cannot be used with distributions of atoms that are far out of thermal equilibrium, it typically fits our data quite well.

A.1 The two-level atom and inhomogeneous broadening

The underlying physics is straightforward. A two-level atom (in the absence of external fields, with an electric dipole allowed transition and in the limit of weak, continuous illumination) has a photon scattering cross-section of

$$\sigma_{2-\text{level}}(\omega) = (3/2\pi)\lambda_0^2 \cdot \frac{(\Gamma/2)^2}{(\omega-\omega_0)^2 + (\Gamma/2)^2} \tag{A.1}$$

near resonance, for photons of the appropriate polarization for driving the transition. Here, Γ, ω_0, and λ_0 are the natural linewidth, angular frequency, and wavelength ($\lambda_0 = 2\pi c/\omega_0$) of the transition, and ω the angular frequency of the scattering photon [127].

The frequency of the transition (ω_0) can be shifted by external fields, the atomic velocity, or the presence of other atoms. The dominant broadening in our experiments is due to the Zeeman shifts in the large, inhomogeneous magnetic fields of the trap. The Zeeman shift arises from the mismatch of the magnetic moments of the ground (g) and excited (e) states of the atom, and is given by

$$\Delta\omega_0 = \frac{(\mu_e - \mu_g)\cdot B}{\hbar} \equiv \frac{\Delta\mu \cdot B}{\hbar} \tag{A.2}$$

Because the Zeeman broadening arises from the magnetic field, which in turn is determined by the atom's location in the trap, our Zeeman broadened spectrum serves as a sensitive probe of the spatial distribution of the atoms. Conversely, because the additional Doppler broadening is often unresolvable, we have no direct way to accurately measure the velocity distribution of the atoms in the trap. However, we would expect the spatial and velocity distributions to typically be in thermal equilibrium with each other.

To calculate the optical density (OD) experienced by an infinitesimal beam propagating through our trap along $\hat{\mathbf{z}}$ at a distance ρ from the trap center and an angle φ, we simply need to integrate the atom density n times its light-scattering cross-section over the length of the trap.

$$OD(\omega, \rho, \varphi) = \int dz\ n(z, \rho) \cdot \sigma(\omega, \mathbf{B}(z, \rho, \varphi)) \tag{A.3}$$

For a retroreflected beam, the OD is a factor of 2 larger. However, the real cross-section $\sigma(\omega)$ differs from the ideal two-level σ due to complications introduced by the the internal structure of the atom, as discussed in Section A.3.

A.2 The atomic distribution and the probe laser

Atom distribution

The distribution of atoms in the trap is modeled as a Boltzmann distribution truncated in position by the trap edge. The density n is given as a function of the peak density n_0 by $n(r) = n_0 \cdot e^{-\mu B(r)/k_{\mathrm{B}}T}$. This spatial truncation tends to overestimate the density of atoms near the trap edge because it includes atoms which lie on untrapped orbits. In the limit of large η, it should be a very good approximation.

Probe beam

The probe beam is modeled as a linearly polarized beam with either a uniform, circular intensity profile (produced in the experiment by passing a large diameter linearly polarized laser beam through a small, near iris) or the intensity profile of the central lobe of an Airy function (produced by a distant, small iris, with the outer lobes blocked by a near iris). We ignore any effects of diffraction from the near iris.

The total power transmitted as a function of frequency (which is what is compared to the data) is calculated by numerically integrating the transmitted power spectra of an infinitesimal beam (Equation A.3) over this beam profile. At each position, the optical density is calculated as a function of frequency. In the case of multiple species and multiple transitions, the OD's of each trapped state and possible transition are computed separately and summed to provide the total OD. The fraction of power transmitted is simply $T(\omega, \rho, \varphi) = e^{-OD(\omega,\rho,\varphi)}$, which is then integrated over the beam profile to obtain the spectrum $T(\omega)$.

A.3 Multi-level atoms and polarization effects

For simplicity, we will restrict our initial discussion of "multi-level" atoms to the case of an atom with two electronic levels but nonzero J.[1] Such an atom is no longer a two-level system due to the presence of multiple m_J sublevels. The additional considerations involved for atoms with hyperfine structure, multiple electronic states, and molecules (with rotation and vibrational structure) are discussed in Section A.6. The additional complications posed by these systems are straightforward to incorporate in a similar manner.

As seen in Equation A.1, a two-level atom always has the same on-resonance light-scattering cross-section: $\sigma_{2-\text{level}}(\omega = \omega_0) = (3/2\pi)\lambda_0^2$ (for photons of the optimal polarization to drive the transition). This cross-section is independent of the oscillator strength ($f_{eg} = (2m\omega_0/\hbar) \cdot |\langle g|z|e\rangle|^2$) of the transition. The physics behind this, along with a derivation of Equation A.1, is explained in beautiful and very lengthy detail in Reference [127]; a crude explanation of the consequences follows.

The Γ terms in the denominator of Equation A.1 arise from the strength of the decay of the excited state; Γ is the true natural linewidth, determined by the radiative

[1] This is an excellent approximation for ^{52}Cr.

decay of e to all possible lower energy levels. However, one of the "Γ" terms in the numerator of Equation A.1 arises instead from the strength of the exciting $g \rightarrow e$ transition; it is the natural linewidth that would result if the only means of decay was to the original ground state. For the special case of the two-level atom, this term is equal to Γ. For a real multilevel atom, the term in the numerator is $\leq \Gamma$.

Thus, the light-scattering cross-section of a multi-level atom is reduced by the presence of additional levels to which the excited atom may decay. Specifically, it is reduced by the ratio of the actual excited state lifetime to the lifetime it would have if its only decay mechanism was spontaneous radiative decay to the state from which it was originally excited.

In the case of atoms with only two electronic levels but multiple m_J states, this "reduction" of the cross-section is obtained simply from Clebsch-Gordan coefficients.

$$\sigma = \sigma_{2-\text{level}} \cdot |\langle J_g, m_{J_g}; 1, \Delta m \mid J_e, m_{J_e}\rangle|^2$$

where Δm represents the change in atomic angular momentum imparted by the scattered photon. The Clebsch-Gordan values for the chromium transitions we observe are given in Figure H.1.

Additional complications are introduced by the polarization of the incident photon. Because the photon carries only one unit ($\hbar$) of angular momentum, $\Delta m_J = 0$ or ± 1 for an allowed transition. There are additional modifications of the cross-section due to this Δm consideration, angular momentum conservation, and the polarization of the incoming photon. In Equation A.1, the polarization of the scattered photon was chosen to maximize σ. Inside our trap, such "alignment" is generically not the case. The effects are illustrated in Figure A.1 and discussed below.

The m_J states are eigenstates of the interaction of the magnetic moment with the external field; m_J value is the projection of angular momentum along the local field B. The photon angular momentum eigenstates have angular momentum $+\hbar$ (σ^+ light) or $-\hbar$ (σ^- light) along the photon's direction of propagation. We take the direction of propagation to be $\hat{\mathbf{z}}$ (which in our experiments is always along the axis of our magnetic trap) and the angle between $\hat{\mathbf{z}}$ and the local magnetic field to be θ.

The probability that a σ^+ photon will have the proper projection along the field axis to drive a $\Delta m_J = +1$ transition is $\cos^2(\theta)$, but *only* if the projection of $\hat{\mathbf{z}}$ along $\mathbf{B}$ is positive. If not, the cross-section for driving a $\Delta m_J = +1$ is zero. Similarly, the probability that a σ^+ photon will have the proper projection to drive a $\Delta m_J = -1$

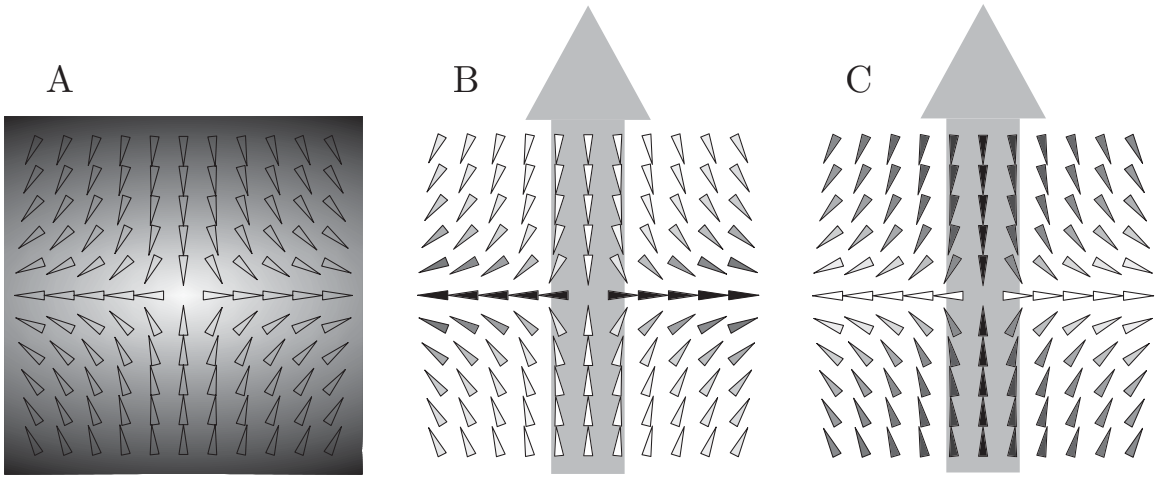

Figure A.1: An illustration of the effect of selection rules on the interaction of a linearly polarized probe laser with atoms in an anti-Helmholtz trap. Shown in figure A is a plot of the field magnitude (black indicates high field; white indicates zero field) and field direction (as shown by the arrows). Shown in figure B is a plot of the "θ" weighting factor for a linearly polarized probe laser (shown in grey) propagating in the $\hat{\mathbf{z}}$ direction driving a $\Delta m = 0$ transition. Black indicates a weighting factor of 1, while white denotes that the cross-section is zero. Shown in figure C is a plot of the weighting factor for $\Delta m = \pm 1$ transitions.
Omitted from B is an additional reduction of the cross-section due to the "ϕ" weighting factor (discussed in the text).
Omitted from C is the restriction that the σ^+ component of the linearly polarized light will only be able to drive $\Delta m = +1$ (-1) transitions on the lower (upper) half of the trap, while the σ^- component drives $\Delta m = +1$ (-1) transitions only in the upper (lower) half of the trap. Because of the symmetry of the trapping potential (ignoring gravity), this introduces no additional calculational complications, as long as care is taken to not overcount absorption.

transition is also $\cos^2(\theta)$, but only if the projection of $\hat{\mathbf{z}}$ along $\mathbf{B}$ is negative. Of course the same applies, with a sign reversal, to σ^- photons.

We probe our atoms with linearly polarized light, which contains both polarizations in equal proportion. However, because of the symmetry of the trap, both circular polarization components have equal opportunity to interact with the atoms on ± 1 transitions. This is depicted graphically in Figure A.1.

The criteria for driving a $\Delta m = 0$ transition is slightly different. The probability that the photon direction of propagation will have the proper projection along the field axis is $\sin^2(\theta)$. But there is an additional constraint relating the photon's po-

larization to the atomic polarization. If ϕ is the angle between the linearly polarized photon's polarization vector and the magnetic field in the plane perpendicular to $\hat{\mathbf{z}}$, the absorption cross-section is modified by an additional factor of $\cos^2(\phi)$, due to the matrix element coupling $|e\rangle$ and $|g\rangle$.

We represent (for brevity) the correction factors for multiple levels and for polarization effects as C_m and C_p. Combining the results of Equations A.1, A.2, and A.3, we find

$$OD(\omega,\rho,\varphi) = \frac{3\lambda_0^2}{2\pi}\cdot C_m \cdot \int dz\ \frac{C_p(\mathbf{B}(z,\rho,\varphi))\cdot n(z,\rho)\cdot(\Gamma/2)^2}{(\Gamma/2)^2+(\omega-\omega_0-\frac{\Delta\mu\cdot B(z,\rho)}{\hbar})^2} \tag{A.4}$$

The special case of unpolarized atoms in zero field

We examine light scattering in the limit of a small magnetic field (so that the m_J levels can be treated as degenerate) and an unpolarized sample (equal populations in the various ground m_J states). If we assume σ^+ light and use $\hat{\mathbf{z}}$ as both our light propagation and m_J quantization axis (without loss of generality, as our sample is unpolarized), we have

$$\sigma_{\text{unpolarized}}(\omega) = \frac{1}{d_g}\sum_{m_{J_g}} |\langle J_g, m_{J_g}; 1, +1 \mid J_e, m_{J_g}+1\rangle|^2 \cdot \sigma_{2-\text{level}}(\omega)$$

where d_g is the degeneracy of the ground state. For an allowed transition ($J_e = J_g$, J_g+1, or J_g-1) this simply reduces to

$$\sigma_{\text{unpolarized}}(\omega) = \frac{\lambda_0^2}{2\pi}\cdot\frac{d_e}{d_g}\cdot\frac{(\Gamma/2)^2}{(\omega-\omega_0)^2+(\Gamma/2)^2}$$

where d_e is the degeneracy of the excited state [109].

This is useful (when used in combination with Doppler broadening and other broadening mechanisms) for calculating the number of atoms produced in the absence of the magnetic trapping fields.

A.4 Actual implementation

The problem of calculating the spectrum of atoms in the trap simply boils down to one of bookkeeping: keeping track of the distribution of atoms and atomic states throughout the trap, the possible transitions and their inhomogeneous broadening

mechanisms, the probe beam profile and its overlap with the atomic distribution, the selection rules, et cetera.

The conceptually simplest way to calculate the absorption spectrum ($OD(\omega)$) of an infinitesimal beam (with specified ρ and φ) would be to numerically integrate Equation A.4 repeatedly at different value of ω. Unfortunately, this method is quite computationally demanding. Fortunately, it can be simplified because the integrations over the trap for different ω are redundant, as they involve identical fields, densities, and polarizations; the only difference is in the detuning factor in the denominator.

To simplify the computational process, we first convert our calculation of the OD from an integral in z to an integral in frequency. We define the "resonant frequency" ω' by the equation

$$\omega' = \omega_0 + \frac{\Delta\mu \cdot B(z,\rho)}{\hbar} \tag{A.5}$$

With this definition, we find

$$OD(\omega,\rho,\varphi) = \frac{3\lambda_0^2}{2\pi} \cdot C_m \cdot \int d\omega' \left|\frac{dz(\omega')}{d\omega'}\right| \cdot n(z(\omega'),\rho) \cdot C_p(\mathbf{B}(z(\omega'),\rho,\varphi)) \cdot \frac{(\Gamma/2)^2}{(\Gamma/2)^2 + (\omega-\omega')^2}$$

Where z is now an explicit function of ω' as defined by Equation A.5.

To numerically integrate this expression, we convert it into a simple sum over an array of evenly spaced ω_i' values, with spacing $\Delta\omega$:

$$OD(\omega,\rho,\varphi) = \frac{3\lambda_0^2}{2\pi} \cdot C_m \cdot \sum_i \Delta\omega \cdot \left|\frac{dz(\omega')}{d\omega'}\bigg|_{\omega_i'}\right| \cdot n(z(\omega_i'),\rho) \cdot C_p(\mathbf{B}(z(\omega_i'),\rho,\varphi)) \cdot \frac{(\Gamma/2)^2}{(\Gamma/2)^2 + (\omega-\omega_i')^2}$$

which is equivalent to

$$OD(\omega,\rho,\varphi) = \sum_i Z(\omega_i') \cdot \frac{(\Gamma/2)^2}{(\Gamma/2)^2 + (\omega-\omega_i')^2} \tag{A.6}$$

where

$$Z(\omega') = \frac{3\lambda_0^2}{2\pi} \cdot n(z(\omega_i'),\rho) \cdot |z(\omega_i' + \Delta\omega/2) - z(\omega_i' - \Delta\omega/2)| \cdot C_m \cdot C_p(\mathbf{B}(z(\omega_i'),\rho,\varphi))$$

This equation appears more complicated than a simple numerical integration of Equation A.4. Its advantage lies in the "separation" of the integrand into the term

($Z(\omega')$) which contains the majority of the computational difficulty but is independent of ω, and a simple Lorentzian. Thus, all calculations concerning atom density and magnetic fields (for an infinitesimal probe beam) need be computed only once per spectrum.

It is vital to note that our method of numerical integration will yield accurate results only if the $\Delta\omega$ spacing of the sum is smaller than the size scale of variation of the summand. Hence, we must choose $\Delta\omega \ll \Gamma$. This is inconvenient when calculating spectra much broader than the natural linewidth, and further computational speedups appropriate for such spectra are discussed in Section A.5.

As a side note, we note that because of the symmetry of the trap potential, $z(\omega')$ is a multiple-valued (two-valued) function. We typically simplify the computation process by confining $z(\omega')$ to one half of the trap and inserting the appropriate factor of two. Additionally, when no value of z will satisfy Equation A.5, $z(\omega')$ should return either 0 or the maximum trap z, as appropriate.

When it is necessary (for the data in this thesis, almost never), we can include the effects of Doppler broadening by (numerically) performing a convolution integral of the above OD with a normalized Doppler profile [182].

Integration over the beam profile

To obtain the spectrum for a real, finite size beam, we calculate the $OD(\omega)$ of an infinitesimal beam at a specified ρ and φ and convert it from $OD(\omega)$ to transmission coefficient $T(\omega)$. We then numerically integrate $T(\omega, \rho, \varphi)$ over the two-dimensional beam profile to find the total transmitted power as a function of frequency.

To speed this computation, we are fortunately able to reduce this two-dimensional integral to a single, one-dimensional integral. We do not attempt to simplify the integral over ρ: the density, fields, and field gradients depend on ρ in nontrivial ways. However, the integration over φ can be eliminated. Because of the cylindrical symmetry of our trap, all parameters *except* the orientation of the field polarization in the x-y plane are independent of φ. Hence, only C_p can have a φ dependence. For $\Delta m = \pm 1$ transitions, the transmission coefficient is independent of φ. For $\Delta m = 0$ transitions, the only consequence is that C_p will have a $\cos^2(\varphi)$ dependence, which cleanly factors out of the integral used to compute OD.

Models of the field and Zeeman shift

At the core of our spectrum computation is the calculation of the Zeeman shift as a function of position and its inverse $z(\omega')$, as given by Equation A.5. Fortunately, the Zeeman shifts of the atoms and molecules encountered in this thesis (over the field ranges used) are predominantly linear, so the constant $\Delta\mu$ approximation implicit in Equation A.5 is valid.

Additionally, in the case of large η ($\eta \gtrsim 7$), we find we can accurately model the field as a linear expansion around the trap center, which can be analytically inverted to quickly obtain $z(\omega')$. In the case of small η (especially in the case when there is measurable signal near the trap edge), we must include the real field. We obtain the magnetic field by linearly interpolating an array of numerically calculated values of $\mathbf{B}(z, \rho)$. We calculate $z(\omega')$ by recursively searching $\mathbf{B}(z, \rho)$.

A.5 Additional computational simplifications

Although the continuing and rapid increase in available computational power has reduced the importance of simplifying our spectrum simulations, when initially fitting the data we often make additional approximations to decrease the time required.

We often omit the broadening effects of the natural linewidth. This allows us to calculate the spectrum by a method which has no restriction on the spacing of points for which the density and fields is calculated.

Working from Equation A.6, if we assume $Z(\omega')$ varies very slowly compared to the Lorentzian, the Lorentzian will act similarly to a delta function, and we can approximate the sum[2] as

$$OD(\omega, \rho, \varphi) = Z(\omega) \sum_i \frac{(\Gamma/2)^2}{(\Gamma/2)^2 + (\omega_i')^2}$$

yielding $OD(\omega, \rho, \varphi) = Z(\omega) \cdot (\Delta\omega)^{-1} \cdot \pi\Gamma/2$, or, more completely,

$$OD(\omega, \rho, \varphi) = \frac{3\lambda_0^2\Gamma}{4} \cdot n(z(\omega), \rho) \cdot \frac{|z(\omega + \Delta\omega/2) - z(\omega - \Delta\omega/2)|}{\Delta\omega} \cdot C_m \cdot C_p(\mathbf{B}(z(\omega), \rho, \varphi))$$

[2]Obviously, these calculations should be done with the expression for OD still in unapproximated integral form. This method used was chosen for notational convenience and leads to an equivalent result.

where $z(\omega)$ is defined to satisfy the usual relationship $\omega = \omega_0 + \frac{\Delta\mu \cdot B(z(\omega),\rho)}{\hbar}$.

This approximation has two advantages: there is no restriction on how finely a grid we must evaluate $Z(\omega)$, and there is no numerical integration (or convolution) required. The disadvantage is obvious: it does not include the broadening effects of the natural linewidth. However, for the day-to-day fitting of Zeeman broadened spectra at $T \gtrsim 100$ mK, this is usually fine.

A.6 Molecules, hyperfine structure, multiple electronic levels, and other reductions of σ

As discussed above, the light-scattering cross-section of a multi-level atom or molecule is reduced by the presence of additional levels to which the excited atom may decay. For the $I = 0$, two-electronic-level atom, the only additional levels were the m_J states, and the modification of the light-scattering physics could be expressed in terms of Clebsch-Gordan coefficients. For light-scattering by molecules or atoms with hyperfine structure or multiple electronic levels, the underlying physics is analogous, but the mathematical factors are less concise, as discussed below.

Hyperfine Structure

For hyperfine structure ($I \neq 0$), the behavior is straightforward in both the strong-field and weak-field coupling limits. In the strong-field limit, m_J and m_I are good quantum numbers. Because the matrix element for allowed electronic dipole transitions does not directly couple to I, m_I must be unchanged in a transition. With this additional constraint, C_m, C_p, and the selection rules for m_J remain unchanged from the $I = 0$ case.

In the weak-field limit, where F and m_F are good quantum numbers, the selection rules and C_p are changed quite simply: J and m_J are replaced by F and m_F. The modification of C_m is only slightly more complicated: it must account for the reduction in cross-section due to decay to all other F and m_F levels (rather than solely different m levels, as in the $I = 0$ case).

In the intermediate field regime, neither m_F nor m_J remain good quantum numbers and the analysis becomes more complicated. Such calculations were not necessary in this thesis.

Other Electronic Levels

The presence of additional electronic levels to which the excited state can decay simply causes an additional reduction of C_m by the ratio of the decay rate to the observed state to the total decay rate Γ of the excited state. C_p is unchanged. For the atoms and molecules discussed in this thesis, the decay of the excited state is dominated by decay to the ground electronic state, so this correction factor was neglected.

Molecules

Molecules have additional modification of C_m due to the decay of the excited state to multiple rotational and vibrational states. An introduction to electronic transitions in molecules can be found in Reference [151]; a more detailed description can be found in Reference [152].

Vibration

The reduction of C_m due to the presence of other vibrational states is simply the square of the Franck-Condon coefficient of the transition probed. Somewhat analogous to the Clebsch-Gordan coefficient, the Franck-Condon coefficient describes the overlap integral of different vibrational states. For CaH and VO, we were able to obtain the relevant Frank-Condon coefficients from the literature.

Rotation

In zero field, the modification of C_m due to the presence of the R, P, and Q transitions can be calculated (for molecules with weak interaction of rotational and electronic motion) from the Hönl-London formulae [152]. In nonzero field, the Hönl-London formulae can no longer be applied, as the magnetic field breaks the degeneracy of the rotational eigenstates. Additionally, a field-induced mixing of different J states can cause significant modifications of the transition probabilities at high field [253].

In the case of CaH and VO, such corrections to the cross-section were omitted. This omission would lead to an overestimation of the true cross-section.[3] Hence,

[3]Because of the splitting of the levels by the magnetic field and our spectroscopic resolution, we excite CaH from a single $|J'', m''_J\rangle$ state and to a nondegenerate $|J', m'_J\rangle$ state, but the excited state can decay to any of multiple rotational states.

the true numbers in the trap would be larger than those stated. From a simple examination of the levels to which CaH can decay, the correction factor is estimated to be $\lesssim 4$.

It is also important to note that because of the symmetry of the states to which the strong and weak field seekers can be excited (and of the ground states to which the excited states can decay), this correction factor will be identical for CaH's $|m''_J = +1/2\rangle$ and $|m''_J = -1/2\rangle$ states, so that our comparison of their relative populations is rigorous.

A.7 The problem with $\Delta m = 0$ transitions

It should be noted that $\Delta m = 0$ transitions are typically poor choices for spectroscopic measurements of the distribution of atoms in the trap. Although certain $\Delta m = 0$ transitions are enticing because they offer smaller magnetic broadening than their $\Delta m = \pm 1$ counterparts (and therefore, under many conditions, a larger signal), the complications added by their selection rules often obscure the very information we are interested in.

The disadvantage of $\Delta m = 0$ transitions arises because the probe beam traverses the trap over its complete extent in the axial direction, but typically covers only a small region in the radial direction. Because of the geometry of the trapping fields, the probe beam can drive $\Delta m = 0$ transitions effectively only over a limited range of trapping fields, as illustrated in Figure A.1.B. Consequently, the limited distribution of atoms probed is strongly determined by the beam profile. By comparison (as shown in Figure A.1.C), probing on a $\Delta m = 1$ transition provides interaction with atoms over a complete range of trap energies.

For example, consider the ridiculous spectrum seen in our 1998 chromium trapping paper [254], shown in Figure A.2. This spectrum was taken on a ${}^7S_3 \rightarrow {}^7P_3$, $\Delta m = 0$ transition. The double-peaked curve results from the probe beam propagating along two non-overlapping paths through the cell: one near the trap center, producing the smaller, less shifted peak, the other further off-center, giving the larger peak to the left. The shape of this Δm spectrum is dominated by the specifics of the shape and location of the probe beam, making it difficult to accurately measure the distribution of atoms across the trap volume.

As an additional caveat concerning $\Delta m = 0$ transitions, the selection rules give

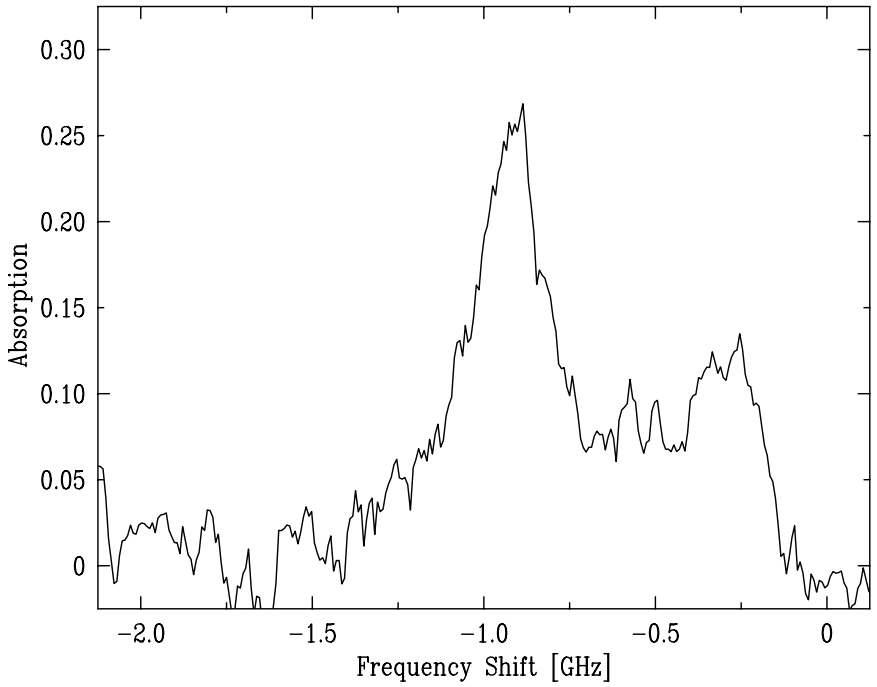

Figure A.2: An experimental spectrum of trapped ^{52}Cr, taken on its $^7S_3 \rightarrow ^7P_3$, $\Delta m = 0$ transition. The frequency shift is plotted relative to the field-free line; this transition is shifted towards negative frequencies linearly in the applied field.

rise to an additional insensitivity to atom number. As indicated in Figure A.1, the $\Delta m = 0$ probe beam absorption (at a given Zeeman shift) occurs predominantly in a "ring". Consequently, (if we do not use a camera to image the absorption) the integrated transmission of the entire beam will depend less sensitively on the atom density. This effect is accentuated if the OD at the ring is high ($\gtrsim 1$).

Appendix B

Adiabatic Expansion

Classical statistical mechanics treatment of adiabatic expansion

The entropy of trapped particles is unchanged by the adiabatic expansion of their trapping potential. To determine the behavior of of trapped particles during adiabatic expansion, we simply need to calculate the entropy of the system as a function of the temperature and trap parameters.

From Reference [255] we find the entropy S is given by

$$S = (\langle E \rangle / T) + \log[(2\pi\hbar)^{-s} \int dp' dq' \; e^{-E(p',q')/T} \;]$$

where $\langle E \rangle$ is the mean energy, and we are working in units such that $k_{\mathrm{B}} = 1$.

If we are in the classical limit ("occupation number" $\ll 1$), the first term in the above expression is a number of order unity and the second term is the logarithm of a thermodynamically large number. Hence we can drop the first term, leaving us with

$$S = \log[\; (2\pi\hbar)^{-s} \int dp' dq' \; e^{-E(p',q')/T} \;]$$

For a trapped ideal gas in a potential $V(x)$, we have $E = \frac{p^2}{2m} + V(x)$, giving

$$S = \log[\; (2\pi\hbar)^{-s} (2\pi m T)^{3/2} \int_{-\infty}^{\infty} d^3x \; e^{-V(x)/T} \;] \tag{B.1}$$

Linear potential (antihelmholtz trap)

With $V = \sqrt{(a_1 x_1)^2 + (a_2 x_2)^2 + (a_3 x_3)^2}$, Equation B.1 reduces to

$$S = \log[\; 8\pi (2\pi\hbar)^{-s} (2\pi m)^{3/2} T^{9/2} (a_1 a_2 a_3)^{-1} \;]$$

If the magnetic field is changed proportionally to a current I, the trap depth and the a_i's will scale linearly with I. So, if the trap potential is modified adiabatically, we have heating (or cooling) according to:

$$T \propto I^{2/3}$$

Harmonic potential

With $V = \frac{1}{2}m\omega_1^2 x_1^2 + \frac{1}{2}m\omega_2^2 x_2^2 + \frac{1}{2}m\omega_3^2 x_3^2$, Equation B.1 becomes

$$S = \log[\ (2\pi\hbar)^{-s}(2\pi T)^3 \frac{1}{\omega_1\omega_2\omega_3}\ ]$$

If the trap potential is modified adiabatically, we will have heating (or cooling) according to:

$$T \propto (\omega_1\omega_2\omega_3)^{1/3}$$

As the magnet current I is changed, the magnetic field will linearly with I, but $\omega \propto \sqrt{I}$, so that for adiabatic changes in I,

$$T \propto \sqrt{I}$$

Alternative derivation

Alternatively, the same results could be obtained in a simpler manner by requiring that the peak phase space density $D = n \cdot \lambda_{\mathrm{dB}}^3$ of the trapped ensemble remain constant as the trap parameters are modified.

Appendix C

Gravity

Although negligible under most conditions described in this thesis, gravity plays an important role inside traps with small field gradients. In linear potentials such as the anti-Helmholtz magnetic trap, gravity does not move the trap center, but does deform the trap potential. Below a certain magnetic field gradient, gravity abruptly eliminates the trap.

For ^{52}Cr, earth gravity (assumed to be $g = 980$ cm s^{-2}) provides a linear potential $U_g(z)$ with gradient $dU_g/dz = 0.61$ mK cm^{-1}. This is equal to the potential gradient a 6 μ_B magnetic moment atom (such as ^{52}Cr in its $m_J = +3$ state) would experience in a field gradient of 1.5 G cm^{-1}.

The magnetic field gradient along the axis of our magnet is $dB/dz = 235$ G cm$^{-1} \cdot (I/\text{Amps})$ at the trap center. The nonlinearity in the trap potential is such that all other locations along the trap axis have smaller field gradients. Consequently, at magnet currents below 6 mA there is no potential minimum in z: there is no trap. The effects of gravity on the trap potential are shown in Figure C.1 at various intermediate magnet currents.

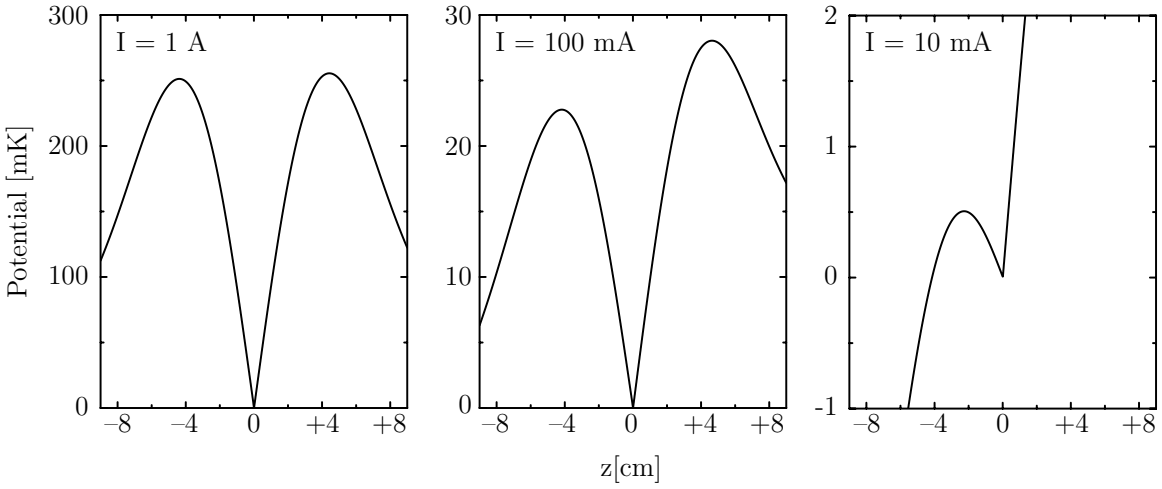

Figure C.1: The trap potential (along the $\hat{\mathbf{z}}$ axis) experienced by $m_J = +3$ chromium at magnet currents of 1000, 100 and 10 mA. At high magnet current ($I \gtrsim 1$ A), gravity has negligible effect on the trap potential. At 100 mA, gravity introduces a slight asymmetry and a small change in the trap depth along the $\hat{\mathbf{z}}$ axis. At 10 mA, gravity makes the trap highly asymmetric and reduces its depth (versus the "zero-g" potential) by a factor of ~ 4. Although the trap depth can be made arbitrarily low, there is no potential minimum for the weak-field seeking state at currents below 6 mA (not shown).

Appendix D

Majorana

In the inhomogenous magnetic fields of our trap, weak-field-seeking atoms and molecules can undergo nonadiabatic spin transitions which cause them to be lost from the trap. Hight, Robiscoe, and Thorson describe these transitions in "Nonadiabatic spin transitions in an inhomogeneous magnetic field":

> Consider a neutral atomic particle of fixed spin j moving classically in a spatially inhomogeneous magnetic field. Since the field seen in the rest frame of the particle is time varying, transitions can occur among the magnetic sublevels. Adiabatic passage occurs if the field changes slowly with respect to the Larmor frequency $\omega = g_j \mu_B H/\hbar$: then a system in state $|jm\rangle$ of the initial field evolves into a system *in the corresponding state* ($|jm\rangle$) *of the local field* at any later time. If on the other hand the field changes rapidly compared to ω, "diabatic passage" occurs: a system in state $|jm\rangle$ of the initial field remains *in that same (fixed) state*, which is a superposition of many states ($|jm'\rangle$) with respect to subsequent local fields. One then speaks of "nonadiabatic spin flips" or "Majorana transitions." For situations intermediate between adiabatic and diabatic limits, the equations of motion for the system must be solved.

Rather than attempt to accurately calculate the loss rate inside the trap, we omit all numerical factors from our calculations of Majorana loss and simply determine how the Majorana loss rate should scale with the trap parameters. We then use this scaling to obtain trap lifetimes from previously measured experimental lifetimes.

For a particle with a magnetic moment μ and a separation between adjacent Zeeman levels of $\Delta\mu$, the adiabaticity condition is violated if the magnetic field is changed on a timescale T such that $\hbar/T > \Delta\mu \cdot B$.

Within a quadrupole trap $B(\mathbf{r}) = B' \cdot r$. Atoms (which travel a distance r in a time $T = r/v$) will therefore change their Zeeman state if they travel inside a radius r_l given by[1]

$$\frac{\hbar}{r_l/v} = \Delta\mu \cdot B' \cdot r_l$$

Solving for r_l, we find $r_l = \sqrt{\frac{\hbar v}{\Delta\mu B'}}$. The rate at which the trapped particles change their magnetic sublevel is given by the flux of particles into this volume,

$$\frac{dN}{dt} = n(r_l) \cdot v \cdot r_l^2$$

where N is the total number of particles and $n(r)$ their density. We assume that r_l is small compared to the expanse of the thermal cloud, so that we can replace $n(r_l)$ with n_0, the density at the trap center. Hence,

$$\frac{dN}{dt} = n_0 \cdot \frac{\hbar v^2}{\Delta\mu B'}$$

To simplify this expression, we note that $v = \sqrt{kT/m}$, and $N = n_0 \cdot R^3$, where $R = \frac{kT}{\mu B'}$ is the spatial extent of the thermal cloud. Consequently,

$$\frac{dN}{dt} = N \cdot \frac{\hbar}{m}(\frac{kT}{\mu B'})^{-3}(\frac{kT}{\Delta\mu B'})$$

which leads to exponential decay with a time constant of

$$\tau = \frac{m}{\hbar}\frac{\Delta\mu}{\mu}R^2$$

Of course, because all numerical factors have been omitted from this calculation, the above relation is one of proportionality, not equality.

Numerical values

In Reference [92], the authors magnetically trap $|F = 1, m_F = -1\rangle$ ^{23}Na in a magnetic quadrupole trap. They estimate the Majorana lifetime to be "$500d^2$ (in seconds),

[1]Here, we assume decoherence of each separate traversal of the trap. This assumption is justified because the different inhomogeneous potentials experienced by the different Zeeman levels would be expected to give rise to decoherence within a single traversal of the trap.

where d is the cloud diameter in mm." Their unpublished experimental observations were found to be "in qualitative agreement with this model." In Reference [87], the authors magnetically trap $|F = 1, m_F = -1\rangle$ ^{87}Rb atoms in a magnetic quadrupole trap. They observe "nonadiabatic loss" with an exponential decay constant of $\tau_0 = \alpha l^2$, where "l is the half width at half maximum" and "α is $3.7(7) \times 10^4$ s/cm^2".

Scaling the latter result for ^{52}Cr trapped in the $m_J = +3$ state, we have an expected lifetime of

$$\tau = 7 \times 10^3 \text{ s } \cdot (\text{HWHM/cm})^2$$

From this, we would expect the effects of Majorana loss in the trap to be small for all data presented in this thesis. Our experimental observations are consistent with this expectation.

Appendix E

Elastic Cross-section Measurement

To determine the elastic collision rate coefficient Γ_{el}, we use a laser to selectively pump atoms out of the trap and perturb the atomic distribution from thermal equilibrium. Typical optical pumping data is shown in Section 6.6. The return of the atomic distribution to equilibrium is driven by elastic Cr–Cr collisions. By measuring this re-equilibration timescale, along with the atomic density, we can extract the collision rate coefficient.

The effects of optical pumping

We optically pump atoms out of the trap using a laser detuned from the atomic resonance to drive atoms on the magnetically shifted $\Delta m = -1$, ${}^7S_3 \rightarrow {}^7P_2$ transition. Because Zeeman broadening is the dominant broadening mechanism in our trap, this laser interacts primarily with atoms near a certain magnetic field. The atomic trap orbits (the atom cloud is collisionally thin) transverse a variety of fields. Atoms whose orbits intersect the field at which they are on resonance with the pump beam are preferentially removed from the trap. This is reflected in the spectra following optical pumping: although the entire absorption spectrum is typically reduced, it is preferentially smaller near the pumping frequency.

The return to thermal equilibrium

We consider Cr–Cr elastic scattering within the narrow magnetic field region from which atoms are optically pumped. We label the density in this region n; upon return to thermal equilibrium, it will have value n_e. To model the scattering properties, we

assume that a single scattering event will remove an atom from this region. Additionally, we assume that all atoms in this region spend all their time in an atom density n.[1] In equilibrium, the rate at which particles are scattered out of the pumping region is equal to $N_e \cdot n_e \cdot \Gamma_{el}$ (where N is the number of particles in our region of interest and N_e its equilibrium value). But in equilibrium, the rate at which particles are scattered out of a region of phase space equals the rate at which particles are scattered out, so that

$$\dot{n}_{\text{in}} = -\dot{n}_{\text{out}} = n_e^2 \cdot \Gamma_{el}$$

If the density in the region of pumping is changed to a nonequilibrium value but the rest of the distribution remains close to its equilibrium value (an accurate description of our optical pumping conditions, as shown Figure 6.16), $\dot{n}_{\text{in}}$ will be unchanged from its equilibrium value, but $\dot{n}_{\text{out}}$ would be reduced to $\dot{n}_{\text{out}} = n^2 \cdot \Gamma$. Hence,

$$\dot{n} = \Gamma_{el} \cdot (n_e^2 - n^2)$$

and

$$n(t) = n_e \cdot \tanh(n_e \cdot (\Gamma_{el} t + C))$$

As seen in Figure 6.17, our data fits this functional form well. Additionally, the collisional cross-sections obtained in this manner were (within the stated error) independent of buth the frequency at which the pumping occurred and the atomic density.

[1] This is not a particularly good assumption, as the various trap orbits transit a large range of densities. However, numerical simulations indicate that the relevant trap orbits (that is, those which intersect the magnetic field regions that we optically pump atoms from) experience an average density within a factor of two of our simple model [245]. We include this factor of two systematic uncertainty in our quoted error.

Appendix F

Wind

If a high density of buffer-gas is present in the cell, atoms will continue to be lost to evaporation and inelastic collisions, but no evaporative cooling can take place (as the atom temperature is essentially fixed by the buffer gas). Thus, once the atoms are thermalized, it is advantageous to remove the buffer-gas quickly.

As the helium buffer-gas is removed from the cell, its flow exerts a force upon particles in the trap. If the helium density is high and its flow rapid, the resulting force can cause significant loss from the trap, as seen in the atomic chromium experiments discussed in Section 6.3. These wind effects place an upper limit on the speed at which the buffer gas can be removed from the cell. In this Appendix, we estimate the force of the helium wind on trapped particles, and compare it to the experimental results observed in Section 6.3.

The relevant parameters to compare are of the helium wind and the force of the magnetic potential gradient. If the wind force equals or exceeds the force exerted by the magnetic trap, the "trapped" particles will no longer see any confining potential. We would expect them to then be lost to the walls on their diffusion timescale or faster.

The force F on a trapped particle subject to a series of impulses is simply $F =$ (Average Impulse) $\cdot$ (Rate of Impulses). Working without close regard to numerical factors, the average net impulse imparted by a helium atom in a collision is $m_{\mathrm{He}} v_{\mathrm{Drift}}$, the helium mass times the helium drift velocity.

The rate at which these impulses occur is roughly $n_{\mathrm{He}} \sigma v_{\mathrm{Thermal}}$, where n_{He} is the helium density, σ the cross-section for collisions between the helium and the trapped particle, and v_{Thermal} the thermal velocity of the helium (which we assume is much

greater than any other velocity in the problem, as helium is lighter than the particles we typically trap). This gives us

$$F = n_{\mathrm{He}}\ \sigma\ m_{\mathrm{He}}\ v_{\mathrm{Drift}}\ v_{\mathrm{Thermal}}$$

which yields

$$F \sim 3 \times 10^{-4}\ \mathrm{K/cm}\ \cdot (\frac{n_{\mathrm{He}}}{\mathrm{cm}^{-3}})(\frac{\sigma}{\mathrm{cm}^2})(\frac{v_{\mathrm{Drift}}}{\mathrm{cm/s}})\sqrt{\frac{T}{\mathrm{K}}}$$

using Kelvin as a unit of energy.

Comparison to experiment

Evaluating the above expression for the conditions of the chromium wind loss data shown in Figure 6.11B, we find $F \sim 0.1$ K/cm $\cdot(\frac{v_{\mathrm{Drift}}}{\mathrm{cm/s}})$, to within an order of magnitude systematic uncertainty. Estimating a helium drift velocity of 10 cm/s in the cell, we find $F_{\mathrm{wind}} \sim 1$ K/cm. This force is comparable to the 6 K/cm axial (and 3 K/cm radial) potential gradient experienced by $m_J = +3$ chromium in the magnetic trap used. To within the accuracy of these calculations, the loss observed is consistent with loss due to helium wind.

Appendix G

Noise

G.1 Shot noise

The only fundamental noise source in our spectroscopic measurements is shot noise. When performing absorption spectroscopy with a (unsqueezed, coherent state) probe beam detected by a photomultiplier tube (PMT), the pulses produced by the PMT exhibit Poissonian statistics. If a beam would, on average, produce N photoelectrons at the photocathode, this number will exhibit fluctuations of approximately $\sqrt{N}$.[1]

For convenience relating these results to experimental parameters, we will express our quantities in terms of the PMT output current I. If the average current is I, and the photomultiplier tube gain is G (meaning that, on average, one photoelectron emitted from the photocathode produces G electrons at the anode), then the average number of photoelectrons N emitted in a time τ is

$$N \sim \frac{(I/\mathrm{A}) \cdot (\tau/\mathrm{s})}{1.6 \times 10^{-19} \cdot G}$$

The $\sqrt{N}$ fluctuations result in current fluctuations of

$$I_{\mathrm{Noise}} \sim \sqrt{N} \cdot \frac{G \cdot 1.6 \times 10^{-19}\ \mathrm{A}}{\tau/\mathrm{s}}$$

Converting from considerations of a time window τ to the equivalent bandwidth

[1] All noise calculations in this Appendix are approximate; various small numerical factors are disregarded and the terms "noise", "average fluctuations", and "RMS fluctuations" are used loosely.

$\Delta\nu \sim \tau^{-1}$, we expect current fluctuations of

$$I_{\text{Noise}} \sim \sqrt{G \cdot (I/\text{A}) \cdot (\Delta\nu/\text{Hz})} \cdot 4 \times 10^{-10}\ \text{A}$$

For the typical parameters from our absorption spectroscopy of chromium, with $G = 10^6$ and a photocurrent of 1 μA (corresponding to a probe power of a few nW), we would expect the shot noise to give noise on the order of 10 nA in a $\Delta\nu = 1$ kHz bandwidth. This would limit absorption spectroscopy to a sensitivity of 1 part in 100 in a 1 ms measurement.

While the shot noise is reduced by operating at higher probe powers, it is frequently desirable to operate at low beam intensities to avoid perturbing the atoms during their measurement. Additionally, technical noise sources, as described in Section G.4, eventually become the limiting factor in our absorption sensitivity.

G.2 Electrical noise

We measure the photomultiplier current by converting it into a voltage with a resistor. The thermal noise of the resistor, called Johnson (or Nyquist) noise [15], contributes to the noise of our measurement. The Johnson voltage noise across a resistor R at temperature T in a bandwidth $\Delta\nu$ is

$$\langle V^2 \rangle = 4Rk_{\text{B}}T\Delta\nu$$

At 300 K, we have

$$\sqrt{\langle V^2 \rangle} = 1.3 \times 10^{-10}\ V \cdot \sqrt{(\Delta\nu/\text{Hz}) \cdot (R/\Omega)}$$

The equivalent current noise is

$$I_{\text{rms}} = 1.3 \times 10^{-10}\ A \cdot \sqrt{(\Delta\nu/\text{Hz}) \div (R/\Omega)}$$

For typical values of $\Delta\nu = 1$ kHz and $R = 10$ kΩ, this gives $I_{\text{rms}} = 0.04$ nA.

The small voltage produced by the resistor is amplified by a low-noise voltage preamplifier [238]. The voltage input noise of our voltage preamplifier is $\lesssim$ 4 nV$\cdot\sqrt{\Delta\nu/\text{Hz}}$. For typical values of $\Delta\nu = 1$ kHz and $R = 10$ kΩ, this gives an equivalent current noise contribution of $I_{\text{rms}} = 0.01$ nA.

For the data presented in this thesis, the Johnson noise and preamplifier noise are smaller than the shot noise. Hence, no appreciable noise is introduced because we use a room temperature resistor to convert our current into voltage, and no gains would be made by operating in a "pulse-counting" mode.

G.3 Absorption vs. fluorescence spectroscopy

Following the shot noise analysis of Section G.1, if we probe an atomic cloud of absorption A (and transmission $T = 1 - A$) with n_p photons, and have a detector of quantum efficiency Q, we expect to observe an average of $N = T \cdot Q \cdot n_p$ photoelectrons produced, with fluctuations of $\sqrt{N} = \sqrt{T \cdot Q \cdot n_p}$. We are interested in measuring the absorption, so our signal is proportional to $(1-T) \cdot Q \cdot n_p$, and the noise proportional to $\sqrt{T \cdot Q \cdot n_p}$. Hence the shot noise limit for the signal-to-noise of an absorption measurement is given by

$$\frac{\text{signal}}{\text{noise}} = \sqrt{Q \cdot n_p} \cdot \frac{A}{\sqrt{T}}$$

For fluorescence spectroscopy, we detect scattered photons, so that if we probe with n_p photons, we expect to observe on average $N = A \cdot Q \cdot C \cdot n_p$ photoelectrons, where C is the capture efficiency of our detector system (the ratio of the number of photons reaching the photodetector to the number of probe photons absorbed). The shot noise fluctuations of this value are, of course, $\sqrt{N} = \sqrt{A \cdot Q \cdot C \cdot n_p}$, leading to a signal-to-noise of our fluorescence detection of

$$\frac{\text{signal}}{\text{noise}} = \sqrt{Q \cdot n_p} \cdot \sqrt{C} \cdot \frac{A}{\sqrt{A}}$$

Comparing the shot-noise limitations of fluorescence spectroscopy and absorption spectroscopy, we find that absorption measurements are favored at high optical densities, and fluorescence at low optical densities; the break-even point is

$$A = \frac{C}{1 + C}$$

Absorption spectroscopy provides better signal-to-noise for $A > \frac{C}{1+C}$, and fluorescence gives higher signal-to-noise for $A < \frac{C}{1+C}$.

In our experiments, the photon capture efficiency for molecular fluorescence is small. The photodetector is placed a significant distance from the atoms and molecules, we detect only those molecule-scattered photons which are frequency shifted, and the transmission of the color-discrimination filters further reduces the collection efficiency. We estimate that typical values of the capture efficiency are $C \sim 10^{-4}$.

Consequently, absorption spectroscopy is superior for the high optical densities encountered with atomic chromium spectroscopy, while fluorescence is superior for the low optical densities of our Zeeman-broadened CaH spectra (see Figure 3.13) and long-time observations of VO.

G.4 Technical noise

Absorption

For low probe beam powers, such as those typically used in the chromium experiments, we have an absorption noise level approaching the shot noise limit. At higher beam powers, as the shot noise becomes lower, technical problems dominate. Common technical problems are listed below.

Power fluctuations in the probe beam give rise to erroneous absorption signal. By intensity stabilizing the probe beam intensity and monitoring the reference beam power, the influence of these power fluctuations can be greatly reduced.

Beam pointing instabilities cause additional fluctuations in the probe power level which also mask the absorption signal. The cell top mirror is most frequent and egregious cause of beam pointing problems (due to vibrations in the dilution refrigerator). By mechanically anchoring the cell to the IVC, these pointing problems can be reduced.

Fabry-Perot etalon effects in the probe beam cause the probe beam power to fluctuate as a function of frequency. This frequency-dependent transmission, when combined with long-term laser frequency drift, gives rises to changes in transmission which obscure small absorption signals.

The aforementioned noise sources cause error in our measurements, and can limit the lowest optical densities which can be observed. Additional errors are introduced into our measurements by errant scattered probe light falling on our detectors. Such scattered light limits the accuracy of our measurements primarily at high OD; not much of our data is taken under such conditions.

Fluorescence

Additional noise contributions to our fluorescence measurements arise from photocurrent induced by sources other than the fluorescing atoms. Although the overall level of such errant signal can be subtracted out from our measurements, the shot noise associated with it cannot.

The simplest example of this is the detector dark current: the photocurrent that flows in the absence of incident light. The dark current can be reduced by cooling our photomultiplier tube (this was not done in the experiments in this thesis). Another

significant source of erroneous photocurrent is the ambient light in the room. This is reduced by shielding the PMT, reducing the room lights to low levels, and by placing narrow-band color filters over the PMT faces. Typically, the most problematic source of errant signal and shot noise is "false fluorescence": probe light scattered by the apparatus. A significant reduction in such scattered light is obtained by using color filters to block elastically scattered light and pass the red-shifted molecular fluorescence.[2]

At low optical densities, the shot noise from these sources provides the limiting noise floor for fluorescence detection.

[2]Because chromium is quite inefficient at emitting frequency-shifted light, the copious apparatus-scattered light precludes the efficient use of fluorescence spectroscopy. Fortunately, the high chromium optical density naturally favors absorption spectroscopy.

Appendix H

Cr Information

Chromium is found in four naturally occurring isotopes, listed in Table H.1. Three of these are zero-nuclear spin Bosons, and the fourth is a Fermion with $I = 3/2$. The Fermion is spectroscopically distinguishable from the Boson isotopes predominantly through its hyperfine structure. The Boson isotopes can be differentiated spectroscopically by their isotopic shifts, listed in Table H.2. Unfortunately, the ^{54}Cr isotope shift is too small for us to resolve it from the ^{52}Cr peak.

A	Natural abundance	Nuclear Spin I	Neutral atom symmetry
50	4.35 %	0	Boson
52	83.79 %	0	Boson
53	9.50 %	3/2	Fermion
54	2.36 %	0	Boson

Table H.1: The stable isotopes of atomic chromium (Z=24) [155].

A	Transition	$\Delta\nu$ [10^{-3} cm^{-1}]	$\Delta\nu$ [GHz]
50	$^7S_3$–$^7P_4$	-4.4 ± 0.2	-0.132 ± 0.006
	$^7S_3$–$^7P_3$	-4.0 ± 0.1	-0.120 ± 0.003
	$^7S_3$–$^7P_2$	-3.6 ± 0.3	-0.108 ± 0.009
54	$^7S_3$–$^7P_4$	-0.0 ± 0.2	-0.000 ± 0.006
	$^7S_3$–$^7P_3$	-0.5 ± 0.2	-0.015 ± 0.006
	$^7S_3$–$^7P_2$	-0.7 ± 0.2	-0.021 ± 0.006

Table H.2: The isotopic shifts of the Boson chromium isotopes relative to ^{52}Cr [256].

Our spectroscopic detection of chromium is done via excitation from its electronic ground state, a $^7S_3$ state with shell structure $1s^2 2s^2 2p^6 3s^2 3p^6 3d^5 4s$. This state is mysteriously labeled "a", and referred to as the $a\,^7S_3$ state of chromium [257]. We excite chromium to the ^7P state with orbital structure $1s^2 2s^2 2p^6 3s^2 3p^6 3d^5 4p$,which is designated "$z\,^7P$". Of course, L and S couple via the fine structure, giving eigenstates with $J = 2$, 3, and 4. The energy levels of these states, along with their radiative lifetimes, are given in Table H.3. It should be noted that the fine structure energy splittings are extremely large compared to the interaction of the atom with the magnetic field; consequently J is always a good quantum number.

State	Energy [cm^{-1}]	Lifetime [ns]
$^7P_4$	23498.84	31.4 ± 0.2
$^7P_3$	23386.35	32.1 ± 0.2
$^7P_2$	23305.01	33.0 ± 0.2

Table H.3: The energies and natural lifetimes of the excited states of chromium used for spectroscopy in this thesis [257, 258].

Various hyperfine coupling constants of ^{53}Cr are given in Table H.4. These are important for computing the hyperfine structure of ^{53}Cr (see Appendix I) and interpreting ^{53}Cr spectra.

State	A (MHz)		B (MHz)	
$^7S_3$	-83.5985	$\pm$ 0.0015	0	
$^7P_4$	-11.8	$\pm$ 0.4	-0.6	$\pm$ 0.6
$^7P_3$	-1.5	$\pm$ 2.0	-2.0	
$^7P_2$	26.6	$\pm$ 0.8	2.7	$\pm$ 3.0

Table H.4: The A and B hyperfine structure coupling constants of ^{53}Cr [258].

A complete list of the known chromium energy levels from the ground state through the ^7P state, along with their respective g_J values, is given in Table H.5. The calculated values of g_J are computed from the usual formula

$$g_J = 1 + \frac{1.0023(J(J+1) + S(S+1) - L(L+1))}{2J(J+1)}$$

Of note in Table H.5 are the multitude of metastable states between the $^7S_3$ ground state and the ^7P states to which we excite. Radiative decay from the ^7P excited states

is dominated by decay to the ground state, as all other transitions are "forbidden" transitions. The decay of the $^7P_4$ state to a metastable state is dominated by its decay to the $^5D_4$ and $^5D_3$ states, which occur at rates of (127 ± 14) s^{-1} and (42 ± 6) s^{-1}, respectively. The ^5D state is extremely long lived, with a natural radiative lifetime ≥ 50 s [251, 252].

e$^-$ Config.	Level	J	Level [cm^{-1}]	Observed g_J	Calculated g_J
$3d^5 4p$	$z\ ^7P$	4	23498.84	1.752	1.7517
$3d^5 4p$	$z\ ^7P$	3	23386.35	1.92	1.9188
$3d^5 4p$	$z\ ^7P$	2	23305.01	2.334	2.3364
$3d^4 4s^2$	$a\ ^3P$	2	24093.16		
$3d^4 4s^2$	$a\ ^3P$	1	23512.00		
$3d^4 4s^2$	$a\ ^3P$	0	23163.27		
$3d^5 4s$	$a\ ^5P$	1	21856.94	2.5	
$3d^5 4s$	$a\ ^5P$	2	21847.88	1.847	
$3d^5 4s$	$a\ ^5P$	3	21840.84	1.60	
$3d^5 4s$	$a\ ^5G$	6	20519.60	1.33	
$3d^5 4s$	$a\ ^5G$	5	20523.94	1.25	
$3d^5 4s$	$a\ ^5G$	4	20523.69	1.13	
$3d^5 4s$	$a\ ^5G$	3	20520.92	0.93	
$3d^5 4s$	$a\ ^5G$	2	20517.40	0.37	
$3d^4 4s^2$	$a\ ^5D$	4	8307.57	1.497	
$3d^4 4s^2$	$a\ ^5D$	3	8095.21	1.501	
$3d^4 4s^2$	$a\ ^5D$	2	7927.47	1.496	
$3d^4 4s^2$	$a\ ^5D$	1	7810.82	1.501	
$3d^4 4s^2$	$a\ ^5D$	0	7750.78	0.000	
$3d^5 4s$	$a\ ^5S$	2	7593.16	2.006	
$3d^5 4s$	$a\ ^7S$	3	0.00	2.007	2.0023

Table H.5: A list of the known energy levels of Cr, up to the z^7P state [257].

Additionally, the Clebsch-Gordan coefficients for the allowed transitions between chromium's ground state and its ^7P levels are shown in Figure H.1. These are im-

portant for understanding spectra inside our trap, as discussed in Section A.3.

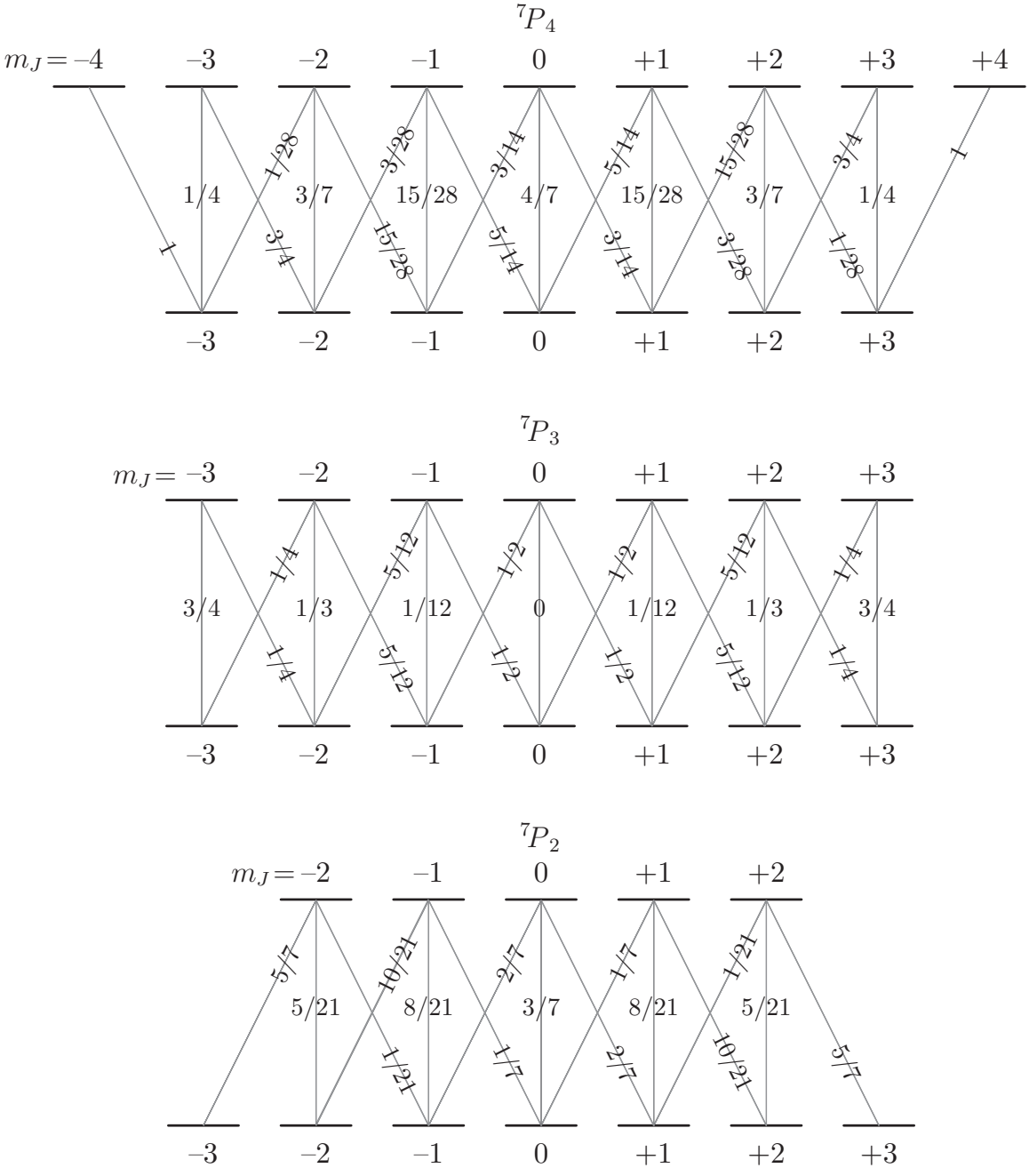

Figure H.1: The squares of the Clebsch-Gordan coefficients for single photon electric-dipole transitions from the $^7S_3$ state to the ^7P states. Generated from Mathematica's `ClebschGordan` function [109], the numbers joining the m_J states are simply $|\langle J_g, m_{J_g}; 1, \Delta m \mid J_e, m_{J_e}\rangle|^2$.

Appendix I

^{53}Cr Hyperfine Structure

Calculating the Zeeman eigenstates of ^{53}Cr is a straightforward exercise in matrix diagonalization. The treatment is identical to the standard textbook quantum mechanical calculation of hydrogen's Zeeman structure [85]. The only additional complication arises from the bookkeeping involved because of the large number of energy levels.

In the magnetic fields of our trap, I and J are good quantum numbers of ^{53}Cr, with $J = 3$ and $I = 3/2$. We concern ourselves primarily with the ground state of ^{53}Cr. The ground state is of primary importance because it is the state we trap. Additionally, because its hyperfine structure is much larger than that of the ^{7}P excited state (see Table H.4) chromium's hyperfine spectroscopic properties are dominated by the ground state.

Hamiltonian

^{53}Cr's ground state hyperfine structure is dominated by the magnetic dipole hyperfine Hamiltonian

$$\mathbf{H}_{\text{Hyp}} = C \cdot \mathbf{I} \cdot \mathbf{J} = (C/2)[\mathbf{F}^2 - \mathbf{J}^2 - \mathbf{I}^2]$$

In the limit that I and J are good quantum numbers, this reduces to

$$\mathbf{H}_{\text{Hyp}} = (C/2)[\mathbf{F}^2 - \hbar^2 J(J+1) - \hbar^2 I(I+1)]$$

The Zeeman Hamiltonian is

$$\mathbf{H}_{\text{Z}} = B((g_J \mu_B/\hbar)\mathbf{m_J} + (g_p \mu_n/\hbar)\mathbf{m_I})$$

For simplicity, we neglect the direct interaction of the nuclear moment with the externally applied field (as $g_p\mu_n \ll g_J\mu_B$), so that our combined Zeeman hyperfine Hamiltonian is

$$\mathbf{H} = B \cdot (g_J\mu_B/\hbar)\mathbf{m_J} + (C/2)[\mathbf{F}^2 - \hbar^2 J(J+1) - \hbar^2 I(I+1)]$$

Applying the $\mathbf{m_J}$ and $\mathbf{F}^2$ operators to the $|m_J, m_I\rangle$ basis set, we find

$$\mathbf{m_J}|m_J, m_I\rangle = \hbar m_J |m_J, m_I\rangle$$

and

$$\begin{aligned}\mathbf{F}^2|m_J, m_I\rangle &= \sum_{F,m_F} \mathbf{F}^2 |F, m_F\rangle\langle F, m_F|m_J, m_I\rangle \\ &= \sum_{F,m_F} \hbar^2 F(F+1)|F, m_F\rangle\langle F, m_F|m_J, m_I\rangle\end{aligned}$$

Hence, the matrix elements of the Hamiltonian in the $|m_J, m_I\rangle$ basis are:

$$\begin{aligned}\langle m'_J, m'_I|\mathbf{H}|m_J, m_I\rangle &= (B \cdot g_J\mu_B m_J - (C\hbar^2/2)[I(I+1) + J(J+1)])\,\delta_{m_J m'_J}\delta_{m_I m'_I} \\ &\quad + (C\hbar^2/2)\sum_{F,m_F} F(F+1)\langle m'_J, m'_I|F, m_F\rangle\langle F, m_F|m_J, m_I\rangle\end{aligned}$$

Equivalently, when expressed in the $|F, m_F\rangle$ basis the Hamiltonian reads:

$$\begin{aligned}\langle F', m'_F|\mathbf{H}|F, m_F\rangle &= B \cdot g_J\mu_B \sum_{m_I, m_J} m_J \langle F', m'_F|m_J, m_I\rangle\langle m_J, m_I|F, m_F\rangle \\ &\quad + (C\hbar^2/2)[F(F+1) - I(I+1) - J(J+1)]\,\delta_{FF'}\delta_{m_F m'_F}\end{aligned}$$

The hyperfine constants of ^{53}Cr (along with g_J and other chromium information) can be found in Appendix H. The constant C used in the above calculations is equal to $A/\hbar^2$ [259].

High Field Limit

In the high-field limit, the eigenstates are the $|m_J, m_I\rangle$ states. The high-field eigenvalues (to first order) are the diagonal matrix elements of H in the $|m_J, m_I\rangle$ basis.

$$E \simeq B \cdot g_J\mu_B m_J - (C\hbar^2/2)\left[I(I+1) + J(J+1) + \sum_{F,m_F} F(F+1)\,|\langle m_J, m_I|F, m_F\rangle|^2\right]$$

which is equal to

$$E \simeq B \cdot g_J\mu_B m_J + C\hbar^2 m_I \cdot m_J$$

Low Field Limit

In the low-field limit, the eigenvectors are the $|F, m_F\rangle$ states, with eigenenergies

$$E \simeq (C\hbar^2/2)[F(F+1) - J(J+1) - I(I+1)] + B \cdot m_F \mu_{\mathrm{B}} \sum_{m_I, m_J} m_J \left|\langle F', m'_F | m_J, m_I \rangle\right|^2$$

which is equal to

$$E \simeq (C\hbar^2/2)[F(F+1) - J(J+1) - I(I+1)] + B \cdot m_F g_F \mu_{\mathrm{B}}$$

where

$$g_F = g_J \cdot \frac{F(F+1) + J(J+1) - I(I+1)}{2F(F+1)}$$

Arbitrary Field

The eigenenergies at arbitary field are simply the eigenvalues of the matrix representation of the Hamiltonian. Although Mathematica [109] can find the analytical eigenvalues of our 28-by-28 matrix Hamiltonian, they are too verbose to reprint in functional form here. The eigenenergies are plotted in Figure I.1.

The Mathematica input to produce the chromium $|m_I, m_J\rangle$ basis set, calculate the explicit matrix form of the Hamiltonian, and evaluate its eigenvalues follows:

```
JJ = 3;
II = 3/2;
A = 0.0835985;
gj = 2.007;
```

defines J, I, the hyperfine A coefficient in GHz, and the g_J factor of chromium.

```
nJ = 2*JJ + 1;
nI = 2*II + 1;
n = nI*nJ;
Delta[a_, b_] := If[a == b, 1, 0];
```

sets up some useful definitions, then

```
x = Table[{Quotient[i, nI] - JJ, Mod[i, nI] - II}, {i, 0, n - 1}];
```

generates the $|m_J, m_I\rangle$ basis. To calculate the Hamiltonian in this basis,

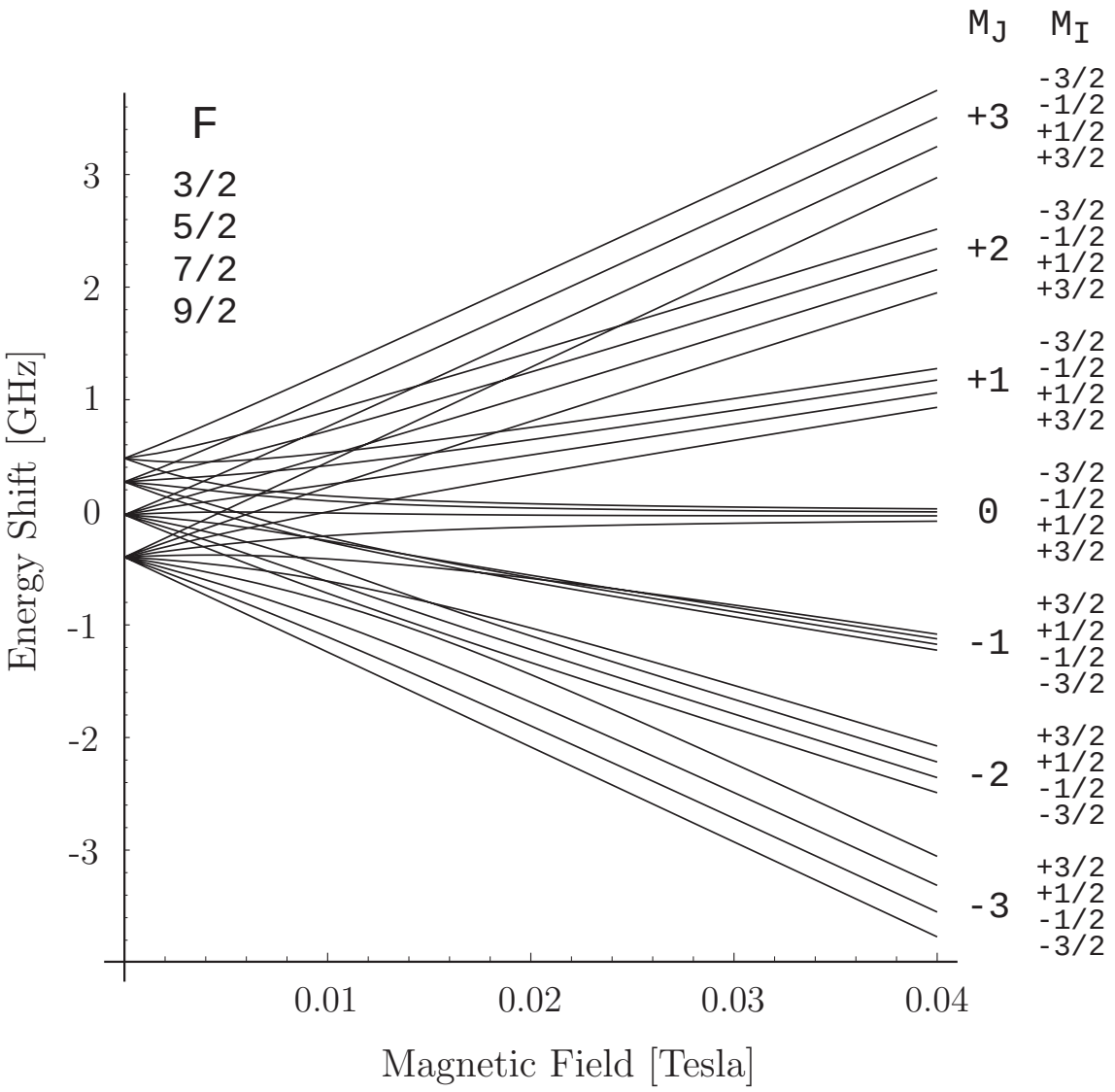

Figure I.1: ^{53}Cr ground state Zeeman structure.

```
ha = Table[(B*gj*14.0*x[[i, 1]] - (A/2)*(JJ*(JJ + 1) + II*(II + 1)))
           *Delta[x[[i, 1]], x[[j, 1]]]*Delta[x[[i, 2]],x[[j, 2]]],
           {i, n}, {j, n}];

F[mjp_, mip_, mj_, mi_, f_, mf_] :=
     (A/2)* f*(f + 1)*
     ClebschGordan[{JJ, mjp}, {II, mip}, {f, mf}]*
     ClebschGordan[{JJ, mj}, {II, mi}, {f, mf}];
```

```
SSF[mjp_, mip_, mj_, mi_] :=
     Sum[Sum[F[mjp, mip, mj, mi, f, mf], {mf, -f, f}],
         {f, Abs[JJ - II], Abs[JJ + II]}]

hb = Table[SSF[x[[i, 1]], x[[i, 2]], x[[j, 1]], x[[j, 2]]],
           {i, n}, {j, n}] ;

h = ha + hb;
```

calculates the Hamiltonian (in GHz) as a function of magnetic field `B` (in Tesla).

```
e = Eigenvalues[h];
Plot[Evaluate[e], {B, 0, 0.04}, AxesLabel -> {B[Tesla], "E" [GHz]}]
```

finds the eigenvalues and plots them.

To obtain the frequency shift of the transition as a function of the field for transitions from the ground state to the $z\ ^7P_3$ excited state, we ignore the hyperfine structure of the upper state, (its hyperfine coefficients are small compared to both the natural linewidth and the hyperfine coefficients of the ground state). The frequency shifts of various transitions can then be easily obtained by subtracting the relevant `e` eigenenergy from the excited state energy level shift.

The allowed transitions to the $^7P_3$ excited state from the four eigenstates which correspond to $m_J = +3$ states in the strong-field limit are shown in Figure I.2. From this, we identify the hyperfine states of ^{53}Cr in Figure 6.8.

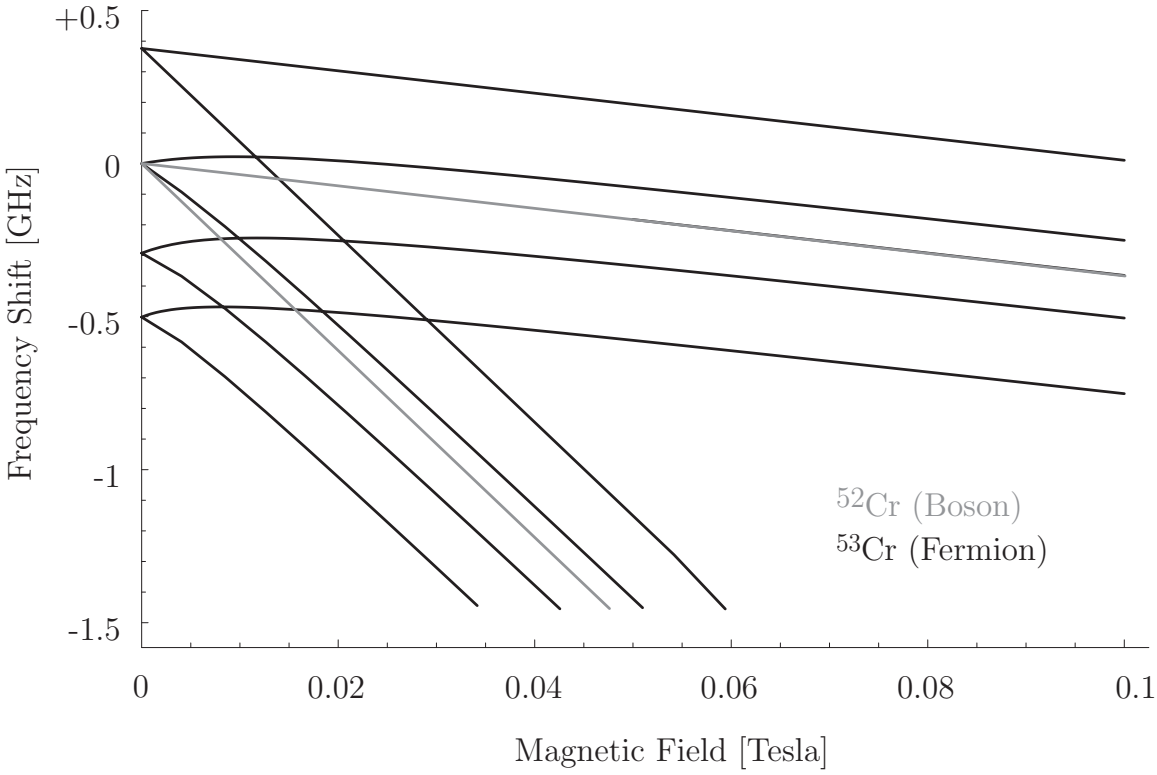

Figure I.2: ^{53}Cr transitions from the $a\ ^7S_3$ eigenstates which correspond to $m_J = +3$ states in the strong-field limit to the $^7P_3$ excited state. Also plotted are the Zeeman shifts of the ^{52}Cr transitions, assuming no relative isotope shift.

Appendix J

Symbol Definitions

A	Absorption coefficient; $A = 1 - T$
$\mathbf{B}$	Magnetic field
B	Mangetic field magnitude
D	Diffusion constant
D	Phase-space density
e	Denotes the excited state of a transition
E	Energy
$\mathbf{F}$	Total angular momentum operator: $\mathbf{F} = \mathbf{J} + \mathbf{I}$
F	Total angular momentum quantum number
g	g-factor, relates angular momentum to its magnetic moment
g	Denotes the ground state of a transition
$\hbar$	Planck's constant
$\mathbf{I}$	Nuclear spin operator
I	Nuclear spin quantum number
$\mathbf{J}$	Total non-nuclear angular momentum ($\mathbf{L} + \mathbf{S}$ for atoms, $\mathbf{L} + \mathbf{S} + \mathbf{N}$ for molecules) operator
J	Total non-nuclear angular momentum quantum number
k	Wavevector magnitude
k_{B}	Boltzman's constant
l	Orbital angular moment quantum number of two colliding atoms
$\mathbf{L}$	Electron orbital angular momentum operator
L	Electron orbital angular momentum quantum number
m_F	The projection of the total angular momentum $\mathbf{F}$ along an axis, typically along the magnetic field axis
m_I	The projection of the nuclear angular momentum $\mathbf{I}$ along an axis, typically along the magnetic field axis
m_J	The projection of the angular momentum $\mathbf{J}$ along an axis, typically along the magnetic field axis

n	Density
n_p	Peak density in the trap
n_0	Density at $t = 0$
N	Number (total number of atoms or molecules)
N	Rotational quantum number
OD	Optical Density. $T \equiv e^{-OD}$. Note that this is the standard "atomic physics" definition, which differs from the usual "optics" definition: $T = 10^{-OD}$.
r	Position
$\mathbf{S}$	Electron spin operator
S	Electron spin
t	Time
T	Temperature
T	Transmission coefficient. The fraction of power transmitted
U	Potential energy
V	Potential energy
$\hat{\mathbf{z}}$	The direction along the axis of the anti-Helmholtz trap, the bore of our magnet, and the propagation axis of our probe beam
z	Axial position (cylindrical coordinates)
$'$	Molecular notation, indicates the upper state of a transition
$''$	Molecular notation, indicates the lower state of a transition
Γ	Loss rate coefficient; various uses, as specified by subscript
Γ	Natural lifetime of an excited atomic state
Δm	The change in angular momentum projection in a transition
$\Delta\mu$	The change in the magnetic moment projection along the field in a transition
η	The ratio of the trap depth (the minimum amount of energy required to escape the trap) to $k_{\mathrm{B}}T$.
θ	The angle between the field direction and $\hat{\mathbf{z}}$
λ	Wavelength, typically of a photon
μ	Reduced mass
$\boldsymbol{\mu}$	Magnetic moment
μ	Magnetic moment projection along the field
μ_B	Bohr magneton
ν	Vibrational quantum number
ρ	Radial position (cylindrical coordinates)
σ	Cross-section
τ	Trap lifetime for exponential decay; $N(t) \propto e^{-t/\tau}$
τ_0	Diffusion lifetime in the cell the absence of a magnetic trap.

ϕ	Angle between a photon's linear polarization vector and the projection of $\mathbf{B}$ in the plane perpendicular to z
φ	Angular position (cylindrical coordinates)
ω	Angular frequency, typically of a photon

Bibliography

[1] Jr. Robert S. Van Dyck, Paul B. Schwinberg, and Hans G. Dehmelt. The electron and positron geonium experiments. In *Atomic Physics 9*, 53–74. World Scientific, 1984.

[2] Michael P. Bradley, James V. Porto, Simon Rainville, James K. Thompson, and David E. Pritchard. Penning trap measurements of the masses of ^{133}Cs, ^{87,85}Rb, and ^{23}Na with uncertainties ≤ 0.2 ppb. *Physical Review Letters* **83**, 4510–4513 (1999).

[3] D. J. Wineland and Wayne M. Itano. High-resolution spectroscopy of stored ions. *Advances in Atomic and Molecular Physics* **19**, 135–186 (1983).

[4] R. J. Rafac, B. C. Young, J. A. Beall, W. M. Itano, D. J. Wineland, and J. C. Bergquist. Sub-dekahertz ultraviolet spectroscopy of $^{199}Hg^{+}$. *Physical Review Letters* **85**, 2462–2465 (2000).

[5] C. A. Sackett, D. Kielpinski, B. E. King, C. Langer, V. Meyer, C. J. Myatt, M. Rowe, Q. A. Turchette, W. M. Itano, D. J. Wineland, and C. Monroe. Experimental entanglement of four particles. *Nature* **404**, 256–259 (2000).

[6] D. Kielpinski, V. Meyer, M.A. Rowe, C.A. Sackett, W.M. Itano, C. Monroe, and D.J. Wineland. A decoherence-free quanum memory using trapped ions. *Science* **291**, 1013–1015 (2001).

[7] Mark Kasevich and Steven Chu. Atomic interferometry using stimulated raman transitions. *Physical Review Letters* **67**, 181–184 (1991).

[8] K. S. Johnson, J. H. Thywissen, N. H. Dekker, K. K. Berggren, A. P. Chu, R. Younkin, and M. Prentiss. Localization of metastable atom beams with optical standing waves: nanolithography at the Heisenberg limit. *Science* **280**, 1583–1586 (1998).

[9] D.B. Sullivan, J.C. Bergquist, R.E. Drullinger, W.M. Itano, S.R. Jefferts, D. Lee, D. Meekhof, T.E. Parker, F.L. Walls, and D.J. Wineland. Primary atomic frequency standards at NIST. *Journal of Research of the National Institute of Standards and Technology* **106**, 47–63 (2001).

[10] H. R. Thorsheim, J. Weiner, and P. S. Julienne. Laser-induced photoassociation of ultracold sodium atoms. *Physical Review Letters* **58**, 2420–2423 (1987).

[11] P. D. Lett, K. Helmerson, W. D. Phillips, L. P. Ratliff, S. L. Rolston, and M. E. Wagshul. Spectroscopy of Na_2 by photoassociation of laser-cooled Na. *Physical Review Letters* **71**, 2200–2203 (1993).

[12] Thad Walker and Paul Feng. Measurements of collisions between laser-cooled atoms. *Advances in Atomic, Molecular, and Optical Physics* **34**, 125–170 (1994).

[13] John Weiner, Varderlei S. Bagnato, Sergio Zilio, and Paul S. Julienne. Experiments and theory in cold and ultracold collisions. *Reviews of Modern Physics* **71**, 1–85 (1999).

[14] J. L. Roberts, N. R. Claussen, Jr. James P. Burke, Chris H. Greene, E. A. Cornell, and C. E. Wieman. Resonant magnetic field control of elastic scattering in cold ^{85}Rb. *Physical Review Letters* **81**, 5109–5112 (1998).

[15] Charles Kittel and Herbert Kroemer. *Thermal Physics*. Second edition. W. H. Freeman, 1980.

[16] M. H. Anderson, J. R. Ensher, M. R. Matthews, C. E. Wieman, and E. A. Cornell. Observation of Bose-Einstein condensation in a dilute atomic vapor. *Science* **269**, 198–201 (1995).

[17] K. B. Davis, M. O. Mewes, M. R. Andrews, N. J. van Druten, D. S. Durfee, D. M. Kurn, and W. Ketterle. Bose-Einstein condensation in a gas of sodium atoms. *Physical Review Letters* **75**, 3969–3973 (1995).

[18] C.C. Bradley, C.A. Sackett, and R.G. Hulet. Bose-Einstein condensation of lithium: Observation of limited condensate number. *Physical Review Letters* **78**, 985–989 (1997).

[19] Dale G. Fried, Thomas C. Killian, Lorenz Willmann, David Landhuis, Stephen C. Moss, Daniel Kleppner, and Thomas J. Greytak. Bose-Einstein condensation of atomic hydrogen. *Physical Review Letters* **81**, 3811–3814 (1998).

[20] A. Robert, O. Sirjean, A. Browaeys, J. Poupard, S. Nowak, D. Boiron, C. I. Westbrook, and A. Aspect. A Bose-Einstein condensate of metastable atoms. *Science* **292**, 461–464 (2001).

[21] F. Pereira Dos Santos, J. Lonard, Junmin Wang, C. J. Barrelet, F. Perales, E. Rasel, C. S. Unnikrishnan, M. Leduc, and C. Cohen-Tannoudji. Bose-Einstein condensation of metastable helium. *Physical Review Letters* **86**, 3459–3462 (2001).

[22] Carl E. Wieman, David E. Pritchard, and David J. Wineland. Atom cooling, trapping, and quantum manipulation. *Reviews of Modern Physics* **71**, S253–S262 (1999).

[23] W. Ketterle, D. S. Durfee, and D. M. Stamper-Kurn. Making, probing and understanding Bose-Einstein condensates. In *Proceedings of the International School of Physics "Enrico Fermi" Course CXL,* M. Inguscio, S. Stringari, and C. E. Wieman, editors. IOS Press, 1999.

[24] H.-J. Miesner, D.M. Stamper-Kurn, M.R. Andrews, D.S. Durfee, S. Inouye, and W. Ketterle. Bosonic stimulation in the formation of a Bose-Einstein condensate. *Science* **279**, 1005–1007 (1998).

[25] E.W. Hagley, L. Deng, M. Kozuma, M. Trippenbach, Y.B. Band, M. Edwards, M.R. Doery, P.S. Julienne, K. Helmerson, S.L. Rolston, and W.D. Phillips. Measurement of the coherence of a Bose-Einstein condensate. *Physical Review Letters* **83**, 3112–3115 (1999).

[26] Jordan M. Gerton, Dmitry Strekalov, Ionut Prodan, and Randall G. Hulet. Direct observation of growth and collapse of a Bose-Einstein condensate with attractive interactions. *Nature* **408**, 692–684 (2000).

[27] J.L. Roberts, N.R. Claussen, S.L. Cornish, E.A. Donley, E.A. Cornell, and C.E. Wieman. Controlled collapse of a Bose-Einstein condensate. *Physical Review Letters* **86**, 4211–4214 (2001).

[28] R. Onofrio, C. Raman, J.M. Vogels, J.R. Abo-Shaeer, A.P. Chikkatur, and W. Ketterle. Observation of superfluid flow in a Bose-Einstein condensed gas. *Physical Review Letters* **85**, 2228–2231 (2000).

[29] J. R. Abo-Shaeer, C. Raman, J. M. Vogels, and W. Ketterle. Observation of vortex lattices in Bose-Einstein condensates. *Science* **292**, 476–479 (2001).

[30] Immanuel Bloch, Theodor W. Hänsch, and Tilman Esslinger. Atom laser with a cw output coupler. *Physical Review Letters* **82**, 3008–3011 (1999).

[31] S. Inouye, T. Pfau, S. Gupta, A.P. Chikkatur, A. Görlitz, D.E. Pritchard, and W. Ketterle. Phase-coherent amplification of atomic matter waves. *Nature* **402**, 641–644 (1999).

[32] L. Deng, E.W. Hagley, J. Wen, M. Trippenbach, Y. Band, P.S. Julienne, J.E. Simsarian, K. Helmerson, S.L. Rolston, and W.D. Phillips. Four-wave mixing with matter waves. *Nature* **398**, 218–220 (1999).

[33] Roahn Wynar, R. S. Freeland, D. J. Han, C. Ruy, and D. J. Heinzen. Molecules in a Bose-Einstein condensate. *Science* **287** (2000).

[34] C. Orzel, A. K. Tuchman, M. L. Fenselau, M. Yasuda, and M. A. Kasevich. Squeezed states in a Bose-Einstein condensate. *Science* **291**, 2386–2389 (2001).

[35] M. D. Barrett, J. A. Sauer, and M. S. Chapman. All-optical formation of an atomic Bose-Einstein condensate. *Physical Review Letters* **87**, 010404 (2001).

[36] B. DeMarco and D.S. Jin. Onset of Fermi degeneracy in a trapped atomic gas. *Science* **285**, 1703 (1999).

[37] Andrew G. Truscott, Kevin E. Strecker, William I. McAlexander, Guthrie B. Partridge, and Randall G. Hulet. Observation of Fermi pressure in a gas of trapped atoms. *Science* **291**, 2570–2572 (2001).

[38] F. Schreck, L. Khaykovich, K. L. Corwin, G. Ferrari, T. Bourdel, J. Cubizolles, and C. Salomon. Quasipure Bose-Einstein condensate immersed in a Fermi sea. *Physical Review Letters* **87**, 080403 (2001).

[39] B. DeMarco, S. B. Papp, and D. S. Jin. Pauli blocking of collisions in a quantum degenerate atomic Fermi gas. *Physical Review Letters* **86**, 5409–5412 (2001).

[40] P. Berman, editor. *Cavity Quantum Electrodynamics*. Academic Press, 1994. (Advances in Atomic, Molecular and Optical Physics Supplement 2).

[41] K. Helmerson, M. Xiao, and D. E. Pritchard. In *IQEC'90 book of abstracts*, QTHH4, 1990.

[42] Th. Busch, J. R. Anglin, J. I. Cirac, and P. Zoller. Inhibition of spontaneous emission in Fermi gases. *Europhysics Letters* **44**, 1–6 (1998).

[43] Janne Ruostekoski and Juha Javanainen. Optical linewidth of a low density Fermi-Dirac gas. *Physical Review Letters* **82**, 4741–4744 (1999).

[44] A. Görlitz, A. P. Chikkatur, and W. Ketterle. Enhancement and suppression of spontaneous emission and light scattering by quantum degeneracy. *Physical Review A* **63**, 041601(R) (2001).

[45] H. T. C. Stoof, M. Houbiers, C. A. Sackett, and R. G. Hulet. Superfluidity of spin-polarized ^{6}Li. *Physical Review Letters* **76**, 10–13 (1996).

[46] G. Bruun, Y. Castin, R. Dum, and K. Burnett. BCS theory for trapped ultracold fermions. *The European Physical Journal D* **7**, 433–439 (1999).

[47] M. Houbiers, R. Ferwerda, H. T. C. Stoof, W. I. McAlexander, C. A. Sackett, and R. G. Hulet. Superfluid state of atomic ^{6}Li in a magnetic trap. *Physical Review A* **56**, 4864–4878 (1997).

[48] John L. Bohn. Cooper pairing in ultracold ^{40}K using Feshbach resonances. *Physical Review A* **61**, 053409 (2000).

[49] L. You and M. Marinescu. Prospects for p-wave paired Bardeen-Cooper-Schrieffer states of fermionic atoms. *Physical Review A* **60**, 2324–2329 (1999).

[50] Eddy Timmermans, Kyoko Furuyab, Peter W. Milonnia, and Arthur K. Kermanc. Prospect of creating a composite Fermi-Bose superfluid. *Physical Review A* **285**, 228–233 (2001).

[51] Eddy Timmermans. Degenerate fermion gas heating by hole creation. *Physical Review Letters* **58**, 240403 (2001).

[52] Iosif B. Khriplovich and Steve K. Lamoreaux. *CP Violation Without Strangeness: Electric Dipole Moments of Particles, Atoms and Molecules*. Springer-Verlag, 1997.

[53] B. E. Sauer, Jun Wang, and E. A. Hinds. Anomalous spin-rotation coupling in the $X^2\Sigma^+$ state of YbF. *Physical Review Letters* **74**, 1554–1557 (1995).

[54] D. DeMille, F. Bay, S. Bickman, D. Kawall, Jr. D. Krause, S. E. Maxwell, and L. R. Hunter. Investigation of PbO as a system for measuring the electric dipole moment of the electron. *Physical Review A* **61**, 052507 (2000).

[55] N. Balakrishnan and A. Dalgarno. Chemistry at ultracold temperatures. *Chemical Physics Letters* **341**, 652–656 (2001).

[56] N. Balakrishnan, R. C. Forrey, and A. Dalgarno. Threshold phenomena in ultracold atom-molecule collisions. *Chemical Physics Letters* **280**, 1–4 (1997).

[57] John L. Bohn. Molecular spin relaxation in cold atom-molecule scattering. *Physical Review A* **61**, 040702(R) (2000).

[58] John L. Bohn. Inelastic collisions of ultracold polar molecules. *Physical Review A* **63**, 052714 (2001).

[59] Alan L. Migdall, John V. Prodan, William D. Phillips, Thomas H. Bergeman, and Harold J. Metcalf. First observation of magnetically trapped neutral atoms. *Physical Review Letters* **54**, 2596–2599 (1985).

[60] William D. Phillips. Nobel lecture: Laser cooling and trapping of neutral atoms. *Reviews of Modern Physics* **70**, 721–741 (1998).

[61] Steven Chu, L. Hollberg, J. E. Bjorkholm, Alex Cable, and A. Ashkin. Three-dimensional viscous confinement and cooling of atoms by resonance radiation pressure. *Physical Review Letters* **55**, 48–51 (1985).

[62] E.L. Raab, M. Prentiss, Alex Cable, Steven Chu, and D.E. Pritchard. Trapping of neutral sodium atoms with radiation pressure. *Physical Review Letters* **59**, 2631–2634 (1987).

[63] William D. Phillips and Harold Metcalf. Laser deceleration of an atomic beam. *Physical Review Letters* **48**, 596–599 (1982).

[64] Wolfgang Ketterle, Kendall B. Davis, Michael A. Joffe, Alex Martin, and David E. Pritchard. High densities of cold atoms in a dark spontaneous-force optical trap. *Physical Review Letters* **70**, 2253–2256 (1993).

[65] Andrew J. Kerman, Vladan Vuletić, Cheng Chin, and Steven Chu. Beyond optical molasses: 3D raman sideband cooling of atomic cesium to high phase-space density. *Physical Review Letters* **84**, 439–442 (2000).

[66] Dian-Jiun Han, Steffen Wolf, Steven Oliver, Colin McCormick, Marshall T. DePue, and David S. Weiss. 3D raman sideband cooling of cesium atoms at high density. *Physical Review Letters* **85**, 724–727 (2000).

[67] Tetsuya Ido, Yoshitomo Isoya, and Hidetoshi Katori. Optical-dipole trapping of Sr atoms at a high phase-space density. *Physical Review A* **61**, 061403(R) (2000).

[68] Harald F. Hess, Greg P. Kochanski, John M. Doyle, Naoto Masuhara, Daniel Kleppner, and Thomas J. Greytak. Magnetic trapping of spin-polarized atomic hydrogen. *Physical Review Letters* **59**, 672–675 (1987).

[69] R. van Roijen, J. J. Berkhout, S. Jaakkola, and J. T. M. Walraven. Experiments with atomic hydrogen in a magnetic trapping field. *Physical Review Letters* **61**, 931–934 (1988).

[70] T. J. Greytak, D. Kleppner, D. G. Fried, T. C. Killian, L. Willmann, D.Landhuis, and S.C.Moss. Bose-Einstein condensation in atomic hydrogen. *Physica B* **280**, 20–26 (2000).

[71] Giacinto Scoles, editor. *Atomic and Molecular Beam Methods*, Volume 1. Oxford University Press, 1988.

[72] M. Gupta and D. Herschbach. A mechanical means to produce intense beams of slow molecules. *Journal of Physical Chemistry A* **103**, 10670–10673 (1999).

[73] Hendrick L. Bethlem, Giel Berden, and Gerard Meijer. Decelerating neutral dipolar molecules. *Physical Review Letters* **83**, 1558–1561 (1999).

[74] Hendrick L. Bethlem, Giel Berden, André J. A. Van Roij, Floris M. H. Crompvoets, and Gerard Meijer. Trapping neutral molecules in a traveling potential well. *Physical Review Letters* **84**, 5744–5747 (2000).

[75] Hendrick L. Bethlem, Giel Berden, Floris M. H. Crompvoets, Rienk T. Jongma, André J. A. Van Roij, and Gerard Meijer. Electrostatic trapping of ammonia molecules. *Nature* **406**, 491–494 (2000).

[76] Y. B. Band and P. S. Julienne. Ultracold-molecule production by laser-cooled atom photoassociation. *Physical Review A* **51**, R4317–R4320 (1995).

[77] William C. Stwalley and He Wang. Photoassociation of ultracold atoms: A new spectroscopic technique. *Journal of Molecular Spectroscopy* **195**, 194–228 (1999).

[78] A. Fioretti, D. Comparat, A. Crubellier, O. Dulieu, F. Masnou-Seeuws, and P. Pillet. Formation of cold Cs_2 molecules through photoassociation. *Physical Review Letters* **80**, 4402–4405 (1998).

[79] A. N. Nikolov, E. E. Eyler, X. T. Wang, J. Li, H. Wang, W. C. Stwalley, and P. L. Gould. Observation of ultracold ground-state potassium molecules. *Physical Review Letters* **82**, 703–706 (1999).

[80] A. Vardi, D. Abrashkevich, E. Frishman, and M. Shapiro. Theory of radiative recombination with strong laser pulses and the formation of ultracold molecules via stimulated photo-recombination of cold atoms. *Journal of Chemical Physics* **107**, 6166–6174 (1997).

[81] P. S. Julienne, K. Burnett, Y. B. Band, and W. C. Stwalley. Stimulated Raman molecule production in Bose-Einstein condensates. *Physical Review A* **58**, R797–R800 (1998).

[82] T. Takekoshi, B. M. Patterson, and R. J. Knize. Observation of optically trapped cold cesium molecules. *Physical Review Letters* **81**, 5105–5108 (1998).

[83] Jinha Kim, Bretislav Friedrich, Dan P. Katz, David Patterson, Jonathan D. Weinstein, Robert deCarvalho, and John M. Doyle. Buffer-gas loading and magnetic trapping of atomic europium. *Physical Review Letters* **78**, 3665–3668 (1997).

[84] W. Ketterle and N.J. Van Druten. Evaporative cooling of trapped atoms. *Advances in Atomic, Molecular, and Optical Physics* **37**, 181–236 (1996).

[85] Claude Cohen-Tannoudji, Bernard Diu, and Franck Laloe. *Quantum Mechanics*. John Wiley & Sons, Inc., 1977.

[86] T. Bergeman, Gideon Erez, and Harold J. Metcalf. Magnetostatic trapping fields for neutral atoms. *Physical Review A* **35**, 1535–1546 (1987).

[87] Wolfgang Petrich, Michael H. Anderson, Jason R. Ensher, and Eric A. Cornell. Stable, tightly confining magnetic trap for evaporative cooling of neutral atoms. *Physical Review Letters* **74**, 3352–3355 (1995).

[88] Tilman Esslinger, Immanuel Bloch, and Theodor W. Hänsch. Bose-Einstein condensation in a quadrupole-Ioffe-configuration trap. *Physical Review A* **58**, R2664–R2667 (1998).

[89] M. O. Mewes, M. R. Andrews, N. J. van Druten, D. M. Kurn, D. S. Durfee, and W. Ketterle. Bose-Einstein condensation in a tightly confining dc magnetic trap. *Physical Review Letters* **77**, 416–420 (1996).

[90] J. J. Skaurai and San Fu Tuan. *Modern Quantum Mechanics*. Revised edition. Addison-Wesley, 1994.

[91] R. D. Hight, R. T. Robiscoe, and W. R. Thorson. Nonadiabatic spin transitions in an inhomogeneous magnetic field. *Physical Review A* **15**, 1079–1087 (1977).

[92] Kendall B. Davis, Marc-Oliver Mewes, Micael A. Joffe, Michael R. Andrews, and Wolfgang Ketterle. Evaporative cooling of sodium atoms. *Physical Review Letters* **74**, 5202–5205 (1995).

[93] David E. Pritchard. Cooling neutral atoms in a magnetic trap for precision spectroscopy. *Physical Review Letters* **70**, 1336–1339 (1983).

[94] John M. Doyle, Bretislav Friedrich, Jinha Kim, and David Patterson. Buffer-gas loading of atoms and molecules into a magnetic trap. *Physical Review A* **52**, R2515–R2518 (1995).

[95] M. W. Reynolds, I. Shinkoda, W. N. Hardy, A. J. Berlinsky, F. Bridges, and B. W. Statt. Electron-spin-resonance studies of spin-polarized hydrogen on the surface of liquid ^{4}He. *Physical Review B* **31**, 7503–7505 (1985).

[96] J. K. Messer and Frank C. De Lucia. Measurement of pressure-broadening parameters for the CO–He system at 4 K. *Physical Review Letters* **53**, 2555–2558 (1984).

[97] Daniel R. Willey, Richard L. Crownover, D. N. Bittner, and Frank C. De Lucia. Very low temperature spectroscopy: The pressure broadening coefficients for CO–He between 4.3 and 1.7 K. *Journal of Chemical Physics* **89**, 1923–1928 (1988).

[98] Daniel R. Willey, Richard L. Crownover, D. N. Bittner, and Frank C. De Lucia. Very low temperature spectroscopy: The pressure broadening coefficients for CH_3F between 4.2 and 1.9 K. *Journal of Chemical Physics* **89**, 6147–6149 (1988).

[99] Frank Pobell. *Matter and Methods at Low Temperatures*. Springer-Verlag, 1992.

[100] Kelvinox 300 Dilution Refrigerator. Oxford Instruments, `http://www.oxford-instruments.com/`.

[101] R. H. Sherman, S.G. Sydoriak, and T.R. Roberts. 1962 He3 scale of temperatures. *Journal of Research of the National Bureau of Standards Section A – Physics and Chemistry* **68**, 579 (1964).

[102] J. Wilks. *The Properties of Liquid and Solid Helium*. Clarendon Press, 1967.

[103] D.W. Sedgley, A.G. Tobin, T.H. Batzer, and W.R. Call. Characterization of charcoals for helium cryopumping in fusion devices. *Journal of Vacuum Science & Technology A (Vacuum, Surfaces, and Films* **5**, 2572–2576 (1987).

[104] Jinha Kim. *Buffer-gas Loading and Magnetic Trapping of Atomic Europium*. PhD thesis, Harvard University, 1997.

[105] Gianfranco Vidali, G. Ihm, Hye-Young Kim, and Milton W. Cole. Potentials of physical adsorption. *Surface Science Reports* **12**, 133–181 (1991).

[106] E. S. Sabisky and C. H. Anderson. Verification of Lifshitz theory of the van der Waals potential using liquid-helium films. *Physical Review A* **7**, 790–806 (1973).

[107] A. M. R. Schechter, J. A. Hoffmann, R. E. Packard, and J. C. Davis. Equilibrium thickness of saturated superfluid ^{3}He films on a copper substrate. *Physica B* **284–288**, 275–276 (2000).

[108] J. B. Hasted. *Physics of Atomic Collisions*. Second edition. American Elsevier, 1972.

[109] *Mathematica 4*. Wolfram Research, Inc., 1999. `http://www.wolfram.com/`.

[110] Robert A. Michniak, private communication.

[111] Peter W. Milonni and Joseph H. Eberly. *Lasers*. John Wiley & Sons, 1988.

[112] Continuum Surelite I-10. Continuum. `http://www.continuumlasers.com/`.

[113] John C. Miller and Richard F. Haglund Jr., editors. *Experimental Methods in the Physical Sciences*, Volume 30, Laser Ablation and Desorption. Academic Press, 1998.

[114] Harald F. Hess. Evaporative cooling of magnetically trapped and compressed spin-polarized hydrogen. *Physical Review B* **34**, 3476–3479 (1986).

[115] Harald F. Hess, Greg P. Kochanski, John M. Doyle, Naoto Masuhara, Daniel Kleppner, and Thomas J. Greytak. Magnetic trapping of spin-polarized atomic hydrogen. *Physical Review Letters* **59**, 672–675 (1987).

[116] A.G. Martin, K. Helmerson, V.S. Bagnato, G.P. Lafyatis, and D.E. Pritchard. rf spectroscopy of trapped neutral atoms. *Physical Review Letters* **61**, 2431–2434 (1989).

[117] N. F. Mott and H. S. W. Massey. *The Theory of Atomic Collisions.* Third edition. Oxford University Press, 1965.

[118] Alexander Roth. *Vacuum Technology.* Third, updated and enlarged edition. Elsevier Science, 1990.

[119] E. R. I. Abraham, W. I. McAlexander, C. A. Sackett, and Randall G. Hulet. Spectroscopic determination of the s-wave scattering length of lithium. *Physical Review Letters* **74**, 1315–1318 (1995).

[120] N. R. Newbury, C. J. Myatt, and C. E. Wieman. s-wave elastic collisions between cold ground-state ^{87}Rb atoms. *Physical Review A* **51**, R2680–R2683 (1995).

[121] M. J. Jamieson, A. Dalgarno, and M. Kimura. Scattering lengths and effective ranges for He–He and spin-polarized H–H and D–D scattering. *Physical Review A* **51**, 2626–2629 (1995).

[122] H. T. C. Stoof, J. M .V. A. Koelman, and B. J. Verhaar. Spin-exchange and dipole relaxation rates in atomic hydrogen: Rigorous and simplified calculations. *Physical Review B* **38**, 4688–4697 (1988).

[123] Rodger L. Gamblin and Thomas R. Carver. Polarization and relaxation processes in He^3 gas. *Physical Review* **138**, A946–A960 (1965).

[124] R. M Herman. Theory of spin exchange between optically pumped rubidium and foreign gas nuclei. *Physical Review* **137**, A1062–A1065 (1965).

[125] T. E. Chupp, M. E. Wagshul, K. P. Coulter, A. B. McDonald, and W. Happer. Polarized, high-density, gaseous ^{3}He targets. *Physical Review C* **36**, 2244–2251 (1987).

[126] John David Jackson. *Classical Electrodynamics.* 2nd edition. John Wiley & Sons Inc., 1975.

[127] Claude Cohen-Tannoudji, Jacques Dupont-Roc, and Gilbert Grynberg. *Atom-Photon Interactions: basic processes and applications.* John Wiley & Sons, Inc., 1992.

[128] J. M. Gerton, C. A. Sackett, B. J. Frew, and R. G. Hulet. Dipolar relaxation collisions in magnetically trapped ^{7}Li. *Physical Review A* **59**, 1514–1516 (1999).

[129] A. J. Moerdijk and B. J. Verhaar. Collisional two- and three-body decay rates of dilute quantum gases at ultralow temperatures. *Physical Review A* **53**, R19–R22 (1996).

[130] Frederick H. Mies, Carl J. Williams, Paul S. Julienne, and Morris Krauss. Estimating bounds on collisional relaxation rates of spin-polarized ^{87}Rb atoms at ultracold temperatures. *Journal of Research of the National Institute of Standards and Technology* **101**, 521–535 (1996).

[131] Paul J. Leo, Eite Tiesinga, Paul S. Julienne, D. K. Walter, Steven Kadlecek, and Thad G. Walker. Elastic and inelastic collisions of cold spin-polarized ^{133}Cs atoms. *Physical Review Letters* **81**, 1389–1392 (1998).

[132] J. Söding, D. Guéry-Odelin, P. Desbiolles, G. Ferrari, and J. Dalibard. Giant spin relaxation of an ultracold cesium gas. *Physical Review Letters* **80**, 1869–1872 (1998).

[133] Thad G. Walker, Joseph H. Thywissen, and William Happer. Spin-rotation interaction of alkali-metal-He-atom pairs. *Physical Review A* **56**, 2090–2094 (1997).

[134] Alexandr V. Avdeenkov and John L. Bohn. Ultracold collisions of oxygen molecules. *Physical Review A* **64**, 052703 (2001).

[135] John L. Bohn. Cold collisions of O_2 with helium. *Physical Review A* **62**, 032701 (2000).

[136] A. J. Moerdijk, H. M. J. M. Boesten, and B. J. Verhaar. Decay of trapped ultracold alkali atoms by recombination. *Physical Review A* **53**, 916–920 (1996).

[137] D. M. Stamper-Kurn, M. R. Andrews, A. P. Chikkatur, S. Inouye, H.-J. Miesner, J. Stenger, and W. Ketterle. Optical confinement of a Bose-Einstein condensate. *Physical Review Letters* **80**, 2027–2030 (1998).

[138] Paul S. Julienne and Frederick H. Mies. Collisions of ultracold trapped atoms. *Journal of the Optical Society of America B* **6**, 2257–2269 (1989).

[139] Eugene P. Wigner. On the behavior of cross sections near thresholds. *Physical Review* **73**, 1002–1009 (1948).

[140] T. Pfau, private communication.

[141] A. J. Moerdijk, B. J. Verhaar, and A. Axelsson. Resonances in ultracold collisions of ^{6}Li, ^{7}Li, and ^{23}Na. *Physical Review A* **51**, 4852–4861 (1995).

[142] Ph. Courteille, R. S. Freeland, D. J. Heinzen F. A. van Abeelen, and B. J. Verhaar. Observation of a Feshbach resonance in cold atom scattering. *Physical Review Letters* **81**, 69–72 (1998).

[143] J. Stenger, S. Inouye, M. R. Andrews, H.-J. Miesner, D. M. Stamper-Kurn, and W. Ketterle. Strongly enhanced inelastic collisions in a Bose-Einstein condensate near Feshbach resonances. *Physical Review Letters* **82**, 2422–2425 (1999).

[144] H. M. J. M. Boesten, C. C. Tsai, J. R. Gardner, D. J. Heinzen, and B. J. Verhaar. Observation of a shape resonance in the collision of two cold ^{87}Rb atoms. *Physical Review A* **55**, 636–640 (1997).

[145] Jr. James P. Burke, Chris H. Greene, John L. Bohn, H. Wang, P. L. Gould, and W. C. Stwalley. Determination of ^{39}K scattering lengths using photoassociation spectroscopy of the 0_g^1 state. *Physical Review A* **60**, 4417–4426 (1999).

[146] C. J. Williams, E. Tiesinga, P. S. Julienne, H. Wang, W. C. Stwalley, and P. L. Gould. Determination of the scattering lengths of ^{39}K from 1_u photoassociation line shapes. *Physical Review A* **60**, 4427–4438 (1999).

[147] B. DeMarco, J. L. Bohn, Jr. J. P. Burke, M. Holland, and D. S. Jin. Measurement of p-wave threshold law using evaporatively cooled fermionic atoms. *Physical Review Letters* **82**, 4208–4211 (1999).

[148] C. J. Williams and P. S. Julienne, private communication.

[149] L.-E. Berg and L. Klynning. Rotational analysis of the $A - X$ and $B - X$ band systems of CaH. *Physica Scripta* **10**, 331–336 (1974).

[150] Hans Martin. Laser spectroscopic investigations of the red band systems of CaH. *Journal of Molecular Spectroscopy* **108**, 66–81 (1984).

[151] Jeffrey I. Steinfeld. *Molecules and Radiation.* Second edition. The MIT Press, 1985.

[152] G. Herzberg. *Molecular Spectra and Molecular Structure*, Volume I. Spectra of Diatomic Molecules. Van Nostrand Reinhold, 1950.

[153] C. H. Townes and A. L. Schawlow. *Microwave Spectroscopy.* Dover Publications, Inc., 1975.

[154] C. I. Frum and H. M. Pickett. High-resolution infrared Fourier transform emission spectrsocopy of metal hydrides: $X^2\Sigma^+$ state of CaH. *Journal of Molecular Spectroscopy* **159**, 329–336 (1993).

[155] J. R. Parrington, H. D. Knox, S. L. Breneman, E. M Baum, and F. Feiner. *Chart of the Nuclides, 15th Edition.* General Electric Co., 1996.

[156] L.-E. Berg, K. Ekvall, and S. Kelly. Radiative lifetime measurement of vibronic levels of the $B^2\Sigma^+$ state of CaH by laser excitation spectroscopy. *Chemical Physics Letters* **257**, 351–355 (1996).

[157] L.-E. Berg and L. Klynning. New laboratory measurements of the $A^2\Pi$ – $X^2\Sigma$ and $B^2\Sigma$ – $X^2\Sigma$ transitions of CaH. *Astron. Astrophys. Suppl.* **13**, 325–344 (1974).

[158] T. Leininger and G. Jeung. Ab initio calculation of rovibronic transition spectra of CaH. *Journal of Chemical Physics* **103**, 3942–3949 (1995).

[159] Robert C. Richardson and Eric N. Smith, editors. *Experimental techniques in condensed matter physics at low temperatures*. Addison-Wesley, 1988.

[160] 99.999% purity indium wire. Electronic Space Products International. `http://espi-metals.com/`.

[161] Copper and Brass Sales. `http://www.copperandbrass.com/`.

[162] Aldrich Chemical #21,332-2, Calcium hydride lumps, -1+4mesh, 95%. Kept under inert atmosphere to prevent decomposition into dust. `http://www.sigma-aldrich.com/`.

[163] Stainless steel VCR metal-gasket face seal fittings. Swagelok Company. `http://www.swagelok.com/`.

[164] Vespel SP-22 polyimide, DuPont Engineering Polymers, `http://www.dupont.com`.

[165] Coherent, Inc., Santa Clara, CA. `http://www.coherentinc.com/`.

[166] Wolfgang Demtröder. *Laser Spectroscopy: basic concepts and instrumentation*. Second edition. Springer-Verlag, 1996.

[167] WA-20 VIS Wavemeter. Burleigh Instruments, Inc. `http://www.burleigh.com/`.

[168] S. Gerstenkorn and P. Luc. *Atlas du Spectre d'Absorption de la Molecule d'Iode*. Centre National de la Recherche Scientifique, 1978.

[169] IntraAction Model AOM-40 acousto-optic modulator. IntraAction Corp., `http://www.intraaction.com/`.

[170] Thorlabs CR200A. Thorlabs, `http://www.thorlabs.com`.

[171] New Focus model 5215 ND-filter wheel. New Focus Inc. `http://www.newfocus.com/`.

[172] Hamamatsu Photonics K.K., `http://www.hamamatsu.com/`.

[173] Coherent–Ealing 35-4092, 690nm (x10 nm) bandpass intereference filter. Coherent, Inc., `http://catalog.coherentinc.com/`.

[174] RG665 Schott Glass color filter, Melles-Griot 03FCG107. Melles Griot Inc., `http://www.mellesgriot.com/`.

[175] SR830 DSP Lock-In Amplifier. Stanford Research Systems, `http://www.srsys.com/`.

[176] Amuneal Manufacturing Corporation, `http://www.amuneal.com/`.

[177] 02MPQ007/001 Melles Griot MAXBRIte mirror. Melles Griot, `http://www.mellesgriot.com`.

[178] Aldrich Chemical, `http://www.sigma-aldrich.com/`.

[179] C. I. Frum, J. J. Oh, E. A. Cohen, and H. M. Pickett. Rotational spectra of the $X^2\Sigma^+$ states of CaH and CaD. *The Astrophysical Journal* **408**, L61–L64 (1993).

[180] Timothy C. Steimle, Timothy P. Meyer, Yahya Al-Ramadin, and Peter Bernath. Excited state magnetic hyperfine interactions in gas phase strontium and calcium monohydride. *Journal of Molecular Spectroscopy* **125**, 225–232 (1987).

[181] Robert Walkup, Annie Spielfiedel, Douglas Ely, William D Phillips, and David E Pritchard. Pressure-broadening rates from the near-wing amplitude. *Journal of Physics B—Atomic and Molecular Physics* **14**, 1953–1961 (1981).

[182] Rodney Loudon. *The Quantum Theory of Light*. Second edition. Oxford University Press, 1983.

[183] William W. Watson and William Bender. The Zeeman effect in the red CaH bands. *Physical Review* **35**, 1513–1523 (1930).

[184] Robert W. Field, private communication.

[185] Bretislav Friedrich, Jonathan D. Weinstein, Robert deCarvalho, and John M. Doyle. Zeeman spectroscopy of CaH molecules in a magnetic trap. *Journal of Chemical Physics* **110**, 2376–2383 (1999).

[186] N. Balakrishnan, R. C. Forrey, and A. Dalgarno. Quenching of H_2 vibrations in ultracold ^{3}He and ^{4}He collisions. *Physical Review Letters* **80**, 3224–3227 (1998).

[187] A.S-C. Cheung, R.C. Hansen, and A.J. Merer. Laser spectroscopy of VO: Analysis of the rotational and hyperfine structure of the $C^4\Sigma^- - X^4\Sigma^-(0,0)$ band. *Journal of Molecular Spectroscopy* **91**, 165–208 (1982).

[188] L. Karlsson, B. Lindgren, C. Lundevall, and U. Sassenberg. Lifetime measurements of the $A^4\Pi$, $B^4\Pi$, and $C^4\Sigma^-$ states of VO. *Journal of Molecular Spectroscopy* **181**, 274 (1997).

[189] S.N. Suchard, editor. *Spectroscopic Data*, Volume 1, Heteronuclear Diatomic Molecules. IFI/Plenum, 1975.

[190] V_2O_5 powder, 99.99%. Aldrich Chemical, `http://www.sigma-aldrich.com/`.

[191] Coherent–Ealing 35-3854, 610 nm (x10 nm) bandpass intereference filter. Coherent–Ealing, `http://catalog.coherentinc.com/`.

[192] OG 590 Schott Glass color filter, Melles-Griot 03FCG098. Melles Griot Inc., `http://www.mellesgriot.com/`.

[193] Stycast 1266 A/B epoxy. Emerson & Cuming Inc., `http://www.emersoncuming.com/`.

[194] M. Mizushima. *The Theory of Rotating Diatomic Molecules*. Wiley, 1975.

[195] K. Nagai, T. Yuri, O. Umezawa, and K. Ishikawa. Fatigue and fracture of Ti alloys at cryogenic temperatures. In *11th International Conference on Magnet Technology (MT-11)*, 754–759, 1990.

[196] O. Umezawa and K. Ishikawa. Electrical and thermal conductivities and magnetization of some austenitic steels, titanium and titanium alloys at cryogenic temperatures. *Cryogenics* **32**, 873–880 (1992).

[197] A Hall probe of unknown origin, operated with a Walker model MG-3A gaussmeter.

[198] Supercon Inc., 830 Boston Turnpike, Shrewsbury MA, USA, `http://www.anomet-supercon.thomasregister.com/`.

[199] American Magnetics, Inc., Oak Ridge, TN, `http://usit.net/ami`.

[200] *BiotSavart 2.2*. Ripplon Software Inc., 1997. `http://www.ripplon.com/`.

[201] Martin N. Wilson. *Superconducting Magnets*. Oxford University Press, 1983.

[202] Round and plate 5Al-2.5Sn titanium alloy was purchased from Trans World Alloys Inc., `http://www.twalloys.com/`. Basic chemical and mechanical tests were perfomed on samples of the titanium to confirm it was the desired alloy: a sample of alledged "5-2.5 titanium" purchased from Supra Alloys, Inc. was revealed to actually be Ti-6Al-4V in testing.

[203] Richard P. Reed and Alan F. Clark, editors. *Materials at Low Temperatures*. American Society for Metals, 1983.

[204] Robert E. Green, editor. *Machinery's Handbook*. 25th edition. Industrial Press, 1996.

[205] Dima Egorov, private communication.

[206] James E. Campbell. Structural alloys at subzero temperatures. In *Metals Handbook,* Hower E. Boyer and Timothy L. Gall, editors. American Society for Metals, desk edition, 1985.

[207] Lakeshore Model 421 Gaussmeter, with MCA-2560-WN and MCT-3160-WN axial and transverse Hall probes. Lake Shore Cryotronics, `http://www.lakeshore.com/`.

[208] 3 inch outer diameter, 0.5 inch thick BK7 windows with a two degree wedge and antireflection coatings at 425 and 532 nm. Esco Products Incorporated, `http://www.escoproducts.com`.

[209] Melles Griot 02WBK328/078: 75 mm diameter, 14 mm thick BK7 windows with a broadband antireflection coating. Melles Griot, `http://www.mellesgriot.com`.

[210] Dale G. Fried. *Bose-Einstein Condensation of Atomic Hydrogen*. PhD thesis, Massachusetts Institute of Technology, 1999.

[211] Spaulding Composites, Co., `http://www.spauldingcom.com`.

[212] AIN Plastics, `http://www.tincna.com/ain1.htm`.

[213] Kimwipes EX-L Delicate Task Wipers. Kimberly-Clark Corporation, `http://www.k-caway.com`.

[214] 0.005" diameter manganin wire with Formvar insulation. California Fine Wire Company, `http://www.califinewire.com`.

[215] Stycast 2850FT Black epoxy, cured with 24LV catalyst. Emerson & Cuming Inc., `http://www.emersoncuming.com/`.

[216] Dennis S. Greywall. Thermal-conductivity measurements in liquid ^{4}He below 0.7 K. *Physical Review B* **23**, 2152–2168 (1981).

[217] 321-6-X-3 stainless steel convoluted flexible tubing. Swagelok Company. `http://www.swagelok.com/`.

[218] P. A. Busch, S. P. Cheston, and D. S. Greywall. Properties of sintered-silver heat exchangers. *Cryogenics* **24**, 445–447 (1984).

[219] Silver Cy-Less (3 Troy oz. per gallon). Technic Inc., `http://www.technic.com/`.

[220] Silver powder, 1-3 micron, 99.9% (metals basis), Alfa Aesar Stock # 11405, Lot # I23I14. Alfa Aesar, `http://www.alfa.com`.

[221] Silver powder, 0.7-13 micron, 99.9% (metals basis). Alfa Aesar, `http://www.alfa.com`. This particular batch was found to not meet its purity specification.

[222] .014" diameter (three strand) Kevlar thread (trade size 69). McMaster-Carr, `http://www.mcmaster.com/`.

[223] L. Duband, L. Hui, and A. Lange. Thermal isolation of large loads at low temperature using kevlar rope. *Cryogenics* **33**, 643–647 (1993).

[224] G. Ventura, M. Barucci, E. Gottardi, and I. Peroni. Low temperature thermal conductivity of Kevlar. *Cryogenics* **40**, 489–491 (2000).

[225] UV-Enhanced aluminum 1" diameter round mirror, Melles Griot 02 MFG 015/028. Melles Griot, `http://www.mellesgriot.com/`.

[226] 99.995% purity chromium pieces, 1–2 mm in size, from Alfa-Aesar "Chromium pieces 2-3mm thick", Stock #38494 Lot# G01G24. Alfa Aesar, `http://www.alfa.com`.

[227] 2.484 ± 0.001 inch diameter, 0.5 inch thick BK7 window, with a 2° wedge, each face wedged 1°. Esco Products part number ZV224500C. Esco Products Incorporated, `www.escoproducts.com`.

[228] Dennis S. Greywall. Specific heat and phonon dispersion of liquid ^{4}He. *Physical Review B* **18**, 2127–2144 (1978).

[229] R. G. Goodrich, Donavan Hall, Eric Palm, and Tim Murphy. Magnetoresistance below 1 K and temperature cycling of ruthenium oxide-bismuth ruthenate cryogenic thermometers. *Cryogenics* **38**, 221–225 (1998).

[230] Dale thick film resistor model RCWP-575, Lot # 737-27. 1 kΩ resistance, 1% tolerance. Vishay Dale, `http://www.vishay.com/brands/dale/main.html`.

[231] AVS-47 Resistance Bridge. Picowatt (RV-Elektroniika Oy), `http://www.picowatt.fi/`.

[232] RX-102A-BR thick film resistor: thick ruthenium dioxide and thick bismuth ruthenate films on an aluminum oxide substrate. Lake Shore Cryotronics, `http://www.lakeshore.com/`.

[233] WA-1500 Wavemeter. Burleigh Instruments, Inc., `http://www.burleigh.com/`.

[234] Laser Analytical Systems Wavetrain CW. No longer manufactured. Superseded by the Spectra-Physics Wavetrain, Spectra-Physics, Mountain View, CA, `http://www.splasers.com/`.

[235] JML Optical SES16505 shutter; 6 mm diameter, 1 ms typical response. JML Optical Industries, Inc., `http://www.jmlopt.com/`.

[236] Thorlabs FT-200-UMT fiber. 3M multimode UV grade silica fiber w/ TECS classing; 200 μm core diameter, 255 μm cladding diameter, 500 μm buffer diameter. Thorlabs, `http://www.thorlabs.com`.

[237] Coherent–Ealing 35-3318, 430nm (x10nm) bandpass interference filter. Coherent, Inc., `http://catalog.coherentinc.com/`.

[238] SR560 Low Noise Preamplifier. Stanford Research Systems, `http://www.srsys.com/`.

[239] D.C. Douglass, J.P. Bucher, and L.A. Bloomfield. Magnetic studies of freenonferromagnetic clusters. *Physical Review B* **45**, 6341–6344 (1992).

[240] Andrew D. Sappey, Thomas K. Gamble, and David K. Zerkle. Absolute copper atom density determination in laser-ablated copper plasmas using hook spectroscopy. *Applied Physics Letters* **62**, 564–566 (1993).

[241] P. R. Huffman, C. R. Brome, J. S. Butterworth, K. J. Coakley, M. S. Dewey, S. N. Dzhosyuk, R. Golub, G. L. Greene, K. Habicht, S. K. Lamoreaux, C. E. H. Mattoni, D. N. McKinsey, F. E. Wietfeldt, and J. M. Doyle. Magnetic trapping of neutrons. *Nature* **403**, 62–64 (2000).

[242] P. C. Hendry and P. V. E. McClintock. Continuous flow apparatus for preparing isotopically pure ^{4}He. *Cryogenics* **27**, 231–138 (1987).

[243] O. J. Luiten, M. W. Reynolds, and J. T. M. Walraven. Kinetic theory of the evaporative cooling of a trapped gas. *Physical Review A* **53**, 381–389 (1996).

[244] J.M. Doyle, J.C. Sandberg, I.A. Yu, C.L. Cesar, D. Kleppner, and T.J. Greytak. Evaporative cooling of atomic hydrogen: Theory of cooling and progress towards the Bose-Einstein transition. *Physica B* **13**, 194–196 (1994).

[245] Robert deCarvalho, private communication.

[246] I would like to gratefully acknowledge and thank John S. Bohn, Paul S. Julienne, and Carl J. Williams for patient discussions explaining collisional physics.

[247] Bernard Zygelman, private communication.

[248] Kristian Helmerson, Alex Martin, and David E. Pritchard. Laser cooling of magnetically trapped neutral atoms. *Journal of the Optical Society of America B* **9**, 1988–1996 (1992).

[249] R.E. Scholten, R. Gupta, J. J. McClelland, R. J. Celotta, M. S. Levenson, and M. G. Vangel. Laser collimation of a chromium beam. *Physical Review A* **55**, 1331 (1997).

[250] A.S. Bell, J. Stuhler, S. Locher, S. Hensler, J. Mlynek, and T. Pfau. A magneto-optical trap for chromium with population repumping via intercombination lines. *Europhysics Letters* **45**, 156 (1999).

[251] C. C. Bradley, J. J. McClelland, W. R. Anderson, and R. J. Celotta. Magneto-optical trapping of chromium atoms. *Physical Review A* **61**, 053407 (2000).

[252] J. Stuhler, P. O. Schmidt, S. Hensler, J. Werner, J. Mlynek, and T. Pfau. Continuous loading of a magnetic trap. *Physical Review A* **64**, 031405(R) (2001).

[253] B. Friedrich, D. R. Herschbach, J-M. Rost, H-G. Rubahn, M. Renger, and M. Verbeek. Optical spectra of spatially oriented molecules: ICl in a strong electric field. *Journal of the Chemical Society, Faraday Transactions* **89**, 1539–1549 (1993).

[254] Jonathan D. Weinstein, Robert deCarvalho, Jinha Kim, David Patterson, Bretislav Friedrich, and John M. Doyle. Magnetic trapping of atomic chromium. *Physical Review A* **57**, R3173–3175 (1998).

[255] L. D. Landau and E. M. Lifshitz. *Statistical Physics*. 3rd edition. Pergamon Press, 1980.

[256] K. Heilig and D. Wendlandt. Isotope shift in Cr I. *Physics Letters* **25A**, 277 (1967).

[257] Charlotte E. Moore. *Atomic Energy Levels As Derived From the Analyses of Optical Spectra*, Volume II. National Bureau of Standards, 1971. NSRDS-NBS 35.

[258] T. Reinhardt, J. Maichel, M. Baumann, and J. Kruger. Hyperfine structure of the resonance lines of ^{53}Cr and lifetimes of some excited states of the Cr I spectrum. *Zeitschrift Fur Physik D* **34**, 1093–1097 (1995).

[259] Guy T. Emery. Hyperfine structure. In *Atomic, Molecular, & Optical Physics Handbook,* Gordon W. F. Drake, editor, Chapter 16. American Institute of Physics, 1996.